The University of Nottingham

UNITED KINGDOM · CHINA · MALAYSIA

Department of Civil Engineering

Faculty of Engineering

The Numerical Simulation of Plate-type Windborne Debris Flight

Bruce Kakimpa, MSc.

Thesis submitted to the University of Nottingham
for the degree of Doctor of Philosophy

December 2011

Abstract

Wind borne debris is one of the principal causes of building envelope failure during severe storms. It is often of interest in windstorm risk modelling to estimate the potential flight trajectories and impact energy of a piece of debris. This thesis presents research work aimed at the development and validation of a numerical model for the simulation of plate-type windborne debris. While a number of quasi-steady analytical models are available at present, these models are unable to account for the fluid-plate interaction in highly unstable flows. The analytical models are also limited to simple launch flow conditions and require extensive *a-priori* knowledge of the debris aerodynamic characteristics. In addition, the use of Euler angle parametrisations of orientation in the analytical models results in mathematical singularities when considering 3D six degree-of-freedom motion.

To address these limitations, a 3D Computational Fluid Dynamics (CFD) model is sequentially coupled with a quaternion based singularity-free six degree of freedom Rigid Body Dynamics (RBD) model in order to successfully simulate the flight of plate-type windborne debris. The CFD-RBD model is applied to the numerical investigation of the flow around static, forced rotating, autorotating and free-flying plates as well as the treatment of complex launch conditions. Key insights into the phenomena of plate autorotation are highlighted including the genesis of the aerodynamic damping and acceleration torques that make autorotation possible. The CFD-RBD model is then validated against measurements of rotational speed and surface pressure obtained from recent autorotation experiments. Subsequently a general 3D spinning mode of autorotation is demonstrated and the CFD-RBD model is extended to include plate translation in order to simulate windborne debris flight.

Using the CFD-RBD flight model, a parametric study of windborne debris flight is carried out and four distinct flight modes have been identified and are discussed. The flight results are contrasted against available free-flight experiments as well as predictions from existing quasi-steady analytical models and an improved quasi-steady force model based on forced rotation results is proposed.

The resulting CFD-RBD model presents the most complete numerical approach to the simulation of plate-type windborne debris, directly simulating debris aerodynamics, and incorporates complex launch flow fields in the initial conditions.

List of Publications

- Martinez-Vazquez, P., **Kakimpa, B.**, Sterling, M., Baker, C.J., Quinn, A.D., Richards, P. and Owen, J., (2011), "Pressure Field of a Rotating Square Plate", Journal of Wind and Structures (Submitted).

- **Kakimpa, B.**, Hargreaves, D.M., Owen, J.S., Martinez-Vazquez, P., Baker, C.J., Sterling, M. and Quinn, A.D., (2010), "CFD Modelling of Free-Flight and Auto-Rotation of Plate Type Debris", Journal of Wind and Structures, Vol. 13-2, pp. 169-189.

- **Kakimpa, B.**, Hargreaves, D.M. and Owen, J.S., (2011), "A Numerical Investigation of the Influence of Launch Conditions on Windborne Debris Flight", In: 13th International Conference on Wind Engineering, July 10-15.

- **Kakimpa, B.**, Hargreaves, D. and Owen, J., (2010), "A Singularity-Free Model for 3D Windborne Debris Flight", In: 9th UK Conference on Wind Engineering, University of Bristol, September 20-22.

- **Kakimpa, B.**, Hargreaves, D. and Owen, J., (2010), "Coupled CFD-RBD Modeling of Wind-borne Debris Flight", In: 5th International Symposium on Computational Wind Engineering, Chapel Hill, North Carolina, USA, May 23-27.

- **Kakimpa, B.**, Hargreaves, D. and Owen, J., (2010), "Aerodynamic Characterisation of Static and Auto-rotating plates using coupled CFD-RBD simulations", In: 5th International Symposium on Computational Wind Engineering, Chapel Hill, North Carolina, USA, May 23-27.

- **Kakimpa, B.**, Hargreaves, D. and Owen, J., (2009), "The Flight of Wind Borne Debris; An Experimental, Analytical, and Numerical Investigation - Part III: CFD Simulations", In: 7th Asia-Pacific Conference on Wind Engineering, Taipei, Taiwan, November 8-12.

- Martinez-Vazquez, P., **Kakimpa, B.**, Hargreaves, D., Baker, C., Sterling, M., Quinn, A. and Owen, J., (2009), "Predicting the flight of wind borne sheet type debris - an analytical and computational approach", In: 17th UK Conference on Computational Mechanics, April 6-8

Acknowledgements

I thank my supervisors, Dr David Hargreaves and Dr John Owen for their dedicated supervision and the invaluable support and encouragement I have received throughout the course of this research. It's been a great joy to learn from and with you. I'm also grateful to Dr Matthew Scase, my internal assessor for his constructive input and interest in this research work.

Special thanks to Prof. Chris Baker, Dr. Pedro Martinez-Vazquez, Dr. Mark Sterling, Dr Andrew Quinn and Prof. Peter Richards for their collaboration and for sharing the experimental data used to validate the numerical model presented in this research.

I also acknowledge the financial support of the University of Nottingham's Dean of Engineering research scholarship and the EPSRC, without which this research would not have been possible.

My thanks also go to all my friends and colleagues at the school, Julia, Waleed, Jean-Francois, Fangfang, Diego, Paloma, Athina, Andy, John, Karwan, Tom, Meinard, Ricardo and the latest arrival, Evgenia. My time at Nottingham would not have been the same without your friendship and support. I will always look back with fond memories.

Last but by no mean least I'm deeply grateful for the love, support and encouragement of my wife and best friend, Gloria, and the rest of my family.

Contents

List of Figures

List of Tables

Chapter 1

Introduction

1.1 Wind Related Damage

A 2003 report from the Association of British Insurers estimates the annual cost of repairing windstorm damage in the UK to be £825 million (ABI, July 2003). In addition, due to climate change, wind-related insured losses from extreme storms are expected to increase. For instance, in the case of European storms, insurance losses are now forecast to increase by at least 5% to €25-30 billion by the 2080s (ABI, June 2005).

Outside Europe, in Japan, almost US$6 billion in damages was paid out for Typhoon Mireille in September, 1991, US$18 billion for Hurricane Andrew in August, 1992, and almost US$8 billion for the 10 typhoons that made landfall on Japan in 2004 (Tamura, 2009). Hurricane Katrina killed 2,541 people in August, 2005 and caused US$28 billion economic loss in the US, Cyclone Sidr in November, 2007 killed 4,234 people and caused US$1.7 billion of losses in Bangladesh, and Cyclone Nargis in May, 2008 killed 138,366 people and caused a US$10 billion economic loss (Tamura, 2009).

While a variety of wind engineering design codes exist to aid in the structural design of buildings against wind pressure loading, according to Minor (1994) extensive evaluations of building performance in wind storms carried out in the 1970s have shown that two wind storm effects, previously not considered in design, leave the building envelopes vulnerable. These effects are *fluctuating pressures* and *windborne debris*. For building fittings such as windows, which are traditionally designed to withstand wind pressure loading, the most common failure mechanism was found to be breakage from impacts by windborne debris (Minor, 1994). Figure 1.1 illustrates wind damage to different types of structures.

1.2 Windborne Debris

Windborne debris refers to loose items, tree branches, street furniture or failed building components that are picked up and carried by the wind during severe

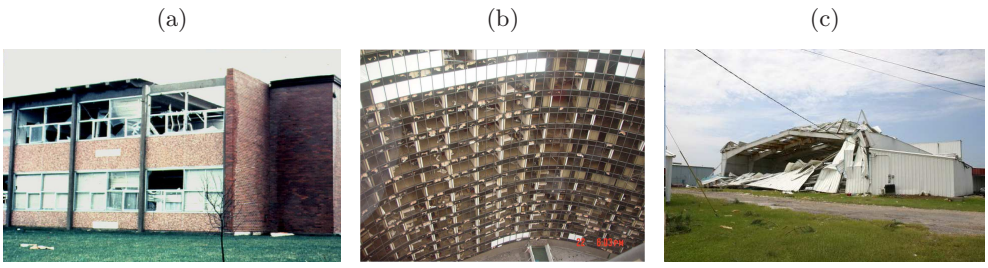

Figure 1.1: Wind damage to different types of structures. (a) Window breakage and roof uplift from an isolated low-rise structures, (b) Building facade damage to an urban high-rise structure, (c) Building envelope failure for a portal framed steel storage building (AAWE, 2011).

storm events. The most commonly used classification of wind borne debris is that presented by Wills et al. (2002) and will be used throughout this thesis. In this classification, debris is grouped into three main categories, which are illustrated in Figure 1.2.

Compact debris whose three spatial dimensions are approximately the same includes near-spherical objects such as gravel.

Sheet/Plate debris with one of the spatial dimensions much smaller than the other two includes roof tiles, roofing sheets and other cladding elements.

Rod debris with one of the spatial dimensions much larger compared to the other two includes objects such as timber pieces and bamboo rods.

Windborne debris has been established as a principal cause for the breaching of the building envelope during wind storms (Minor, 1994). This research is mainly interested in plate type windborne debris - such as roofing sheets, shingles and tiles (Figure 1.3) - which has been found to be the dominant type in a residential setting (NAHB Research Center, 2002). Plate debris also presents a unique modelling challenge due to the six-degree-of freedom motion and non-linear Fluid-Structure Interaction (FSI) involved. For the purposes of this study, the debris plates have been assumed to be rigid.

According to Holmes (2010), observations of wind damage from severe storms such as tropical Cyclone Tracy in Darwin, Australia in 1974, and Hurricane Andrew in southern Florida in 1992 suggest that windborne debris may produce

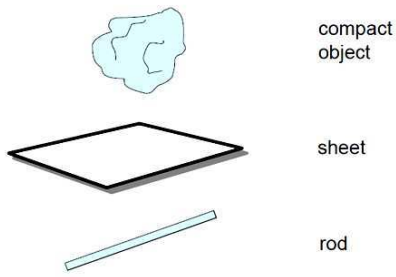

Figure 1.2: Commonly used debris type classifications by Wills et al. (2002).

Figure 1.3: Photo from a damaged roof in Birmingham showing the typical UK roofing tile with nailing only at the top making bottom uplift easy (Marshall and Robinson, 2006).

(a) (b)


Figure 1.4: Damage to (a) building facades (Marshall and Robinson, 2006) and (b) cars due to windborne debris generated during the 2005 Birmingham Tornado (BBC, 2005).

(a)

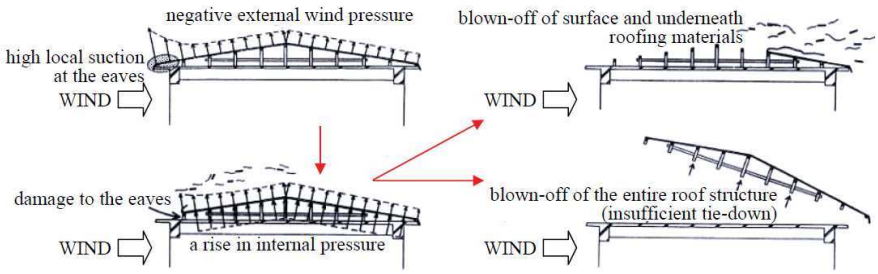

(b)

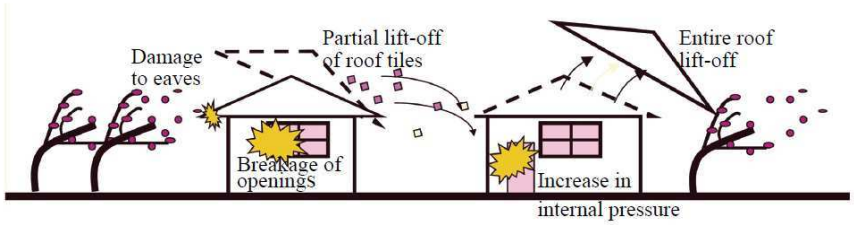

Figure 1.5: Illustrations of (a) Building damage correlation during severe storms (Uematsu et al., 1992), and (b) the debris damage chain (Tamura, 2009).

nearly the same amount of wind damage as direct wind loads on buildings in urban areas. Damage assessment reports of extreme windstorms in the UK, such as the Birmingham Tornado in 2005 - which at £30 million was the most costly tornado in the UK to date - also suggest a significant contribution to the failure of downstream structures by windborne debris generated from upstream structures (Marshall and Robinson, 2006) (Figure 1.4). This pattern, illustrated in Figure 1.5, has been consistently observed during severe storms and is referred to as the *debris damage chain* (Minor and Beason, 1976; Holmes, 2010).

The debris damage chain begins with debris generated from failed building components, street furniture and loose items upstream. These flying projectiles are carried by the wind, eventually impacting onto downstream buildings and breaching the roof structures, building glazing and wall cladding. This leads to several harmful situations: high internal pressure resulting in failure of the principal structural frame (this could include entire roof uplift as observed by Marshall and Robinson (2006)), exposure of occupants to wind and rain, damage to building contents, additional debris in the wind stream, hazardous debris falling to the street, disrupted business, and a blemished image of the building.

In addition to contributing significantly to wind related property damage, there is also evidence to suggest that windborne debris poses a substantial risk to human life during severe storms. Katsura et al. (1992) reported that of the 63 fatalities due to Typhoon Mireille, which struck Japan in 1991, the causes of death were; 31% blown by wind, 30% caught under collapsed or blown obstacles, and 23% hit by wind-borne debris.

Understanding the aerodynamics of windborne projectiles is also of importance to a number of related environmental and safety problems (see Figure 1.6). In order to model *fire spotting* - the ignition of forest fuel beds and houses ahead of the main fire by firebrands - accurate numerical models of the trajectories of cylindrical and disk shaped firebrands are required (Kortas et al., 2009). Similarly, windborne projectile models are increasingly playing a significant role in the numerical estimation of the risk presented by wind turbine *ice-throws*, where fragments of ice thrown-off from turbine rotor during winter conditions are transported by the wind, posing a threat to downstream infrastructure and human life (Seifert et al., 2003; Cattin et al., 2007). In the aerospace and aviation sector, safety studies to assess the vulnerability of both aerospace vehicles (Gomez, 2006), and the general public on the ground (Lin et al., 2003) to debris resulting from shuttle failure also require accurate windborne debris trajectory models.

A number of debris damage models and risk assessment models have previously been presented (Wills et al., 2002; Schneider and Schauer, 2006; Lin and Vanmarcke, 2008, 2010) to address the problem of windborne debris. Additionally, new impact tests have also been developed for building cladding elements in hurricane prone regions (Masters et al., 2010). However, the successful implementation of these debris risk models and impact test procedures requires adequate knowledge of:

i.) The sources and aerodynamic properties of the various debris types,

ii.) The debris flight behaviour, trajectory and impact velocities,

iii.) The damage resulting from debris impact.

Empirically derived analytical models are currently used to predict debris flight behaviour and impact energy. However these analytical models are limited to

(a)

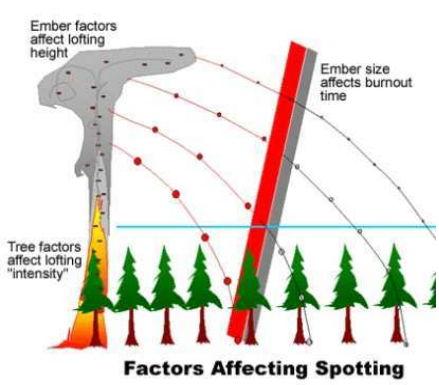

(b)

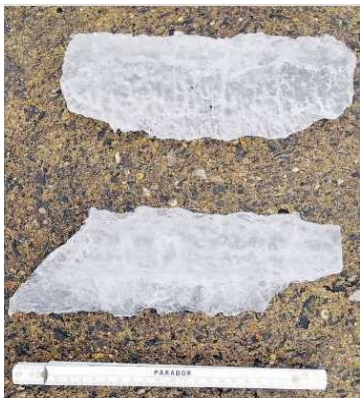

(c)

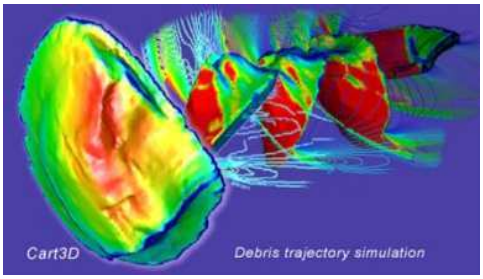

Figure 1.6: Windborne projectile models have potential applications beyond the modelling of storm debris. These include: (a) Modelling fire spotting (FARSITE, 2011), (b) Wind turbine ice-throw modelling (Aerospace, 2011), (c) Modelling aerospace debris risk to space vehicles and human life on the ground (NASA, 2011).

simplified cases and further improvement is precluded by the limited understanding of the non-linear coupling between the free-flying plate and the surrounding fluid.

There is therefore a need to develop a better understanding of the unsteady aerodynamic behaviour involved in windborne debris flight and to create more complete numerical models for the accurate simulation debris flight trajectories in realistic conditions. A more complete model would be particularly useful in the evaluation of debris types for which experimental measurements are currently unavailable.

1.3 Research Aims and Objectives

This research is primarily concerned with the development of more accurate models for the flight behaviour and trajectory of plate-type debris. The research has been carried out with the aim of:

> *simulating the flight of plate-type debris in extreme winds based on an improved understanding of the non-linear fluid-structure interaction involved.*

To achieve the stated aim, the following specific objectives have been met:

I. Develop a numerical model to simulate the aerodynamic characteristics of static, autorotating and free-flying plates.

II. Identify the primary flow mechanisms involved in the autorotation and free-flight of low-aspect-ratio plates.

III. Validate the numerical models against available experimental force measurements on static, autorotating and free-flying plates.

IV. Carry out a parametric study to identify the key parameters controlling debris flight behaviour.

V. Demonstrate the application of the numerical model to a more complete simulation of debris flight with near-real launch conditions and flow fields.

1.4 Methodology

Numerical simulations using coupled Computational Fluid Dynamics (CFD) and Rigid Body Dynamics (RBD) models are used as the central tool for this research. Commercial code ANSYS FLUENT (FLUENT Inc., 2009) is used for the CFD modelling. Simulations are run in parallel using a Beowulf Linux cluster with a total of 64 2.21 GHz CPUs and 20 1.95 GHz CPUs, each holding 8GB of RAM.

Initially two- and three-dimensional CFD simulations of the flow around a static flat plate have been performed to assess the performance of different turbulence models. The aerodynamic force coefficients and the coherent flow structures in the wake of the plate are validated against existing experimental measurements from ESDU (1970) and Taira and Colonius (2009). Model verification studies are also performed in order to inform the selection of turbulence model, optimal grid and time-step resolution and discretisation schemes.

The CFD model is subsequently coupled with a RBD model using User Defined Functions (UDF) written in the C programming language. This coupled CFD-RBD model is used to simulate the forced rotation and autorotation of flat plates in a uniform wind stream about a fixed axis, with the aim of developing a better understanding of the mechanisms leading to and sustaining plate autorotation. Validation of the CFD-RBD results is achieved by comparisons against recent autorotation experiments by Martinez-Vazquez et al. (2010). The key observations used for CFD-RBD verification include the aerodynamic force and torque coefficients, the net pressure distribution across the plate surface and the rotational speed. In all the CFD simulations, the coherent flow structures present in the flow around the plate are identified from the CFD-RBD flow solution and their interaction with the plate is investigated to provide some insight into the non-linear Fluid-Structure Interaction (FSI) taking place. CFD predictions for scalar flow variables such as pressure, velocity magnitude and vorticity magnitude are also presented throughout the thesis in contour plots. In these contours plots, the convention has been to present the figures with a height to width aspect ratio of 1 and a horizontal scale bar to indicate the dimensional scale of the figure in metres.

Finally, the model is extended to the simulation of full debris flight in uniform

flow conditions as well as in non-uniform flow fields such as those typically present during roof-top launch situations. Comparisons are also made against existing analytical models for smooth flow solutions, and improvements to these quasi-steady analytical models are proposed based on the findings of this study.

1.5 Thesis Outline

This thesis has 7 chapters, including the Introduction.

Chapter 2 presents a review of literature that documents relevant research into the aerodynamics of plate-type windborne debris. Previous wind tunnel and numerical investigations into the aerodynamics of static, autorotating and free-flying flat plates are presented, highlighting the key findings on the nature of the aerodynamic forces and unsteady flow structures involved. Existing debris flight modelling research is discussed and the key limitations and criticisms are presented.

Chapter 3 provides an introduction to Computational Wind Engineering with a discussion on the numerical approaches to solving the Navier-Stokes equations and developments in the simulation of fluid flow around moving wall boundaries. An introduction to the problem of turbulence is also presented, with a review of the different turbulence modelling approaches currently available. The chapter also includes a brief introduction to the wind in the atmospheric boundary layer. This is followed by Chapter 4 which describes the singularity free 3D, six degree-of-freedom Rigid Body Dynamics (RBD) model used in this study. In Chapter 5, the CFD-RBD model development, verification and validation is presented. This includes a description of the model domain, numerical discretisation schemes used and the various sensitivity studies carried out for spatial and temporal discretisation, solution schemes and turbulence modelling approach. The chapter then presents results for CFD simulation of static and autorotating plates as well as a forced rotation study performed to assess the accuracy of existing quasi-steady force models. Finally, preliminary results from both two- and three-dimensional simulations are presented for plate free-fall, free-flight and autorotation and validated against existing experimental measurements.

Chapter 6 then presents the results of a parametric study of over 130 CFD simulations of plate free-flight, assessing the sensitivity of plate free-flight to initial orientation, Tachikawa number, Mass moment of Inertia, Aspect Ratio, Froude

Number and complex launch conditions. The different flight modes observed are categorised.

Finally, Chapter 7 summarises the main conclusions of this research and includes recommendations for future research.

Chapter 2

Literature Review

This chapter presents existing literature on; the fundamentals of plate aerodynamics, existing quasi-steady models of debris flight and their limitations, as well as wind tunnel experiments and full scale studies of plate debris flight. Recent applications of numerical modelling to related problems such as plate autorotation, free-falling aerofoils and shuttle ascent foam debris are also discussed. A further review of CFD applications to wind engineering is presented in Chapter 5.

2.1 Flat Plate Aerodynamics

A number of fundamental studies have been carried out on the aerodynamics of static and rotating flat plates. Early experiments on fluid flow over a flat plate found that the flow could be generally described as *streamlined flow* at low angles of attack, *transitional or stalling flow* at moderate angles of attack and *bluff-body flow* at high incidence (Abernathy, 1962). The angle at which the flow first begins to separate from the plate, resulting in bluff-body behaviour, is known as the stall angle. This angle varies with plate shape and size and will further be influenced by the flow Reynolds number, turbulence levels in the incoming flow and whether the plate is static or rotating (ESDU, 1970). Because of the qualitative differences between each type of flow, the modelling of rotating plates exhibiting all three types of flow presents a complex problem.

Figure 2.1 shows a typical plate with common descriptive parameters that will be used throughout the rest of this thesis, where B is the plate breadth, L is the plate chord, h is plate thickness, c is the plate's projected chord length onto a vertical plane normal to the horizontal wind speed, α_z is the angle of attack in the X-Y plane (corresponding angles of attack exist in the X-Z and Y-Z planes). u, v and w are the components of plate velocity in the X-, Y- and Z-directions. ω represents the angular velocity of the plate about an axis through its centre of mass and parallel to the Z-axis, additional angular velocities exist for axes parallel to the Y- and X-axes during full 3D rotation. U_{w} is the absolute mean

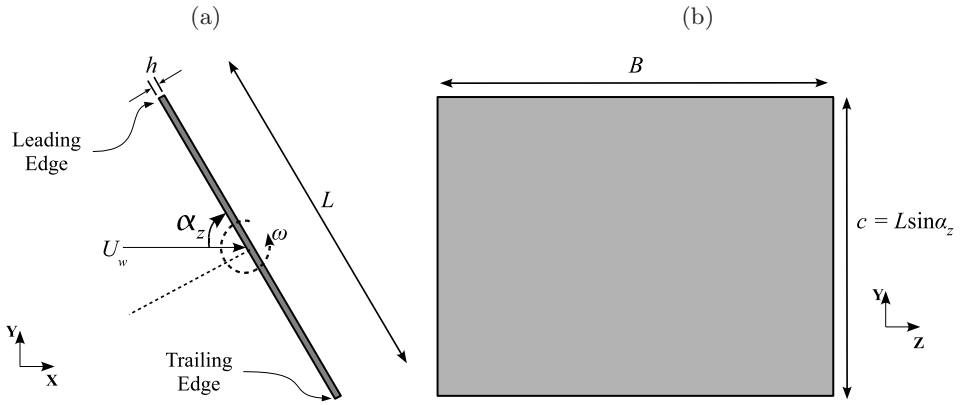

Figure 2.1: Typical plate dimensions, orientation and motion conventions.

horizontal wind speed, which acts in the positive X-direction. A translating plate with plate velocity (u, v, w) can be viewed from a plate-fixed reference frame as a static plate in 3D wind field given by the relative wind velocity $((U_{\mathrm{w}} - u), v, w)$. Abernathy (1962) describes bluff body flow around a high aspect ratio static plate (occurring at between approximately 30° to 90° angles of attack) as beginning with the movement of fluid from the stagnation point at the front of the plate towards the leading and trailing edges. As the fluid is unable to turn around these edges it separates from the plate at both points giving rise to a region of low static pressure behind the plate. The separated free-boundary layers are unstable and through an interaction with the mean flow or with each other are partially transformed into a von Karman vortex street in the plate's wake (Figure 2.2).

The von Karman vortex sheet consists of alternating vortex shedding from the plate's leading and trailing edges characterized by a regular non-dimensionalised frequency known as the Strouhal number, St.

$$St = \frac{fc}{U_o} = \frac{fL\sin\alpha_z}{U_o}, \tag{2.1}$$

where f is the frequency of vortex shedding in Hertz, c, L and α_z are as defined in Figure 2.1 and U_o is the free stream mean wind speed. Abernathy also presents a modified form of the Strouhal number (S^*) defined as,

$$S^* = \frac{fD}{U_s} = \frac{f1.41c\sin\alpha}{kU_o} = \frac{f1.41c\sin\alpha}{\sqrt{1 - C_p^*}U_o}. \tag{2.2}$$

S^* uses the separation distance between free-vortex layers, D, as the characteristic length which is independent of lateral flow constriction and angle of attack.

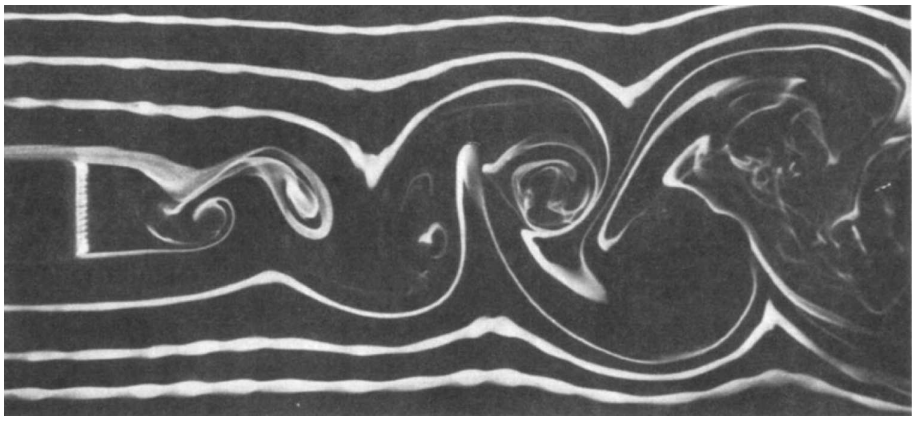

Figure 2.2: Smoke filaments around a bluff body showing a von Karman vortex street in the two-dimensional flow around a high aspect ratio bluff body, and the interaction between the top shear layer and the vortex forming on the opposite side of the wake (Bearman, 1984).

U_s is the maximum local speed in the free-vortex layers from the inclined plate (which occurs at the outer boundary of the free-vortex layer), $k = U_s/U_o$ is the velocity ratio, and $C_p^* = 2(p_s - p_o)/\rho U_o^2$ is the pressure coefficient behind the plate. p_s is the pressure behind the plate measured at the geometric centre of the plate model, and p_o is the free stream pressure.

The von-Karman vortex street is a special case of two-dimensional bluff body vortex shedding involving the periodic shedding of vortices from the leading and trailing edges (Bearman, 1984). However, in the case of low aspect ratio bluff bodies, a more complex and three-dimensional wake is observed. In addition to leading- and trailing-edges vortices, tip vortices exist at the side-edges of the plate and depending on the angle of attack and aspect-ratio (AR $= B/L$) of the plate, different types of wake behaviour may be observed.

For instance, given a plate at 30° angle of attack in a flow of Re = 300, as shown in Figure 2.3(a) for a square plates with an aspect ratio (AR) of 1, the leading edge vortex remains attached due to the downward induced velocity from the two counter-rotating tip vortices covering the entire span of the plate leading to a *stable steady wake* (Taira and Colonius, 2009). However, for plates with an aspect ratio of 2, at the same angle of attack, the tip vortices are not strong enough to keep the leading edge vortex attached, Figure 2.3(b), which leads to the unsteady shedding of hair-pin vortices. Taira and Colonius (2009) also

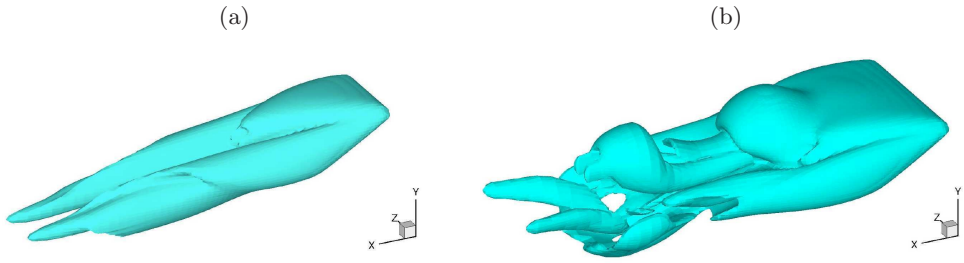

Figure 2.3: Leading edge and tip vortices in the wake of a static flat plate at 30° angle of attack and Re = 300. (a) Steady wake behind plate of AR=1; (b) Unsteady wake behind plate of AR=2 (Taira et al., 2007).

observed that at higher angles of attack, the tip vortices that form along the side edges of the plate became vertically aligned and of similar strength to the leading and trailing edge vortices. The interaction of tip vortices with leading edge vortices then results in a suppression of the dominant shedding frequency, the development of a span-wise asymmetry in the wake and the aperiodic nature of the flow. Figure 2.4 summarises the findings from Taira and Colonius (2009). This wake topology and the vortical structures observed at the low Reynolds numbers although less diffusive, have been found to be qualitatively similar to those observed at higher Reynolds numbers (Dong et al., 2006). The Reynolds number is also observed to affect the stability of the wake, with higher Reynolds number flows more likely to exhibit unsteady wake behaviour as well as aperiodic vortex shedding at higher angles of attack. Results from extensive computational investigations by Taira and Colonius (2009) are summarised in Figure 2.4. These results show that depending on the Reynolds number, aspect ratio and angle of attack, low aspect ratio plates can exhibit; (i) a steady wake with no vortex shedding; (ii) an unsteady wake with periodic vortex shedding; (iii) an unsteady wake with aperiodic vortex shedding and span-wise asymmetry.

Taira et al. (2007) further observed that plate shape also played a role in the wake behaviour and onset of vortex shedding. For rectangular plates, the right angled corners created a thinning-out of vortex sheets in these regions resulting in the formation of separate vortex core structures at the leading edge, trailing edge and side edges. With no convective vorticity flux in the span-wise direction (which would act to stabilise the leading-edge vortex), the only mechanisms left

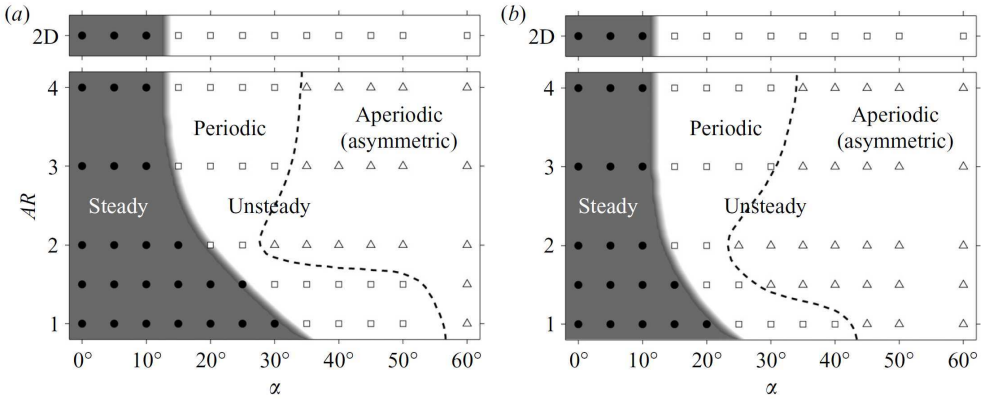

Figure 2.4: Wake stability and behaviour for a range of α and AR at (a) Re = 300 and (b) Re = 500. The shaded area and the dashed line represent the regions of stability and the transition from periodic to aperiodic shedding respectively (Taira and Colonius, 2009).

to transport the vorticity being fed into the leading-edge are diffusion and vortex shedding (Taira et al., 2007).

It is important to note that in the context of windborne debris flight, if the relative wind speed is used as the reference wind speed, then during launch stages flow may be characterized by a high Reynolds number flow while in the long-term flight stages as the plate velocity tends towards the mean wind speed, the flow would be characterized by a low Reynolds number.

2.2 Aerodynamic Forces on Static Flat Plate

As the fluid flows around a flat plate, fluid pressure and viscous forces are exerted on the plate. These forces may be steady or unsteady depending on the behaviour of the wake behind the plate and are dependant on the plate's angle of attack α.

At angles of attack higher than the stall angle, the plate enters into normal or static stall if it is static or steadily translating. Plates in static stall experience a decrease in the aerodynamic lift with increasing angle of attack. In addition to static stall, there exists a dynamic stall that occurs in rotating plates. During dynamic stall, rotating plates experience a momentary increase in the plate's normal force coefficient - C_N - due to non-linear interaction between the plate and the leading edge vortex (or dynamic stall vortex). As the leading edge

vortex dissipates, the normal force then rapidly falls and the plate returns to normal stall (Gupta and Leishman, 2006; Larsen et al., 2007). Both static and dynamic stall phenomena are of interest in the study of windborne debris which has been experimentally observed to exhibit either pure translational motion or more commonly, combined translational and rotational motion (Kordi and Kopp, 2011). However this section focuses on the behaviour of static plates.

For static plates, vortex shedding and wake unsteadiness beyond the stall angle result in unsteady fluctuating pressure forces on the plate. As shown in Figure 2.5, due to the absence of the stable tip vortices, the two-dimensional flow exerts larger fluctuation in force per unit span compared to the low aspect ratio flow cases (Taira and Colonius, 2009). In cases, where the wake behind a low-aspect-ratio plate remains steady, a steady body force time-series is observed.

A number of experimental studies have previously been carried out to determine the aerodynamic forces acting on flat plates at different angle of attack in a steady, uniform flow (Hoerner, 1958) and the results are compiled in ESDU (1970). Subsequent measurements of static plate forces such as Richards et al. (2008) agree with older records and extend the data to more three dimensional plate orientations involving an orientation of the plate about both a horizontal cross-wind axis as well a vertical cross-wind axis. The values typically measured in these studies are the time-averaged pressure forces acting normal to the plate, N, and the time-averaged aerodynamic torque, M, about the horizontal axis through the plate's centre and perpendicular to the flow.

From these values, the non-dimensionalised normal force coefficient, C_N, and the centre of pressure positions, x_{cp}, shown in Figures 2.6 and 2.7 respectively, are determined as

$$C_N = \frac{N}{0.5\rho A {U_w}^2}, \tag{2.3}$$

$$x_{cp} = \frac{c}{2} - \frac{M}{N}, \tag{2.4}$$

where c is the chord length. ESDU (1970) defines x_{cp} as the distance along the plate centre-line of the centre of pressure behind the leading edge of the plate. Other studies, however, define x_{cp} as the distance from the plate's geometric centre of the centre of pressure, and this is the convention used in this research. x_{cp} is usually non-dimensionalised by c.

The discontinuities in the curves in Figures 2.6 correspond to incidence of stall

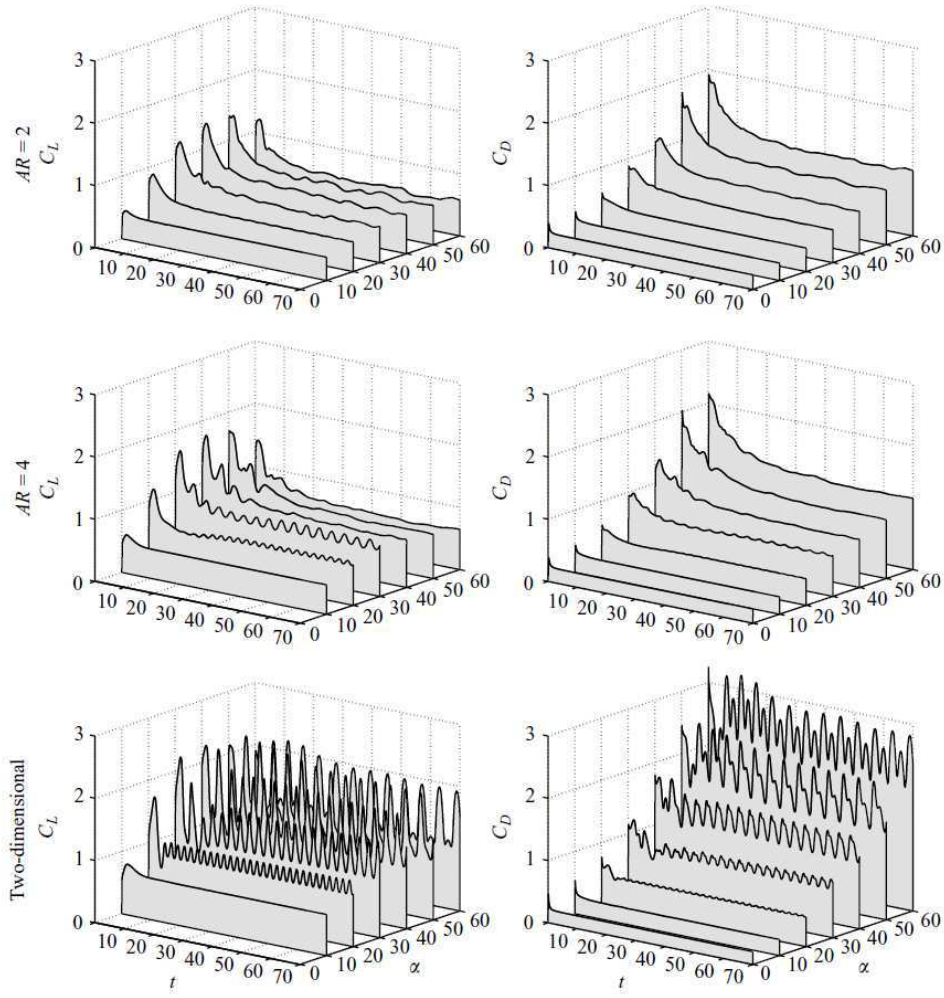

Figure 2.5: Lift, C_L, and Drag, C_L, force coefficient time series for rectangular flat plates of different AR for a range of angles-of-attack at Re=300 (Taira and Colonius, 2009).

which may be expected to lie within $\pm 5°$ of the vertical lines shown. From Figures 2.6 and 2.7, x_{cp}/c and C_N values may be obtained to within an accuracy of $\pm 5\%$ except in the stall region where data was more widely scattered (ESDU, 1970). With these values, the aerodynamic drag, lift and torque may then be computed for a plate at a given angle of attack and are shown in Figure 2.8 for a square flat plate. However as the ESDU data presents only the time-averaged measurements on static plates, they do not capture the unsteady/fluctuating component of the body forces which could play a significant role in the non-linear interaction expected in windborne debris flight.

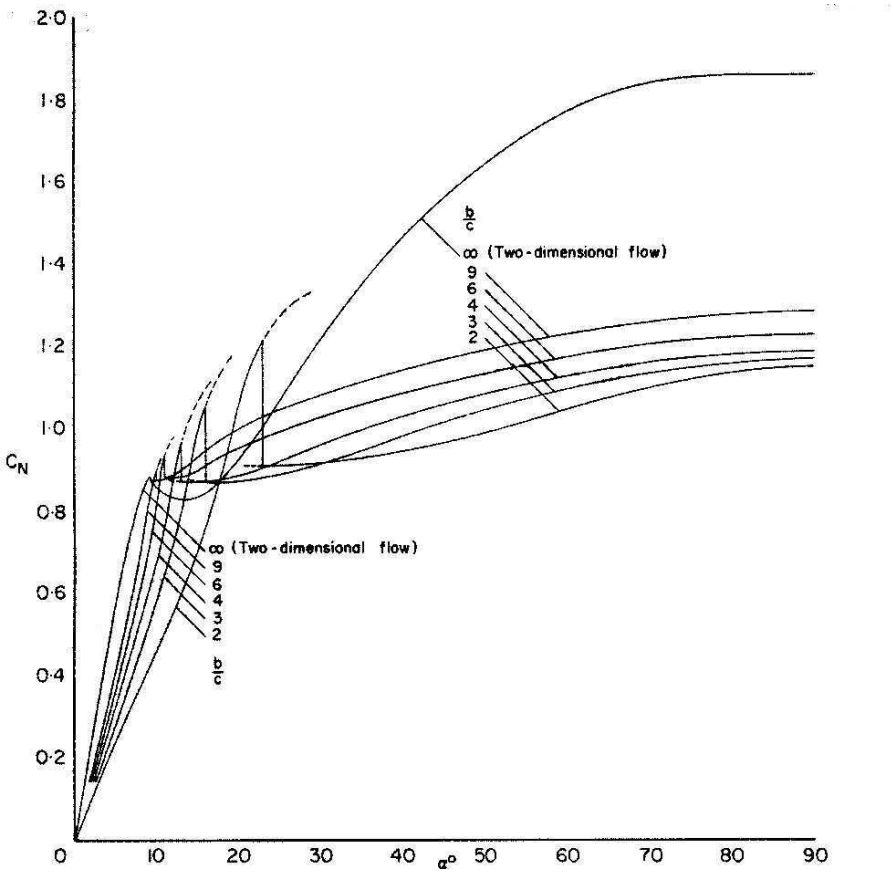

Figure 2.6: Variation of rectangular flat plate normal force coefficients (C_N) with angle of attack (α^o) and plate aspect ratio (b/c) (ESDU, 1970).

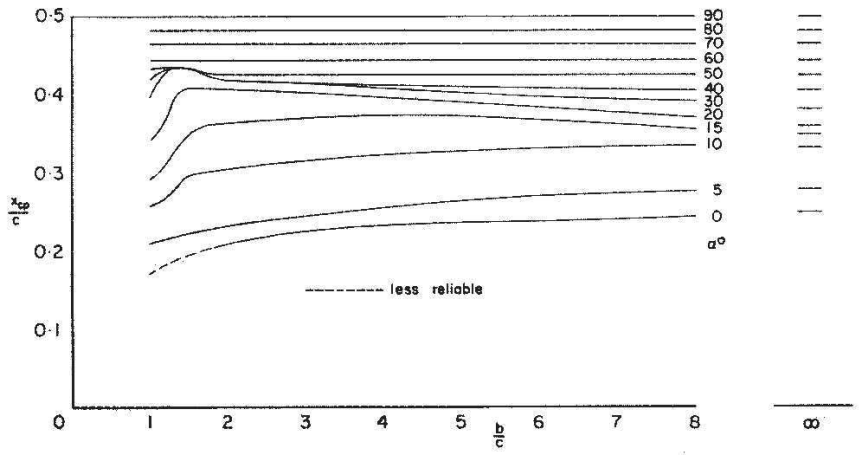

Figure 2.7: Variation of rectangular flat plate centre of pressure position (x_{cp}/c) with plate aspect ratio (b/c) and angle of attack (α^o) (ESDU, 1970).

(a)

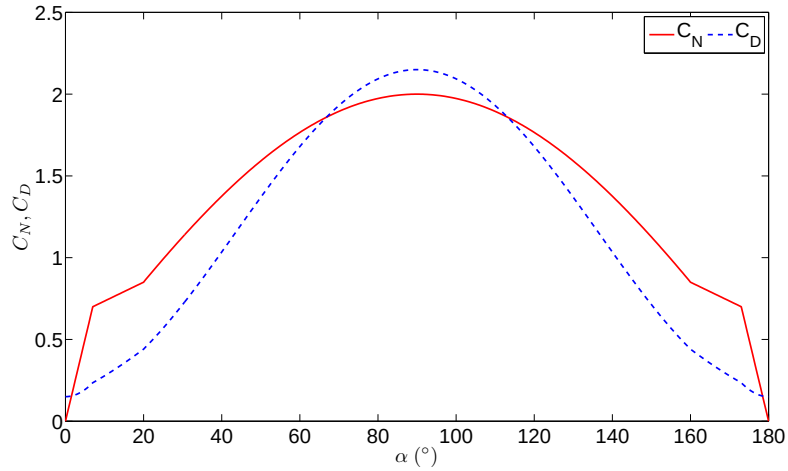

(b)

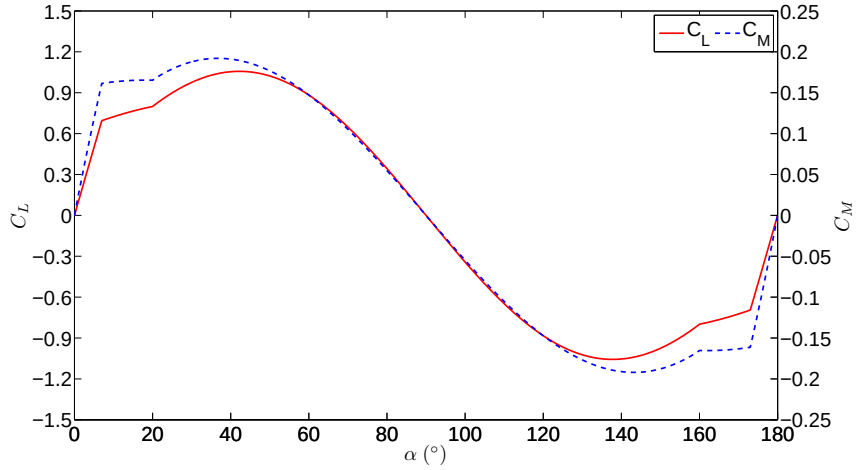

Figure 2.8: Steady-state curves showing the variation of (a) Normal Force and Drag coefficients, (b) Lift and Torque coefficient, with angle of attack for static square flat plates held in a uniform steady flow. Curves are computed using piece-wise linear approximations of C_N and x_cp curves from ESDU (1970).

2.3 Autorotation

Windborne debris flight can be viewed as a special case of combined plate autorotation and translation. In addition to the aerodynamics of translating plates, understanding the phenomenon of autorotation is central to understanding the aerodynamics of windborne debris.

Autorotation is defined as the continuous rotation, without external power of a body exposed to an air stream (Skews, 1990; Smith, 1971). The study of the theory of autorotation dates as far back as Maxwell (1854) who studied the rotation of falling cards and Riabouchinsky (1935), who introduced the term "autorotation". Some authors (Lugt, 1983; Riabouchinsky, 1935), however, consider this to be pseudo-autorotation and insist that proper/classical autorotation can occur only if one or more stable positions exist at which the fluid flow exerts no torque on the resting body. Symmetric plate-type debris, because of the absence of significant aerodynamic torque at 0° or 90° angles of attack satisfies the definition of classical autorotation although other irregular or asymmetric debris shapes might not. For the purposes of the present research, no distinction is made between classical and pseudo autorotation.

Figure 2.9 illustrates the point of stable autorotation for a Lancaster propeller as defined by Riabouchinsky (1935) for autorotation about an axis perpendicular to the flow. The experiments involved using a motor to drive the propeller at a constant angular velocity Ω, with the torque T acting on the propeller measured as a function of Ω.

Although in reality a free plate may rotate about any arbitrary axis, two special cases have been the focus of existing literature and research into autorotation. These are; autorotation about an axis parallel to the flow (e.g; in the Lancaster propeller, spinning airfoil, horizontal axis wind turbines), and autorotation about an axis perpendicular to the flow (e.g; in falling rectangular pieces of cardboard rotating about a free or moving axis and vertical axis wind turbines). The fundamental difference between the two cases is essentially that while the rate of stable autorotation is constant for bodies autorotating about an axis parallel to the flow (provided the wake is fairly constant), the rate of autorotation for bodies autorotating about an axis perpendicular to the flow is periodic (Lugt, 1983).

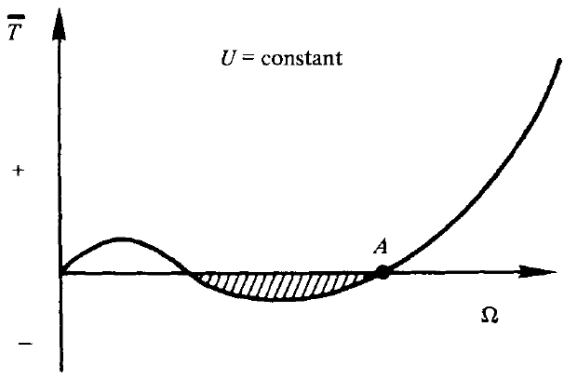

Figure 2.9: The Riabouchinsky curve (Riabouchinsky, 1935) showing the average torque $\overline{T}$ required to drive a Lancaster propeller at a constant rotational speed Ω. Positive $\overline{T}$ means that an external driving torque is required, while negative $\overline{T}$ (in the shaded area) indicates a braking torque. If a plate in the shaded area is free to rotate, it will autorotate and increase its angular velocity until the point of stable autorotation (point A).

During the flight of wind-borne debris, plate debris has been observed to exhibit a complex three-dimensional (3D) spinning mode of autorotation that is the dominant mode (Kordi and Kopp, 2011). However due to the numerical and experimental difficulties involved, there is lack of existing research on this type of autorotation.

2.3.1 Autorotation Parallel to the Flow

During autorotation about an axis parallel to the flow, the fluid motion is qualitatively steady in the stable state of a body-fixed reference frame (Lugt, 1983). The local angle of attack of the flow against a blade element, α, changes due to the rotational velocity, $V = \Omega R$, according to,

$$\alpha = \alpha_o + \Delta\alpha, \quad \Delta\alpha = \tan^{-1} p, \quad p = \frac{V}{U}, \tag{2.5}$$

where U is the constant speed of the parallel flow, R is the radius of the wing-type body, Ω is the angular velocity, α_o the local angle of attack for $V = 0$ and p the roll parameter.

In this case, the aerodynamic forces will support autorotation if $V/U = p > L/D$, where L is the lift and D is the drag. To meet this criterion, the total angle of attack must be in the stall region so that the slope $dL/d\alpha$ is negative and its

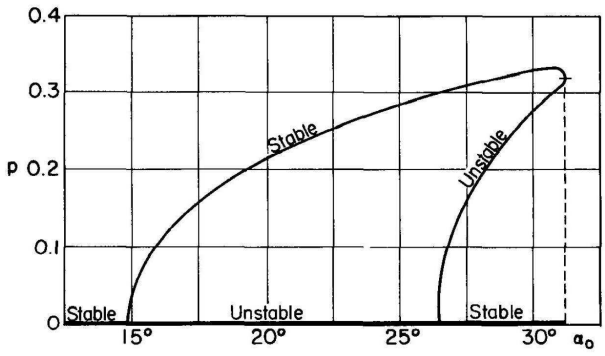

Figure 2.10: The rate of autorotation, p for an autorotating wing as a function of α_0 (Lugt, 1983).

absolute value large enough to satisfy the condition (Lugt, 1983):

$$\frac{dL}{d\alpha} + D < 0. \tag{2.6}$$

Figure 2.10 shows for an autorotating wing the rate of autorotation, p as a function of α_0.

2.3.2 Autorotation Perpendicular to the Flow

Unlike autorotation parallel to the flow where steady fluid flow is observed, during autorotation perpendicular to the flow, the fluid flow is qualitatively observed to be unsteady and periodic. In addition, while it is immediately obvious that asymmetric plates and aerofoils held about an axis perpendicular to the flow should autorotate, this is not the case for symmetrical plates.

Consider the steady lift and moment coefficient shown in Figure 2.8(b). As the angle of attack slowly increases, lift force and torque increase until the plate begins to stall. At the stall point, these values decrease and eventually become insignificant when the plate is perpendicular to the flow. As the wing continues to rotate from 90° to 180° angle of attack, the cycle is repeated with reversed sign on the moment and lift. Therefore assuming a quasi-steady behaviour (i.e. that the plate is rotating so slowly that the aerodynamic forces at a given angle of attack can be assumed to be the static plate equivalents), a symmetrical plate exposed to a steady air stream would be expected to experience equal accelerating and retarding torque during different halves of the cycle (either side of $\alpha = 90°$), resulting in a static plate at the stable $\alpha = 90°$ position, with no autorotation. A number of empirically derived theories have therefore been

suggested to explain the phenomenon of autorotation in symmetric plates, and how it is influenced by additional factors.

Smith (1971) experimentally investigated the autorotation of symmetrical wings about a span-wise axis perpendicular to the flow. Smith observed that in practice, a wing released from rest at an angular position at which the flow was stalled would come to rest (after a number of oscillations) in a statically stable position with the wing perpendicular to the free stream. However, if the wing was released at a small enough initial angle of attack, α_o, so that the flow was un-stalled, the wing usually began autorotating with the final direction of rotation determined by the initial orientation. Smith also reported that the wing would not autorotate if its moment of inertia, I, was too low as it was then unable to store enough angular momentum to pass through the stalled portion of its cycle during which it received a retarding torque.

Autorotation was therefore found to be dependant on both the initial angle of attack, α_o, and the plate's mass moment of inertia, I. As I was increased, the roll parameter, p, increased since the wing slowed less during the stalled portion of its cycle. However, Iversen (1979) later found that for non-dimensionalised inertia $I^* = I/(\rho B L^4) > 1$ (where ρ, B, L are density of fluid, span and chord length), the roll parameter p becomes independent of I and here the difference between free-flight and fixed-axis autorotation becomes indistinguishable (Lugt, 1983).

For free rotation, Smith (1971) found the roll parameter to be sensitive to, and greatly determined by, the Reynolds number. Apart from the Reynolds number, other factors influencing the rate of autorotation about an axis perpendicular to the flow are; plate thickness, plate aspect ratio, lift and drag coefficients and the moment of inertia (Lugt, 1983).

To account for the influence of plate thickness ratio, $\tau = h/L$, and aspect ratio, $A = B/L$, Iversen (1979) obtained the correlation function given by (2.7), (2.8) and (2.9) for tip speed ratio ($p = V/U$) based on data from experiments by Bustamante and Stone (1969), Smith (1971) and Glaser and Northup (1971).

$$p = \frac{V}{U} = f_1(A) f_2(\tau), \tag{2.7}$$

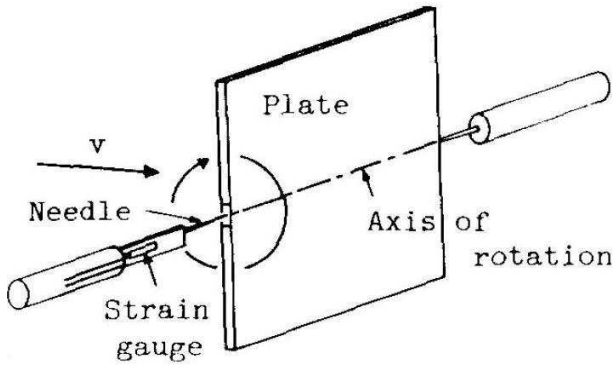

Figure 2.11: Tachikawa's experimental plate autorotation set-up (Tachikawa, 1983).

where functions $f_1(A)$ and $f_2(\tau)$ are defined as;

$$f_1(A) = \left\{ \left[\frac{A}{2 + (4 + A^2)^{\frac{1}{2}}} \right] \left[2 - \left(\frac{A}{A + 0.595} \right)^{0.76} \right] \right\}^{\frac{2}{3}}, \tag{2.8}$$

$$f_2(\tau) = \left(0.329 \ln \left(\frac{c}{h} \right) - 0.0246 \ln \left(\frac{c}{h} \right)^2 \right). \tag{2.9}$$

The experiments (Bustamante and Stone, 1969; Smith, 1971; Glaser and Northup, 1971) involved plates of aspect ratios, $0.25 \leq A \leq 4$, and thickness ratios, $0.0054 \leq \tau \leq 0.5$. According to Iversen (1979), for plates with aspect ratio, $A > 5$, the influence of A on p can be ignored. τ was also found to have a negligible effect on p for values less than 0.01 (Lugt, 1983).

Although Iversen's correlation has become widely accepted and even applied to quasi-steady models of debris flight (Kordi and Kopp, 2009b), later investigations by Tachikawa (1983) and Skews (1990) pointed to some limitations. Tachikawa (1983) performed low-speed wind tunnel experiments to determine the force coefficients and angular velocity of autorotating square and rectangular flat plates (as shown in Figure 2.11), with the motivation of applying results to windborne debris flight modelling. The plate thickness ratios were in the range $0.029 \leq \tau \leq 0.057$ and the results for rectangular plates did not necessarily agree with Iversen's correlation equations and suggested a large influence of thickness ratio (Tachikawa, 1983).

Later, Skews (1990) carried out wind tunnel experiments of two-dimensional plate autorotation (for which effects of aspect ratio can be neglected) and extended the range of thickness ratio, τ, of plates tested up to to 1.0. Skews found

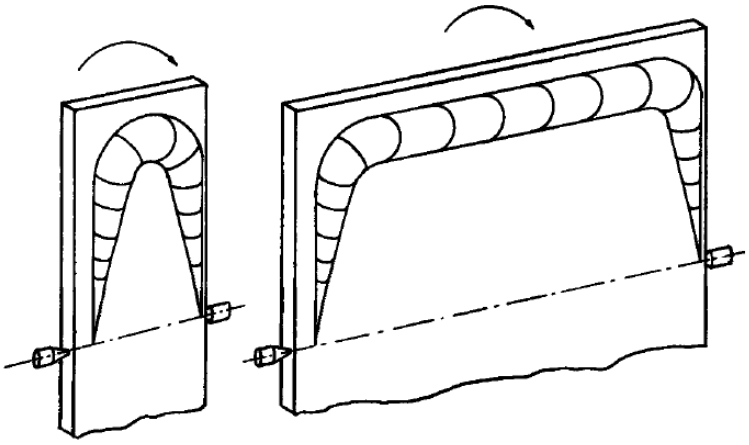

Figure 2.12: A schematic showing span-wise and side-edge vortices shed from the retreating edges of an autorotating plate as postulated by Skews (1990).

that for instance, although Iversen's correlation, (2.7) - (2.9), does not allow for autorotation of square plates of large thickness, $\tau = 1.0$, this was experimentally achieved just as easily as for thin plates with , $\tau < 0.1$. The experimental results by Skews (1990) were in good agreement with 2D numerical predictions by Lugt (1980) and Skews concludes that Iversen's correlation does not correctly account for effects of aspect ratio beyond $A > 4$ and should therefore be limited to low aspect ratio plates. Skews attributes the variations in behaviour with aspect-ratio to differences between the flow structure in low- and high-aspect-ratio plates as illustrated in Figure 2.12.

2.3.2.1 Flow Around Autorotating Plates

During plate autorotation, a distinctly different flow pattern was observed in experiments by Smith (1971), Figure 2.13, compared to the flow over a static plate described in section 2.1. The main difference being that the wing stalled much later than in the static case and the flow reattached later to the lower surface. As a result of this delayed stall, in the first 90° cycle, positive lift and moment were increased while the negative lift and moment during the second half of the cycle were reduced by the delayed reattachment. The net driving torque created by this delayed stall phenomena gradually led to an increase in the wing's angular velocity until a steady speed was reached at which the average torque was reduced to zero by aerodynamic damping effects.

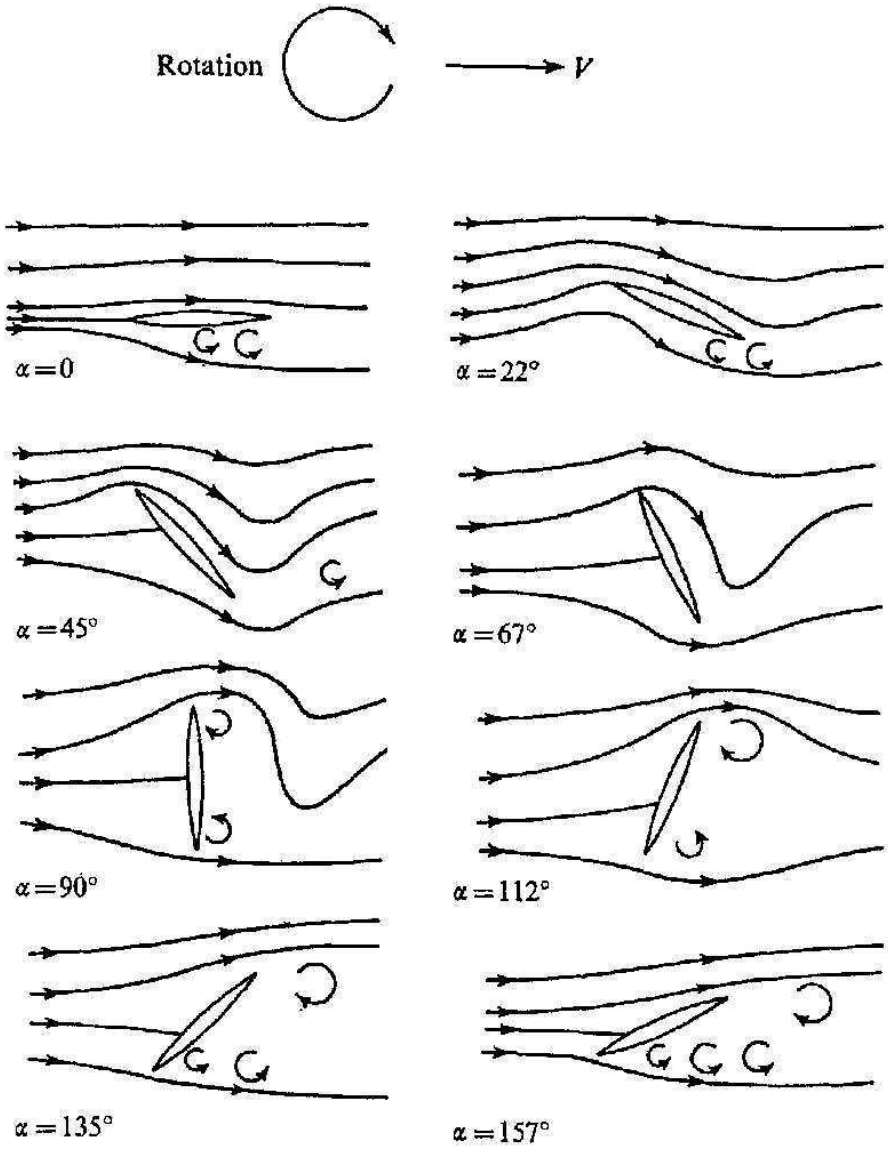

Figure 2.13: Schematic flow pattern over autorotating wing at Re = 90,000 and non-dimensionalised wing rotation rate, $S = (nL/U_w) = 0.35$, where n is the rotation rate in Hz. (Smith, 1971).

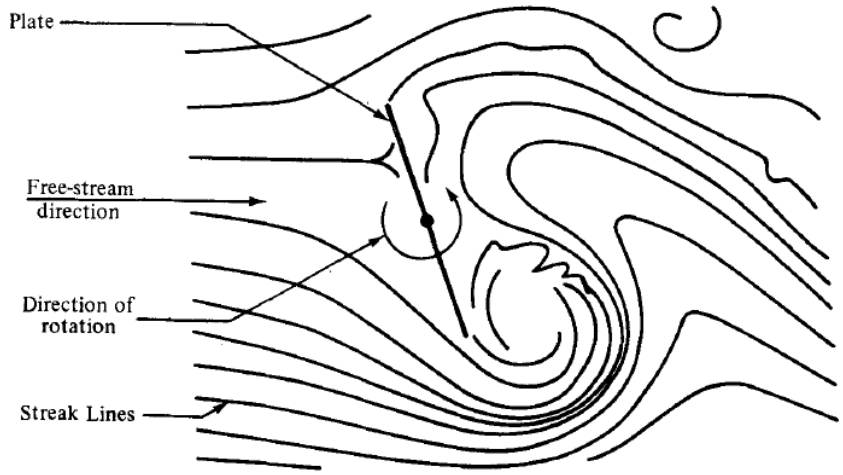

Figure 2.14: Sketch from smoke-tunnel photograph of an autorotating flat plate by Yelmgren (1966), showing a large vortex downstream of the retreating edge (Iversen, 1979).

Smith (1971) went on to speculate that there were two possible causes for the delayed stall. Firstly, he argued that the boundary layer on the upper (suction) surface of the wing takes time to thicken and separate when the angle of attack is rapidly increasing, such that the wing can reach a higher angle of attack before it stalls. Secondly, the flow over the upper surface of a wing with a rapidly increasing angle of attack is accelerating - this reduces the adverse pressure gradient thereby delaying stall.

According to Smith (1971), it is this hysteresis in the lift, resulting from unsteady aerodynamic effects, that causes autorotation. Bustamante and Stone (1969), Iversen (1979) and Smith (1971) suggested that these unsteady aerodynamic effects could themselves be attributed to the large vortex shed from the retreating face of the plate which then creates an aerodynamic torque supporting autorotation due to the low pressure at its core. The sketch in Figure 2.14 from a smoke-tunnel photograph of streak lines around an autorotating plate (Yelmgren, 1966) shows this large vortex that remains attached and is eventually shed from the retreating face of a rotor while no similar vortex is visible from the advancing face.

Related experiments by Lentink et al. (2009) on scaled models of maple seed flight show similar findings, with a pronounced leading edge vortex present

during seed autorotation. Unlike with rectangular plates, however, the vortex around a smooth edged maple seed remains stable and attached due to significant span-wise vorticity transport from the leading-edge vortex to the tip vortex (Lentink et al., 2009), which is not present in square flat plates with sharp corners.

There are still a few unanswered questions regarding the flow around low aspect ratio autorotating plates. As described by Lugt (1983) and Skews (1990), for autorotating plates and the theory of low aspect ratio static flat plates, in addition to a pronounced leading edge vortex, large tip vortices are present in the flow. These tip vortices have a complex non-linear interaction with the leading edge vortex which is expected to play an important role during low aspect ratio plate autorotation.

In addition, the cause of the aerodynamic damping that ultimately limits the angular velocity of the wing to the stable speed of autorotation is not fully understood (Smith, 1971). Lugt (1980) based on 2D numerical modelling suggested there was linkage between the vortex shedding frequency and the plate rotational speed. Lugt reported that during stable autorotation, the vortex shedding frequency is *locked-in* to the plate's rotational speed. The aerodynamic damping is therefore likely to be due to premature or delayed shedding that occurs when the plate's instantaneous rotational speed exceeds the mean autorotational speed. There is, however, a need to study this damping effect in more detail for low aspect ratio plates.

Smith (1971) also suggested the centre of gravity location was important especially if the wing was rotating about a horizontal axis or freely falling and recommended further studies into this.

2.3.3 Numerical Modelling of Autorotation

In addition to experimental investigations of plate autorotation, a number of of two-dimensional (2D) numerical studies of plate autorotation about a horizontal axis perpendicular to the flow in a steady uniform flow stream have previously been carried out including Lugt (1980), Seshadri et al. (2003), Mittal et al. (2004) and Andronov et al. (2007). These studies involve solving the 2D Navier-Stokes equations to obtain the unsteady flow field around an autorotating plate and the aerodynamic forces resulting. Early simulations by Lugt (1980) have been

compared against experiments by Skews (1990), showing good agreement.
A number of other 2D numerical studies have also recently been conducted with a focus on understanding the aerodynamics of related problems such as the motion of falling paper (Andersen et al., 2005; Jin and Xu, 2008) and the aerodynamics of insect flight (Wang, 2005).
These studies have all focused on autorotation of high-aspect-ratio plates, exhibiting 2D motion, in low Reynolds number flow. The only low-aspect-ratio studies performed, such as Dong et al. (2006) and Taira and Colonius (2009) relate to the aerodynamics of plates undergoing prescribed rotations such as those involved in insect flight as opposed to the non-linear motion involved in autorotation.
The present research therefore aims to carry out a numerically investigation into 3D fixed axis autorotation about an axis perpendicular to the flow, as well as the full 3D complex spinning autorotation about the centre of mass, which are relevant to the aerodynamics of windborne debris.

2.4 Empirical Modelling of Windborne Debris

2.4.1 Early Numerical Models

Early work on windborne debris modelling began during the 1970s and was focused on the safety design of nuclear power plant structures from tornado borne missile damage. At the time it was necessary to estimate the tornado borne missile ejection velocities in order to assess the potential damage scenarios. Lee (1974) presents one of the procedures for calculating this velocity using a simplified three-dimensional tornado model to represent the wind. This was used together with a set of equations for calculating missile motion from estimated body forces and linear momentum conservation principles. Conservative orientations and aerodynamic characteristics of the missile were taken into account and the ejection velocities obtained were found to be highly dependant on the missile characteristics. The three-dimensional equations of motion presented by Lee (1974) allowed for only three translational degrees of freedom and did not solve for changes in debris attitude. During this period, other compact type debris such as roof gravel received considerable attention because of its established role in urban window glass damage (Minor and Beason, 1976). Plate

type debris however received little attention because of the complexity of the combined autorotation and translation involved.

Most of these earlier approaches generally took a deterministic approach to the problem of debris flight, employing three-degree-of-freedom (3DOF) particle trajectory models that only allowed for translation within a vortex field (Lee, 1974). However, considering the random behaviour observed in the displacements of objects transported by tornadoes and the high turbulence associated with tornado winds, an alternative probabilistic approach to tornado missile analysis was suggested by Twisdale et al. (1979). This approach was justified by the fact that for missile transport near the ground surface, flow modification, wind turbulence, and missile interactions all play a significant role. As a result of this, identical objects having similar initial conditions were found to exhibit significantly different terminal conditions, suggesting that the variations can be assumed to result from probabilistic mechanisms (Twisdale et al., 1979). In view of these considerations and the computational requirements of a 6DOF model, Twisdale et al. (1979) presented a modified 6DOF random missile orientation model in which the instantaneous rigid body orientation of the missile was specified by two randomly determined angles. The aerodynamic forces were computed using available ballistic coefficients (ratio of drag force to gravity force) for spherical particles and drag, lift, and side force coefficients for fully characterised debris shapes. Although the results were found to be time step dependant due to the use of a random orientation model, comparisons of a series of trajectories indicated that, an update frequency of 1 Hz for the random orientation model provided the transport variance expected of rigid bodies in three-dimensional tornado flows. The results also suggest that ballistic transport (with 3DOF translations and no rotation) underestimates the velocity and range characteristics of tornado-generated missiles (Twisdale et al., 1979). For the debris generation, Twisdale et al. (1979) used a force exceedance criterion to initialize the missile release where a restraint force was applied that must be exceeded before debris is injected into the flow.

The main limitation of Twisdale's approach is that full 3D aerodynamic characteristics of expected debris shapes are still required and these may not be available *a-priori*. An additional criticism arises from the fact that although debris orientations are chaotic, they are not random, and therefore randomly

selecting orientation from one time-step to the next can result in fictitious and unrealistic rotations.

2.4.2 Analytical Modelling

2.4.2.1 The Tachikawa Equations

To address these challenges, Tachikawa (1983) carried out a pioneering study on the trajectories of typhoon-generated missiles in which he investigated the two-dimensional (2D) trajectories of square and rectangular flat plates in a low turbulence (with a turbulence intensity of $\approx 1\%$) uniform horizontal wind flow. Rather than assume a random debris orientation, Tachikawa's model directly computed translational and rotational velocities based on linear and angular momentum conservation principles according to

$$m\frac{\mathrm{d}^2x}{\mathrm{d}t^2} = \frac{1}{2}\rho A\left[\left(U_w - \frac{\mathrm{d}x}{\mathrm{d}t}\right)^2 + \left(\frac{\mathrm{d}y}{\mathrm{d}t}\right)^2\right]\left(C_D\cos\beta - C_L\sin\beta\right), \tag{2.10}$$

$$m\frac{\mathrm{d}^2y}{\mathrm{d}t^2} = mg - \frac{1}{2}\rho A\left[\left(U_w - \frac{\mathrm{d}x}{\mathrm{d}t}\right)^2 + \left(\frac{\mathrm{d}y}{\mathrm{d}t}\right)^2\right]\left(C_D\sin\beta + C_L\cos\beta\right), \tag{2.11}$$

$$I\frac{\mathrm{d}^2\theta}{\mathrm{d}t^2} = \frac{1}{2}\rho Al\left[\left(U_w - \frac{\mathrm{d}x}{\mathrm{d}t}\right)^2 + \left(\frac{\mathrm{d}y}{\mathrm{d}t}\right)^2\right]C_M, \tag{2.12}$$

where x and y are the horizontal and vertical displacements of the plate's centre of mass, g is the acceleration due to gravity, m is the mass of the plate, ρ is the air density, U_w = mean horizontal wind speed, I is the moment of inertia, $\beta = \tan^{-1}\{(\frac{\mathrm{d}y}{\mathrm{d}t})/(U_w - \frac{\mathrm{d}x}{\mathrm{d}t})\}$ is the effective angle of attack. By incorporating dimensionless variables: $\bar{x} = (gx/U_w^2)$, $\bar{y} = (gy/U_w^2)$, $\bar{t} = (gt/U_w)$, $\bar{u} = (u/U_w)$, and $\bar{v} = (v/U_w)$, (where $u = \frac{\mathrm{d}x}{\mathrm{d}t}$ and $v = \frac{\mathrm{d}y}{\mathrm{d}t}$), Tachikawa (1983) presented a set of non-dimensionalised 2D equations of motion for plate type debris,

$$\frac{\mathrm{d}^2\bar{x}}{\mathrm{d}\bar{t}^2} = K\Big[(1-\bar{u})^2 + \bar{v}^2\Big]\Big[C_D\cos\beta - C_L\sin\beta\Big], \tag{2.13}$$

$$\frac{\mathrm{d}^2\bar{y}}{\mathrm{d}\bar{t}^2} = 1 - K\Big[(1-\bar{u})^2 + \bar{v}^2\Big]\Big[C_D\sin\beta + C_L\cos\beta\Big], \tag{2.14}$$

$$\frac{\mathrm{d}^2\theta}{\mathrm{d}\bar{t}^2} = KFr_L^2\Delta\Big[(1-\bar{u})^2 + \bar{v}^2\Big]C_M. \tag{2.15}$$

Tachikawa's non-dimensionalised formulation of the debris flight equations showed that plate type debris flight was controlled by a number of dimensionless parameters; $K(=\rho U_w^2 A/2mg)$ - the ratio of aerodynamic force to gravity force,

$Fr_L(= U_w/\sqrt{gL})$ - a Froude number and $\Delta(= mL^2/I)$ - the dimensionless mass moment of inertia parameter, and C_D, C_L, C_M - the aerodynamic drag, lift and moment coefficients,

$$C_D = \frac{F_D}{\frac{1}{2}\rho U_w^2 A} \ , \ C_L = \frac{F_L}{\frac{1}{2}\rho U_w^2 A} \ , \ C_M = \frac{M}{\frac{1}{2}\rho U_w^2 AL}, \tag{2.16}$$

where $A(= Lb)$ is the plate reference area and F_D, F_L, M are the aerodynamic drag force, lift force and pitching moment acting on the plate. Tachikawa's model relied on experimentally obtained flat plate aerodynamic coefficients. K, later proposed as the Tachikawa number (Holmes et al., 2006a), has been suggested as the main non-dimensional parameter controlling the trajectories of windborne debris. For any given missile type (i.e. compact, plate/sheet, or rod type), a higher value of K indicates a greater propensity of a missile to become air-borne and travel further and faster under wind action. K may also be expressed either as a function of Froude number, Fr_L, thickness ratio, $\tau = h/L$, and the specific gravity of the plate with respect to air, $\mathrm{S_G} = \rho_m/\rho_a$, or as a product of Fr_L and a buoyancy parameter ($\phi = 0.5\rho AL/m$),

$$K = \frac{\rho U_w^2 A}{2mg} = \frac{1}{2}\left(\frac{\rho_m}{\rho_a}\right)^{-1}\left(\frac{h}{L}\right)^{-1}\left(\frac{U_w^2}{gL}\right) = \frac{\mathrm{Fr}_L^2}{\tau \mathrm{S_G}} = \mathrm{Fr}_L^2\phi. \tag{2.17}$$

Tachikawa (1983) validated the model against wind tunnel free flight tests on different aspect ratio plates, revealing the existence of three modes of motion: autorotation, pure translation and intermediate motion. Tachikawa's experiments revealed a relationship between a plate's mode of flight, the aspect-ratio and the initial angle of attack, as shown in Figure 2.15.

Results of these plate free fight tests were compared against results from the numerical integration of Tachikawa's 2D equations of debris flight. Modelled plate trajectories were found to be distributed in a wide range and not always in agreement with the free flight tests (Tachikawa, 1983). Tachikawa (1988) later reported that based on a limited experimental trial, the debris flight equations could sufficiently predict the upper and lower limits of the wide distribution of trajectories observed as shown in Figure 2.16.

In his studies, Tachikawa only considered uniform flow fields and the 2D debris flight of high aspect ratio plates. The influence of atmospheric turbulence, complex launch conditions remained unknown (Tachikawa, 1988). The treatment

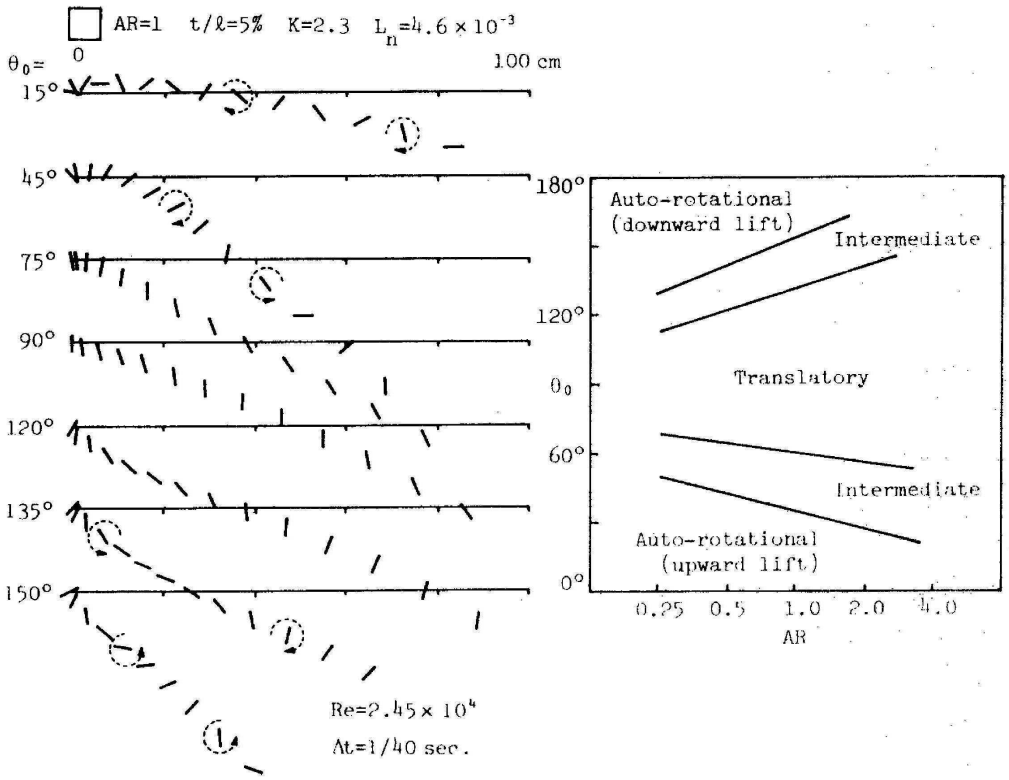

Figure 2.15: Change of plate mode of motion with initial angle of attack (left) and plate aspect ratio (right) observed in wind tunnel experiments by Tachikawa (1983).

Tachikawa suggested for building wake effects was also focused mainly on vertical adjustments of distribution ranges and ignored any influence building wake effects might have on the lateral motion of debris. There are also some fundamental questions regarding the validity of the quasi-steady force model proposed by Tachikawa and subsequently used in future studies. Aerodynamic forces used in the analytical solution are estimated from experimentally obtained aerodynamic coefficients of static plates and the time-averaged coefficients of autorotating plates (Tachikawa, 1983). Tachikawa, assumed a decomposition of the unsteady aerodynamic forces coefficients, C, into a mean (autorotational) component, $C_R(\bar{\omega})$, that is a function of the plate's rotational speed and a fluctuating component, $C_f(\alpha_{eff})$, that is a function of the plate's instantaneous angle of attack, according to,

$$C = C_f(\alpha_{eff}) + C_R(\bar{\omega}). \tag{2.18}$$

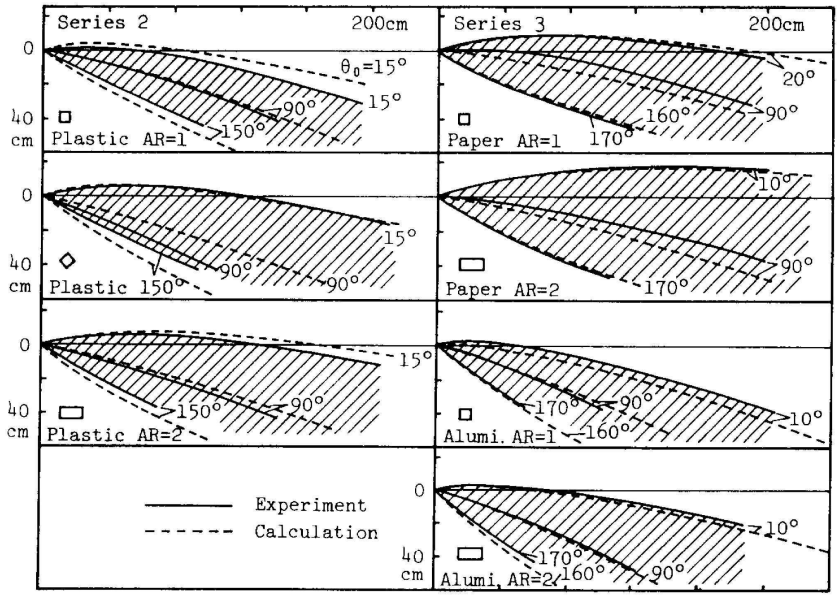

Figure 2.16: Computed and experimental upper and lower limits of debris trajectories (Tachikawa, 1983).

Tachikawa obtained expressions for $C_R(\bar{\omega})$ from experimental measurements of the time-averaged force and torque acting on a rotating plate, as a function of the plate's rotational speed. However, due to the lack of sufficient data on the nature of the fluctuating component about the mean, $C_f(\alpha_{eff})$, Tachikawa assumed it to be equivalent to the fluctuations in the static coefficients according to

$$C_f(\alpha_{eff}) = C_s(\alpha_{eff}) - \bar{C}_s, \tag{2.19}$$

where $C_s(\alpha_{eff})$ are the instantaneous drag, lift and torque coefficients for a static flat plate (see Figure 2.8), and $\bar{C}_s$ is the α-average of $C_s(\alpha_{eff})$ over one revolution.

However, Tachikawa's assumption expressed in (2.19) has no empirical basis and has recently been found to be invalid (Martinez-Vazquez et al., 2010), with much larger force fluctuations observed in autorotating plates compared to the fluctuations in static coefficients.

2.4.2.2 2D Quasi-steady Debris Flight Models

More recently, a number of quasi-steady models of debris flight have been furthered, the most notable of which are discussed in this Section.

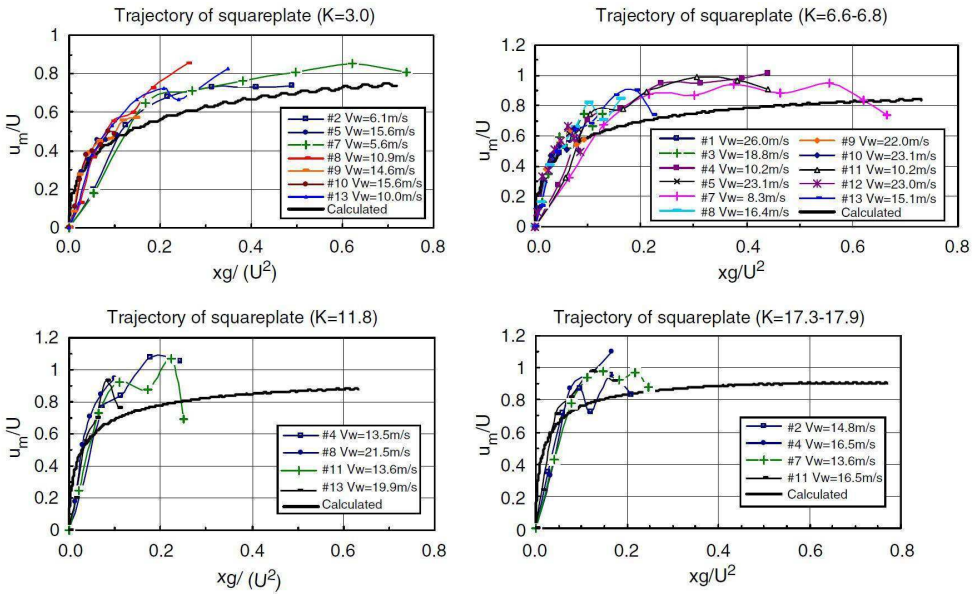

Figure 2.17: Experimental and computed plots of non-dimensionalised horizontal plate velocity versus non-dimensionalised displacement for various Tachikawa numbers (Holmes et al., 2006b).

Holmes et al. (2006b) presented a three degree of freedom (3DOF) model for the 2D flight of plate type debris, using a quasi-steady force model similar to Tachikawa (1983). Magnus effects due to plate rotation on drag and pitching moment were ignored and linear segmented models of experimentally obtained data of normal force coefficients and centre of pressure motion presented in Hoerner (1958) and ESDU (1970) were used to estimate the aerodynamic characteristics of static plates. Non-dimensionalised predictions of horizontal plate velocity against horizontal displacement are shown in Figure 2.17.

The model of Holmes et al. (2006b) does have some limitations. Firstly, debris flight is artificially constrained to 3DOF whereas in reality it would occur with 6DOF. The model does not incorporate the effects of turbulence on plate motion, with a uniform wind speed applied throughout the simulations, under the assumption that the time scale of flight would be too small for temporal turbulence effects to have any impact. Spatial turbulence effects on aerodynamic coefficients were also neglected assuming the length scales the plate interacts with to be much larger than the plate and hence that the smooth flow wind tunnel coefficients should be appropriate for full-scale trajectory calculations. These assumptions, however, neglect the turbulent length and time scales that

would be created as a result of complex launch conditions and the interaction of the plate with its own wake.

Baker (2007) also presented a 2D numerical model for compact, rod and plate type debris, allowing for three degrees of freedom. In his model, Baker incorporates autorotational lift (C_{LA}) as well as moment (C_{MA}) coefficients based on Tachikawa (1983) and Iversen (1979),

$$C_{LA} = k_{LA}(\bar{\omega}/\bar{\omega}_m), \tag{2.20}$$

$$C_{MA} = k_{MA}(1 - (\bar{\omega}/\bar{\omega}_m))(\bar{\omega}/\bar{\omega}_m), \tag{2.21}$$

where $\bar{\omega} = \omega L/U$ is the non-dimensionalised rotational velocity, $\bar{\omega}_m$ is the maximum numerical value of $\bar{\omega}$, taken to be 0.64, hence imposing an artificial upper limit on debris rotational speed. This upper limit of $\bar{\omega}$ has been shown by Kordi and Kopp (2009a) to be inconsistent with the debris flight behaviour. The constants k_{LA} and k_{MA} in these equations are taken to have the values of 0.4 and 0.12, respectively.

Baker (2007) incorporated simulations of atmospheric turbulence by allowing horizontal and vertical fluctuations in wind speed. He states that this approach to turbulence modelling, which is similar to that presented for spheres in Holmes (2004), assumes a spatial uniformity of the velocity field across the debris trajectory and thus does not fully represent the velocity field experienced by the debris (Baker, 2007). The implications of using a three dimensionally spatially varied flow field as opposed to the two dimensional spatially uniform flow fields assumed by debris research so far are unclear and need to be assessed. Baker (2007) identified from his results that the major parameters that characterise debris flight are $\Omega(= Mg/(0.5\rho AU^2))$ which is an inverse of the Tachikawa parameter and $\Delta(= ML^2/I)$ with plate rotational direction sensitive to initial angle of attack as well (Figure 2.18).

Baker also proposes a set of theoretical equations relating dimensionless velocity to dimensionless horizontal displacement which are of practical use in design. He suggests that because of the sensitivity to initial boundary conditions, especially in the case of sheet type debris, a broad range of trajectories would be of more practical use than precise trajectory values. Baker recommends further research into the influences of turbulence and initial conditions to debris flight. A number of other authors such as Kordi and Kopp (2009b) and Scarabino and Giacopinelli

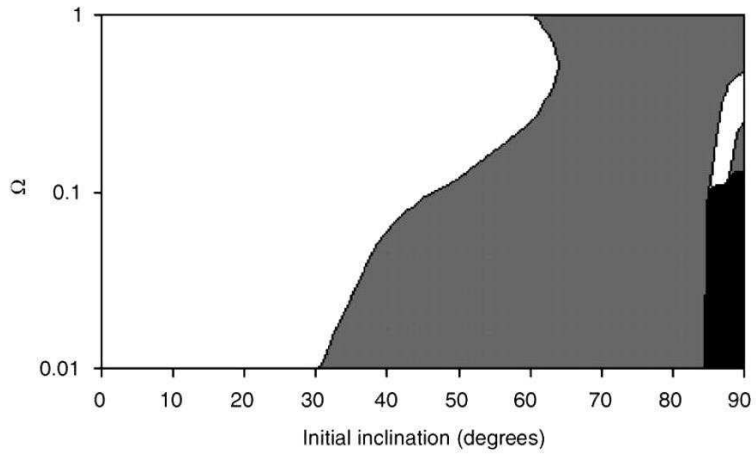

Figure 2.18: Regions of positive and negative asymptotic rotations for sheet debris in $\Omega\Theta_0$ plane. White areas indicate clockwise rotation, grey areas anti-clockwise rotation, and black areas regions of small rotation of variable sign (Baker, 2007).

(2010) have more recently performed further investigations into the 2D quasi-steady modelling of windborne debris.

2.4.2.3 3D Quasi-steady Debris Flight Models

While most of the numerical models of plate type debris flight presented so far were 2D in nature, in reality plate debris orientations and translations are three dimensional in nature. Richards et al. (2008) presented a full 6DOF debris flight model based on linear and angular momentum conservation principles and incorporating a 3D Euler rotational matrix to handle rotations. The complex three dimensional motion is described using a set of translating and rotating coordinate axes as shown in Figure 2.19.

The model makes use of experimentally measured aerodynamic body forces and a centre of pressure position estimation model. Richards carried out experiments on different aspect ratio plates and demonstrated that the normal force coefficients of plates, especially in the case of rectangular plates, are dependant on both the angle of attack and the tilt angle. Richards et al. (2008) also presented a more detailed treatment of aero-elastic effects, incorporating damping terms and hysteresis effects due to dynamic stall and apparent camber. The trajectory model results were found to match full scale flight tests of large roofing sheets, with significant lateral motion observed as well as horizontal plate speeds very

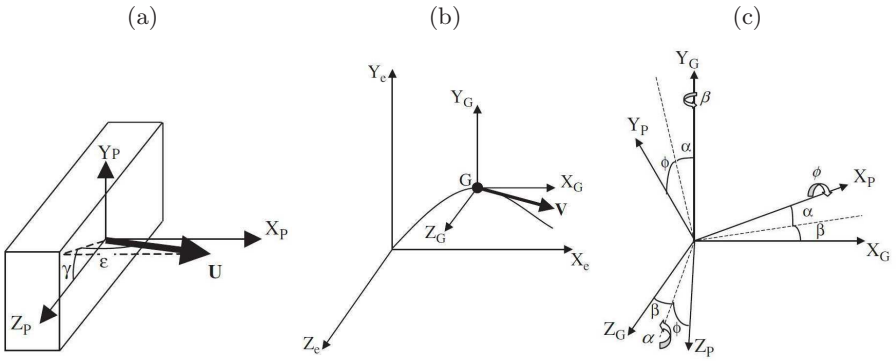

Figure 2.19: (a) The principal axes of a rectangular object, (b) the ground fixed and translating axes and (c) the angles defining the orientation of the object (Richards et al., 2008).

close to, or even exceeding, the wind speed are predicted. Figure 2.20 shows the comparison between experimental and computational results.

2.4.3 Wind Tunnel and Full-Scale Testing

In order to validate these quasi-steady flight models and to gain more insights into plate-type debris flight behaviour, a number of wind tunnel and and full-scale debris flight tests were performed.

Lin et al. (2006) extended the early work by Holmes (2004) on compact debris to plate type debris. Model experiments and full-scale tests on plates were conducted and the plate's mode of motion was observed, together with measurements of plate trajectory, and velocities, all of which are affected by the wind field, model characteristics, and initial support configuration. Results are non-dimensionalised according to Tachikawa (1983) and simple empirical expressions are derived to estimate the horizontal flight speed and flight distance of plate-type debris (Lin et al., 2006). The wind-tunnel and full-scale test results were found to be in reasonable agreement.

Experimental results presented indicate that for a certain debris shape, the debris trajectory, T, is a function of at least nine parameters: wind speed, U, air density, ρ_a, plate dimensions, b, L, and t, plate density, ρ_m, support dimension, D, support position, s, (e.g., centre, corner or edge), and initial angle of attack, α_o.

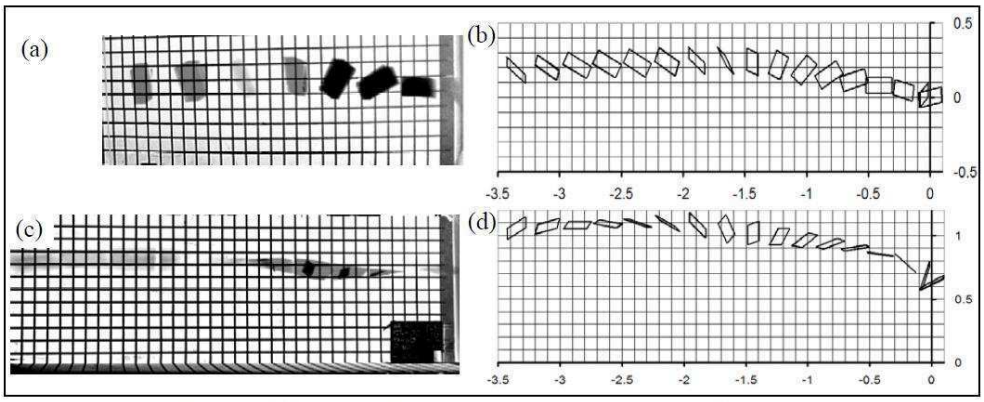

Figure 2.20: Top and side views of the motion of a 2:1 side ratio plate as captured on video: (a) top and (c) side views, and computed: (b) top and (d) side views (Richards et al., 2008).

Lin et al. (2006) identified the Tachikawa parameter, K (Holmes et al., 2006a), the side ratio L/b, and the debris initial support configuration as the main influences on plate trajectories in the vertical direction, with K as the key influence on horizontal trajectories. Empirical equations based on extensive experimental data were presented for use in estimating the plate speed at a given flight distance,

$$\bar{u} \approx 1 - e^{-\sqrt{1.8K\bar{x}}}, \qquad \sigma_{\bar{u}} = 0.0814, \tag{2.22}$$

and the horizontal travel distance covered by a plate after a given flight time,

$$K\bar{x} \approx 0.456(K\bar{t})^2 - 0.148(K\bar{t})^3 + 0.024(K\bar{t})^5, \qquad \sigma_{K\bar{x}} = 0.134, \tag{2.23}$$

where σ are the standard deviations of the experimental data points from the fit-expressions, K is the Tachikawa number, and $\bar{x}$, $\bar{u}$ are non-dimensionalised horizontal displacement and horizontal plate speed, according to Tachikawa (1983). It should be noted that these expressions were derived for approximately two-dimensional flight trajectories in uniform wind flow conditions with little cross-wind deflection being seen. The expressions are also derived for a narrow range of data, with a flight time of up to 0.6 s ($\bar{t} < 0.8$) before debris it hit the ground, depending on the initial height of debris and the vertical trajectory. In addition, the effect of support position on the results is not altogether clear. Lin et al. (2006) recommended further investigation of debris vertical trajectories which are key for estimating landing location. These experimental expressions (Lin

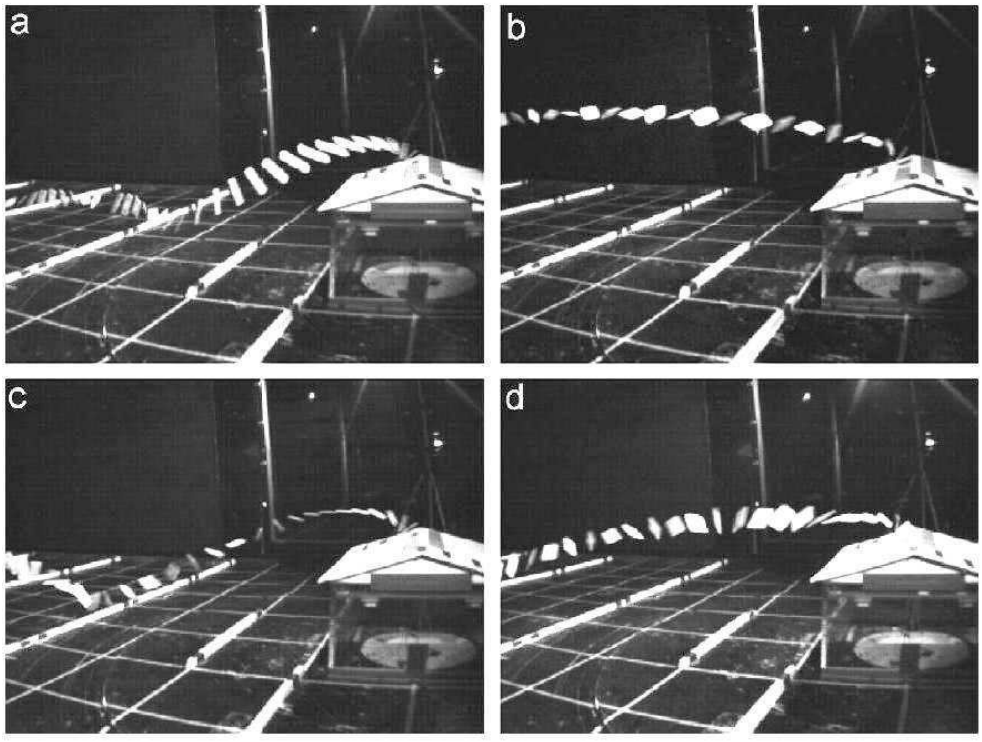

Figure 2.21: High-speed digital images of typical panel flight trajectories following overturning failure (Visscher and Kopp, 2007).

et al., 2006) have been compared against results from 2D quasi-steady models in Holmes et al. (2006b) with good agreement.

2.4.3.1 "Failure Model" Wind Tunnel Testing

Further experimental studies into windborne debris flight have recently been performed, mainly focused on investigating the effects of atmospheric turbulence and complex launch conditions on debris flight. Visscher and Kopp (2007), Kordi et al. (2010) and Kordi and Kopp (2011) have recently undertaken pioneering experimental work involving a destructive wind tunnel modelling approach that more realistically represents the unsteady force coefficients on the plate which change dramatically as the panel lifts off of the roof, leaving a hole beneath. The experiments also included a simulated turbulent atmospheric boundary layer. This work has provided some insights into the influence of initial conditions (i.e: the fixing conditions and complex flow environment around the plate initially mounted on a roof) and flow turbulence to the mechanics of plate flight.

A 1:20 scale, aero-elastic failure model of a 1.2m $\times$ 2.4m roof sheathing panel on a

scaled house model was used in a scaled, open country, turbulent boundary layer. The panel is initially held to the model house with electromagnets which apply a scaled restraining forces. The initial failure mechanism and the trajectory of the panel in flight were captured with high-speed digital video, Figure 2.21 contains sample images (Visscher and Kopp, 2007). For nominally similar initial conditions, Visscher and Kopp (2007) observed different modes of flight including translational, autorotational and intermediate modes. For the particular model arrangement examined, the translational mode was observed 75% of the time, while the autorotational mode was observed 25% of the time (Visscher and Kopp, 2007). Translational trajectories were found to have a short range with less absolute scatter, resulting in less dispersion in the landing location, while autorotational trajectories were far more variable in landing location and tended to display greater ranges as shown in Figure 2.22. An initial overturning failure was observed for every test although the results were noted to be dependant on hold down strength, panel mass and size as well as the angle of attack of the wind and the house geometry.

Visscher and Kopp (2007) suggest that the effects of variability of the flow field on the resulting aero-dynamic normal forces play a critical role in determining the flight mode and this is probably most significant during the initial overturning and the first few moments thereafter. They therefore conclude that the sensitivity to particular flight conditions appears to be greater even than indicated by Baker (2007) when actual panel failures are considered. Visscher and Kopp (2007) also found the speed at which sheathing panels fly to be a fraction of the mean wind speed and was calculated as 0.60 with standard deviation of 0.08 for the translational mode, and 0.70 with standard deviation of 0.12 for the autorotational mode for the particular panel, wind angle, roof location and hold-down force examined. These failure wind speed distributions were found to fit a Gumbel distribution (Visscher and Kopp, 2007) as shown in Figure 2.23.

Kordi et al. (2010) and then Kordi and Kopp (2011) applied the same failure model approach to investigate the effect of varying wind direction, debris properties and the surrounding neighbourhood structures. They observed that with oblique wind approach angles relative to the roof ridge, complex 3D spinning was the most dominant mode of flight and that the mode of flight was dependant on the approaching wind direction. Comparisons with the theoretical asymptotic

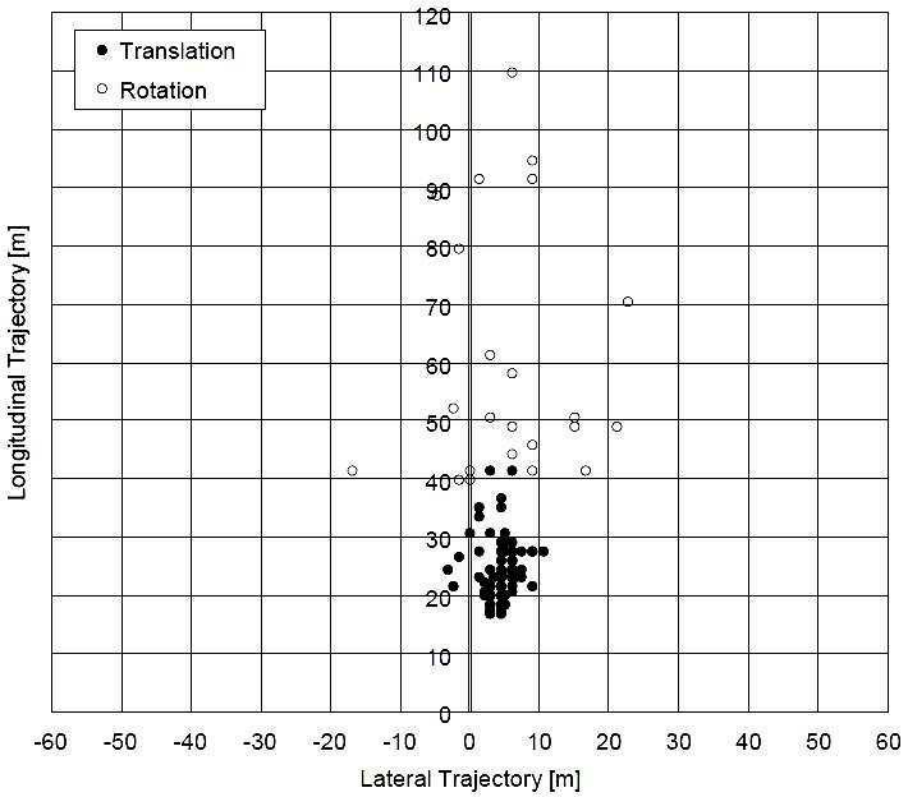

Figure 2.22: Scatter plot of equivalent full scale panel flight distances. The graph origin is located at the center of the house with the panel being tested located at approximately 3.7m (12 ft) to the right, and 0.6m (2 ft) downstream in equivalent full scale dimensions (Visscher and Kopp, 2007).

limit from analytical models revealed conflicting results for different debris types with shingles flying close to the theoretical asymptotic limit speed while tiles did not.

2.5 Debris Damage and Risk Modelling

Subsequent to debris generation, flight and impact onto a target building, there is a need to estimate the potential damage on the target building due to debris impact. This is the central application of information on impact location and impact velocity obtained from debris flight models.

Unanwa et al. (2000) presented a debris damage model using the concept of wind damage bands which employ an objective weighting technique driven by building component cost factors, component fragilities, and location parameters to obtain

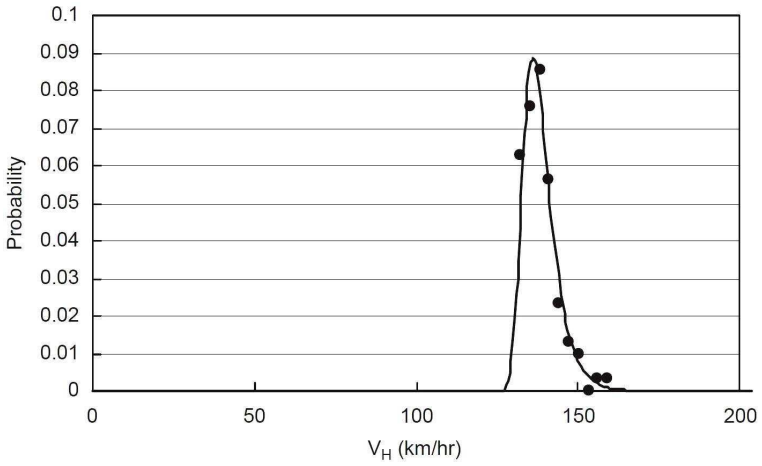

Figure 2.23: Distribution of 10-min mean wind tunnel speeds for the observed failures with units in equivalent full scale (Visscher and Kopp, 2007).

upper and lower bounds to building damage thresholds. These wind damage bands formed the basis for the proposed methods of wind damage prediction of individual buildings and groups of buildings, wind damage mitigation, and emergency management planning.

Wills et al. (2002) later presented a model definitively linking the aerodynamics of debris particles with the damage caused when flying debris strikes a building or structure. The model defined a critical wind speed at which different types of debris became airborne based on the fixing conditions and weight for compact debris, mass per unit area for plate debris and mass per unit length for rod debris. The kinetic energy of the debris was then expressed as a fraction of the notional kinetic energy which is the kinetic energy it would posses if it were flying at the velocity of the wind. A debris damage function based on estimated impact kinetic energy was then presented as,

$$D = \frac{1}{16}\rho_m\{(C_{F\rho_a})/(\rho_m I g)\}^3 J^2 U^8, \tag{2.24}$$

where ρ_m is the material density, ρ_a is the air density, $C_{F\rho_a}$ is a generalized body force coefficient, I is the ratio of fixing strength to material weight, g is the gravitational acceleration, J is the fraction of the wind speed at which the object flies before impact, and U is the mean wind speed. Expression (2.24) assumed the damage sustained by the structure (D) to be proportional to the missile impact kinetic energy.

The damage model presented by Wills et al. (2002), characterizes debris flight

and damage mainly by density, size and shape with many aspects of the debris flight and damage being simplified in order to make useful prediction. As a result it might not give accurate predictions for non-compact debris types. Full scale observations of flying debris damage in real storm conditions were recommended in order to validate the model.

A study by Vickery et al. (2003) on hurricane pressure cycling following missile impact for residential buildings further provided a link between realistic storm wind speed simulations, debris generation, debris flight and impact on buildings or the ground. As part of the model, simulated hurricane data with changing wind speed and direction was used to generate debris from the model buildings, track the debris as it flew through the air, and record its final impact position and velocity. The debris was generated using a load resistant approach, where once the calculated wind load at a time step exceeded the resistance of a component, the component was released into the wind field from the structure and becomes a wind-borne missile. The trajectory module used tracks the movement in a turbulent wind field by numerically solving a set of equations of motion for a rigid body. The process continues until the trajectory intersects with a wall or roof surface of a structure or the ground, at which point the module records such variables as impact time, location, impact speed, incident angle, missile orientation and mass, for subsequent impact and pressure cycle counting analysis. Figure 2.24 illustrates the overall debris modelling framework presented by this study.

The work presented by Vickery et al. (2003) represented a complete debris modelling cycle with a contribution through more detailed storm simulation and a more elaborate debris generation and damage modelling approach. However, the model neglects a number of factors affecting debris flight such as the sensitivity to initial orientation, complex launch conditions and atmospheric turbulence.

Due to the broad range of factors influencing debris flight, its behaviour can be inherently chaotic, as a result, stochastic approaches to the problem have emerged. Recently, Lin and Vanmarcke (2008, 2010) have proposed a probabilistic model, based on the application of Poisson random measure theory to the prediction of windborne debris damage in residential areas and the estimation of economic losses due to severe storms. The model uses four probabilistic distributions for each type of debris generated from each building in an area: (i)

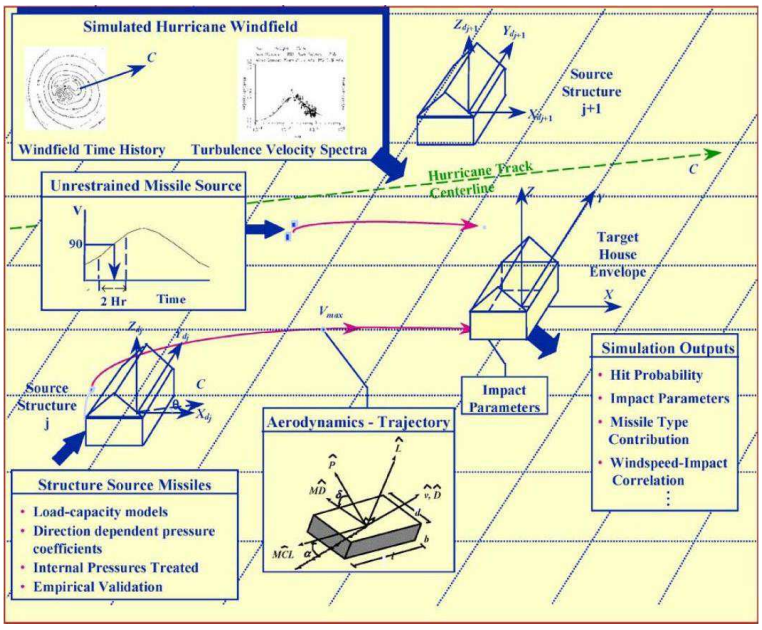

Figure 2.24: Wind borne debris modelling methodology (Vickery et al., 2003).

the mean number of debris objects generated, λ, (ii) the probability distribution of debris landing positions on the horizontal plan, μ, (iii) the conditional probability of debris impacting a vulnerable building component, p, and (iv) the conditional probability distribution of horizontal impact momentum, ϕ (Lin and Vanmarcke, 2010). The two probabilistic quantities, μ and ϕ, are estimated from experimental and numerical simulations based on previous work by Tachikawa (1983), Lin et al. (2006), Holmes et al. (2006b) and Lin et al. (2007).

However, these models are not without limitations, the most notable being their two-dimensional nature. Lin and Vanmarcke (2010) admit that debris trajectories by their nature, are much less predictable, due to other effects that are not easily parameterised, such as the irregularity of actual debris shapes, initial support conditions, and turbulence in hurricane winds. Lin and Vanmarcke (2010) therefore recommend that in order to estimate the probability distributions of actual debris trajectory parameters, larger data sets obtainable from Monte-Carlo type numerical simulations, model-scale and full-scale experiments, and storm observations and post-damage surveys are needed.

The Monte-Carlo approach has itself been separately demonstrated in determining the debris risk to the public due to the columbia breakup during reentry (Lin et al., 2003). In this approach, key parameters are randomized over repeated tri-

als while keeping the trajectory model itself deterministic. The trajectory model used may be a detailed CFD model as used in the Monte-Carlo simulation of shuttle ascent foam debris modelling by Murman et al. (2005). Other Monte-Carlo simulations have however used simplified analytical/ballistic models for estimating cylindrical mine motion in water (Mann et al., 2007) or modelling the risk to ground based populations of aerospace debris (Lin et al., 2003).
Although the present research has not been directly concerned with the probabilistic modelling of windborne debris flight, the CFD-RBD model presented can be used as a deterministic trajectory model for the Monte-Carlo simulation of windborne debris flight.

2.6 CFD Modelling of Debris

Relatively little work has been carried out in the area of Computational Fluid Dynamics (CFD) based modelling of debris flight. Most of the relevant CFD modelling work so far done has been concerned with 2D simulations of plates falling freely under calm conditions (see for example Andersen et al. (2005) and Jin and Xu (2008)). Similarly, work on the CFD modelling of plate autorotation (previously discussed in section 2.3.3 of this report) has been restricted to 2D autorotation of high-aspect-ratio plates which, as earlier explained, is qualitatively different from the low-aspect-ratio plate behaviour. Some work has been performed on the CFD simulation of low aspect ratio plate translations and rotations but this has been mainly concerned with the prescribed motion of wing shaped plates (Wang, 2005; Dong et al., 2006; Taira and Colonius, 2009) with the exception of Murman et al. (2005).
Murman et al. (2005) present an automated CFD process for determining the aerodynamic characteristics of debris shedding from a Space Shuttle Launch Vehicle (SSLV) during ascent. This work was initiated by the Colombia Accident Investigation Board (CAIB) in the after-math of the Columbia Shuttle accident, with the aim of determining a credible flight path and impact velocity for a piece of foam debris from a SSLV.
One of the recommendations of the CAIB for Return-To-Flight (RTF) of the shuttle fleet was an analysis of the complete debris environment experienced by a SSLV during ascent, including a categorization of all possible debris sources, their probable geometric and aerodynamic characteristics, and their potential for

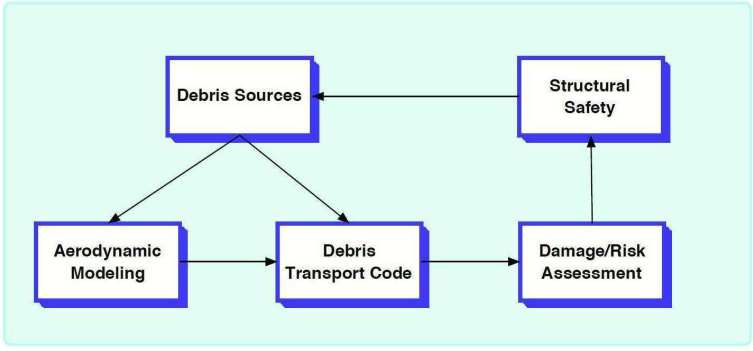

Figure 2.25: Debris analysis feedback loop. Damage from potential debris sources is assessed, and those which are not tolerable are eliminated. This cycle then continues until a safe tolerance is achieved (Murman et al., 2005)

damage (Murman et al., 2005). These aerodynamic characteristics were required for the debris transport analysis, Figure 2.25, to predict flight path, impact velocity and angle, and provide a statistical distribution to support risk analyses where appropriate. According to Murman et al. (2005), existing debris transport analysis codes simplified many aspects of the problem in order to provide quick and efficient engineering analysis of debris flight. Firstly, it was assumed that the debris had no effect on the flow field and, secondly, these ballistic models did not account for any potential rotation of the body or for dispersion of trajectories about the zero-lift trajectory. However, in reality the debris trajectories are highly non-linear, involving uncontrolled three-axis rotations (Murman et al., 2005) and the debris was also found to have significant effects on the flow field (Gomez et al., 2004). Traditional aerodynamic modelling techniques developed for controlled manoeuvres of aerodynamically-trim aircraft are therefore not sufficient.

While free-flight ballistic range testing can provide the trajectory data needed for model development, this type of testing is time-consuming, costly, and limited in the types of shapes and conditions that can be efficiently tested (Murman et al., 2005). Unsteady 6DOF CFD methods which provide the same trajectory data as free-flight testing without these limitations were therefore found more suitable. Depending on the available computing power, CFD methods can efficiently provide hundreds of trajectories in a relatively short period of time for an arbitrary geometry and the use of numerical simulations frees the ballistic

testing to concentrate on a critical subset of the requirements, such as structural limit testing or reference validation cases (Murman et al., 2005).

In light of this, Gomez et al. (2004) and Murman et al. (2005) presented a strategy involving an unsteady CFD simulation fully coupled with a 6DOF solver based on an implicit Cartesian moving-boundary solver described in Murman et al. (2003a,b). The CFD code was used to solve the Navier-Stokes equations using a finite difference formulation in body-fitted curvilinear meshes and the Spalart-Allmaras turbulence model. Added enhancements to the CFD code included: on-the-fly generation of off-body grid systems, MPI enabled scalable parallel computing, automatic load balancing, aerodynamic force and moment computations, general 6DOF model, rigid-body relative motion between an arbitrary number of bodies, domain connectivity, solution error estimation, and grid adaptation in response to body motion (Gomez et al., 2004). This allowed for a significantly more accurate determination of the aerodynamic forced and moments acting on the debris using the CFD code while the 6DOF motion solver computed the debris movement in response to these forces.

This level of automation of the CFD/6DOF simulations allowed for a Monte-Carlo based simulation approach to the characterisation of debris trajectories. This was necessary in order to achieve a stochastic description of debris trajectories which were found to be sensitive to Mach number, altitude, geometry and initial conditions. Figure 2.26 presented by (Murman et al., 2005) illustrates the Monte Carlo 6-DOF trajectory analysis process. To achieve this Monte Carlo 6DOF/CFD simulation approach, the geometry was held fixed while the flight conditions, initial orientation and initial rotation rate of the debris were varied, with multiple trajectories being run in parallel.

Six different debris shapes and sizes were simulated based on the several possible foam-shedding scenarios with various initial velocity and rotation conditions applied to each piece of debris (Gomez et al., 2004). The debris path was found to be sensitive to initial conditions, however the axial velocity of the debris relative to the vehicle was nearly independent of the debris initial conditions and depended primarily on the mass of the debris (Figure 2.27). The 6-DOF calculations also showed that debris of the dimensions captured on film would strike the wing with a relative velocity of nearly 950 feet/sec. In large part due to the CFD results, the CAIB determined that the most likely debris size and this was

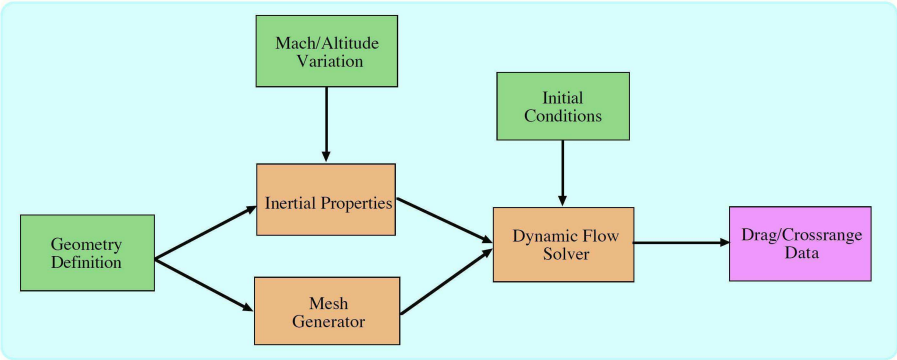

Figure 2.26: Process diagram for Monte Carlo 6-DOF trajectory analysis. Green boxes are process inputs which are given a range of inputs, orange boxes are internal modules, and the purple box is output fed to the debris transport software (Murman et al., 2005).

used in foam firing tests into actual flight RCC panels. The study also concluded that the debris does have a significant influence on the flow field around it, with calculations showing a lowering in leading edge pressure of approximately 0.4 psi just before debris impact.

Experimental free-flight tests were conducted to validate the numerical predictions and the results are presented in Brown et al. (2006). These free-flight tests were carried out in the NASA Ames Gun Development Facility (GDF) for unconstrained, isolated debris pieces with representative shapes and flight conditions (Murman et al., 2005).

Polyethylene frustums - nominally 3.56 cm in diameter, 0.71 cm long, and 4 grams in mass - were launched into 1 atm air at a Mach number of approximately 2.8. Their rapid-decelerating, often highly-lifting, and sometimes tumbling 6DOF trajectories were recorded over a distance of 12 feet by arrays of top and side view high speed cameras (Murman et al., 2005; Brown et al., 2006). In addition, the response of the debris to perturbation was obtained by "tripping" the debris projectile before it entered the test section, thereby changing its orientation and providing a high initial rotation rate.

Brown et al. (2006) and Murman et al. (2005) conclude from the results that under conditions dynamically similar to SSLV insulating foam debris flight, symmetric frustums oscillate about the bluff-body, static-stability orientation and do not tumble. The perturbation has the effect of inducing larger amplitude

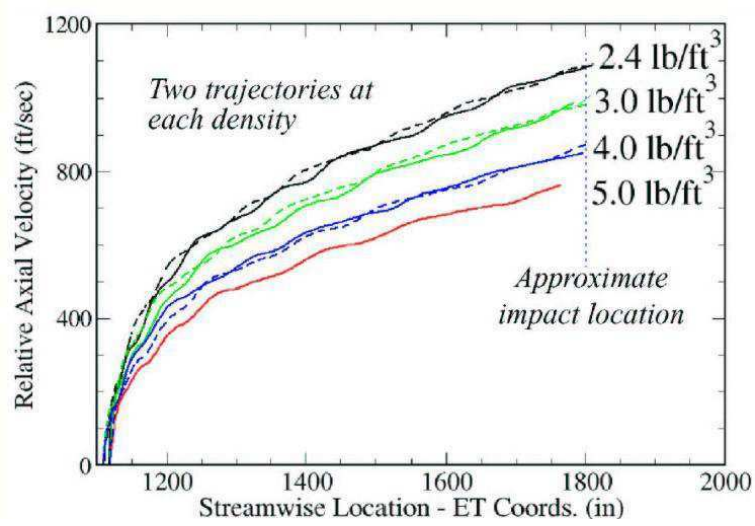

Figure 2.27: Axial velocities for debris pieces with volume of 704 cubic inches and different foam densities. Dotted and dashed line indicate different initial condition sets (Gomez et al., 2004).

damped oscillations about the bluff-body orientation but still does not tumble. Comparison between the measured axial translation distance and the model pitch and yaw variations and the CFD/6DOF computations showed excellent agreement and is shown in Figure 2.28 for symmetrical unperturbed debris and Figure 2.29 for symmetrical but perturbed (or tripped) debris.

It was noted that the dynamical stability observed for the idealized symmetrical frustums is due to the low rotational inertia and idealized aerodynamic and inertial symmetry, although actual debris would not exhibit these properties resulting in significant tumbling motion (Murman et al., 2005). While the average drag for the oscillating trajectory of an idealized frustum and the tumbling trajectory of a highly asymmetric debris piece are similar, this is not the case when considering the cross-range behaviour. Simulations of actual foam divots which were asymmetric both aerodynamically and inertially (in terms of geometry and mass distribution) showed trajectories developing significant cross-range (lateral dispersion) as the debris rotates about all three body axes. Figure 2.30 illustrates the computed cross-range of different foam debris geometric and inertial asymmetries.

Rather than model the aerodynamic properties, a cross-range envelope is developed from the results of the Monte Carlo process and superimposed on the

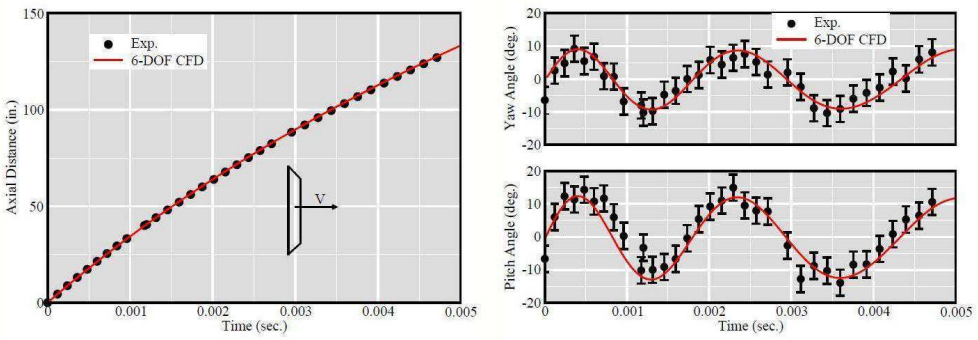

(a) Axial displacement. (b) Pitch and yaw orientation.

Figure 2.28: Comparison of free-flight and computed translation and rotation variations for un-tripped frustum trajectory obtained in the NASA Ames GDF. Initial Mach number is 2.74. Uncertainty approximated from visual inspection of reduced data. $(D/t = 5, \theta = 40°)$ (Gomez et al., 2004; Murman et al., 2005).

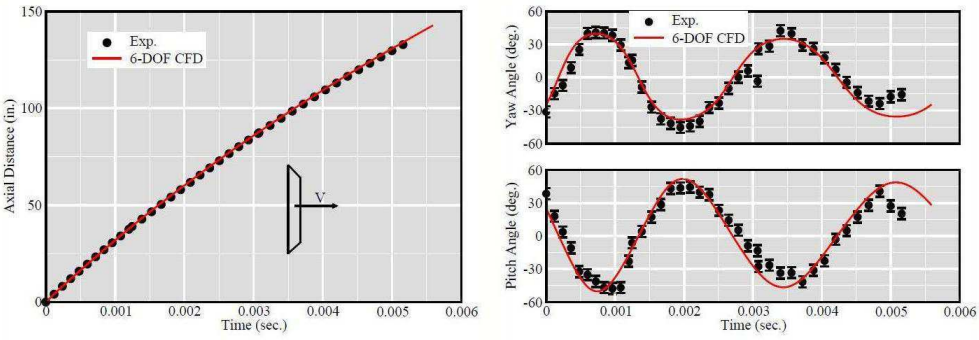

(a) Axial displacement. (b) Pitch and yaw orientation.

Figure 2.29: Comparison of free-flight and computed translation and rotation variations for initially perturbed frustum trajectory obtained in the NASA Ames GDF. Initial Mach number is 2.56. Uncertainty approximated from visual inspection of reduced data. $(D/t = 5, \theta = 40°)$ (Gomez et al., 2004; Murman et al., 2005).

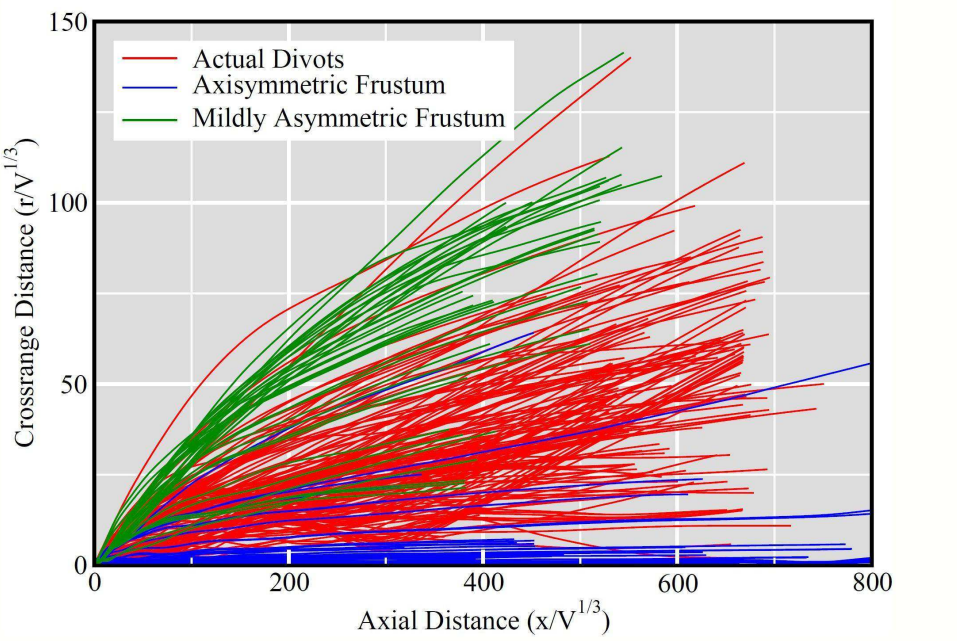

Figure 2.30: Computed cross-range behaviour from Monte Carlo 6-DOF trajectories for foam debris shapes at a release Mach number of 2.5 (Murman et al., 2005).

zero-lift trajectory as shown in Figure 2.31 (Murman et al., 2005). The cross-range envelope was then used to determine the possible impact area while the drag (zero-lift) model determines the impact velocity. Further, Murman et al. (2005) suggests that a complete statistical distribution of cross-range behaviour can be provided so that a probability function can be queried for any point within the envelope.

The process focused on modelling the resulting behaviour of Monte-Carlo 6DOF simulations, rather than developing highly accurate aerodynamic models, due to the short term nature of the project and in the interest of efficiency of the process. More proximate aerodynamic models are recommended as a longer-term research topic which can build on the model presented (Murman et al., 2005).

CFD-Rigid Body Dynamics (RBD) coupling approaches have also been widely used in military applications (Costello et al., 2007) to generate the aerodynamic coefficients needed for the simulation of rigid projectile flight. During a CFD-RBD simulation, aerodynamic forces and moments and the full rigid body state

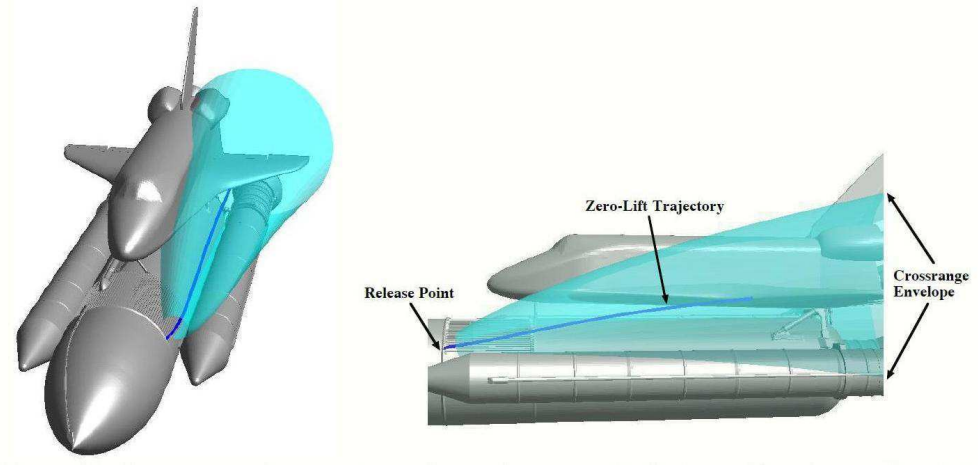

Figure 2.31: Cross-range envelope superimposed upon the computed ballistic zero-lift trajectory (Murman et al., 2005).

vector of the projectile are generated at each time step in the simulation. A 3D unsteady Reynolds-Averaged Navier-Stokes (RANS) solver is used for computation of turbulent flows (Costello et al., 2007).

The coupled CFD-RBD simulations were used to provide a full solution of the aerodynamic forces and moments along with the full state of the rigid projectile at every time step in the solution. This data was then used for the estimation of projectile aerodynamic coefficients which are required for more rapid trajectory modelling. Through this approach, Costello et al. (2007) attempted to exploit the benefits of CFD-RBD simulations while avoiding the high computational time required in the application of accurate CFD-RBD to generate the thousands of 'simulations required for dynamic analysis.

These different studies demonstrate the potential for the application of coupled CFD-RBD motion to wind borne debris flight simulations.

2.7 Concluding Remarks

A review of existing literature on the aerodynamics of static and rotating flat plates has been presented. The availability of extensive measurements on flat plates have allowed a complete understanding of the aerodynamics of static 2D and 3D flat plates. This quantitative information on the aerodynamic characteristics of the static plates and the qualitative knowledge of the flow structures in the wake of the flow would be useful in the preliminary validation of numerical

models for debris flight.

In comparison, there remain a number of open questions regarding the phenomena of plate autorotation and the limitations of autorotational theory. The origin of the aerodynamic damping that allows stable autorotation to occur is hitherto unclear and there is a need to investigate this phenomena. In addition, although wind-borne debris has been observed to exhibit a complex three-dimensional (3D) spinning modes of autorotation, most numerical models and experimental studies have been pre-occupied with a fixed-axis (2D) autorotation and there is a need to extend these models to full 3D autorotation. CFD-RBD simulations which have been demonstrated as useful tools for the investigation of low aspect ratio winged flight and high aspect ratio autorotation can play an important role in the further development of low aspect ratio autorotational theory and be extended to full 3D autorotation.

Although number of quasi-steady analytical models of windborne debris flight have been presented, these models remain largely limited to 2D debris flight in uniform flows and simple debris shapes for which a full aerodynamic characterisation is available. The quasi-steady forces used by these analytical models are based on a decomposition into static and autorotational components which needs to be adequately verified.

Further more, debris trajectories are sensitive to effects that are not easily parameterised, such as atmospheric boundary layer turbulence and the complex support and launch conditions, as demonstrated by the results of recent failure model experiments. Existing analytical models are however unable to account for these effects. The reliable and accurate prediction of debris risk and damage calls for a more robust approach to the numerical simulation of plate type windborne debris which does not require extensive *a-priori* knowledge of the aerodynamic behaviour of the debris and easily allows for the incorporation of complex launch conditions.

Recent applications of CFD-RBD simulations to the debris transport analysis of shuttle ascent foam debris have demonstrated the potential that these methods hold as valuable tools for understanding the behaviour of plate-type windborne debris. This has been the major inspiration for this research whose goal is to present a more complete numerical model which would allow for the Monte-carlo simulation of plate type windborne debris.

Chapter 3

Computational Wind Engineering (CWE)

This chapter introduces Computational Wind Engineering (CWE), which is the application of Computational Fluid Dynamics (CFD) to wind engineering problems. The chapter begins with a discussion of the wind in the atmospheric boundary layer, followed by an introduction to CFD, turbulence modelling and developments in the modelling of fluid flow around moving wall boundaries.

3.1 The Wind

The wind is generally defined as the bulk motion of air in the earth's atmosphere. This motion is initiated a considerable distance above the Earth's surface, beyond the influence of surface friction, in the *free atmosphere*. Here, the air is driven by large scale synoptic pressure gradients arising from differential heating of the earth's surface and the atmosphere, and subsequently influenced by Coriolis forces due to the earth's rotation. As a result of the geostrophic balance between Coriolis and pressure forces, the resulting geostrophic wind direction is parallel to the isobars as shown in Figure 3.1. This perfect geostrophic balance rarely occurs in nature due to the presence of other forces such as ground friction as well as the fact that the pressure isobars were never perfectly straight. It is however, still a valuable approximation.

Closer to the earth's surface, the wind is affected by the drag imparted by the earth's surface creating an Atmospheric Boundary Layer (ABL) in which flow is no longer parallel to the isobars. Burton et al. (2001) highlight the principal effects governing the properties of the ABL as; the strength of the geostrophic wind, the surface roughness, Coriolis effects due to the earth's rotation, and thermal effects.

The influence of thermal effects is classified into three categories; stable, unstable and neutral stratification. A neutrally stratified ABL often occurs in strong winds, when turbulence caused by ground roughness causes sufficient mixing of

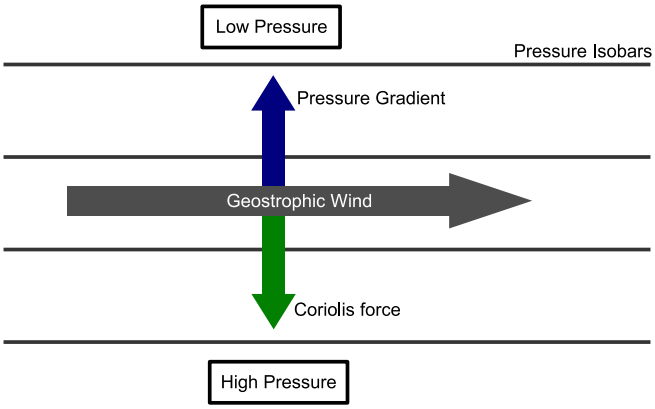

Figure 3.1: The geostrophic balance between pressure and coriolis forces in the free atmosphere.

the boundary layer to disrupt any thermal effects. As the air rises and cools adiabatically, it remains in thermal equilibrium with its surroundings and leads to what is known as a *Neutral Atmospheric Boundary Layer* (Burton et al., 2001). For wind engineering applications, where extreme wind storm conditions are of interest, neutral stability is the more relevant scenario to consider.

Sutton (1953) described the neutral ABL as composed of two regions: a surface layer 50-100m deep with constant shear stress and a region above this extending to a height of 500-1000m where the shear stress varies with height. The surface layer region is characterised by approximately constant shear stress in the vertical direction and is not affected by the earth's rotation. As a result, the structure of the wind in this layer is determined predominantly by surface friction and vertical temperature gradients (Kaimal and Finnigan, 1994).

For surfaces covered with a large number of discrete bluff obstacles (such as in urban and forest canopies), a roughness sub-layer is observed with a vertical extent of up to several tens of metres, which is characterized by inhomogeneous regions of reduced mean velocity and enhanced levels of turbulence (Macdonald, 2000).

Above the surface layer region, shear stress becomes variable and the wind structure is determined by surface friction, temperature gradients and the earth's rotation. This intermediate region between the surface layer and the geostrophic wind can be described as an Ekman layer in which a balance exists between pressure forces, Coriolis forces and surface friction (Tennekes and Lumley, 1997).

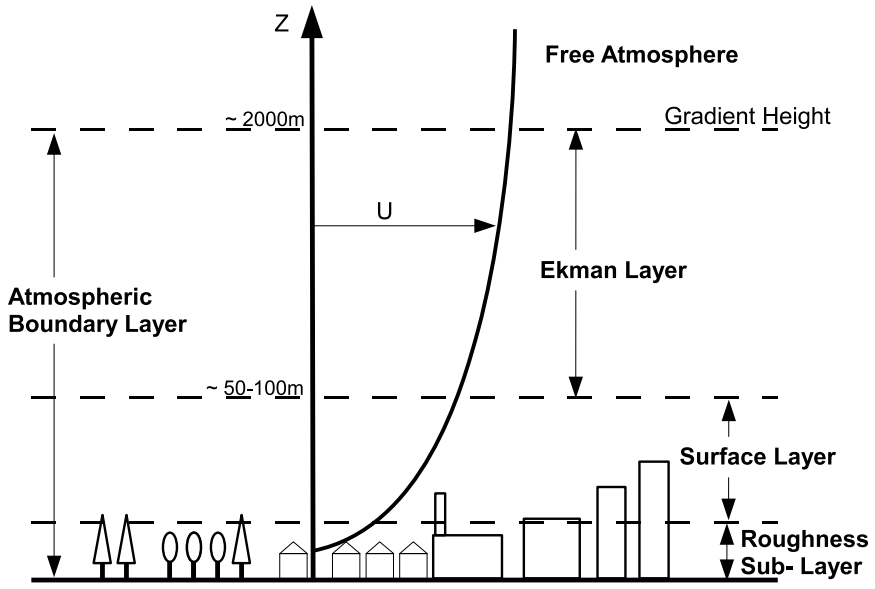

Figure 3.2: The different regions of the atmospheric boundary layer.

Figure 3.2 illustrates the different layer of the Neutral ABL.
Winds are typically classified by their spatial scale, speed, the types of forces that cause them, the geographic regions in which they occur, and their effect. Wind speeds are usually obtained as averages over a ten minute period. These measured wind speeds can be thought of as consisting of a mean wind speed determined by annual, seasonal, synoptic and diurnal effects which vary on a time scale of one to several hours, with superimposed turbulent effects which have a zero mean when averaged over the ten minute window (Burton et al., 2001). Figure 3.3 illustrates this mean wind speed composition, where $\bar{U}$ is the mean annual wind speed at a given location, while Table 3.1 compiled from Burton et al. (2001), summarizes the different wind speed variations, their associated time scales and causes, as well as their common mathematical representations. The temporal and spatial fluctuations of the wind are, for practical and modelling applications, its most important characteristics.

3.1.1 The ABL Velocity Profile

In the neutral equilibrium atmospheric boundary layer, the mean horizontal wind speed in the surface layer has been observed to follow a log-law profile

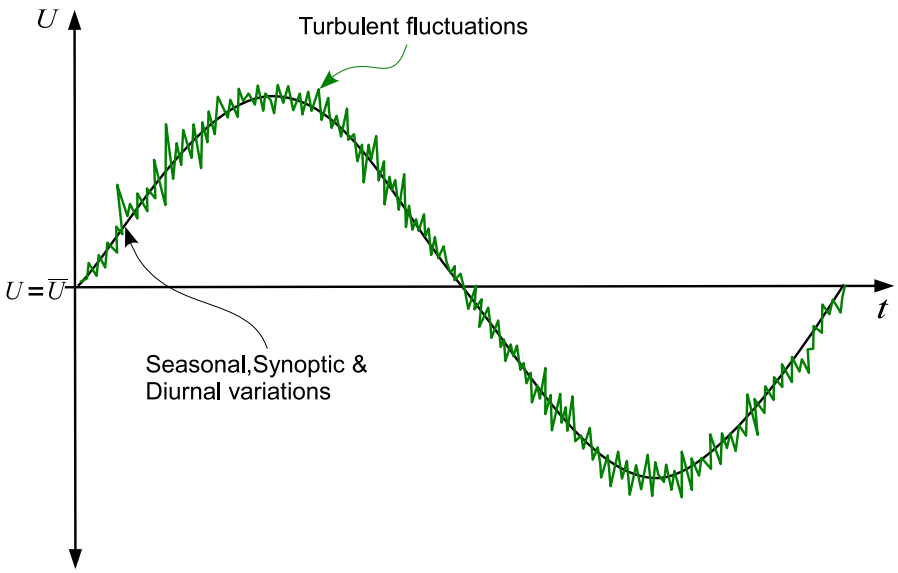

Figure 3.3: Mean and turbulent wind speed fluctuations.

described in ESDU (1985) as,

$$\frac{\bar{U}(z)}{u^*} = \frac{1}{\kappa}\left[\ln\left(\frac{z-d}{z_o}\right) + 34.5\frac{fz}{u^*}\right], \tag{3.1}$$

with

$$f = 2\Omega\sin(|\lambda|), \tag{3.2}$$

where κ is the von Karman constant, z_o is the aerodynamic roughness length, d is the zero-plane displacement height, f is the Coriolis parameter defined for temperate regions in (3.2), Ω is the angular velocity of the earth's rotation, and λ is the latitude. From a mean wind speed measurement, $\bar{U}_{ref}$, taken at a reference height, z_{ref}, the friction velocity, u^*, is computed according to

$$\frac{u^*}{\bar{U}_{ref}} = \frac{\kappa}{\left[\ln\left(\frac{(z_{ref}-d)}{z_o}\right) + 34.5\frac{fz}{u^*}\right]}. \tag{3.3}$$

The aerodynamic roughness length, z_o, is a measure of surface roughness and is proportional to the average height of upstream roughness elements, while the zero-plane displacement height, d, is the height at which wind speed becomes zero when the logarithmic wind profile $\bar{U}(z)$ is extrapolated. Together, z_o and d characterise the surface roughness and Table 3.2 shows approximate values for these parameters from ESDU (1985).

Table 3.1: Wind speed variation components and their corresponding time scales (Burton et al., 2001).

Type of Variability	Characteristics	Causes	Modelling
Long Term Variations	Variation in mean annual speed from year to year.	El'Nino, Climate change, etc.	Not well understood.
Annual and Seasonal variations	Annual mean wind speed variations within the year.	Random, Tilt in Earth's rotation axis, seasonal climates.	Weibull, Rayleigh, "bi-Weibull" distributions.
Synoptic Variations	$\approx$ 4 day frequency.	Large scale weather fronts, Coriolis forces.	Numerical Weather Prediction Models.
Diurnal Variations	$\approx$ 24 hr frequency.	Local thermal effects	Numerical Weather Prediction Models.
Turbulence	Less than 10 min frequency. Gaussian nature.	Friction with Earth's surface, Thermal effects.	Complex deterministic equations, Statistical descriptors.

Table 3.2: Typical Surface Roughness Lengths, z_o (ESDU, 1985).

Type of Terrain	z_o (m)	d (m)
Cities, forests	0.7	15 - 25
Suburbs, wooded countryside	0.3	5 - 10
Villages, countryside with trees and hedges	0.1	0 - 2
Open farmland, few trees and buildings	0.03	0
Flat grassy plains	0.01	0
Flat desert, rough sea	0.001	0

The log-law profile is valid throughout the surface layer up to the free atmosphere. From purely theoretical considerations, Tennekes and Lumley (1997) showed that the height of the boundary layer, h may be estimated using

$$h = C\frac{u^*}{f}, \tag{3.4}$$

where C is an empirical constant, and a value of $C = 0.25$ has been found to yield boundary layer heights close to day time conditions (Kaimal and Finnigan, 1994). Depending on the nature of the surface forcing, the depth of the ABL may vary from 0.1 - 3km (Stull, 1988).

3.2 Turbulence

In wind engineering, turbulence generally refers to fluctuations in wind speed on a relatively short time-scale, typically less than about 10 minutes. Wilcox (1994) presents a definition proposed by Taylor and Von Karman describing turbulence as

> *an irregular motion which in general makes its appearance in fluids, gaseous or liquid, when they flow past solid surfaces or even when neighbouring streams of the same fluid flow past or over one another.*

According to Burton et al. (2001), wind turbulence in particular is generated mainly from two often interconnected causes *friction effects* between the wind and the earth's surface including topographical features, buildings and vegetation, and *thermal effects* which can cause air masses to move vertically as a result of variations of temperature and hence of the density of the air.
Tennekes and Lumley (1997) list some of the characteristics of turbulent flow as:

I. **Irregularity.** Turbulent flow is irregular and chaotic. The flow consists of a spectrum of different length scales (eddy sizes) where the largest eddies are of the order of the flow geometry and characterize the production range and the smallest eddies characterize the dissipation range where energy is extracted from the flow by viscous forces (stresses) and dissipated as internal energy. Even though turbulence is chaotic, it is deterministic and is described by the Navier-Stokes equations.

II. **Diffusivity.** Turbulent flows exhibit increased diffusivity. The turbulence increases the exchange of momentum in the fluid and thereby reduces or

delays separation at bluff bodies. Increased diffusivity also increases the resistance (wall friction) in internal flows such as channels and pipes.

III. **Large Reynolds Numbers.** Turbulent flow occurs at high Reynolds number. For example, the transition to turbulent flow in pipes occurs at $\mathrm{Re}_D \approx 2300$, and in boundary layers at $\mathrm{Re}_x \approx 10^5$, where the subscripts, x and D refer to the characteristic length scale of the flow.

IV. **Three-Dimensional.** Turbulent flow is always three-dimensional, however in some cases, when the equations are time averaged the flow can be treated as two-dimensional.

V. **Dissipation.** Turbulent flow is dissipative, which means that kinetic energy in the small (dissipative) eddies is transformed into internal energy. The small eddies receive the kinetic energy from slightly larger eddies. The slightly larger eddies receive the energy from even larger eddies and so on. The largest eddies extract their energy from the mean flow. This process of transferred energy from the largest turbulent scales (eddies) to the smallest is called the *Energy Cascade* process.

VI. **Continuum.** Even though we have small turbulent scales in the flow they are much larger than the molecular scale and we can treat the flow as a continuum.

Since turbulence is in nature a very complex phenomena, the conscientious engineer will strive to use as conceptually simple an approach as possible to achieve his ends (Wilcox, 1994) while at the same time providing a satisfactory representation of turbulence and its effects. Historically, there are two main approaches to turbulence modelling: stochastic and deterministic methods. Stochastic approaches treat turbulence as a random process and make use of statistical descriptions to represent its effects. In reality however, turbulence is deterministic and can be modelled using the Navier-Stokes equations and a number of CFD based modelling approaches for the simulation of turbulence flows exist.

3.2.1 Turbulence Scales

As previously mentioned, turbulent flow is characterized by irregularity, exhibiting a wide range of scales in the flow. The larger production scales are of the

order of the flow geometry with length scale ℓ and velocity scale $\mathcal{U}$. Production scales extract kinetic energy from the mean flow. These disturbances which are initially laminar, organized and well defined are turned into chaotic three-dimensional random fluctuations through interactions with the main flow that are defined by the idealized phenomena of: *vortex stretching* and *vortex tilting* (Davidson, 2003). These interactions will on average create smaller and smaller scales with the kinetic energy of the larger scales lost to slightly smaller scales with which they interact. Most of the energy that goes into the large scales (approximately 90% of it) is finally dissipated at the smallest (dissipative) scales (Davidson, 2003).

While the large scales which interact with the main flow contain detailed information about the mechanism of energy production, if the number of steps in the *cascade* is sufficiently large, we could presume that the small scales would know only how much energy they were receiving (Lumley et al., 1996). The smaller scales might then be assumed to be isotropic having lost all information about the anisotropy of the energy containing scales. This state of isotropy would however exist only at infinite Reynolds number flows with infinitely many steps in the *cascade*. According to Lumley et al. (1996), at any finite Reynolds number, the small scales would be expected to be less anisotropic than the energy containing scales, but still somewhat anisotropic.

For high Reynolds numbers, the dissipation scales will only be aware of the amount of energy they receive which is then dissipated into internal energy. The dissipation rate is denoted by ε which is energy per unit time and unit mass. In equilibrium conditions, we could assume the smallest scales where dissipation occurs to be dependant on only the dissipation rate, ε, and kinematic viscosity, ν.

This assumption gives us the *Kolmogorov scales*: the velocity scale, v, the length scale, η, and the time scale, τ, that define the dissipative range and using dimensional analysis, can be expressed in terms of viscosity and dissipation as

$$v = (\nu\varepsilon)^{1/4},\ \eta = \left(\frac{\nu^3}{\varepsilon}\right)^{1/4},\ \tau = \left(\frac{\nu}{\varepsilon}\right)^{1/2}. \tag{3.5}$$

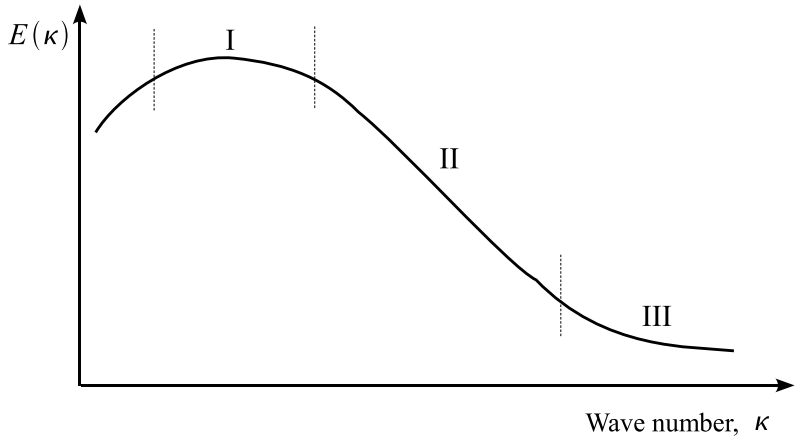

Figure 3.4: The Energy spectrum of turbulence showing the energy density per unit wave number, $E(\kappa)$, against wave number, κ. Region I is the range for the large, energy containing eddies, region II is the inertial sub-range and region III corresponds to the range for small isotropic scales (Davidson, 2003).

3.2.2 Energy Spectrum

The energy spectrum of turbulence is a representation of kinetic energy distribution across the various eddies present in the flow as a function of wave number κ. Turbulence length scales which are a measure of eddy sizes present in the flow can be expressed in terms of a wave number which is proportional to the inverse of an eddy's radius r, i.e $\kappa \propto 1/r$. In wave number space, the energy contributed by eddies with wave number between κ and $\kappa + d\kappa$ to the turbulent kinetic energy, k, is expressed by $E(\kappa)d\kappa$. The total turbulent kinetic energy over the whole wave number space is then given as;

$$k = \int_0^\infty E(\kappa)d\kappa, \tag{3.6}$$

where turbulent kinetic energy refers to the sum of the kinetic energy of the three fluctuating velocity components. The resulting energy spectrum (Figure 3.4) is subdivided into the production range, I, the inertial sub-range, II, and the dissipation range, III.

3.2.3 Stochastic Descriptions of Turbulence

In the practice of wind engineering, statistical descriptors of turbulence are traditionally used in the modelling of the atmospheric boundary layer. These include simple turbulence intensities and gust factors as well as detailed descriptions of

the way in which the three components of turbulence vary in space and time as well as their frequency composition. These descriptors are discussed in this section.

3.2.3.1 Turbulence Intensity

Turbulence intensity, I is a measure of the overall level of turbulence and is defined as

$$I = \frac{\sigma}{\bar{U}}, \tag{3.7}$$

where σ is the standard deviation of wind speed about the mean wind speed $\bar{U}$ with the turbulent wind speed variations usually assumed to be Gaussian (Burton et al., 2001). For the longitudinal component of turbulence, the standard deviation σ_u is approximately constant with height, so the turbulence intensity decreases with height. ESDU (1985) present an expression for σ_u based on experimental observations as

$$\sigma_u = \frac{7.5\eta(0.538 + 0.09\ln(z/z_o))^p u^*}{1 + 0.156\ln(u^*/fz_o)}, \tag{3.8}$$

where

$$\eta = 1 - 6fz/u^*, \tag{3.9}$$

$$p = \eta^{16}. \tag{3.10}$$

u^*, z_o and f are as previous defined in (3.3), (3.1) and (3.2). The longitudinal turbulence intensity, I_u is then obtained as

$$I_u = \sigma_u/\bar{U}, \tag{3.11}$$

while based on ESDU (1985) data, the lateral, I_v, and vertical, I_w, turbulence intensities are defined as

$$I_v = \frac{\sigma_v}{\bar{U}} = I_u\left(1 - 0.22\cos^4\left(\frac{\pi z}{2h}\right)\right) \tag{3.12}$$

$$I_w = \frac{\sigma_w}{\bar{U}} = I_u\left(1 - 0.45\cos^4\left(\frac{\pi z}{2h}\right)\right) \tag{3.13}$$

3.2.3.2 Turbulence Spectra

The variance, σ_i^2, of a fluctuating signal is made up of contributions over a range of frequencies (ESDU, 1986). Turbulent spectra describe the frequency composition of wind speed variations, and according to the Kolmogorov law, must

approach an asymptotic limit proportional to $n^{-5/3}$ in the high frequency limit, where n is the frequency in Hz. Burton et al. (2001) presents the two alternative expressions commonly used for the spectrum of the longitudinal components of turbulence which are, the Kaimal spectra,

$$\frac{nS_{uu}(n)}{\sigma_u^2} = \frac{4nL_{1u}/\bar{U}}{(1+6nL_{1u}/\bar{U})^{5/3}}, \tag{3.14}$$

and the Von Karman Spectra,

$$\frac{nS_{uu}(n)}{\sigma_u^2} = \frac{4nL_{2u}/\bar{U}}{(1+70.8(nL_{2u}/\bar{U})^2)^{5/6}}, \tag{3.15}$$

where $S_{uu}(n)$ is the auto-spectral density function for the longitudinal component and L_{1u} and L_{2u} are length scales and $L_{1u} = 2.329L_{2u}$. The length scale L_{2u} is defined as the integral length scale of the longitudinal component in the longitudinal direction, denoted ${}^xL_u$.

The von Karman spectrum gives a good description of turbulence in wind tunnels while the Kaimal spectrum may give a better fit to field observations of atmospheric turbulence although even in these cases the von Karman spectrum is often used for consistency (Petersen et al., 1998). The Kaimal spectra have the same form for the lateral and vertical components of turbulence as the longitudinal component but with different length scales, L_{1v} and L_{1w} respectively (Burton et al., 2001).

The von Karman spectrum however has a different form for the lateral cross-wind and vertical components, v and w respectively, which is given by

$$\frac{nS_{ii}(n)}{\sigma_i^2} = \frac{4(nL_{2i}/\bar{U})(1+755.2(nL_{2i}/\bar{U})^2)}{(1+283.2(nL_{2i}/\bar{U})^2)^{11/6}}, \tag{3.16}$$

where index $i = v$ or w, with $L_{2v} = {}^xL_v$, the integral length scale of the lateral component in the longitudinal direction, and $L_{2w} = {}^xL_w$, the integral length scale of the vertical component in the longitudinal direction. Identification of the appropriate length scales for use in these spectra is discussed in section 3.2.3.3.

3.2.3.3 Turbulence Length Scales

Turbulence length scales are a measure of the size of eddies present in a flow due to turbulence. In order to use turbulence spectra, the length scales need to be defined. Length scales are dependant on the surface roughness, z_o, as well

as on the height above ground, z, since proximity to the ground constrains the size of turbulent eddies and hence reduces the length scales. Above a critical height from the ground, $z_i = 1000 z_o^{0.18}$, the turbulence is no longer constrained by the ground surface and becomes isotropic with ${}^{x}L_u = 280$ m and, ${}^{y}L_u = {}^{z}L_u = {}^{x}L_v = {}^{z}L_v = 140$ m (Burton et al., 2001). For $z < z_i$, the length scales are anisotropic and corrections are applied according to

$$\begin{aligned} {}^{x}L_u &= 280(z/z_i)^{0.35}, & {}^{y}L_u &= 140(z/z_i)^{0.38}, \\ {}^{z}L_u &= 140(z/z_i)^{0.45}, & {}^{x}L_v &= 140(z/z_i)^{0.48}, \\ {}^{z}L_v &= 140(z/z_i)^{0.55}, & {}^{x}L_w &= {}^{y}L_w = 0.35z. \end{aligned} \tag{3.17}$$

3.2.3.4 Cross-spectra and Coherence functions

The von Karman and Kaimal turbulence spectra provide a description of the temporal variation of each of the turbulence components at a given point in space. These are known as Eulerian spectra. The spatial variations of turbulence in space from one point to another is however often required. Therefore the spectral definition of turbulence needs to be extended to including information about the cross-correlations between turbulent fluctuations at points separated by a given distance.

According to ESDU (1986), these correlations will decrease as the distance separating two points increases and are also smaller for higher-frequency than for low-frequency variations. They can therefore be described by *Coherence functions* which describe the correlation as a function of frequency and separation. Burton et al. (2001) defines the coherence $C(\Delta r, n)$ as

$$C(\Delta r, n) = \frac{|S_{12}(n)|}{\sqrt{S_{11}(n) S_{22}(n)}} \tag{3.18}$$

where n is frequency, $S_{12}(n)$ is the cross-spectrum of variations at the two points separated by Δr, and $S_{11}(n)$ and $S_{22}(n)$ are the spectra of variations at each of the points which can usually be assumed to be equal.

Starting from the von Karman spectral equations, and assuming Taylor's frozen turbulence hypothesis (Taylor, 1938), an analytical expression for the coherence of wind-speed turbulence is derived and presented in Burton et al. (2001).

3.2.3.5 Gust factors

It is often useful to know the maximum gust speed which can be expected to occur in any given time interval. This is usually expressed by a gust factor G, which is the ratio of the gust wind speed to the hourly mean wind speed (Burton et al., 2001). The gust factor is a function of turbulence intensity, and also depends on the duration of the gust, with shorter duration gust factors larger than those for longer durations. Although gust factors can be derived from turbulence spectrum, the empirical expression from Wieringa (1973) are often used for simple and theoretically accurate method of estimating gust factors according to

$$G(t) = 1 + 0.42 I_u \ln \frac{3600}{t}. \tag{3.19}$$

Wind-borne debris flight is often characterized by short flight times and gust winds can have a controlling influence on the resulting debris flight trajectories (Baker, 2007).

3.3 Computational Fluid Dynamics

Computational Fluid Dynamics (CFD) has been defined as the analysis of systems involving fluid flow, heat transfer and associated phenomena such as chemical reactions by means of computer-based simulation (Versteeg and Malalasekera, 2007). CFD applications span a wide variety of industrial and non-industrial applications including; aircraft and vehicle aerodynamics, hydrodynamics, turbomachinery, chemical process engineering, hydrology and oceanography, environmental engineering and biomedical engineering. The main goal of CFD is to provide an economical and sufficiently complete predictions of complex fluid flow problems by solving the governing equations of fluid flow often coupled with additional equations for any associated phenomena. For the purposes of this research which is concerned with very low Mach number flows, the wind is treated as an incompressible fluid in which fluid density is independent of pressure. The rest of this chapter will therefore only be concerned with the CFD modelling of incompressible fluid flow.

Three-dimensional incompressible fluid flow, is governed by a set of non-linear partial differential equations known as the Navier-Stokes equations,

$$\frac{\partial \mathbf{U}}{\partial t} + \mathbf{U} \cdot \nabla \mathbf{U} = \frac{1}{\rho}(-\nabla p + \nabla \cdot \boldsymbol{\tau} + \mathbf{F_B}), \tag{3.20}$$

which are derived from the principle of momentum conservation. Where $\mathbf{U} = (u, v, w)$ is the fluid velocity vector, p is fluid pressure, ρ is the fluid density, t denotes time, $\boldsymbol{\tau}$ is the viscous stress tensor and $\mathbf{F_B}$ is the vector of body-force per unit volume such as those arising from gravity, buoyancy, rotation and electromagnetic fields. The Navier-Stokes equations are often solved together with supplementary equations representing additional physical conservation laws governing the fluid flow, such as the law of mass conservation represented by the incompressible form of the continuity equation

$$\nabla \cdot \mathbf{U} = 0, \tag{3.21}$$

and the first law of thermodynamics expressed as the temperature equation

$$\frac{\partial e}{\partial t} + \mathbf{U} \cdot \nabla e = \frac{1}{\rho}(\nabla \cdot (k \nabla T) + S_T), \tag{3.22}$$

where T is the temperature, k is the thermal conductivity, e is the specific internal energy and S_T is the temperature source/sink. For an isothermal system with negligible contribution from body-forces, the Navier-Stokes equations reduce to (3.21) and (3.20).

The viscous stress tensor, $\boldsymbol{\tau}$, is obtained by introducing a suitable fluid viscosity model. For a Newtonian fluid, the viscous stresses are proportional to the rates of deformation. The three-dimensional form of Newton's law of viscosity for compressible flows involves two constants of proportionality: the first (dynamic) viscosity, μ relates stresses to linear deformations, and the second viscosity, λ relates stresses to volumetric deformation and for gases is usually estimated by taking the value $\lambda = (-2\mu/3)$ (Schlichting, 1979). The nine components of the viscous stress tensor are expressed as

$$\tau_{xx} = 2\mu \frac{\partial u}{\partial x} + \lambda\Big(\frac{\partial u}{\partial x} + \frac{\partial v}{\partial y} + \frac{\partial w}{\partial z}\Big), \tag{3.23}$$

$$\tau_{yy} = 2\mu \frac{\partial v}{\partial y} + \lambda\Big(\frac{\partial u}{\partial x} + \frac{\partial v}{\partial y} + \frac{\partial w}{\partial z}\Big), \tag{3.24}$$

$$\tau_{zz} = 2\mu \frac{\partial w}{\partial z} + \lambda\Big(\frac{\partial u}{\partial x} + \frac{\partial v}{\partial y} + \frac{\partial w}{\partial z}\Big), \tag{3.25}$$

$$\tau_{xy} = \tau_{yx} = \mu\Big(\frac{\partial u}{\partial y} + \frac{\partial v}{\partial x}\Big), \tag{3.26}$$

$$\tau_{xz} = \tau_{zx} = \mu\Big(\frac{\partial u}{\partial z} + \frac{\partial w}{\partial x}\Big), \tag{3.27}$$

$$\tau_{yz} = \tau_{zy} = \mu\Big(\frac{\partial v}{\partial z} + \frac{\partial w}{\partial y}\Big). \tag{3.28}$$

A detailed discussion of the CFD modelling process is provided in Appendix A while Appendix B provides a brief theoretical background to the Arbitrary Lagrangian-Eulerian formulation of the Navier-Stokes equations which is useful in the numerical modelling of fluid flow around moving wall boundaries.

3.3.1 Turbulence Modelling for CFD

The accurate simulation of high Reynolds number flows requires that the effects of all the flow scales involved, from the integral length scale all the way down to the dissipative length scale, be taken into consideration. This would require solving the NavierStokes equations with a sufficient spatial and temporal resolution to capture the smallest scales in the flow. This approach is referred to as the Direct Numerical Simulation (DNS) and requires no additional modelling. The first DNS was performed by Orszag and Patterson (1972), however, due to the very high grid and time-step resolution required, the method remains unfeasible for practical engineering problems with high Reynolds numbers. For such applications, additional turbulence modelling approaches are introduced to avoid having to resolve all the scales in the flow and these are discussed in this section, starting with the Reynolds Averaged Navier-Stokes (RANS) method which enjoys widespread popularity.

Rather than directly simulate the flow, the RANS approach attempts to model its statistical properties. Fluid properties such as velocity, $\mathbf{U}$, and pressure, p, are decomposed into a mean and fluctuation components according to the Reynolds decomposition

$$\mathbf{U} = \bar{\mathbf{U}} + \mathbf{u}', \qquad p = \bar{p} + p', \tag{3.29}$$

where the "$^-$" denotes a time-averaged component and "$'$" represents the fluctuating component. When we combine this Reynolds decomposition with the incompressible Navier-Stokes equations, we obtain a set of time averaged continuity and momentum equations known as the Reynolds Averaged Navier-Stokes (RANS) equations for incompressible flow:

$$\nabla \cdot \bar{\mathbf{U}} = 0, \tag{3.30}$$

$$\frac{\partial \bar{\mathbf{U}}}{\partial t} + \nabla \cdot \left(\bar{\mathbf{U}} \otimes \bar{\mathbf{U}}\right) = -\frac{1}{\rho}\nabla \bar{p} + \nabla \cdot \left(\nu \nabla \bar{\mathbf{U}} - \overline{\mathbf{u}' \otimes \mathbf{u}'}\right). \tag{3.31}$$

where $\nu = \mu/\rho$ is the kinematic viscosity. The term RANS is often used to refer to steady models for stationary flow with $\frac{\partial \bar{\mathbf{U}}}{\partial t} = 0$ while in non-stationary flows

where $\frac{\partial \bar{\mathbf{U}}}{\partial t} \neq 0$, the equations are refered to as the unsteady RANS (URANS) equations. A new term $\overline{\mathbf{u}' \otimes \mathbf{u}'}$ known as the *Reynolds stress tensor* is introduced which is composed of nine Reynolds stresses, $\overline{u_i' u_j'}$ computed from the dyadic product of the fluctuating velocity vectors as

$$\overline{u_i' u_j'} = \overline{\mathbf{u}' \otimes \mathbf{u}'} = \begin{bmatrix} \overline{u_1' u_1'} & \overline{u_1' u_2'} & \overline{u_1' u_3'} \\ \overline{u_2' u_1'} & \overline{u_2' u_2'} & \overline{u_2' u_3'} \\ \overline{u_3' u_1'} & \overline{u_3' u_2'} & \overline{u_3' u_3'} \end{bmatrix}, \tag{3.32}$$

where u_1', u_2', u_3' are the fluctuating components of velocity in the X, Y and Z directions. The Reynolds Stress tensor represents the correlations between fluctuating components of velocity and is symmetric, with $\overline{u_i' u_j'} = \overline{u_j' u_i'}$, hence introducing an additional *six unknowns* to be solved for. This results in what is known as the *closure problem* since the system of equation now has ten unknowns (3 mean velocity components, 1 pressure value, and six Reynolds stresses) to solve for but only four equations (1 continuity equation and 3 momentum equations). We therefore require an additional model to predict the six Reynolds stresses. There are a number of RANS turbulence models available to solve the closure problem and they can be classified as: *Eddy Viscosity Models* and the *Reynolds Stress Models* (RSM).

Reynolds Stress Models (RSM) or second-closure models originally proposed by Launder et al. (1975) introduce six additional partial differential equations which are solved to obtain each of the Reynolds stresses directly. Wilcox (1994) presents a derivation of these partial differential equations. This approach is computationally expensive on account of having to solve six additional coupled differential equations. Further complexity results from the fact that in order to solve these resulting six differential equations for the Reynolds Stresses, a total of 22 additional unknown terms must be modelled. These additional unknowns are modelled in a calibration based approach, with no verifiable physics to support their modelling (McDonough, 2007). According to McDonough (2007), what is actually accomplished by RSM is not a model containing more physics but rather one containing far more closure constants that can be adjusted at will in efforts to match observed flow field behaviours. This has served to obscure further development of RSMs.

Therefore despite the increased computational cost, there is no significantly im-

proved predictability, and as a consequence, RSMs are not as widely used. While it is noted that they do offer improved performance in predicting anisotropic turbulence, Wilcox (1994) concludes that it is unlikely that RSMs would yield any significant improvement for separating and reattaching flow.

Eddy Viscosity models on the other hand relate the Reynolds stresses to the velocity gradients via the turbulent viscosity in a relation known as the *Boussinesq assumption*:

$$\overline{u_i' u_j'} = -\nu_t \Big(\nabla \bar{\mathbf{U}} + \nabla \bar{\mathbf{U}}^{\mathrm{T}} \Big) = -\nu_t \bigg(\frac{\partial \bar{U}_i}{\partial x_j} + \frac{\partial \bar{U}_j}{\partial x_i} \bigg), \tag{3.33}$$

where ν_t is the turbulent (eddy) viscosity and $\Big(\nabla \bar{\mathbf{U}} + \nabla \bar{\mathbf{U}}^{\mathrm{T}} \Big)$ is the mean strain-rate tensor. A turbulence model is then used to estimate the eddy viscosity ν_t in order to solve for the Reynolds stresses. A number of eddy viscosity turbulence models exist and the choice of appropriate turbulence model is largely problem specific. They include algebraic models (zero equation) models such as the Baldwin and Lomax model (Baldwin and Lomax, 1978) and one-equation turbulence models such as the Spalart-Allmaras model (Spalart and Allmaras, 1992). However, the most complete models of turbulence are the two-equation eddy viscosity models in which two separate transport equations allow for the flow history, turbulence energy and length scales of turbulence to be determined. These include the standard $k - \varepsilon$ (Launder and Sharma, 1974) and the $k - \omega$ model (Wilcox, 1994). For the present research, two equation turbulence models have been used and these are discussed in the following section.

It is worth nothing that while these models have gained wide spread applicability, the Boussinesq approximation at the centre of the eddy viscosity models has no physical basis. In fact, using several different experimental and numerical databases for which the Reynolds stress tensors are known, Schmitt (2007) shows that the Boussinesq hypothesis is almost never valid. As a consequence, eddy viscosity models often fail in applications involving flows with sudden changes in mean strain rate, flow over curved surfaces, flow in rotating and stratified fluid and flows with boundary layer separation (Wilcox, 1994). Recent developments have focused on introducing modifications and constraints to improve model performance in these cases.

3.3.1.1 The $k-\varepsilon$ Model

The standard $k-\varepsilon$ model by Launder and Sharma (1974) is based on transport equations for the turbulence kinetic energy, $k = \frac{1}{2}(u'^2 + v'^2 + w'^2)$, and its dissipation rate, $\varepsilon = \mathrm{d}k/\mathrm{d}t$. The model transport equation for k is mathematically derived from the Navier-Stokes equations, while the transport equation for ε is empirically derived (Wilcox, 1994). The final equations for the standard $k-\varepsilon$ model are

$$\frac{\partial k}{\partial t} + \bar{\mathbf{U}} \cdot \nabla k = \mathcal{P} - \varepsilon + \nabla \cdot \Big[\Big(\nu + \frac{\nu_t}{\sigma_k}\Big)\nabla k\Big], \tag{3.34}$$

$$\frac{\partial \varepsilon}{\partial t} + \bar{\mathbf{U}} \cdot \nabla \varepsilon = C_{\varepsilon 1}\frac{\varepsilon}{k}\mathcal{P} - C_{\varepsilon 2}\frac{\varepsilon^2}{k} + \nabla \cdot \Big[\Big(\nu + \frac{\nu_t}{\sigma_\varepsilon}\Big)\nabla \varepsilon\Big], \tag{3.35}$$

where σ_k, σ_ε, $C_{1\varepsilon}$, $C_{2\varepsilon}$ are model constants with experimentally obtained values of 1.00, 1.30, 1.44, 1.92. The term $\mathcal{P}$ represents turbulent kinetic energy production

$$\mathcal{P} = \frac{\nu_t}{2}|\nabla \bar{\mathbf{U}} + \nabla \bar{\mathbf{U}}^{\mathrm{T}}|^2 \tag{3.36}$$

The $k-\varepsilon$ model, like all other eddy viscosity models assumes fully turbulent flow with isotropic turbulence, such that $u'^2 = v'^2 = w'^2$. The turbulence velocity scale, ϑ and length scale, l, are then computed from the obtained solutions for k and ε as

$$l = \frac{k^{\frac{3}{2}}}{\varepsilon}, \qquad \vartheta = k^{\frac{1}{2}}. \tag{3.37}$$

Finally the turbulent viscosity is computed according to

$$\nu_t = C_\mu \vartheta l = \rho C_\mu \frac{k^2}{\varepsilon}. \tag{3.38}$$

For the standard $k-\varepsilon$ model, C_μ is a constant with a value of 0.09.

3.3.1.2 The Realisable $k-\varepsilon$ Model

In some conditions, such as at stagnation flows and at separation points, the standard $k-\varepsilon$ turbulence model might make non-physical predictions (Wilcox, 1994). This makes it necessary to impose some mathematical constraints that are consistent with the basic physical and mathematical principles to which any turbulent flow must conform.

The Realisable $k-\varepsilon$ model proposed by Shih et al. (1995) is one of the modifications to the standard $k-\varepsilon$ model in which this approach is applied. In the Realisable $k-\varepsilon$ model, two new mathematical constraints are introduced into

the $k-\varepsilon$ equations. These are *Realisability* and *Shwarz' inequality*. Realizability is defined as the requirement of the non-negativity of turbulent normal stresses (i.e; $\overline{u_i' u_i'} \geqslant 0$) while the Schwarz inequality between any fluctuating quantities, is a basic physical and mathematical principle that the solution of any turbulence model equation should obey. It also represents the minimal requirement to prevent a turbulence model from producing non-physical results (Shih et al., 1995). A new formulation of the turbulent viscosity imposing these constraints is obtained by deriving a new transport equation for the dissipation rate ε from an exact equation for the transport of the mean-square vorticity fluctuation.
For the Realisable $k-\varepsilon$ model, the eddy viscosity is still computed from (3.38) however C_μ is no longer a constant but is computed form an expression involving the mean strain and rate of rotation, and $C_{1\varepsilon}$ is defined as

$$C_{1\varepsilon} = \max\left[0.43, \frac{\eta}{(\eta+5)}\right], \tag{3.39}$$

where $\eta = \frac{k}{\varepsilon}S$, with S representing the modulus of the mean strain-rate tensor.

3.3.1.3 The $k-\omega$ Model

The standard $k-\omega$ turbulence model by Wilcox (1988) is a two-equation model based on transport equations for turbulent kinetic energy, k, and the specific dissipation or turbulence frequency, $\omega \propto \varepsilon/k$. This model has an advantage over the standard $k-\varepsilon$ model in regions of low turbulence such as wall boundary layers, when both k and ε go to zero. In these regions, the $k-\varepsilon$ model becomes numerically unstable due to the destruction term in the ε equation, (3.35), which has a ε^2/k term and this causes problems as $k \to 0$ even if ε goes to zero except in rare occasions where both k and ε tend to zero at a correct rate (Davidson, 2003). This however is not the case for the ω equation, (3.41), in the $k-\omega$ model.

$$\frac{\partial k}{\partial t} + \bar{\mathbf{U}} \cdot \nabla k = \mathcal{P}_k - \beta^* \rho k \omega + \nabla \cdot \left[\left(\nu + \frac{\nu_t}{\sigma_k}\right)\nabla k\right], \tag{3.40}$$

$$\frac{\partial \omega}{\partial t} + \bar{\mathbf{U}} \cdot \nabla \omega = \mathcal{P}_\omega - \beta_1 \rho \omega^2 + \nabla \cdot \left[\left(\nu + \frac{\nu_t}{\sigma_\omega}\right)\nabla \omega\right], \tag{3.41}$$

where P_k and P_ω are the rates of production of k and ω respectively. σ_k, σ_ω, γ_1, β_1 and β^* are model constants with values of 2.0, 2.0, 0.553, 0.075 and 0.09 respectively (Versteeg and Malalasekera, 2007).

The turbulence length scale, l, and the eddy viscosity, μ_t, can then be defined as

$$l = \frac{\sqrt{k}}{\omega}, \qquad \mu_t = \rho\frac{k}{\omega}. \tag{3.42}$$

3.3.1.4 Large Eddy Simulation (LES)

In order to account for the deficiencies in the eddy viscosity and RSMs, an alternative approach known as Large Eddy Simulation (LES) was suggested by Smagorinsky (1963). The LES approach involves decomposing flow variables into large-scale and small-scale components using a filtering process known as the LES decomposition (Deardorff, 1970),

$$\mathbf{U}(\mathbf{x}, t) = \widetilde{\mathbf{U}}(\mathbf{x}, t) + \mathbf{u}'(\mathbf{x}, t), \tag{3.43}$$

where $\widetilde{\mathbf{U}}$ is the large- or resolved-scale component and $\mathbf{u}'$ is the unresolved- or small- or sub-grid scale component. An LES formulation of the Navier-Stokes equations is solved to obtain the large-scale (resolved) components while the small-scale components are modelled using sub-grid scale models.

Although LES offers a more physically correct approximation of turbulent flow it is more computationally intensive than RANS models and the number of grid points required to adequately resolve the flow increases with Reynolds number. For this reason, LES has therefore been largely unfeasible for the purposes of this research where a fairly rapid computation of a large number of simulations was required.

3.3.1.5 Turbulence and Wall Functions

The presence of wall boundaries has an affect on turbulent flows that needs to be adequately modelled. Very close to the wall, the velocity is affected by the no-slip condition which results in a thin layer of laminar flow known as the *viscous sub-layer* where viscous effects are dominant. In this layer, sharp velocity gradients are observed and the tangential and normal velocity fluctuations are affected by viscous damping and kinematic blocking respectively, reducing their magnitude. Above this viscous sub-layer is a *buffer layer* where viscous and turbulent effects are of similar magnitude. This is followed by an outer *fully-turbulent boundary layer* where turbulent effects are dominant due to interaction with the mean flow where turbulence kinetic energy is produced by large gradients in the mean velocity (Versteeg and Malalasekera, 2007).

The more straightforward approach to treating wall boundaries would be to have a sufficiently fine grid to be able to resolve the steep velocity gradients prevailing in the boundary layer. However this very fine grid would have a high computational cost associated with it and is often not feasible. Therefore a wall function approach is often used in order to adequately model turbulent flows at wall boundaries. Two wall function modelling approaches are commonly used, the standard wall function and the enhanced wall function approach.

The Standard Wall Function approach by Launder and Spalding (1974), assumes the flow in the layer of cells adjacent to the wall to be in the fully-turbulent region of the wall boundary layer. Semi-empirical equations are then used to model the flow in the viscosity affected viscous sub-layer and buffer layer of the boundary layer. In the fully-turbulent region of the boundary layer, the velocity profile is described using an equation known as the log-law

$$u^+ = \frac{1}{\kappa} \ln\left(Ey^+\right), \tag{3.44}$$

with,

$$u^+ = \frac{U}{u_\tau}, \tag{3.45}$$

where κ is the von Karman constant with a value of 0.4, E is a constant with a value of 9.8 for flows past smooth walls at high Reynolds number, u^+ is a non-dimensionalised velocity defined by (3.45), y^+ is a non-dimensionalised wall distance defined by (A.1), u_τ is a characteristic velocity known as the friction velocity which is defined by (A.2) and U is the mean velocity at a point. This log-law has been found to be valid for $(30 < y^+ < 500)$ with the upper limit dependant on the Reynolds number (Versteeg and Malalasekera, 2007).
Expressions for the turbulent kinetic energy, k and rate of dissipation, ε in the wall-adjacent cells can then be computed as

$$k = \frac{u_\tau^2}{\sqrt{C_\mu}}, \qquad \varepsilon = \frac{u_\tau^3}{\kappa y}. \tag{3.46}$$

Instead of using the expression for k in (3.46), ANSYS FLUENT solves the k-equation in the wall-adjacent cells. The standard wall function approach is derived under the assumption of a local equilibrium turbulent boundary layer such that the production of k, $\mathcal{P}$, and its dissipation rate, ε, are assumed to be equal in the wall-adjacent control volume. However, this local equilibrium

assumption is not valid when the near-wall flow is subjected to severe pressure gradients, and when the flows are in strong non-equilibrium. Such conditions are likely to occur in complex flows involving large separation, recirculation and flow reattachment (Kim and Choudhury, 1995).

A Non-Equilibrium Wall Functions has therefore been proposed by Kim and Choudhury (1995) in order to extend the standard wall function by incorporating two-layer wall functions which are sensitized to pressure gradient. A new pressure-sensitive log-law for the mean velocity is introduced in place of (3.44) together with a two-layer approach for computing k in the wall neighbouring cells.

The two-layer approach assumes wall neighbouring cells to consist of a viscous sub-layer and a fully turbulent layer in varying proportions from cell to cell. A viscous sub-layer thickness, y_v is computed according to

$$y_v = \frac{\mu y_v^*}{\rho C_\mu^{1/4} k^{1/2}}, \tag{3.47}$$

where $y_v^* = 11.225$. Different expressions for turbulent quantities, k, ε and τ_w are then assumed for the viscous sub-layer and turbulent layer. The local equilibrium assumption is discarded and using the assumed expressions for the turbulence quantities, a local cell-averaged production, $\overline{\mathcal{P}}$, and dissipation rate, $\overline{\varepsilon}$ of k may be computed. These cell-averaged production and dissipation terms take into account the varying proportions of the viscous and turbulent layer, hence relaxing the local equilibrium assumption.

Due to this ability to partly account for the effects of pressure gradients and departure from equilibrium conditions, the non-equilibrium wall function approach has showed improved performance in the prediction of skin-friction coefficients in complex flows involving separation, reattachment, and impingement where the mean flow and turbulence are subjected to severe pressure gradients and change rapidly (FLUENT Inc., 2009).

Although the standard and non-equilibrium wall functions are applicable to the majority of flows, they are confined to coarse mesh applications, with the cell centre located in the turbulent region of the boundary layer. For some flow problems, such as those involving strong body forces around a rotating disk, it is necessary for a successful simulation to employ a fine near wall mesh in order

to resolve the important near wall features (FLUENT Inc., 2009).

The Enhanced Wall Function is a near-wall modelling method that is applicable throughout the entire near-wall region including the laminar sub-layer, buffer region, and fully-turbulent outer region. The approach is based on a reformulation of the law of the wall by blending linear (laminar) and logarithmic (turbulent) laws into a single wall law for the entire wall region (Kader, 1993). A two-layer zonal model is further incorporated for the turbulence quantities by dividing the computational domain into a viscosity-affected region and a fully turbulent regions using a wall-distance based Reynolds number,

$$Re_y = \frac{\rho y \sqrt{k}}{\mu}, \tag{3.48}$$

where y is the normal-distance from the wall to the cell centres, and cells with $\mathrm{Re}_y > 200$ are considered by FLUENT to be in the fully-turbulent region (FLUENT Inc., 2009). A one-equation model is used in the viscosity-affected near-wall region, while the two-equation turbulence modelling approach is used in the fully-turbulent region, with a blending function.

3.4 Progress in Computational Wind Engineering

In recent years, there has been an increased application of CFD to the numerical simulation of a number of wind engineering problems ranging from pollutant transport and wind energy resource estimation to urban meteorology and modelling wind effects on urban infrastructure. Progress in this area is highlighted in the proceedings of the fifth international symposium on Computational Wind Engineering (CWE)- Chapel Hill, 2010.

CFD holds a number of advantages of traditional wind tunnel models of wind engineering problems such as; the ability to model problems in full scale as opposed to the model scale used in many experimental models, CFD flow data is available at a much greater spatial and temporal resolution and readily visualised in an useful format and CFD simulations also offer the only means of investigating certain complex phenomena where physical modelling is not feasible.

Early work in the field of CWE was concerned with providing an accurate numerical simulation of atmospheric flow over large scale topography such as hills. Such information is key to a number of engineering problems such as assessing

the local wind resource for positioning of wind farms or determining the dispersion of pollutants. Initially, Jackson and Hunt (1975) presented a linear analysis of turbulent flow over low hills, defining an inner layer close to the hill where turbulent effects were important and an outer layer above that which could be modelled as inviscid flow. This two-layer approach has been shown to perform adequately when validated against full scale experimental data obtained from controlled measurements over simple topography (such as the Black Mountain and Askervein hill). Hunt et al. (1988a), and Belcher and Hunt (1998) presented further improvements to this theory, which now forms the basis of numerical models used for the prediction of wind fields and dispersion over arbitrary topography. In these methods, an algebraic mixing-length model is typically used to approximate Reynolds Stresses in the inner layer where turbulent effects are important.

At the urban scale, there has been an increased academic and industrial application of CFD to predict wind effects on pedestrians, pollution dispersion and, in preliminary wind loading studies on buildings and bridges. CFD offers the advantage of relatively rapid and low cost modelling of different scenarios compared with physical model testing. However, there are a number of challenges associated with CWE in the urban environment, and these include turbulence modelling, accuracy of the numerical schemes and the treatment of the viscous sub-layer at walls (Murakami, 1990). More recent CWE developments have largely been focused on addressing these challenges.

For urban scale wind engineering applications, a more complete treatment of atmospheric turbulence than the mixing-length model used in the linear analysis of turbulent flow over low hills is required and two-equation RANS models which provide information on turbulence history as well as an estimate of the local turbulence velocity and length scale offer the best alternative (Wilcox, 1994). The most widely used two-equation RANS model in CWE is the linear standard $k - \varepsilon$ model (Murakami, 1990).

During the 1980s, a number of numerical simulations of wind flow around surface mounted bluff bodies with sharp edges were performed (Murakami, 1990) and these revealed the weaknesses of RANS models in accurately simulating these complex flows. The focus in the development in CWE therefore switched to providing several ad-hoc modifications to the two-equation RANS turbulence

models, such as Wright and Easom (2003) and Luna et al. (2007), to improve predictions of the pressure distributions on the surface of simple building structures. These modifications in general improved the performance of two-equation RANS models in predicting pressure coefficients in the front of the building but led to worse predictions of the velocities especially in the wake (Franke et al., 2004). More advanced two-equation RANS models, such as the RNG $k-\varepsilon$ by Yakhot et al. (1992) and the realizable $k-\varepsilon$ by Shih et al. (1995) which provide better stagnation pressure predictions without leading to worse velocity predictions in the wake have also become increasingly used in CWE (Franke et al., 2004).

Wood (2000) expresses scepticism regarding whether RANS can adequately represent CWE flow and instead advocates the continued development of LES models in this field, and this seems to be the generally accepted view on the use of CFD techniques for such problems. LES also has the particular advantage of being able to predict flow fluctuations, extreme values etc, which are often the parameters required in practical situations. Although RANS models can accurately predict mean pressures on buildings for a given mean wind speed, they are unable to accurately predict the resulting peak pressures experienced by the structure. Driven by the need to improve CFD predictions for pressure on bluff bodies, Murakami et al. (1987) applied LES to simple problems, such as the surface-mounted cube, and obtained good agreement between numerical predictions and wind tunnel experiments.

Due to the high computational cost associated with and LES in contrast with RANS models, hybrid LES/RANS models such as Detached Eddy Simulation (DES) model of Spalart et al. (1997) have gained increased popularity. Bechmann and Sorensen (2010) recently present an application of a hybrid RANS/LES model to the simulation of wind flow over complex terrain.

Aside from the turbulence model, appropriate boundary conditions are also required for CWE simulations. It is often necessary to simulate an equilibrium neutral atmospheric boundary layer profile and in order to achieve this, appropriate velocity and turbulence quantity boundary conditions are required as well as an adequate representation of surface roughness. Richards and Hoxey (1993) formalised the specification of the logarithmic profile at the inlet of the domain and their work has recently been revisited by a number of authors including

Hargreaves and Wright (2007), Yi et al. (2009) and Richards and Norris (2011). Xie and Castro (2008) also present turbulent inflow boundary conditions suitable for LES, which includes both temporal and spacial correlations of wind speed and allows for the simulation of gusts. Since most turbulence models use a sand-grain representation of roughness together with a wall function, it is also necessary to adapt these for equivalent ABL ground roughness heights. Parente et al. (2011) recently proposed a consistent approach to the treatment of inflow and wall boundary conditions for the simulation of a neutral equilibrium ABL using a modified $k - \varepsilon$ turbulence model.

With improvements in technology that allow fluid-structure coupling, and the simulation of moving boundaries, CWE has also been extended to the direct simulation of the wind induced oscillation of tall buildings. In these applications, there is evidence to suggest that in cases where the motion of the structure contributes the dominant frequency to the flow, even URANS models can produce meaningful results (Owen et al., 2006). This is especially true for tall, flexible structures where URANS model inaccuracies in flow separation on the roof play only a small part in the structural response (Braun and Awruch, 2009). The implications are also of relevance to windborne debris flight where rotational frequency of a flying plate contributes the dominant frequency.

Although there are still persistent challenges in improving the accuracy and ability of CFD to simulate complex wind engineering problems, it has largely been recognised as a valuable tool in analysing these flows. Provided that there is sufficient data for validation of the model, then its results can be relied upon to give well-founded conclusions. A detailed understanding of fluid mechanics and how the CFD code works is also necessary in order to correctly evaluate the results. Increasingly, a number of guidelines on the verification and validation of CFD simulations, such as AIAA (1998), are becoming available and these should be used as guidelines to the CWE process.

Chapter 4

Rigid Body Dynamics Model

4.1 Background

Rigid Body Dynamics is one of the central components for the accurate numerical modelling of rigid wind-borne debris. A rigid body may be viewed as a special case of a system of particles in which the particles are rigidly interconnected with each other (Greenwood, 2003).

Rigid body motion in real three-dimensional (3D) space consists of at most six degrees of freedom - three translational degrees of freedom of a base point (usually the body's centre of mass) and three independent rotational degrees of freedom about suitably chosen axes. The Euler equations of rigid body dynamics, define a set of six differential equations of motion based on linear and angular momentum conservation principles,

$$m\frac{\mathrm{d}\mathbf{u}_\mathrm{g}}{\mathrm{d}t} = \mathbf{F}_\mathrm{g}, \tag{4.1}$$

$$\mathbf{I}_\mathrm{p}\frac{\mathrm{d}\boldsymbol{\omega}_\mathrm{p}}{\mathrm{d}t} = \mathbf{M}_\mathrm{p} - \boldsymbol{\omega}_\mathrm{p} \times \mathbf{I}_\mathrm{p}\boldsymbol{\omega}_\mathrm{p}, \tag{4.2}$$

where a p subscript indicates that a quantity is expressed in the plate-fixed coordinate system and a g subscript indicates that the quantity is expressed in the global inertial reference frame. m is the mass of the body, $\mathbf{I}$ is the mass moment of inertia tensor, $\mathbf{u}$ is the translational velocity vector, $\mathbf{F}$ is the applied force vector, $\boldsymbol{\omega}$ is the angular velocity vector and $\mathbf{M}$ is the vector of applied torque. These equations provide the complete system of six scalar equations required to compute the general 6DOF motion of a rigid body.

At any given instant during the motion of the rigid body, its configuration is described by specifying the location of the chosen base point and the orientation of the body in space. This can be achieved using a combination of inertial and rotating reference frames. Section 4.2 discusses the two main representations of orientation that have been considered during this research, and the merits and drawbacks of each approach.

4.2 Representing Orientation

The location of a body in three dimensional space is described by specifying its position relative to a fixed inertial reference frame. This is represented in Figure 4.1 by the cartesian $X_g Y_g Z_g$ coordinate system. In order to specify the orientation of the body, a set of cartesian axes $X_p Y_p Z_p$ corresponding to the body's principal axes are fixed onto the body with the origin at the body's centre of mass. This body-fixed reference frame is allowed to rotate with the plate and is therefore a non-inertial reference frame. The orientation of this body fixed reference frame ($X_p Y_p Z_p$) relative to the fixed inertial reference frame ($X_g Y_g Z_g$) is obtained via a translating inertial reference frame, $X_t Y_t Z_t$, which has its origin at the body's centre of mass. Figure 4.1 illustrates these three coordinate reference frames.

The angles - ϕ, θ, ψ - as illustrated result from a series of three rotations on the $X_t Y_t Z_t$ reference frame. Firstly a rotation of ψ about the positive Z_t axis, displacing the X_t and Y_t axes (onto the dotted lines). This is followed by a rotation of θ about the displaced positive Y_t axis, which rotates the displaced X_t axis onto the final X_p axis. Thirdly, a rotation of ϕ is performed about the X_t axis, which is now at its final X_p position, and this rotates the displaced Y_t and Z_t axes onto their final Y_p and Z_p positions. Any plate orientation in real three-dimensional space can be decomposed into a series of three rotations about different axes.

4.2.1 Euler Angles and Rotational Matrices

The most common representation of rigid body orientation is a set of three Euler angles that define the rotation of the plate-fixed reference frame relative to the inertial reference frame. Euler angles have become very widely used largely because of their intuitive nature.

Euler angles employ a rotational matrix, $\mathbf{R}$, based on the Euler angles in order to transform coordinates from the inertial to the rotated reference frames. A rotational matrix is defined as the matrix that when pre-multiplied by a vector expressed in the global inertial reference frame yields the same vector in the body-fixed reference frame according to

$$\mathbf{x}' = \mathbf{R}(\phi, \theta, \psi)\mathbf{x}, \tag{4.3}$$

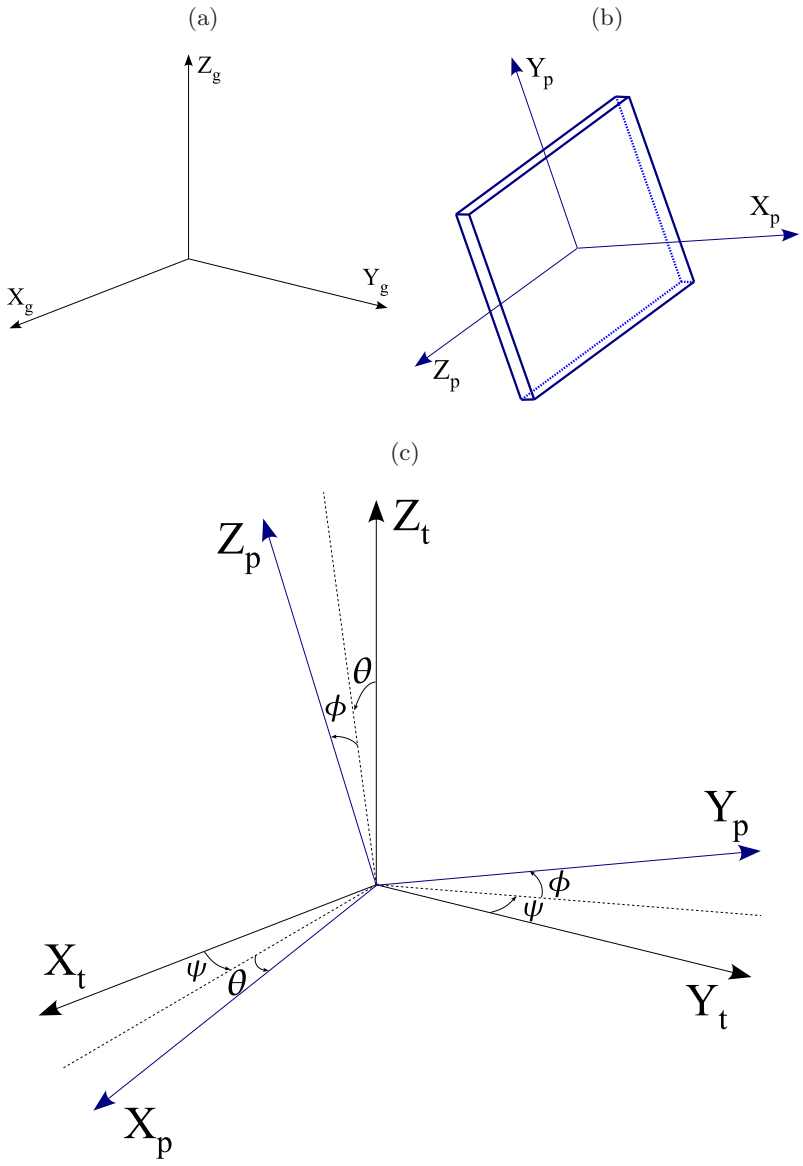

Figure 4.1: Illustration of (a) the fixed global inertial reference frame, $X_gY_gZ_g$, (b) the translating inertial reference frame, $X_tY_tZ_t$ and (c) the rotating plate-fixed reference frame, $X_pY_pZ_p$ with the angles - ϕ, θ, ψ - which describe the plate's orientation relative to the translating plate-fixed reference frame.

where $\mathbf{x}$ is a vector in the global inertial reference frame, $\mathbf{R}$ is the rotational matrix, and $\mathbf{x}'$ is the same vector in the body-fixed reference frame. A rotational matrix must always be orthogonal in order to constitute a pure rotation and its determinant must be equal to +1. In plain terms this implies that if a vector is subjected to a rotation, followed by a subsequent inverse rotation, the final vector should be the same as the original vector before the rotations.

The fundamental assumption behind Euler rotational matrices is that the rotation of a rigid body from one reference frame to another can be achieved using three rotations in a given sequence as illustrated in Figure 4.1. 12 unique Euler angle parametrisations exist depending on the sequence in which the rotations are carried out. Of the 27 possible sequences, only 12 satisfy the constraint that no two consecutive rotations occur about the same axis. These are listed in Diebel (2006) and their corresponding matrices derived.

For aerodynamics applications, the most common sequence of Euler angle rotations is the XYZ sequence, with the angles $[\phi, \theta, \psi]$ representing rotations about the X,Y,and Z axes respectively. In this parametrisation of orientation, the Euler Rotational Matrix, $\mathbf{R}$, is defined as a function of the Euler angles - $[\phi, \theta, \psi]$ - according to:

$$\mathbf{R}(\phi,\theta,\psi) = \mathbf{R}_{\mathrm{X}}(\phi)\mathbf{R}_{\mathrm{Y}}(\theta)\mathbf{R}_{\mathrm{Z}}(\psi) =$$

$$\begin{bmatrix} \cos\theta\cos\psi & \cos\theta\sin\psi & -\sin\theta \\ \sin\phi\sin\theta\cos\psi - \cos\phi\sin\psi & \sin\phi\sin\theta\sin\psi + \cos\phi\cos\psi & \cos\theta\sin\phi \\ \cos\phi\sin\theta\cos\psi + \sin\phi\sin\psi & \cos\phi\sin\theta\sin\psi - \sin\phi\cos\psi & \cos\theta\cos\phi \end{bmatrix}. \tag{4.4}$$

In addition to the rotational matrix, a *Euler angle rates matrix* is also required. This Euler angle rates matrix, $\mathbf{E}$, relates the rate of change of the Euler angles to the angular velocity of the body according to

$$\boldsymbol{\omega} = \mathbf{E}(\boldsymbol{\Psi})\dot{\boldsymbol{\Psi}}, \tag{4.5}$$

where $\boldsymbol{\omega}$ is the angular velocity vector, $\boldsymbol{\Psi} = [\phi, \theta, \psi]$ and $\dot{\boldsymbol{\Psi}} = [\dot{\phi}, \dot{\theta}, \dot{\psi}]$.

During rigid body dynamics computations, the angular velocity, $\boldsymbol{\omega}$, will usually be determined from solving the Euler equations of rotational motion, (4.2), in a body-fixed reference frame. As a result of the rotational motion, there will be a change in plate orientation and in order to update the rotational matrix, $\mathbf{R}$,

it is necessary to compute the updated vector of Euler angles, $\boldsymbol{\Psi}$, by numerical integration of the Euler angle rates vector, $\dot{\boldsymbol{\Psi}}$. This Euler angle rates vector is obtained from the computed angular velocities as

$$\dot{\boldsymbol{\Psi}} = [\mathbf{E}'(\boldsymbol{\Psi})]^{-1}\boldsymbol{\omega}_{\mathrm{p}}, \tag{4.6}$$

where the inverse conjugate Euler angle rates matrix, $[\mathbf{E}'(\boldsymbol{\Psi})]^{-1}$, which is defined as

$$[\mathbf{E}'(\boldsymbol{\Psi})]^{-1} = \begin{bmatrix} 1 & \sin\phi\tan\theta & \cos\phi\tan\theta \\ 0 & \cos\phi & -\sin\phi \\ 0 & \sin\phi\sec\theta & \cos\phi\sec\theta \end{bmatrix}. \tag{4.7}$$

A cursory examination of (4.7) reveals that if $\theta = \pm\frac{\pi}{2}$, then $\dot{\phi}$ and $\dot{\psi}$ can be infinite for finite values of $\boldsymbol{\omega}_{\mathrm{p}}$. This constitutes a mathematical singularity for the Euler angle parametrisation creating what is commonly known as *gimbal lock*. Stuelpnagel (1964) proves that it is topologically impossible to have a global three-dimensional parametrisation of orientation based on Euler angles that does not have singular points.

The direct implication for this unavoidable singularity in debris flight modelling is that existing six degree of freedom RBD models for debris flight which rely on Euler angle parametrisation of orientation are not globally valid for all possible orientations in real 3D space. One therefore has to restrict the rotation of the plate to remain within the singularity-free range of motions or force the code to switch parametrisations when a singular orientation is approached.

Therefore, although Euler angles offer an intuitive representation of orientation that is fairly straight forward to implement, the two main disadvantages of Euler angle parametrisation are:

- **Mathematical Singularities:** Because certain trigonometric functions used in the Euler angle parametrisations (e.g. tan and sec) have singularities, all Euler angle parametrisations have orientations at which the parametrisation breaks down. It is therefore necessary, when using Euler angles to ensure that the motion of the rigid body does not approach the singular orientations. However, for chaotic three-dimensional motions such as those in debris flight, this might not be possible to judge *a priori*. A globally singularity free parametrisation of orientation is therefore required.

- **Accuracy and Computational Efficiency:** Studies by Robinson (1958) proved that Euler angle parametrisations of orientation are less accurate and less computationally efficient than other methods (e.g. Rotational Quaternions), especially when used to integrate incremental changes in orientation over time. This is partly due to the relatively higher computational effort (solving six additional equations) required to enforce the orthogonality constraint on the rotational matrix as well as the accumulating numerical errors in successive calculations, resulting in angular drift.

4.2.2 Rotational Quaternions

Due to the limitations in Euler angle parametrisation of orientation, alternative parametrisations of orientation have been formulated, among which are the *Euler parameters*, commonly referred to as *rotational/unit quaternions*.
Quaternions, were first proposed by William Rowan Hamilton in 1843, in an attempt to present a higher dimensional generalisation of complex numbers (Hamilton, 1847). A quaternion, $\mathbf{q}$, may be represented as a vector in four-dimensional space,

$$\mathbf{q} = [q_0, q_1, q_2, q_3]^T. \tag{4.8}$$

Given a rotation α about an axis $\mathbf{n}$, a rotational quaternion may be defined as:

$$\mathbf{q} = \begin{bmatrix} \cos(\frac{1}{2}\alpha) \\ \mathbf{n}\sin(\frac{1}{2}\alpha) \end{bmatrix}. \tag{4.9}$$

Rotational quaternions are additionally constrained to have a unit norm, in order for them to represent a pure rotation (Greenwood, 2003). This is achieved by enforcing the algebraic constraint:

$$\|\mathbf{q}\| = \sqrt{\mathbf{q}\cdot\bar{\mathbf{q}}} = \sqrt{q_0^2 + q_1^2 + q_2^2 + q_3^2} = 1, \tag{4.10}$$

where $\bar{\mathbf{q}} = [q_0, -q_1, -q_2, -q_3]^T$ is the adjoint of the quaternion.
Given a vector, $\mathbf{x}$ in the global inertial reference frame, then $\mathbf{x}'$ - its representation in the body-fixed reference frame - can be obtained using rotational

quaternions according to:

$$\mathbf{x}' = \mathbf{q} \cdot \begin{bmatrix} 0 \\ \mathbf{x} \end{bmatrix} \cdot \bar{\mathbf{q}} = \mathbf{R}_{\mathbf{q}}(\mathbf{q})\mathbf{x}, \tag{4.11}$$

$$\mathbf{R}_{\mathbf{q}}(\mathbf{q}) = \begin{bmatrix} q_0^2 + q_1^2 - q_2^2 - q_3^2 & 2q_1q_2 + 2q_0q_3 & 2q_1q_3 - 2q_0q_2 \\ 2q_1q_2 - 2q_0q_3 & q_0^2 - q_1^2 + q_2^2 - q_3^2 & 2q_2q_3 + 2q_0q_1 \\ 2q_1q_3 + 2q_0q_2 & 2q_2q_3 - 2q_0q_1 & q_0^2 - q_1^2 - q_2^2 + q_3^2 \end{bmatrix}, \tag{4.12}$$

where $\mathbf{R}_{\mathbf{q}}(\mathbf{q})$ is a quaternion based rotational matrix. As with Euler angles, it is necessary to compute the vector of quaternion rates, $\dot{\mathbf{q}}$, and its mapping to the angular velocity vector $\boldsymbol{\omega}$ in body-fixed coordinates. This is achieved using the *inverse conjugate quaternion rates matrix*, $[\mathbf{W}'(\mathbf{q})]^T$, according to:

$$\boldsymbol{\omega} = 2W(\mathbf{q})\dot{\mathbf{q}}, \tag{4.13}$$

$$\dot{\mathbf{q}} = \frac{1}{2}[W'(\mathbf{q})]^T\boldsymbol{\omega}_{\mathrm{p}}, \tag{4.14}$$

$$[\mathbf{W}'(\mathbf{q})]^T = \begin{bmatrix} -q_1 & -q_2 & -q_3 \\ q_0 & -q_3 & q_2 \\ q_3 & q_0 & -q_1 \\ -q_2 & q_1 & q_0 \end{bmatrix}. \tag{4.15}$$

Unlike the Euler angle rates matrix, the quaternion rates matrix is valid for all possible orientations in real 3D space. Because of their accuracy, computational efficiency and lack of any singularities, quaternions have become widely applied in Rigid Body Dynamics applications. In some applications, such as robotics and aerospace, a full quaternion formulation of the kinematic and dynamic equations of motion is used (Chou, 1992).

The resulting system of equations consists of differential equations of motion which must be solved together with appropriate enforcement of the algebraic unity norm constraint, ξ, based on (4.10) and defined as

$$\xi = q_0^2 + q_1^2 + q_2^2 + q_3^2 - 1 = 0. \tag{4.16}$$

The unity norm constraint, (4.16), is however quadratic in form and this often results into instabilities during algebraic constraint enforcement (Baumgarte, 1972).

Despite their benefits, Quaternion based representations of orientation in rigid body dynamics therefore have two main drawbacks:

- **Less Intuitive:** Unlike the three Euler rotation angles, the four quaternion parameters have no physical meaning. As a result, quaternions are generally less intuitive than Euler angles when it comes to representing orientation.

- **Instability of Resulting Differential-Algebraic Equations:** When quaternions are used as generalized coordinates in formulating a rigid body dynamics problem, a system of Differential-Algebraic Equations results, which has an algebraic constraint that is quadratic in nature. Enforcing this constraint is problematic as it results in numerical instabilities even for stable physical systems as illustrated by Baumgarte (1972) and Greenwood (2003).

Greenwood (2003) discusses a number of methods for constraint enforcement. Due to the holonomic nature of the unit norm constraint (i.e. a constraint that can be formulated without explicitly including velocity) this study investigated two approaches to holonomic constraint enforcement: *Baumgarte's method for holonomic constraints* and *the one-step method for holonomic constraints*. These methods are discussed briefly in sections 4.2.2.1 and 4.2.2.2

4.2.2.1 Baumgarte Method for Holonomic Constraints

In this method, proposed by Baumgarte (1972), the full quaternion kinematic and dynamic differential equations of motion are solved together with the algebraic unit norm constraint, (4.16). This unit norm constraint on the rotational quaternions is enforced using the method of Lagrange multipliers. The unit norm equation, (4.16), is then differentiated twice in order to obtain a differential equation describing the acceleration constraint. It is this double differentiation with respect to time that introduces numerical instabilities into the final system.
Baumgarte (1972) presented a method for stabilising the differential representation of the holonomic constraint by introducing two damping terms that depend on two suitably chosen stabilisation constants (α and β which may themselves depend on time step size) as well as the algebraic constraint error and its first derivative.
The main drawback of Baumgarte's method is the difficulty in finding suitable values for the stabilisation constants α and β. Often this cannot be done *a priori*

and requires repeated simulations before suitable values are obtained (Cline, 2002). In addition, if multiple constraints exist the terms added to stabilise one constraint could increase the error of a second constraint (Greenwood, 2003).

4.2.2.2 One-step Method for Holonomic Constraints

Although the Baumgarte method works well in stabilizing kinematic constraints, there remained a need to eliminate the complexity in selecting the stabilisation constants. Later studies found that one could improve the accuracy of constraint representations by using a one-step method (Greenwood, 2003). The goal of the one-step method is to minimize the error at the end of each time step and to do so in such a manner that the dynamical response of the system will not be significantly affected.

In this method, the angular velocity in the body-fixed coordinate system is obtained from solving the traditional equations of motion, (4.1) and (4.2), to obtain the body-fixed rotational speeds. The quaternion rates vector is then computed according to (4.14). This quaternion rates vector is numerically integrated to obtain the updated quaternion.

At the end of each time-step, a correction is then made separately to eliminate the numerical drift in the unit quaternion. If the initial errors are unusually large due to the use of a large step-size, the one-step corrections can be repeated to yield negligibly small final constraint errors. Since in the one-step method, the Euler parameters do not directly enter the equations of motion (unlike the full quaternion formulation used in Baumgarte's method), the correction of the unit quaternion does not cause numerical instability (Greenwood, 2003). The one-step method is also relatively easy to implement as it does not require a full quaternion formulation of the RBD equations.

Greenwood (2003), Cline and Pai (2003) and Cline (2002) present comparisons between the two methods for constraint enforcement discussed above and the one-step method was found to yield more accurate results. The one-step method was also found to be relatively easier to implement, and for the purposes of this study, the approach proposed by Greenwood (2003) was implemented and is discussed here.

Consider the quaternion unit norm constraint, ξ, as presented in (4.16). Although this constraint should usually hold, due to a small numerical drift occur-

ring at each time step, in reality $\xi \neq 0$. We therefore need to apply a correction $\Delta\xi$ to the constraint equation, (4.16), such that

$$\Delta\xi = -\xi. \tag{4.17}$$

In order to apply this correction through corrections to the individual quaternion vector components, the one step method first calculates the gradient vector of the constrain equation in **q**-space as

$$\nabla\xi = [2q_0, 2q_1, 2q_2, 2q_3]^T. \tag{4.18}$$

The constraint correction $\Delta\xi$ is then calculated according to

$$\Delta\xi = \nabla\xi \cdot \Delta\mathbf{q}, \tag{4.19}$$

where $\Delta\mathbf{q}$ is the quaternion correction vector that exactly compensates for the constraint error at the end of each time step. $\Delta\mathbf{q}$ is assumed to act in the direction of the gradient $\nabla\xi$, such that:

$$\Delta\mathbf{q} = C\nabla\xi, \tag{4.20}$$

where C is a coefficient. From combining (4.20), (4.19), (4.18) and (4.17), C is calculated as

$$C = \frac{-\xi}{\nabla\xi \cdot \nabla\xi} = \frac{-\xi}{4(q_0^2 + q_1^2 + q_2^2 + q_3^2)} \approx \frac{-\xi}{4}. \tag{4.21}$$

Finally by combining (4.21), (4.20) and (4.18), the values for the corrections to the quaternion vector are given by Greenwood (2003):

$$\Delta q_0 = -\frac{1}{2}q_0\xi, \quad \Delta q_1 = -\frac{1}{2}q_1\xi, \quad \Delta q_2 = -\frac{1}{2}q_2\xi, \quad \Delta q_3 = -\frac{1}{2}q_3\xi. \tag{4.22}$$

By applying this quaternion correction vector to the new quaternion at the end of each time step, the normality constraint would be effectively enforced. This correction step is repeated iteratively at the end of each time-step until the desired accuracy, δ, is met such that $\xi \leq \delta$.

4.3 Conclusions

A rigid body dynamics model based on rotational quaternions has been successfully implemented in this research to ensure the accurate and singularity-free simulation of plate type debris flight. A one-step post-correction method for

holonomic constraints is used to enforce the unit norm constraint in order to ensure orthogonality of the rotational matrix.

The resulting singularity-free 6DOF RBD model constitutes a key improvement to the Euler angle parametrisations currently used in analytical models of plate type windborne debris flight. Appendix C contains the RBD model code implementation in the C programming language as a FLUENT User Defined Function (UDF). This RBD model has been applied to simulate 3D plate free flight (Kakimpa et al., 2010a) and autorotation (Kakimpa et al., 2010b).

Chapter 5

Static and Rotating Plate Simulations

This chapter presents preliminary studies carried out with the aim of developing and validating a CFD-RBD model to simulate the combined translation and rotation involved in windborne debris flight. First, a URANS CFD model has been developed and is used to simulate the flow around static 2D and 3D plates. Based on the results of sensitivity studies of 2D and 3D static plates, appropriate spatial and temporal resolution, discretisation schemes, pressure-velocity coupling and turbulence modelling approach have been selected.

The static plate CFD model has been verified against experimental measurements by ESDU (1970) and then extended to rotating plate cases, starting with the simulation of forced rotation at a prescribed constant speed. Coupling the CFD model with a single degree of freedom (1DOF) RBD model allows for the simulation of low aspect ratio plate autorotation. CFD-RBD predictions for rotational speed, aerodynamic torque and wall pressure distribution on a plate that is autorotating about a fixed axis are validated against existing experimental measurements by Martinez-Vazquez et al. (2010). Finally the CFD-RBD model is applied to unconstrained three-degree-of-freedom (3DOF) free-axis autorotation about a fixed point, in which the axis of rotation is not fixed but rather determined by the Fluid-Structure Interaction (FSI).

The result is a validated CFD-RBD model capable of simulating free autorotation as well as an increased understanding of the key flow phenomena leading to stable autorotation.

5.1 2D Static Plate Simulations

A 2D URANS model has been used to simulate the aerodynamics of a high aspect-ratio static plates. The goal is to assess the sufficiency of CFD models for predicting the aerodynamics of high aspect-ratio flat plates. Figure 5.1 shows Mesh B, the main computational mesh used for the 2D sensitivity studies.

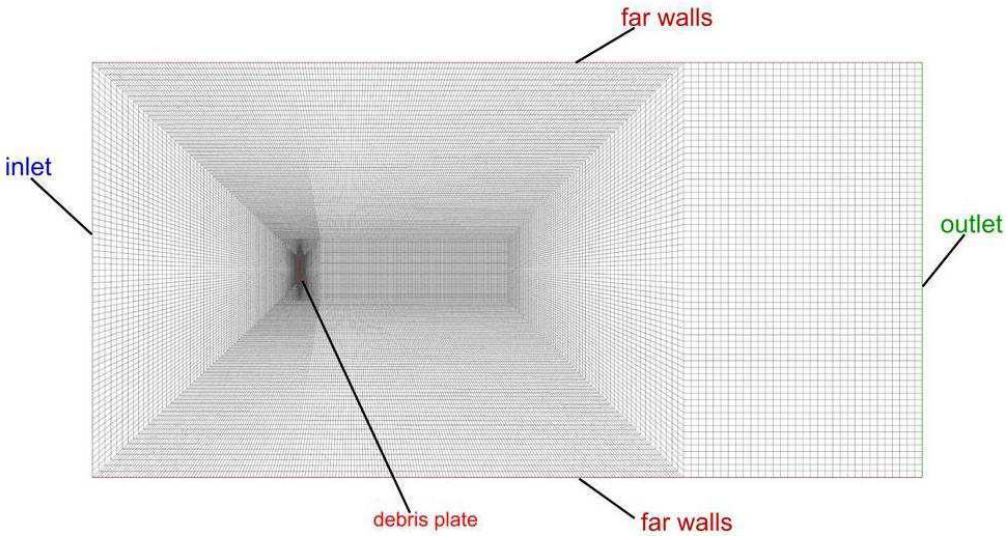

Figure 5.1: Computational domain and mesh used in 2D simulations.

Mesh dependency studies were performed using a finer and coarser mesh, referred to as Mesh C and Mesh A respectively, and the drag predictions for the worst case angle of attack, $\alpha_z = 90°$, are found to be mesh independent as shown in Table 5.1. Mesh B is therefore used for the rest of the simulations.

The plate is modelled as an infinitely thin flat plate of length $L = 0.3$ m and thickness $h = 0.0$ m having only two faces. The plate's two faces together with the domain's top and bottom boundaries are modelled as wall boundaries with zero normal velocity and a no-slip condition for tangential velocity. A velocity inflow boundary condition is applied at the inlet with a Dirichlet condition for velocity together with a homogeneous Neumann condition for pressure, while the outlet boundary is modelled as a pressure outlet with a Dirichlet condition for pressure and a homogeneous Neumann condition for velocity. In all the simulations performed, inlet turbulence intensity and length scales of 1% and 0.02 m respectively are used, which are consistent with low turbulence wind tunnel values reported by ESDU (1970).

The plate is positioned $10L$ from each of the top and bottom boundaries giving a blockage ratio of 5% which is well within the 6% limit where blockage effects are negligible (West and Apelt, 1982). The plate is also $10L$ from the inlet boundary and $30L$ from the outlet so as to reduce the effect of the truncated solution represented by the boundary conditions. The domain is discretised using a structured grid into approximately 57,000 rectangular cells.

Table 5.1: Grid size sensitivity study for the 2D CFD computations.

	Mesh A	Mesh B	Mesh C
No of Cells	31,744	57,344	207,360
Wall Adj. Cell Size, $\overline{\Delta x}$ (m)	1.73×10^{-2}	4.74×10^{-3}	2.53×10^{-3}
Maximum Cell Volume (m^3)	6.03×10^{-1}	1.19×10^{-1}	1.25×10^{-1}
Minimum Cell Volume (m^3)	9.00×10^{-5}	6.75×10^{-6}	1.93×10^{-6}
U_w (m/s)	2.75	2.75	2.75
Δt (s)	1.0×10^{-3}	1.0×10^{-3}	1.0×10^{-3}
Courant Number, Cr	1.59×10^{-1}	5.80×10^{-1}	1.09
$(C_D)_{\alpha_z=90^\circ}$	2.068	2.125	2.123

5.1.1 Simulation Results

Simulations were performed at a Re $= 5.46 \times 10^4$ which corresponds to a 2.75 m/s inlet velocity. For the CFD results presented in this section, a second order upwind scheme is used for advection terms, with the standard Rhie-Chow interpolation scheme for the pressure term and the SIMPLE algorithm for pressure-velocity coupling.

The Realisable $k - \varepsilon$ turbulence model is used, together with a two-layer enhanced wall function approach. The sensitivity studies for advection scheme and pressure-velocity coupling scheme are presented in Section 5.1.2, while the choice of turbulence model and near-wall modelling approach is reported in Section 5.2.1.

The predicted flow field is illustrated using contours of pressure, velocity, vorticity magnitude, and Q-criterion in Figures 5.2 and 5.3. For incompressible flow the Q-value, an objective method of vortex identification proposed by Hunt et al. (1988b), is computed as

$$Q = \frac{1}{2}(|\mathbf{\Omega}|^2 - |\mathbf{S}|^2), \tag{5.1}$$

where $\mathbf{\Omega} = \frac{1}{2}[\nabla\mathbf{U} - (\nabla\mathbf{U})^{\mathrm{T}}]$ is the vorticity tensor and $\mathbf{S} = \frac{1}{2}[\nabla\mathbf{U} + (\nabla\mathbf{U})^{\mathrm{T}}]$ is the strain-rate tensor. The Q-criterion (Hunt et al., 1988b) identifies a vortex as a region where $Q > 0$ such that flow swirl, represented by $|\mathbf{\Omega}|$, is more prominent than flow shear, represented by $|\mathbf{S}|$. This method of vortex identification has been preferred over vorticity magnitude since vorticity has been shown not to

distinguish between pure shearing motions and the actual swirling motion of a vortex (Kolar, 2007), as illustrated by Figure 5.3(a) and (b).

As previously discussed in Section 2.1, the results in Figures 5.2 and 5.3 show that at lower angles of attack the flow remains steady and attached to the plate with no significant vortex shedding. However, at higher angles of attack, beyond the stall angle, $\alpha_z \approx 15^\circ$, the flow around the plate becomes unsteady. Strong vortex shedding is observed from the leading and trailing edges of the plate as shown in Figure 5.3, resulting in periodic fluctuations in the force coefficients (Figure 5.4). A von Karman vortex street results, characterised by a Strouhal number St ≈ 0.15, which is consistent with experimental measurements by Chen and Fang (1996) where a value of 0.16 ± 0.003 was measured for 2D plates at $20^\circ \leq \alpha_z \leq 90^\circ$ in a high Reynolds number flow.

The time-averaged aerodynamic force coefficients for all the angles of attack tested are shown in Figure 5.5, contrasted against experimental measurements from ESDU (1970) for infinite aspect ratio plates in a flow of $(5 \times 10^4) \leq \text{Re} \leq (5 \times 10^5)$. The results show that for lower angles of attack, the CFD predictions are in good agreement with experimental measurements while at higher angles of attack, the CFD predicted much higher aerodynamic forces, with the maximum drag approximately 20% higher than experimental measurements.

Contrary to findings by Breuer et al. (2003) using a Spalart-Allmaras model, where both 2D and 3D URANS simulations of flow around a static plate did not show any vortex shedding, using the Realisable $k-\varepsilon$ model in this study, with a two-layer enhanced wall function approach, 2D URANS models have been shown to be capable of accurately predicting vortex shedding.

5.1.2 2D Sensitivity Studies

5.1.2.1 Advection and Pressure-Velocity Coupling Schemes

Simulations have been performed to assess the sensitivity of model predictions to advection schemes and pressure-velocity coupling method. Findings from these sensitivity studies have been applied to the 3D cases. The studies are performed for the $\alpha_z = 90^\circ$ position and the Strouhal number is used as the key parameters for assessing model performance. A description and results for each of the cases I to VIII are reported in Table 5.2 along with predicted results.

Results from cases I to IV show that while the first order upwind advection

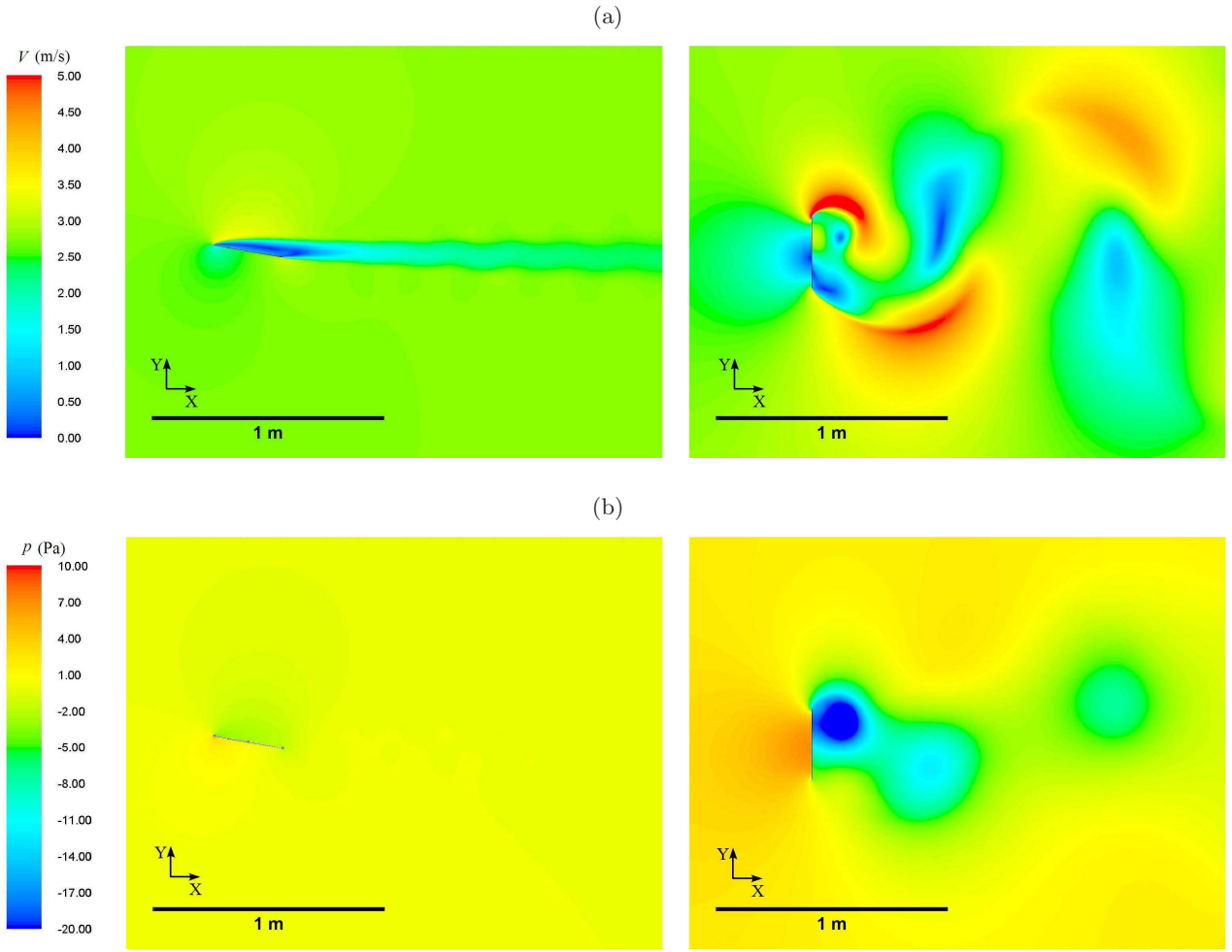

Figure 5.2: CFD predictions for (a) velocity magnitude, V (m/s), and (b) pressure, p (Pa), in the wake of a 2D static plate held at $\alpha = 10°$ (left) and $\alpha = 90°$ (right) in a uniform flow of $\mathrm{Re} = 5.46 \times 10^4$.

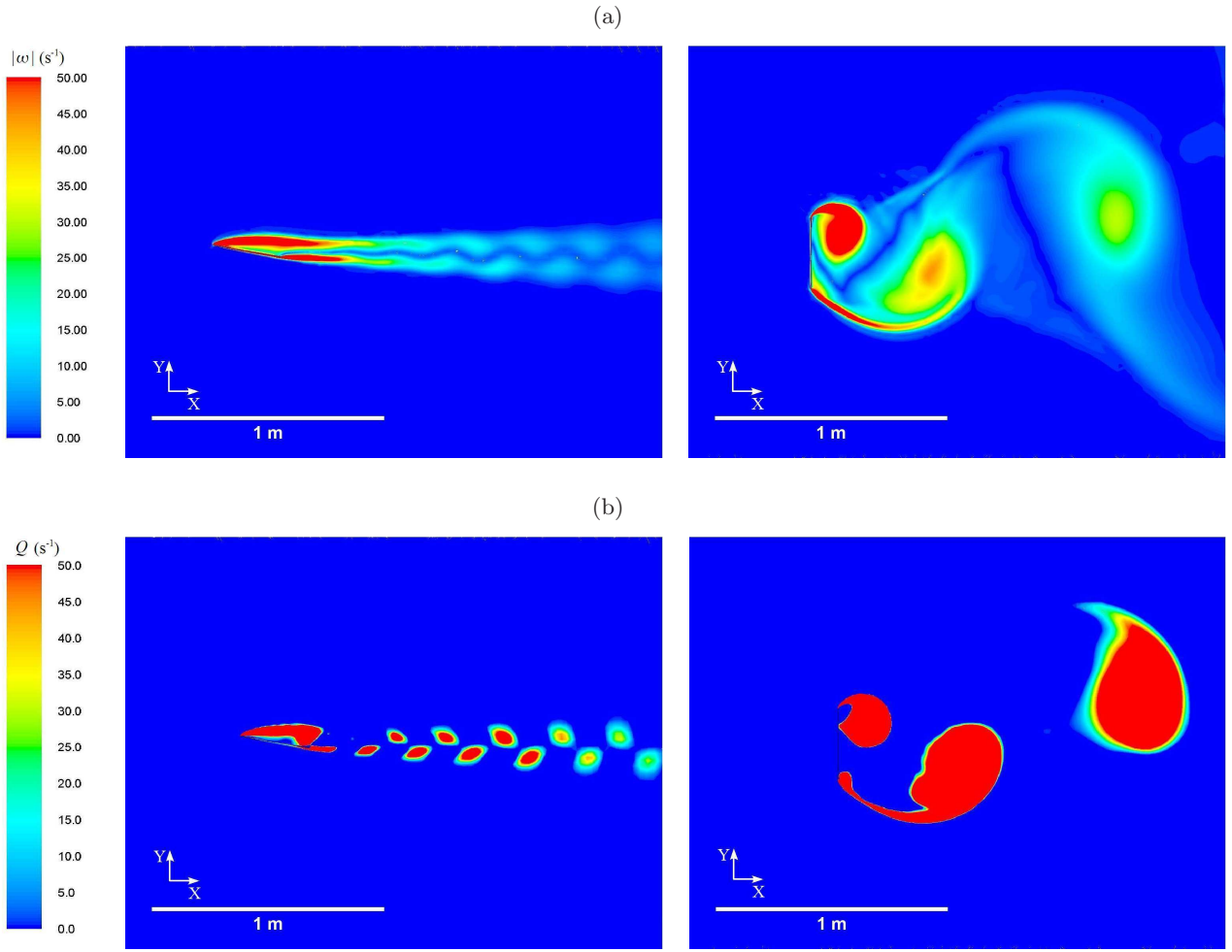

Figure 5.3: CFD predictions for (a) vorticity magnitude, $|\,\omega\,|$ (s^{-1}) and (b) Q-criterion value, Q (s^{-1}), in the wake of a 2D static plate held at $\alpha = 10°$ (left) and $\alpha = 90°$ (right) in a uniform flow of $Re = 5.46 \times 10^4$.

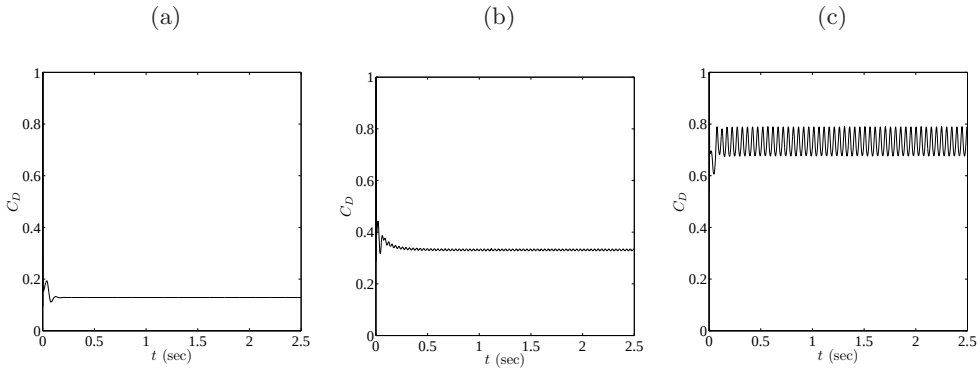

Figure 5.4: CFD predicted time series of drag force coefficient for a 2D static flat plates at (a) $\alpha = 10°$, with no force fluctuation due to steady wake, (b) $\alpha = 20°$ with weak fluctuations due to weak vortex shedding, and (c) $\alpha = 30°$ with strong fluctuations due to stronger vortex shedding.

scheme gives good agreement between mean drag predictions and experimental measurements, this is at the expense of relatively poor performance in predicting the vortex shedding frequency, as indicated by the relatively low value of Strouhal number.

Higher order advection schemes such as second order upwind, QUICK and third order MUSCL schemes have been preferred together with either coupled or SIMPLE algorithms for Pressure-Velocity coupling, as shown in cases V to VIII. The QUICK and third order MUSCL schemes gave comparable performance to the second order upwind scheme in drag prediction but like the first order upwind scheme, this occurred with worse predictions for vortex shedding frequency.

Coupling the pressure and velocity equations improved overall accuracy and rate of convergence but resulted in significantly increased computational cost. Therefore a coupled solver was only used in obtaining an initial solution, while a segregated solver with the SIMPLE algorithm is used in the actual computations. Using higher order discretisation schemes for the pressure term was found to have no effect on the results so the standard Rhie-Chow interpolation scheme is satisfactory (Rhie and Chow, 1983).

5.1.2.2 Time-step Dependency Study

The choice of time step size, Δt, is initially based on the desire to achieve a sampling frequency $1/\Delta t$ that is at least an order of magnitude greater than the

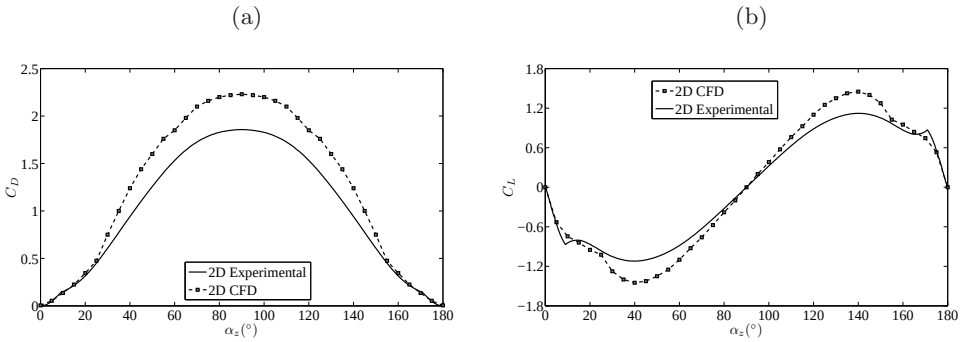

Figure 5.5: Experimental measurements (ESDU, 1970) and CFD predictions for time averaged (a) drag and (b) lift coefficients for 2D static plates at different angles of attack

dominant frequency of an unsteady flow. For a 2D static flat plate which has a Strouhal number $St \approx 0.16$, a time-step size $\Delta t \leq 0.07$ s would be required. A generalised Grid Convergence Index (GCI) based on the Richardson extrapolation approach (Roache, 1997; Oberkampf and Trucano, 2002) is used to estimate the solution error due to temporal discretisation.

Simulations are performed at three time levels h_1, h_2 and h_3 with a refinement ratio, $r = \frac{h_3}{h_2} = \frac{h_2}{h_1} = 10.0$. The Richardson extrapolation assumes the error ϵ_h on a grid i to be defined as,

$$\epsilon_h = (f_{\text{exact}} - f_i) = \alpha h_i^p + \mathcal{O}(h_i^{p+1}), \tag{5.2}$$

where f is a quantity, such as drag whose value is sought and h_i is the time-step size for discretisation i, p is the order of convergence, $\mathcal{O}(h^{p+1})$ is the truncation error due to higher order terms and α is a constant which can be computed using the solution on two separate grids as

$$\alpha = \frac{f_1 - f_2}{h_2^p - h_1^p} + \mathcal{O}(h_1^{p+1}) + \mathcal{O}(h_2^{p+1}). \tag{5.3}$$

Neglecting higher order terms, the error on fine grid ϵ_1, and coarse grid ϵ_2, can be computed according to (Roache, 1997):

$$\epsilon_1 = \|f_{\text{exact}} - f_1\| \approx \left| \frac{f_2 - f_1}{1 - r^p} \right|, \tag{5.4}$$

$$\epsilon_2 = \|f_{\text{exact}} - f_1\| \approx \left| \frac{r^p (f_2 - f_1)}{1 - r^p} \right|, \tag{5.5}$$

Table 5.2: Unsteady CFD sensitivity study of various pressure and advection schemes for a thin flat plate held normal to a flow of Re=5.4×10^4.

Case	Δt (s)	Advection Scheme	Pressure Scheme	P-V Coupling	St
I	1.0×10^{-3}	1st Order Upwind	Standard	SIMPLE	0.145
II	5.0×10^{-2}	1st Order Upwind	Standard	SIMPLE	0.146
III	5.0×10^{-2}	1st Order Upwind	Standard	Coupled	0.135
IV	5.0×10^{-2}	1st Order Upwind	2nd Order	Coupled	0.135
V	5.0×10^{-3}	2nd Order Upwind	Standard	SIMPLE	0.157
VI	5.0×10^{-2}	2nd Order Upwind	2nd Order	Coupled	0.148
VII	5.0×10^{-2}	QUICK	2nd Order	Coupled	0.147
VIII	5.0×10^{-2}	3rd Order MUSCL	2nd Order	Coupled	0.135

where the order of convergence, p, is calculated by using the solution on three separate grids as

$$p = \ln\left(\frac{f_{h3} - f_{h2}}{f_{h2} - f_{h1}}\right) / \ln(r), \tag{5.6}$$

where $r > 1$. Finally, the Grid Convergence Index (GCI) is computed by applying a factor of safety F_s to the computed error ϵ in order to account for uncertainty in Richardson's extrapolation error estimates,

$$\mathrm{GCI}_i = F_s[\epsilon_i]. \tag{5.7}$$

Roache (1997) recommends a factor of safety $F_s = 1.25$ to be sufficiently conservative.

Results of the time-step sensitivity study are shown in Table 5.3. The order of convergence, p was computed as 0.68, with f_{exact} approximated as 2.371. Based on the findings of this study, a second order implicit time stepping scheme with a time step size of 5×10^{-2} s has been found to be sufficient.

5.1.2.3 Reynolds Number Dependence

Additional simulations were performed to asses the sensitivity of the solution to Reynolds number by varying the inflow velocity. The results, shown in Table 5.4 were found to be fairly Re independent in the $5.5 \times 10^4 \leq \mathrm{Re} \leq 5.5 \times 10^5$ range for which experimental data from ESDU (1970) is valid.

Table 5.3: Temporal Discretisation Error estimated using a Richardson's extrapolation approach (Roache, 1997) on a 2D computational grid.

i	Δt_i (s)	$f_i = C_D$	ϵ_i	GCI (%)
1	5.0×10^{-4}	2.366	5.667×10^{-3}	0.299%
2	5.0×10^{-3}	2.344	2.735×10^{-2}	1.445%
3	5.0×10^{-2}	2.239		

Table 5.4: Reynolds number sensitivity studies

Re	U (m/s)	$(C_d)_{avg}$
5.46×10^3	0.275	2.197
5.46×10^4	2.75	2.342
1.10×10^5	5.5	2.342
5.46×10^5	27.5	2.341

Drag predictions from an additional case with $\mathrm{Re} = 5.46 \times 10^3$ showed relatively lower mean drag indicating some dependency of results on Re. Similar Reynolds number effects have been identified in experimental studies of slender sharp edged bodies and are attributed to changes in the topological structure of the wake due to transition from laminar to turbulent boundary layer flows (Schewe, 2001).

Although 2D URANS models successfully predicted vortex shedding and its frequency, the aerodynamic force predictions showed poor comparison with experimental measurements at higher angles of attack with an error of up to 20% in the drag prediction compared to ESDU results. Some of the differences may be attributed to plate thickness in this case, however the principal weaknesses of 2D CFD simulations is the suppression of vortex stretching and the lateral 3D breakup of vortices. This 2D representation of inherently 3D turbulence results in idealised vortex tubes of superficially high vorticity resulting in an over-prediction of aerodynamic forces by 2D URANS models. Therefore in order to adequately simulate the three dimensional nature of the flow structures, it is necessary to use full 3D simulations for even high aspect ratio plates.

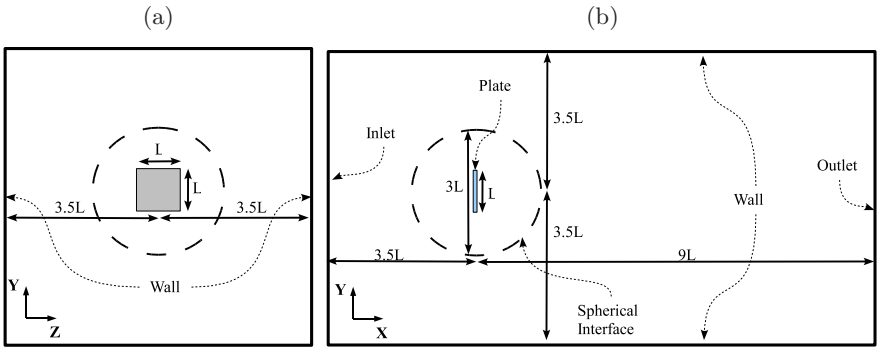

Figure 5.6: Vertical sections (a) Normal to the wind flow and (b) Parallel to the wind flow, showing the plate and the computational domain and boundaries.

5.2 3D Static Plate Simulations

To extend the CFD model to three-dimensional cases, 3D URANS CFD simulations have initially been carried out on static plates. The computational domain described in Figure 5.6 is used, with a square flat plate of side length L =1 m and thickness h =0.0254 m which is consistent with experimental measurements by Martinez-Vazquez et al. (2010) that are later used for model validation (see Section 5.5). The plate is positioned with its centre $3.5L$ from each of the inlet, top, bottom and side boundaries, and $9L$ from the outlet boundary. This results in a maximum blockage ratio of 2.04% when the plate is normal to the flow, therefore blockage effects may be neglected (West and Apelt, 1982).

The computational mesh is split into two regions, a spherical inner region and an outer region. The plate was held within the spherical inner volume of radius $1.5L$, which can be rotated relative to the fixed outer region to allow for ease in aligning the plate orientation relative to the oncoming flow without re-meshing the domain. The spherical boundary of the inner region is connected to the co-incident spherical boundary of the outer region through a non-conformal grid interface. This involves first computing a virtual layer of faces which is an intersection between the two boundaries making up the interfaces. Fluxes across the non-conformal interface are then interpolated via the new virtual layer of faces FLUENT Inc. (2009).

The domain is discretised into approximately 291,000 hexahedral cells, with grid refinement close to the plate boundary such that the cell centroid of the wall

neighbouring cell, y_p is between (3.6×10^{-3}) m to $\leq (8.6 \times 10^{-3})$ m, while the dimensionless wall distance, y^+ is in the range $10 \leq y^+ \leq 130$. An enhanced wall function with a two layer approach was used to approximate turbulence quantities near the wall.

Simulations were performed for angles of attack $0^\circ \leq \alpha \leq 90^\circ$ at 10° intervals, with the Realisable $k - \varepsilon$ turbulence model and the SIMPLE algorithm for pressure-velocity coupling. Second order upwind scheme is used for advection terms with the second order implicit scheme for time discretisation. The results are assumed to be symmetric about the 90° position, and are shown for $0^\circ \leq \alpha \leq 180^\circ$ in Figure 5.7.

The CFD predictions for 3D static plate drag, lift and torque compare well with experimental data for similar plates and Reynolds number (ESDU, 1970). At the stall region, the CFD model slightly under-predicts the aerodynamic forces, showing a gradual transition as opposed to a distinct peak in the force coefficients at the stall angle that is shown in the ESDU data. Recent experimental data such as Martinez-Vazquez et al. (2010) based on surface pressure measurements shows a less distinct peak at the stall angle compared to the ESDU (1970) data. However this difference could be explained by insufficient angle of attack resolution to capture the exact stall angle in both the CFD results and Martinez-Vazquez et al. (2010) experiment which use angle of attack resolutions of 5° and 15° respectively. Further experimental investigation of plate aerodynamics at the stall angle is recommended.

Overall, however, the body force predictions from the model were found to compare well with experimental results, with a maximum deviation from the experimental values of approximately 10%, which occurs at a 90° angle of attack and is comparable to a reported experimental uncertainty range of $\pm 5\%$ in the ESDU (1970) results.

URANS turbulence models have had limited success in predicting massively separated bluff body flows (Rodi, 1997). Because URANS models predict the statistical nature of the turbulent flow and not the actual realisations of the flow, they have been shown not to reproduce unsteady phenomena well (Breuer et al., 2003) due to an inability to distinguish between turbulent fluctuations and unsteady flows. As a result, excessively large turbulent viscosities are often predicted, creating an artificial diffusion and steady wake behaviour where

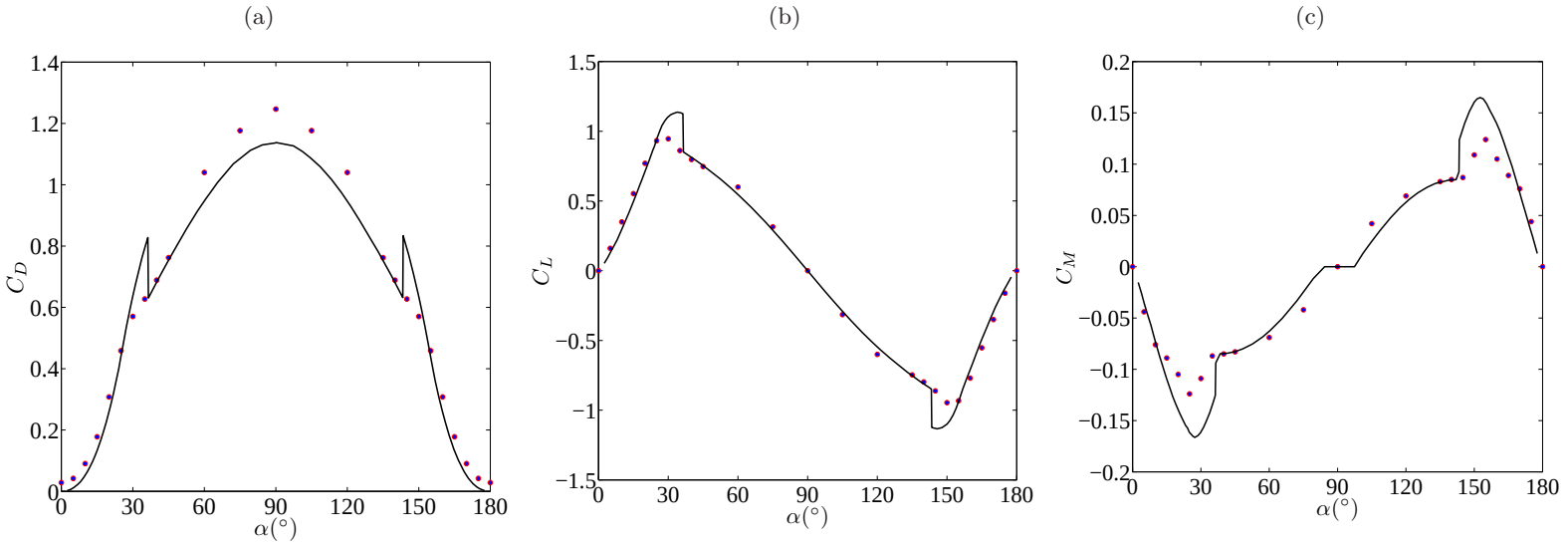

Figure 5.7: Comparison between experimental (ESDU, 1970)(-) and 3D CFD (•) predictions for (a) drag, (b) lift and (c) torque coefficients for a flat square plate at different angles of attack.

unsteady behaviour is expected. However, some researchers such as Iaccarino et al. (2003) present conflicting results, with URANS models successfully used to predict the underlying statistics of the highly unsteady flow around 3D surface mounted cube. Results from Iaccarino et al. (2003) also showed that in the case of the surface mounted cube, vortices shed from the side of the cube induced a side-to-side oscillation that creates instability in the main arch vortex, eventually leading to periodic unsteadiness of the wake. This flow separation and vortex shedding from the sides of the cube is likely to be affected by the near wall treatment since the assumptions of a logarithmic velocity distribution and local equilibrium of turbulence made in the wall function approach are questionable in separated flows and a two layer approach is recommended (Rodi, 1997). For his successful simulations, Iaccarino et al. (2003) uses a $y^+ \approx 1$, resolving the viscous sub-layer, however for practical computations, much higher y^+ values would have to be considered in order to reduce the computational cost.

In order to address these concerns, additional studies have been performed to assess the influence of near wall grid refinement and turbulence modelling approach on wake behaviour and force predictions.

5.2.1 Influence of Near-wall Grid Size and Turbulence Model

Initially a relatively coarse computational grid contained 291,000 cells is used which has a near-wall cell distance in the range $10 < y^+ < 130$. Although a two-layered enhanced wall function approach is used, since the majority of cell points lie within the turbulent boundary layer ($y^+ > 30$) a standard log-law wall function is effectively applied.

This coarse grid resolution at the plate side edges also restricts the development of a secondary recirculation at the plate side edges resulting in more stable shear layers. For different angles of attack investigated, Figures 5.8 and 5.9 show the pressure and velocity contours on a vertical section through the centre of the plate while Figure 5.10 shows the 3D flow structures in the wake of the plate. These 3D flow structures in the wake are visualised using a Q-criterion iso-surface, which shows the vortex cores.

The flow structure is composed of a leading edge vortex that remains stably attached to the plate, together with tip vortices at the side edges and a vortex sheet from the trailing edge. In all the cases where no vortex shedding

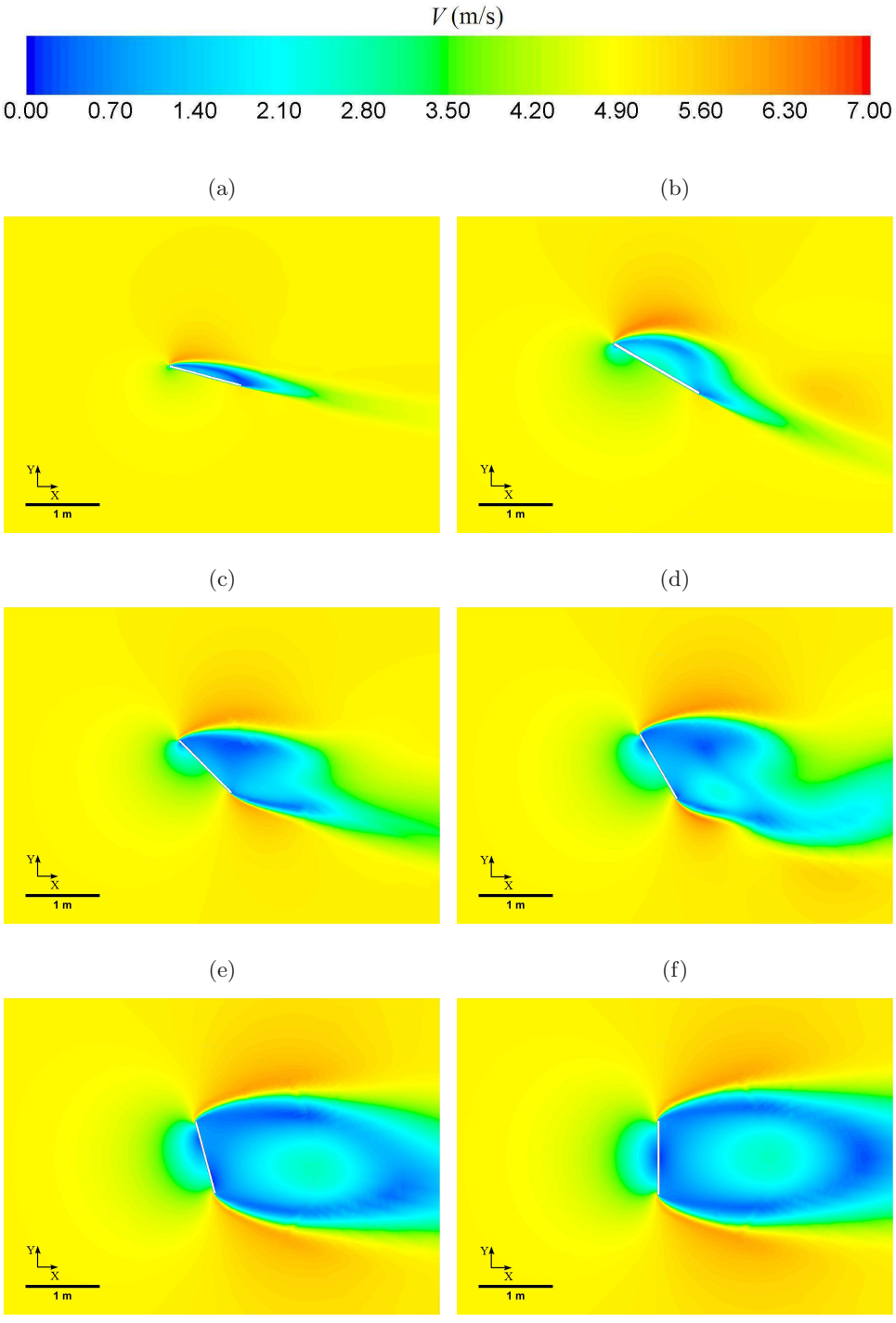

Figure 5.8: Instantaneous CFD contours of velocity magnitude, V (m/s), for a 1 m square flat plates at angles of attack, α_z, of: (a) 15°, (b) 30°, (c) 45°, (d) 60°, (e) 75° and (f) 90°, in a flow of $U_w = 5.0$ m/s.

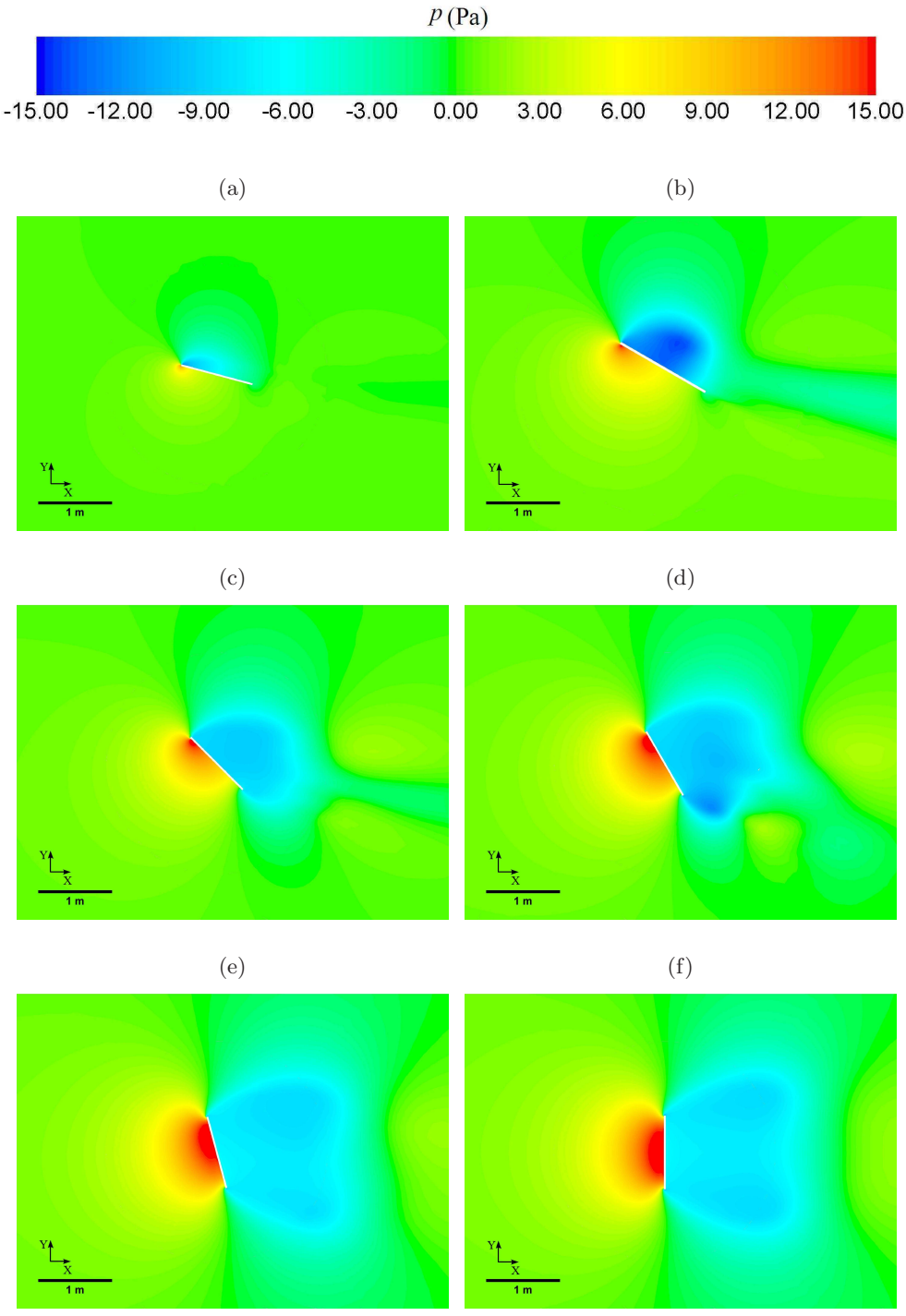

Figure 5.9: Instantaneous CFD contours of pressure, p (Pa), for a 1 m square flat plates at angles of attack, α_z, of: (a) 15°, (b) 30°, (c) 45°, (d) 60°, (e) 75° and (f) 90°, in a flow of $U_w = 5.0$ m/s.

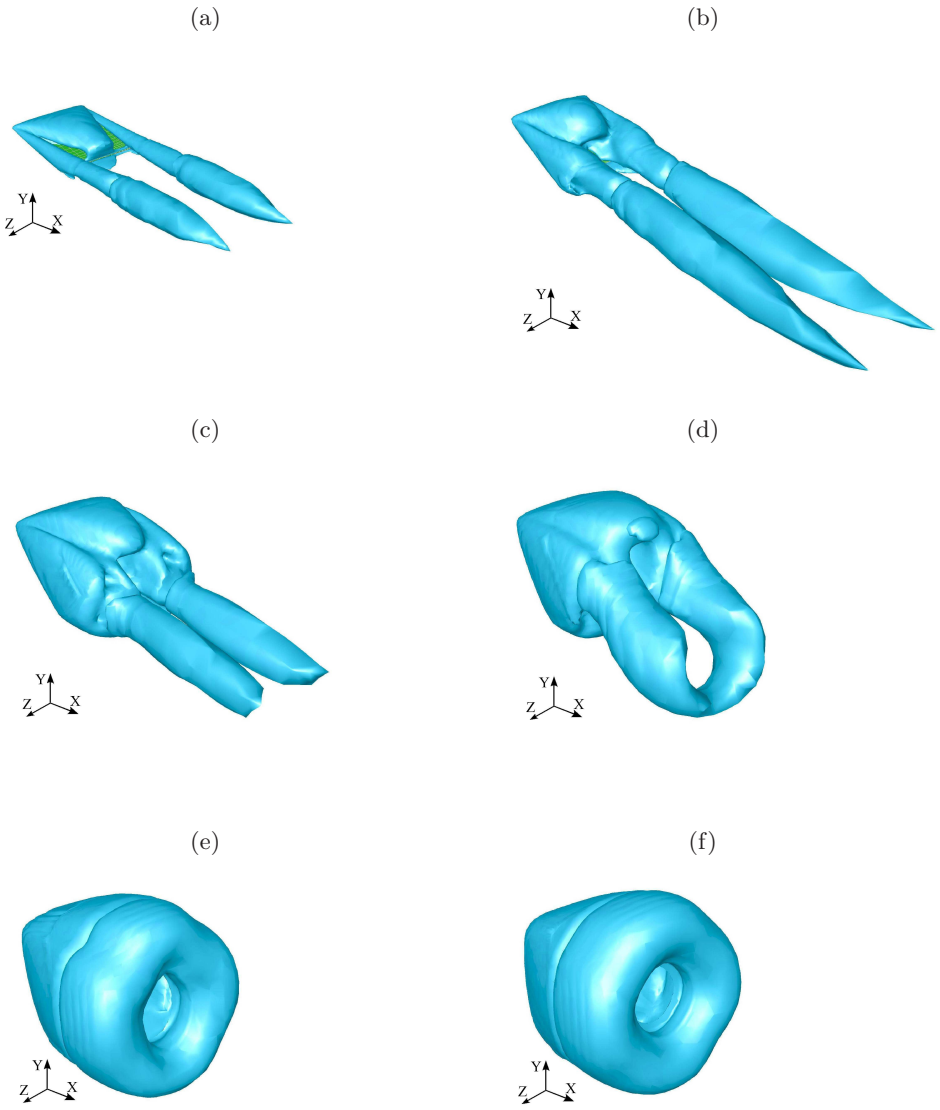

Figure 5.10: Instantaneous CFD iso-surfaces of Q-criterion, $Q = 10$ s^{-1}, for a 1 m square flat plates at angles of attack, α_z, of: (a) 15°, (b) 30°, (c) 45°, (d) 60°, (e) 75° and (f) 90°, in a flow of $U_w = 5.0$ m/s.

is observed, a steady separated wake results as illustrated by the velocity and pressure contours in Figures 5.8 and 5.9. Larger flow structures are observed for higher angles of attack as illustrated in Figure 5.10(c)-(f). At very high angles of attack, the tip vortices become nearly vertical and merge together with the leading and trailing edge vortices to form a stable ring vortex as shown in Figure 5.10(f). In the $\alpha_z = 60°$ case, Figure 5.10(d), weak shedding of hair-pin vortices was observed due to the interaction between the tip vortices and the leading and trailing edge vortices. This vortex shedding has not been observed for the other angles of attack, and the reasons for this are unclear. The onset of vortex shedding at higher angles of attack appears to be chaotic and sensitive to flow perturbations.

Since the coarse grid URANS simulations predicted stably attached vortices in the wake of the plate, with no flow unsteadiness, no aerodynamic force fluctuations are observed, except in the 60° case. The steady aerodynamic coefficients predicted are however found to compare well with experimental results as previously shown in Figure 5.7 despite being unable to predict wake unsteadiness.

In order to assess the sensitivity of the wake flow behaviour to turbulence model and grid resolution, additional simulations have been performed with adjustments to the turbulence modelling approach and the near-wall grid resolution.

Firstly, the computational mesh has been refined in the near wall region so that $y^+ \approx 1$, at the first grid point away from the wall. Table 5.5 describes all three grids used. The initial grid refinement is referred to as the "FINE1" mesh and contained a total of over 918,000 computational cells with near wall y^+ values in the range $0.19 \leq y^+ \leq 17.28$. Refinement is focused in the near wall region with no significant wake region mesh refinement. An additional refinement of the "FINE1" grid is performed, focusing on the wake region and resulting in a third grid referred to as "FINE2" composed of 2,370,000 cells.

Secondly, in order to assess the sensitivity of results to turbulence modelling approach, DES simulations have been performed. In the DES cases, the Realisable $k - \varepsilon$ model is used as the sub-gird scale model for the LES region, while URANS is used in the near wall region. The LES region is defined as the region where the local grid cell size is sufficient to resolve the estimated turbulent length scale $l = k^{(3/2)}/\varepsilon$. Aerodynamic force and wake structure from the more computationally expensive hybrid RANS/LES approach in DES is compared to

Table 5.5: Description of the computational grids used in predictions for the flow around a static falt plate held at 45° angle of attack.

	COARSE	FINE1	FINE2
$y^+_{\min}$	12.23	0.19	0.17
$y^+_{\max}$	127.67	17.28	16.68
No. of Cells	291,328	918,668	2,370,370
$\Delta V_{\min}$	1.65×10^{-6}	6.03×10^{-10}	6.03×10^{-10}
$\Delta V_{\max}$	1.56×10^{-2}	1.56×10^{-2}	1.56×10^{-2}

Table 5.6: A summary of computational cases run to compare results from different grid resolutions and turbulence models for the flow around a static flat plate at $\alpha_z = 45°$ in a flow of $U_{\text{w}} = 5$ m/s.

No	Mesh	Turbulence Model	Δt (s)	$\overline{C_L}$	$(C_L)_{\text{RMS}}$
I	COARSE	R $k-\varepsilon$	2×10^{-2}	7.47×10^{-1}	–
II	COARSE	R $k-\varepsilon$	1×10^{-3}	7.47×10^{-1}	–
III	FINE1	R $k-\varepsilon$	2×10^{-2}	7.55×10^{-1}	1.3×10^{-3}
IV	COARSE	DES	1×10^{-3}	7.61×10^{-1}	1.7×10^{-2}
V	FINE1	DES	5×10^{-3}	8.25×10^{-1}	2.3×10^{-2}
VI	FINE2	DES	1×10^{-2}	7.99×10^{-1}	1.5×10^{-2}

the URANS approach. Table 5.6 summarises the results from different cases run for a 45° angle of attack with different combinations of turbulence modelling approach and grid resolution. The lift force time-series for the different cases are shown in Figure 5.11.

The results were found to be time-step independent as illustrated by URANS Cases I and II. Results for Cases I and III reveal that for the URANS cases, using a finer near-wall resolution with a two-layer wall function approach can result in unsteady flow behaviour and the onset of stable vortex shedding where a standard wall function with a coarse near wall grid would predict a steady separated wake. A two-layer wall treatment with a fine near-wall grid spacing has therefore been recommended. Figure 5.12 shows the velocity profile along a line normal to each of the the leading and trailing edges in Case I and Case III.

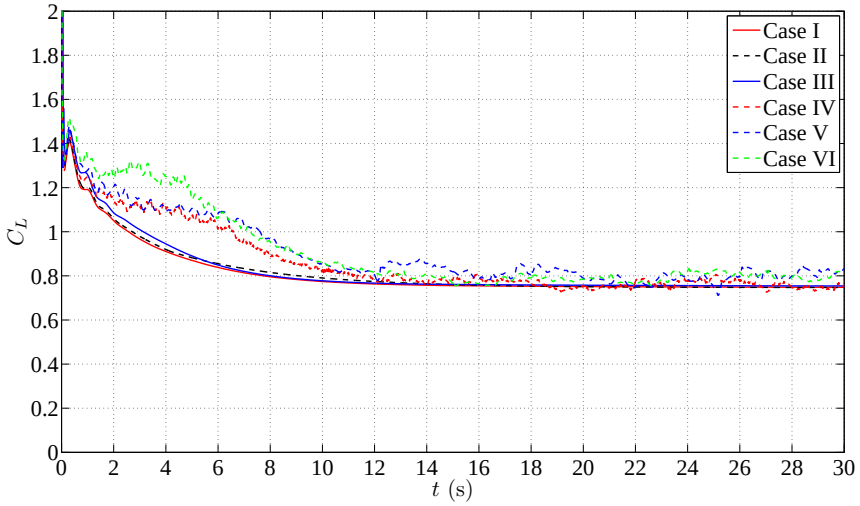

Figure 5.11: CFD predicted lift time-series for a flat plate at $\alpha_z = 45°$ in a 5 m/s stream using different computational grids and turbulence models. A uniform velocity field of 5 m/s in the along wind direction is used as an initial velocity condition at $t = 0$ s.

For Case III with the finer grid, a small recirculation region is observed along the leading and trailing edges which is not present in the coarse grid Case I solution. The results reveals that adequate grid resolution at the plate tips is necessary in order to reproduce the secondary vortices at the side edges that play a role in the onset of vortex shedding.

Despite being able to predict vortex shedding and wake unsteadiness using URANS with a finer near-wall grid, as shown in Figure 5.13(a), the leading edge vortex remains steady and stably attached and as a result only weak force fluctuations associated with shedding of tip and trailing edge vortices are observed. However, this is not the case with the DES simulations.

Unlike the URANS cases (I - III) where steady force predictions are obtained, in all the DES cases (IV - VI) an unsteady wake is observed with aperiodic shedding of tip and trailing edge vortices as well as chaotic instability in the leading edge vortex (Figure 5.13(b)) that is associated with smaller scale turbulent motions. Further refinement of the wake region in case VI allowed for the resolution of smaller scales in the wake but gave no significant improvement in the overall lift force prediction as shown in Figure 5.11.

The findings of these studies reveal that although coarse URANS does not accur-

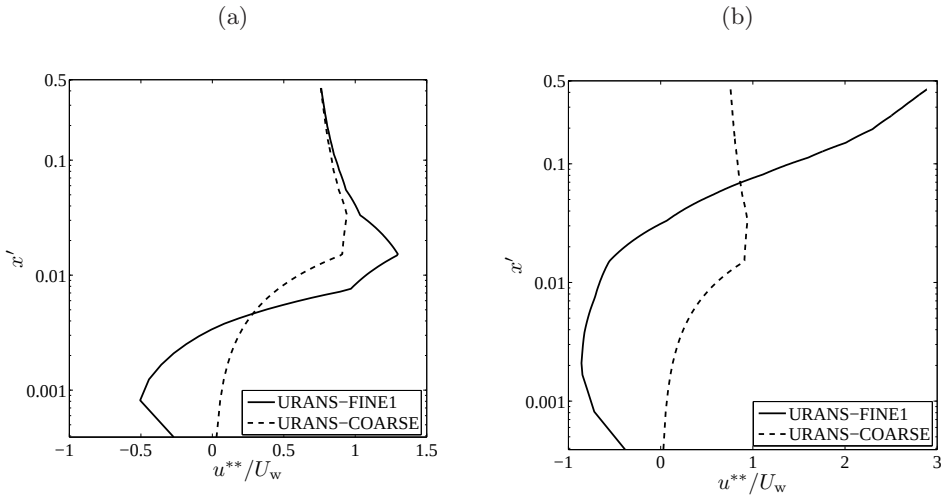

Figure 5.12: Instantaneous profiles of the velocity component parallel to the plate edge, u^{**}, taken along a line normal to the plate edge and at mid-span. x' is the normal distance from (a) the trailing edge face (b) the leading edge face.

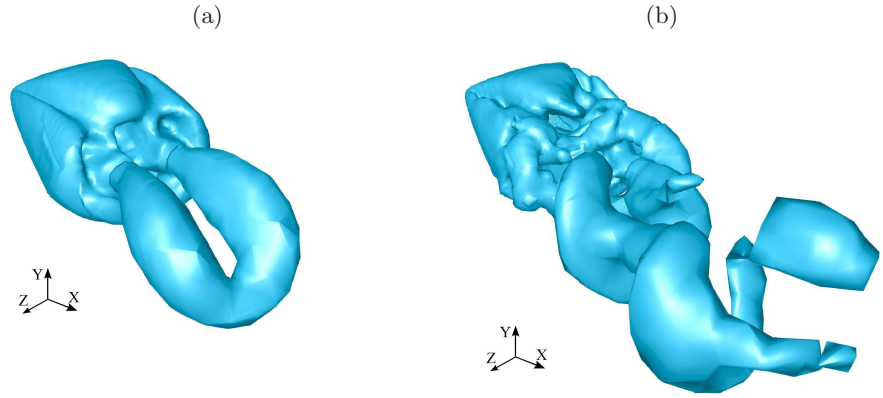

Figure 5.13: Instantaneous iso-surfaces of Q-criterion value, $Q = 10\ \mathrm{s}^{-1}$, showing CFD predicted flow structure in the wake of a static flat plate using (a) URANS and (b) DES to model flow turbulence on the FINE1 mesh.

ately simulate wake unsteadiness and the resulting small scale force fluctuations it gives acceptable values of the mean aerodynamic forces acting on the plate at a low computational cost. Fine grid URANS ($y^+ \approx 1$) simulation results show that the URANS wake behaviour is dependant on the near-wall grid resolution although this has no significant impact on the aerodynamic forces. Even in cases where unsteady wakes are observed, the resulting force fluctuations in URANS simulations are weaker than those shown in DES since the very large leading edge vortex remains steadily attached in all the URANS cases.

DES simulations successfully predicted the small scale wake unsteadiness together with the associated weak aerodynamic force fluctuations. The DES predicted mean force values however show only marginal improvements compares with the URANS predictions and this comes at an increased computational cost for fine-grid DES simulations. Previous experimental studies for low aspect ratio bluff bodies, which are the focus of this study, reveal that the resulting force fluctuations due to small scale wake unsteadiness in these cases are expected to be too weak to cause any significant oscillation (Bearman, 1984). Therefore in the context of windborne debris flight, there is no practical benefit gained from being able to accurately predict these weak force fluctuations arising from the small scale turbulent motion.

Since the computationally low-cost URANS models have been shown to be capable of predicting the mean forces acting on the plate and, as will later be illustrated in the rotational cases, of re-producing the large scale wake unsteadiness when it occurs, these models have been preferred for the rest of the simulations presented in this thesis. Adopting these URANS models allowed for the fairly rapid computation of an accurate solution to the aerodynamic forces acting on a piece of debris. This feature is central to the study of windborne debris flight where several flight simulations would be required to develop a database for debris risk analysis.

Although the numerical error introduced by ignoring the weak small scale force fluctuations is assumed to be acceptable based on previous experimental findings (Bearman, 1984), these experiments were focused largely on static plates. LES studies of plate autorotation are therefore recommended in order to verify this assumption and to further quantify the numerical improvements that are obtainable from using a more computationally intensive LES simulation of the

flow around a rotating plate.

5.3 Simulating Forced Rotation

The CFD model has been used to investigate the aerodynamics of rotating plates, which is central to plate type windborne debris flight behaviour. The computational domain used for the 3D static plate cases and shown in Figure 5.6 is used. The plate is rotated at a constant angular speeds, ω_z, ranging from 0.0873 rad/s to 10.0 rad/s, about the Z-axis, which is a fixed horizontal axis perpendicular to the flow and corresponding to the plate's centroidal axis. In these forced rotation simulations, rotations about the Z-axis are taken to be anti-clockwise positive, according to the right-hand rule as illustrated in Figure 2.1. To achieve plate rotation, the inner spherical grid region containing the plate's wall boundaries is rotated at the prescribed angular speed while keeping the outer region fixed. The two mesh regions are connected using a non-conformal grid interface and the rest of the domain boundary conditions are similar to the 3D static plate setup described in Section 5.2. The Arbitrary Lagrangian-Eulerian formulation of the Navier-Stokes equations, described in Section B, is solved to obtain the unsteady velocity and pressure flow field around the rotating plate. Aerodynamic forces acting on the plate are also computed from wall pressure and skin friction values. In all the simulations, a uniform inflow speed of $U_{\mathrm{w}} = 5$ m/s is used with low turbulence intensity and length scale values similar to the static plate 3D cases. The Realisable $k-\varepsilon$ turbulence model is used with a two-layer near wall spacing and the coarse grid containing approximately 290,000 computational cells.

Table 5.7 summarises the key results for all the forced rotation simulations performed. The "avg" subscript denotes a time-averaged force coefficient while the "rms" subscript denotes the root mean square (RMS). Figure 5.14 shows force and torque coefficients, plotted against non-dimensionalised time $\bar{t} = t/T_o$, where $T_o = 2\pi/\omega$, for different rotational speeds. The mean and peak aerodynamic force coefficients are shown to vary with non-dimensionalised rotational speed, $\bar{\omega} = \omega L/U$. As clearly illustrated in Figure 5.15, the mean and RMS of aerodynamic drag have an inverse exponential relationship with rotational speed, up to $\overline{\omega} \approx 1.0$, beyond which further increase in rotational speed has no significant effect. The mean and RMS aerodynamic lift show a power law relationship with rotational speed, while the aerodynamic torque shows a complex

Table 5.7: A summary of forced rotation simulations and the resulting aerodynamic forces.

Case No	I	II	III	IV	V	VI	VII	VIII	IX
ω (rad/s)	0.087	0.175	0.349	0.698	1.396	2.793	5.0	5.236	10.0
$\overline{\omega} = \frac{\omega L}{U_\infty}$	0.018	0.035	0.07	0.14	0.28	0.559	1.0	1.047	2.0
$(C_D)_{\text{avg}}$	0.771	0.789	0.865	0.970	1.096	1.258	1.331	1.329	1.357
$(C_D)_{\text{rms}}$	0.891	0.936	1.054	1.211	1.392	1.607	1.759	1.765	1.808
$(C_L)_{\text{avg}}$	-0.123	-0.165	-0.227	-0.278	-0.373	-0.473	-0.627	-0.640	-0.747
$(C_L)_{\text{rms}}$	0.632	0.661	0.713	0.778	0.867	1.011	1.093	1.100	1.240
$(C_M)_{\text{avg}}$	0.012	0.016	0.023	0.030	0.041	0.023	-0.036	-0.044	-0.226
$(C_M)_{\text{rms}}$	0.080	0.087	0.101	0.120	0.125	0.130	0.130	0.131	0.295

exponential-power law relationship.

Based on these results, appropriate fit expressions for mean and RMS of the aerodynamic coefficients have been derived for $0 \leq |\overline{\omega}| \leq 2.0$ as,

$$(C_D)_{\text{avg}} = c - a\exp(-bx), \text{RMSE} = 8 \times 10^{-3}, \tag{5.8}$$

where $a = 0.6211, b = 3.27$ and $c = 1.354$,

$$(C_D)_{\text{rms}} = c - a\exp(-bx), \text{RMSE} = 1.82 \times 10^{-2}, \tag{5.9}$$

where $a = 0.9472, b = 3.049$ and $c = 1.802$,

$$(C_L)_{\text{avg}} = ax^b + c;, \text{RMSE} = 1.98 \times 10^{-2}, \tag{5.10}$$

where $a = -0.6723, b = 0.3164$ and $c = 0.06843$,

$$(C_L)_{\text{rms}} = ax^b + c;, \text{RMSE} = 1.52 \times 10^{-2}, \tag{5.11}$$

where $a = 0.6644, b = 0.3055$ and $c = 0.4266$,

$$(C_M)_{\text{avg}} = a\exp(-bx) + c\exp(-dx) + ex^f, \text{RMSE} = 5.24 \times 10^{-3}, \tag{5.12}$$

where $a = -4.831, b = 2.85, c = 4.837, d = 2.779, e = -0.06257$ and $f = 1.86$,

$$(C_M)_{\text{rms}} = a\exp^{(bx)} + c\exp^{(dx)} + e\exp^{(fx)} + gx^h, \text{RMSE} = 2.24 \times 10^{-2}, \tag{5.13}$$

where $a = 6.929, b = 0.3161, c = -6.63, d = -0.611, e = -0.2188, f = -11.13, g = -5.781$ and $h = 0.8997$.

(a)

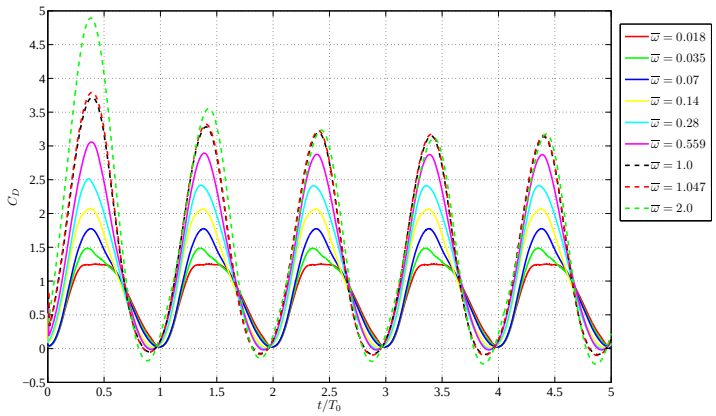

(b)

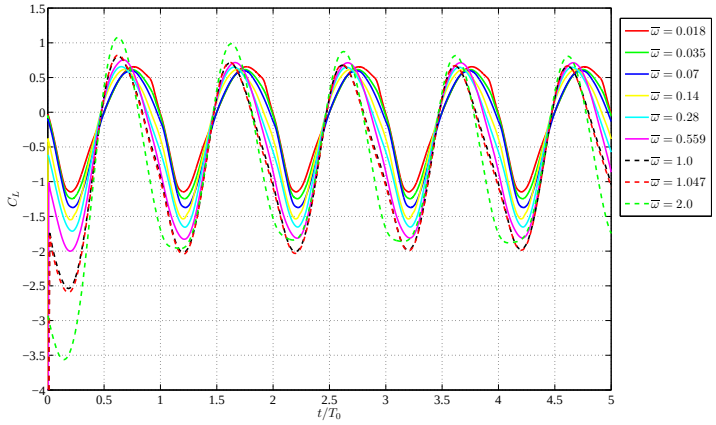

(c)

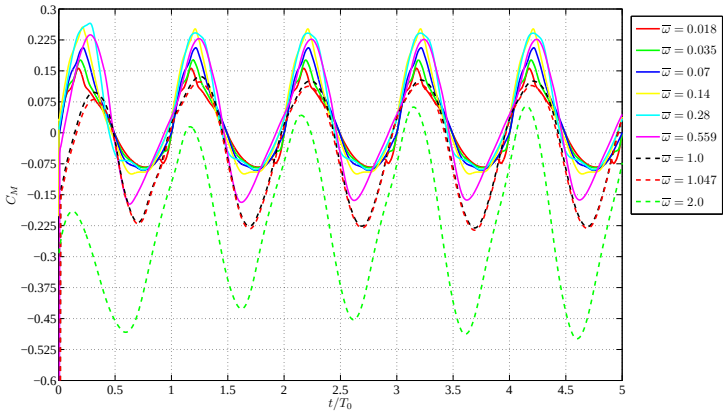

Figure 5.14: (a) Drag, (b) lift and (c) torque coefficients for a 1 m square flat plate rotating at various constant speeds in a uniform wind stream of 5 m/s.

(a)

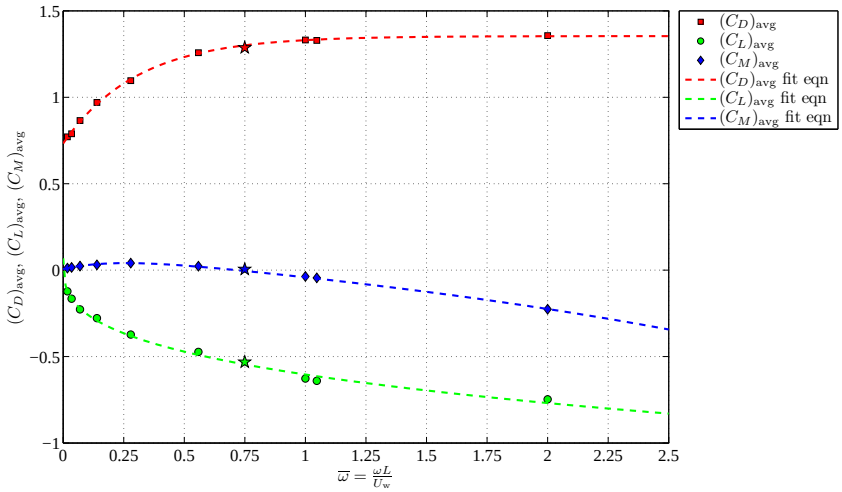

(b)

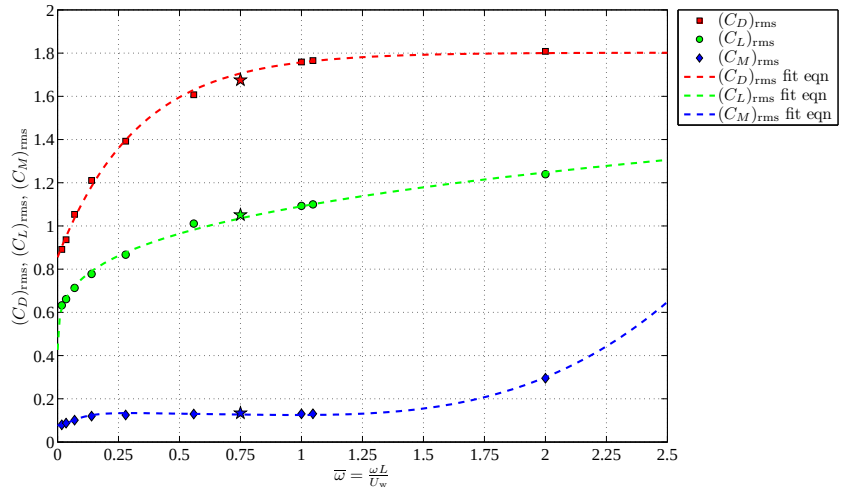

Figure 5.15: CFD predictions and data fit expressions for (a) Mean, and (b) RMS of drag, lift and moment coefficients of a rotating plate as a function of rotational speed. The (★) points indicate mean and RMS results for a forced rotations simulations performed at the plate's expected mean autorotational speed, $\overline{\omega} = 0.75$.

These fit expressions would be useful for quasi-steady force predictions in analytical models of windborne debris flight. The fluctuations of aerodynamic force about the mean are shown to be significantly different to those of static plates and dependant on the rotational speed. The direct implication of this finding is that the quasi-steady force assumption made by Tachikawa (1983) and expressed in (2.19) is incorrect. Existing quasi-steady models for windborne debris flight can therefore be improved by incorporating the expressions for aerodynamic force fluctuations presented.

Based on the results of the simulations, three distinct types of motion may be derived depending on rotational speed: *pre-autorotational* with $\bar{\omega} < 0.75$, *autorotational* with $\bar{\omega} \approx 0.75$ and *post-autorotational* with $\bar{\omega} > 0.75$. In the pre-autorotational cases, the aerodynamic torque acting on the plate is positive and supporting plate rotation creating an accelerating effect, while in the post-autorotational cases the aerodynamic torque is negative and opposes plate rotation resulting in an aerodynamic damping effect. The point of stable autorotational motion is the point at which the mean aerodynamic torque acting on the plate is zero and the predicted value of $\bar{\omega} \approx 0.75$ is noted to be consistent with empirical predictions represented by Iversen (1979) in expressions (2.7) - (2.9).

During debris flight, where no external driving torque is present, plates are expected to fly at this stable auto-rotational speed, with strong aerodynamic damping limiting the plate's rotational speed beyond this point. As a result of this aerodynamic damping effect, very large rotational speeds $|\overline{\omega}| \gg 1.0$ are not expected in free-flying plates. None-the-less, since these fit expressions have not been investigated in the asymptotic limit, caution should be taken in applying them in cases with $|\overline{\omega}| > 2.0$.

The following section discusses some of the key findings with regards to the flow structures around rotating flat plates in different modes of motion, in order to better understand the mechanisms creating the aerodynamic acceleration and damping that make stable autorotation possible.

5.3.1 Flow Around Rotating Plates

As previously discussed in Section 2.3.2.1, the nature and origins of the aerodynamic damping effect present in plate autorotation have been attributed to

the complex interaction between a rotating plate and the flow structures in its wake. This FSI phenomena has so far not been fully understood. Based on the flow predictions from URANS CFD simulations of rotating plates, an analysis of the evolution of flow structures in the wake of a rotating plates is presented and used to identify the source of the aerodynamic acceleration and damping effects.

To achieve this, a comparison is made of the flow around plates in the pre-autorotational and post-autorotational range, while the flow around autorotating plates is itself discussed later in Section 5.5. The behaviour of plate with speeds in the pre-autorotational range is illustrated by results of the $\overline{\omega} = 0.28$ case, while for the plates with speeds in the post-autorotational range, results of $\overline{\omega} = 1.0$ and $\overline{\omega} = 2.0$ are presented.

Contours of Q-value on a vertical plane through the centre of the plate are used to identify the coherent structures in the flow and their time evolution. These contours are taken at 10° intervals of instantaneous angles of attack in a typical 180° cycle and are presented in Figures 5.16 - 5.18 for the pre-autorotational speeds and Figures 5.19 - 5.21 for the post-autorotational speeds.

The main flow structures in the wake of the flow are hair-pin vortices shed from the leading and trailing edges as the result of an interaction between the tip vortices and the leading and trailing edge vortices similar to observations in static plate cases. In both the pre- and post-autorotational cases, vortex shedding is dependant on the rotational frequency of the plate with two hair-pin vortices shed in a complete 180° cycle. For purposes of clarity, it is important to note that in a rotating plate, the leading and trailing edges may either be advancing towards the oncoming flow or retreating towards the wake at different points in the rotational cycle. A distinction has therefore be made between, what is referred to as the retreating leading edge and the advancing leading edge, as well as between the retreating and advancing trailing edges, all of which represent different key stages in the rotation of the plate.

For the pre-autorotational case, $\overline{\omega} = 0.28$, at $\alpha_z \approx 0°$ (Figure 5.16(a)) the leading edge is retreating while the trailing edge is advancing. The flow around the plate is streamlined at these very low angles of attack, with no coherent vortex structures attached to the plate. At these very low angles of attack, the mean and RMS of aerodynamic forces have been found to exhibit a weak

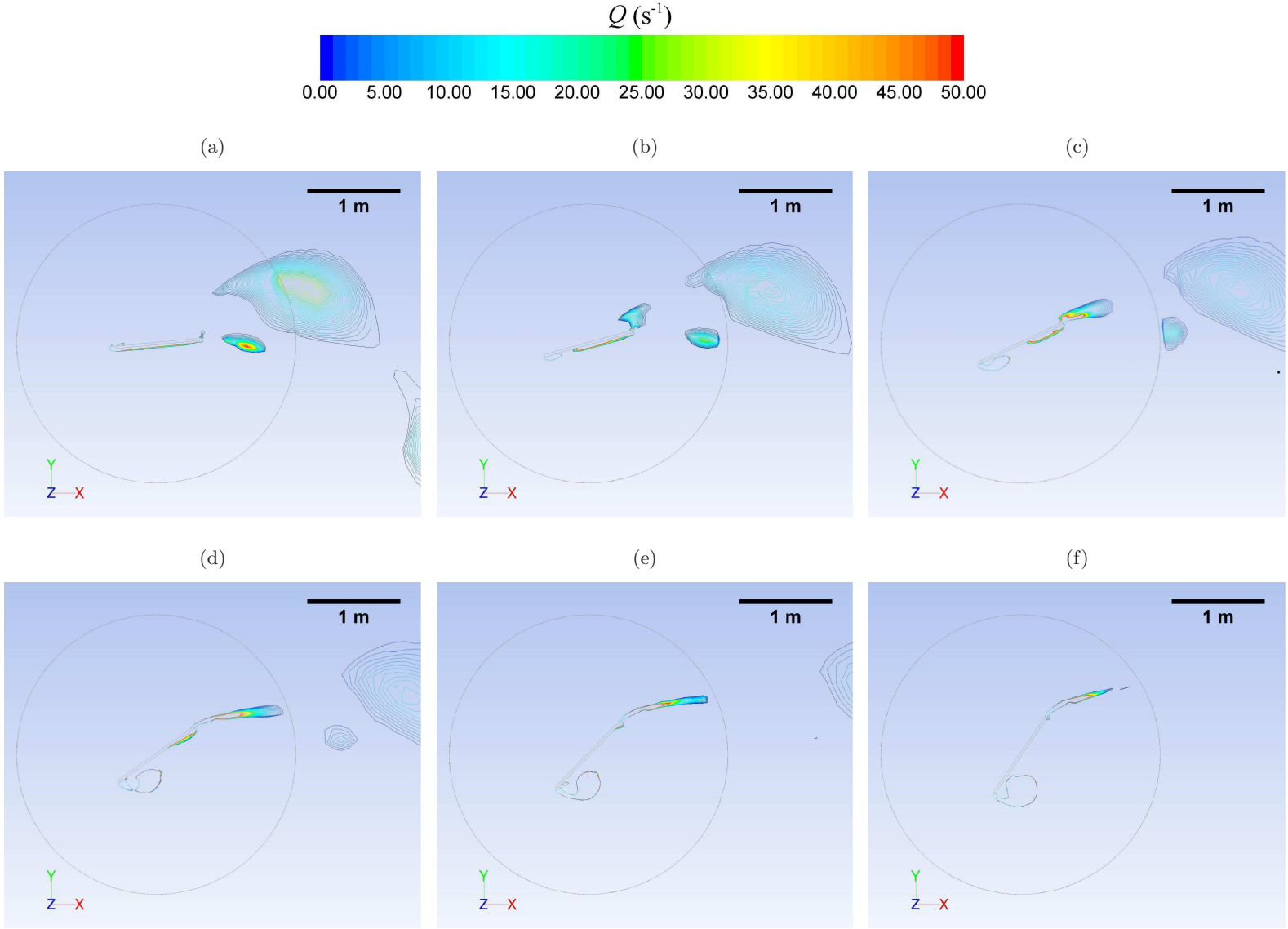

Figure 5.16: Q-value contours on a vertical plane through the centre of a pre-autorotating plate of dimensionless rotational speed $\overline{\omega} = 0.28$. Contours are taken at instantaneous angles of attack of (a) 0°, (b) -20° and (c) -40°.

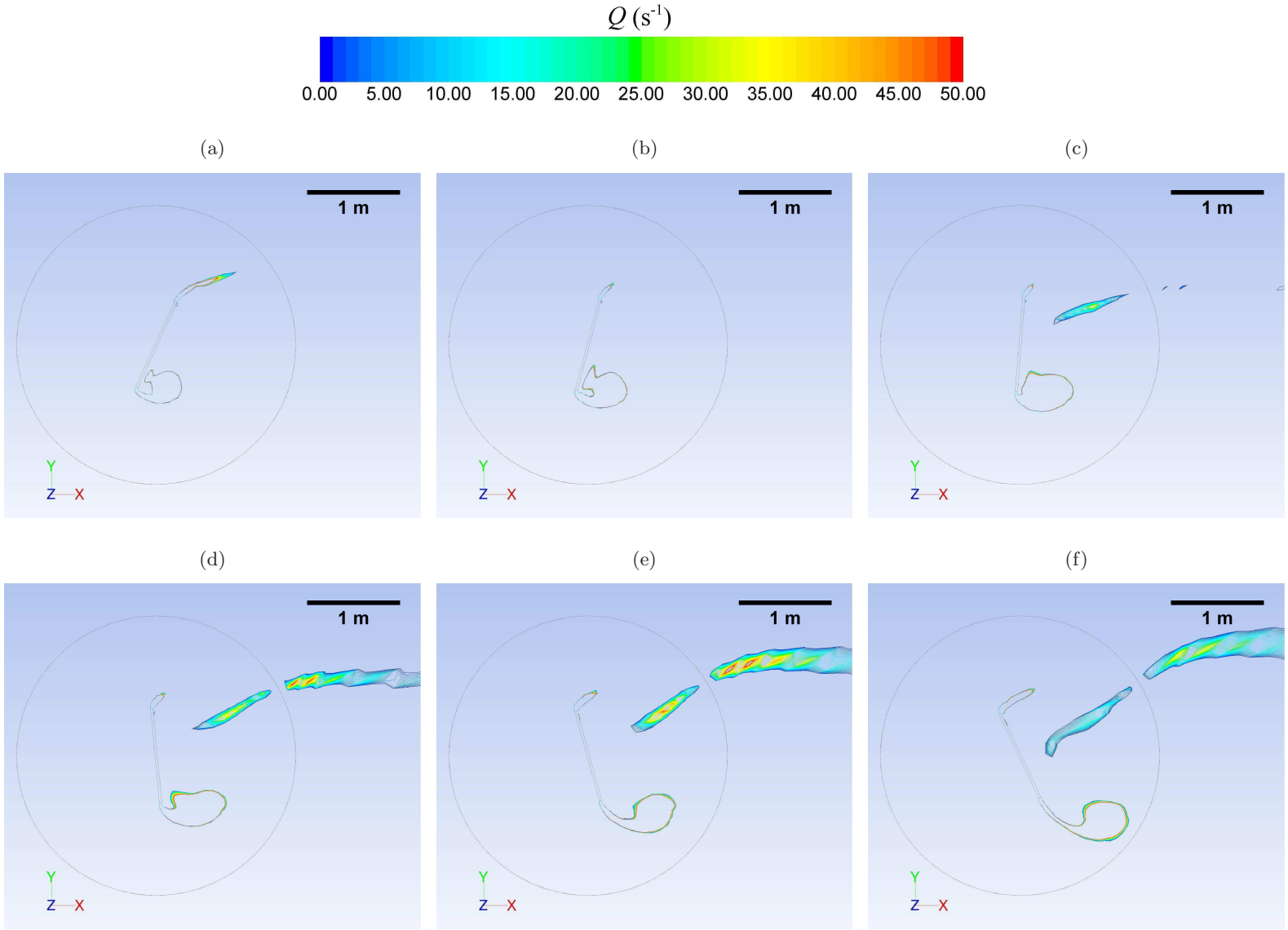

Figure 5.17: Q-value contours on a vertical plane through the centre of a pre-autorotating plate of dimensionless rotational speed $\overline{\omega} = 0.28$. Contours are taken at instantaneous angles of attack of (a) -60°, (b) -80° and (c) -100°.

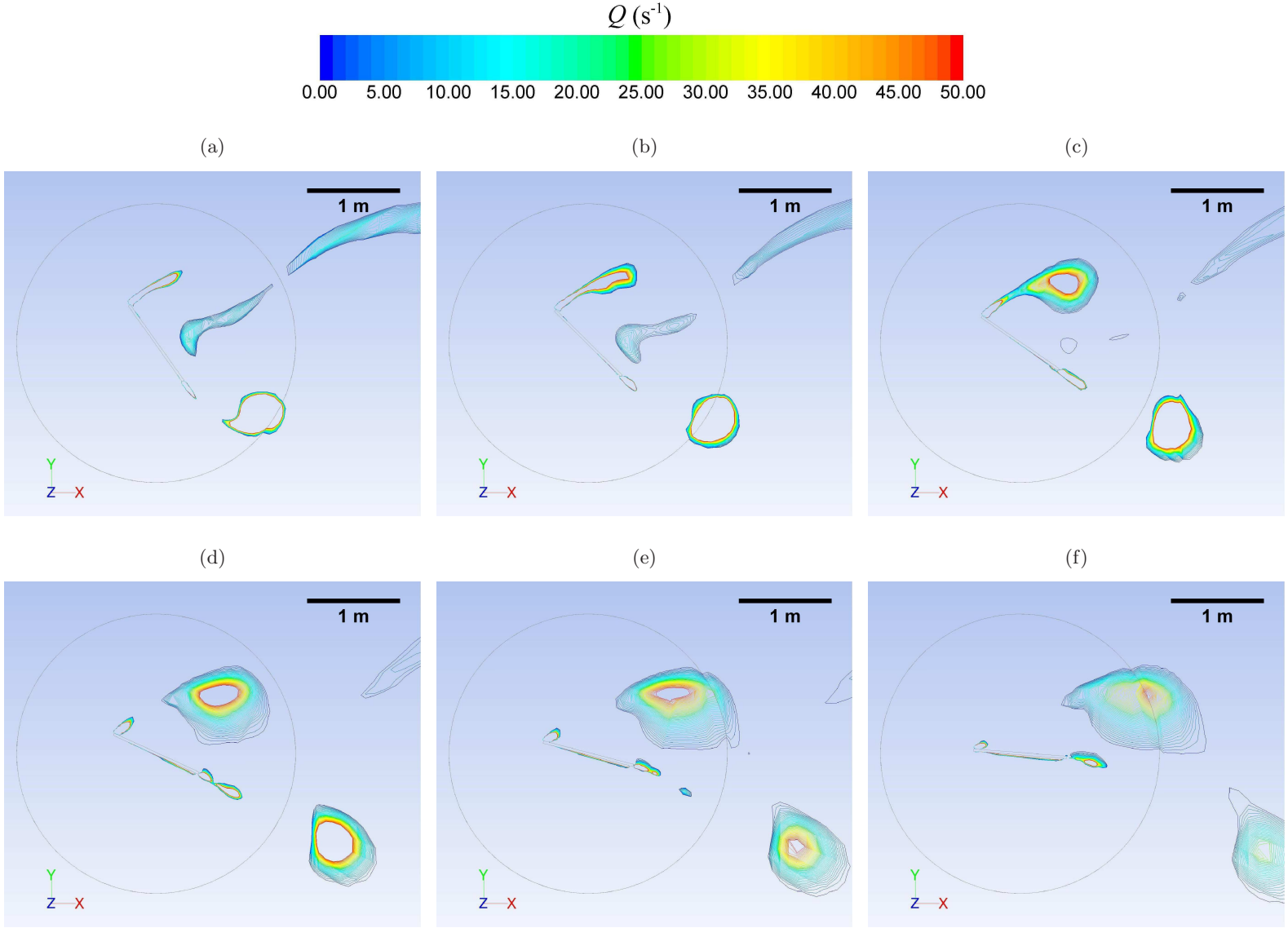

Figure 5.18: Q-value contours on a vertical plane through the centre of a pre-autorotating plate of dimensionless rotational speed $\overline{\omega} = 0.28$. Contours are taken at instantaneous angles of attack of (a) -120°, (b) -140° and (c) -160°.

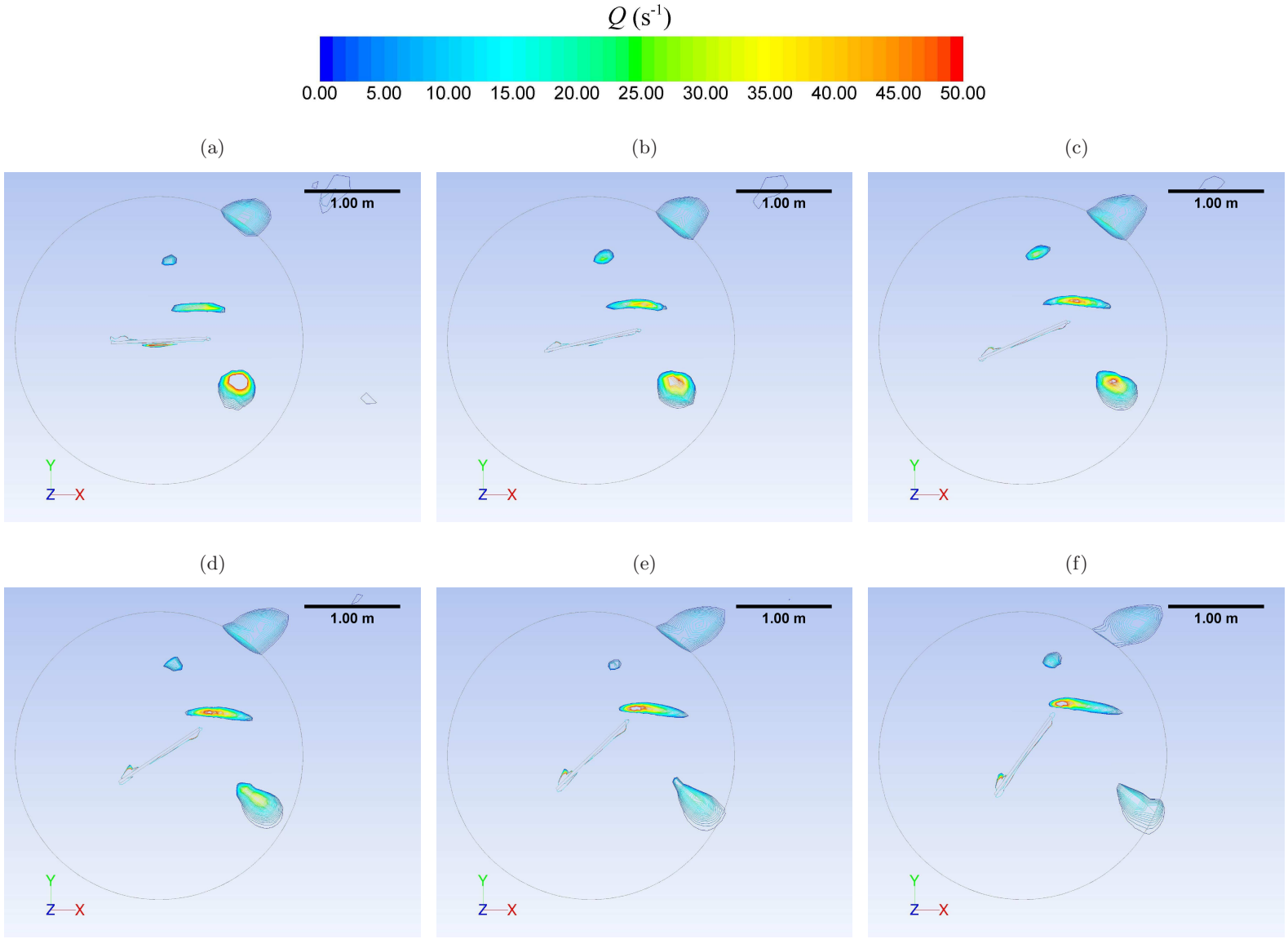

Figure 5.19: Q-value contours on a vertical plane through the centre of a post-autorotating plate of dimensionless rotational speed $\overline{\omega} = 2.0$. Contours are taken at instantaneous angles of attack of (a) 0°, (b) -20° and (c) -40°.

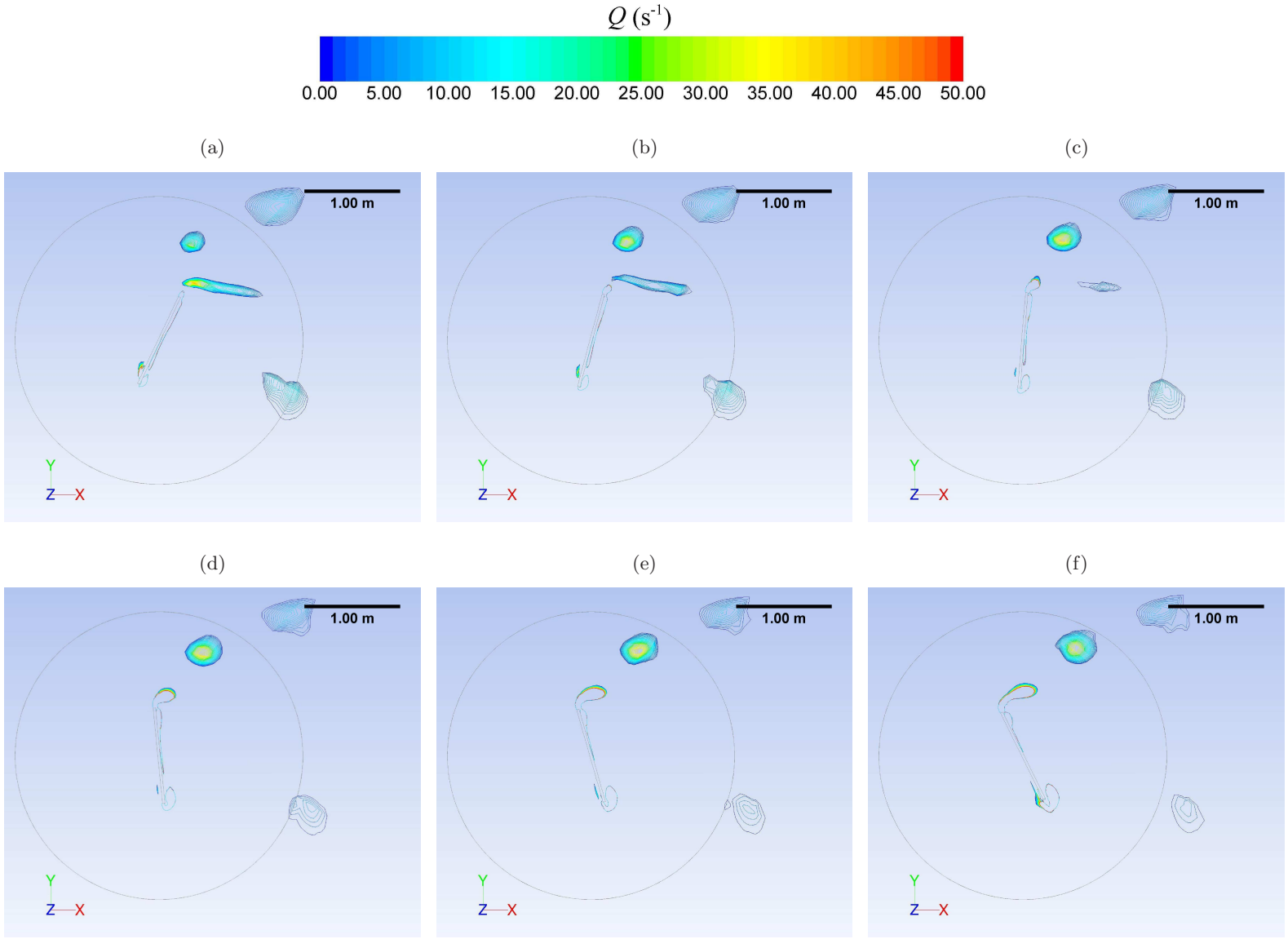

Figure 5.20: Q-value contours on a vertical plane through the centre of a post-autorotating plate of dimensionless rotational speed $\overline{\omega} = 2.0$. Contours are taken at instantaneous angles of attack of (a) -60°, (b) -80° and (c) -100°.

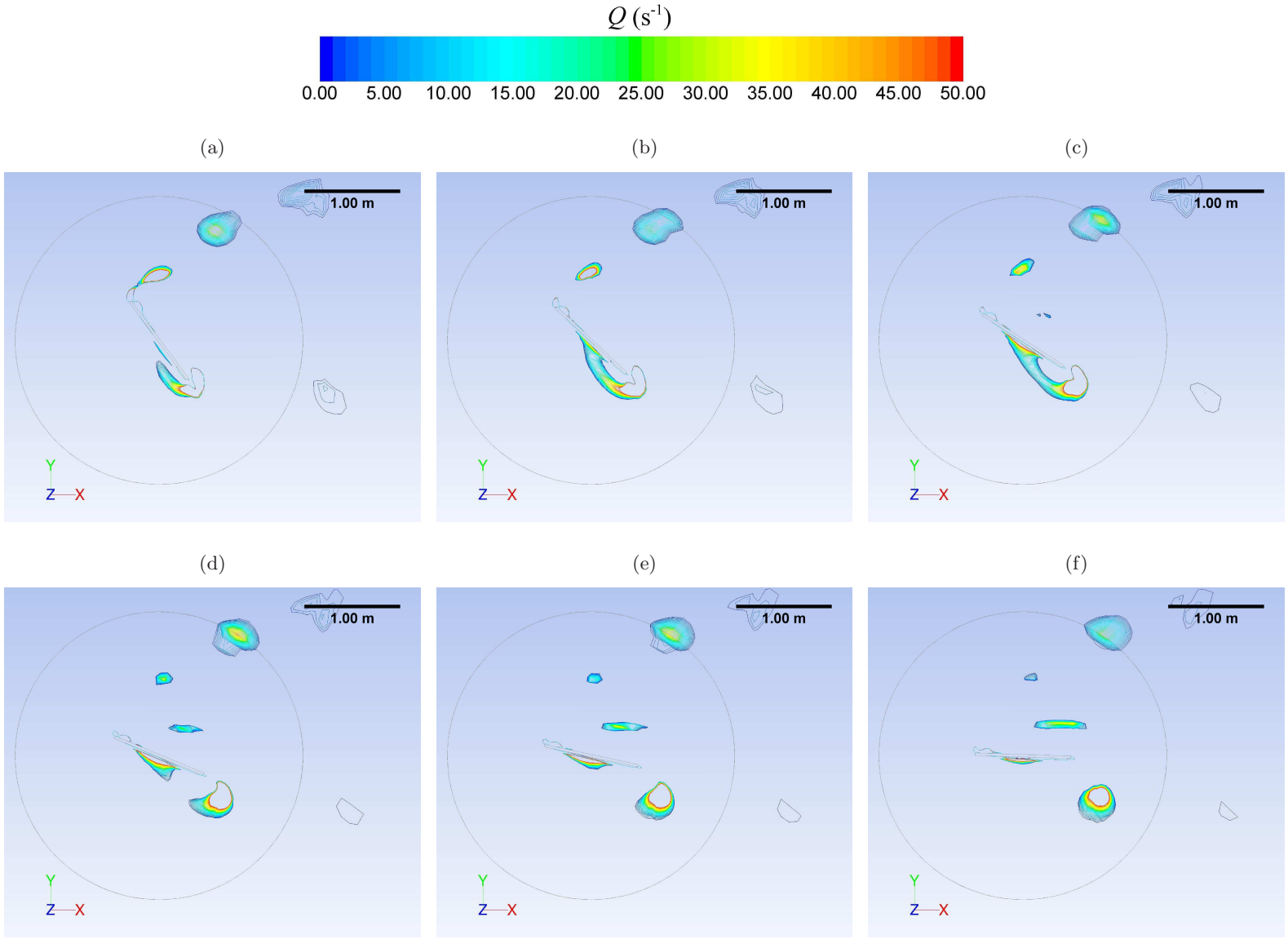

Figure 5.21: Q-value contours on a vertical plane through the centre of a post-autorotating plate of dimensionless rotational speed $\overline{\omega} = 2.0$. Contours are taken at instantaneous angles of attack of (a) -120°, (b) -140° and (c) -160°.

sensitivity to rotational speed. As the angle of attack increases (in the negative sense due to anti-clockwise rotations), a leading edge vortex begins to form at the retreating leading edge as illustrated by the high Q-value at this edge in Figures 5.16(b) - 5.17(a). A vortex sheet also forms at the advancing trailing edge and is visible at the top edge in Figures 5.16 - 5.18. Large tip vortices, which increase in size with increasing angle of attack, also form at the plate's side edges and these are illustrated using helicity iso-surfaces shown in Figure 5.22 for $\alpha_z \approx 90°$. These large tip vortices manifest as long vorticity streaks on the mid-plane at higher angles of attack as seen in Figures 5.17(b) - 5.18(a).

The vortex at the retreating leading edge (bottom edge of Figures 5.16 - 5.18) remains stably attached for the first part of the cycle and grows in size, with increasing angle of attack up to the $\alpha_z \approx -90°$ position where it is shed into the wake, interacting with the tip vortices from the side edges of the plate to form a hair-pin vortex. The negative pressure associated with the core of this stably attached leading edge vortex is responsible for the net positive aerodynamic torque experienced by plates with pre-autorotational speed. Figure 5.23 illustrates the pressure field around the pre-autorotating plate at approximately $0°$ and $-30°$ angles of attack.

At $\alpha_z \approx -90°$, the plate is normal to the flow with no leading or trailing edge. Beyond this point, what was previously the advancing trailing edge becomes the advancing leading edge and a vortex sheet at this edge begins to curl-up into a leading edge vortex at the advancing edge (Figure 5.19(c)). Unlike the retreating leading edge vortex, this advancing leading edge vortex is not stably attached to the plate and is quickly shed into the wake to form a second hair-pin vortex. Similar flow structures are observed for the post-autorotational plates as shown in Figures 5.19 - 5.21 for a plate rotating at $\overline{\omega} = 2.0$. However, there are a number of key differences. Firstly, while a phase-lag of $\approx 40°$ exists between the shedding of the retreating edge vortex and the shedding of the advancing edge vortex in pre-autorotational cases, the two vortices are shed almost simultaneously in the post-autorotational cases. In addition, the formation of the stably attached retreating edge vortex commences at a much higher angle of attack in post-autorotational cases, and remains attached over a shorter range of angles. The strength of the swirling flow associated with this retreating edge vortex is also lower than in pre-autorotational cases, possibly due to the lower relative wind

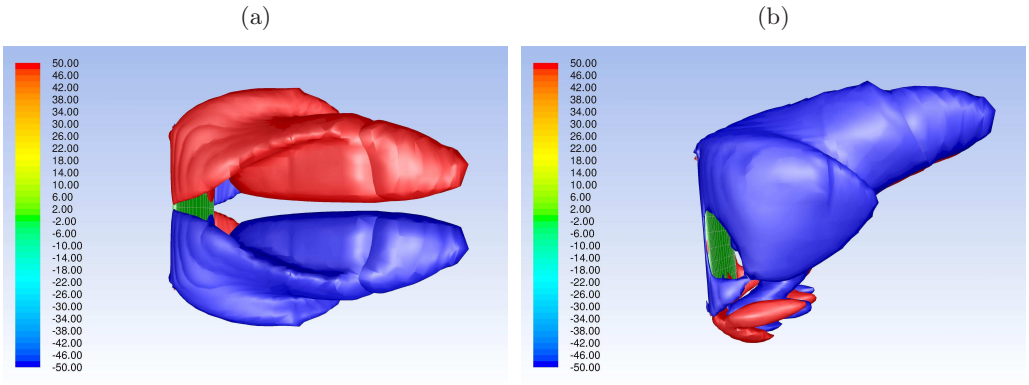

Figure 5.22: Iso-surfaces of positive and negative helicity showing the two counter-rotating tip vortices as regions of high helicity near the advancing edge for a plate rotating with $\overline{\omega} = 0.28$. (a) Plan view and (b) side view.

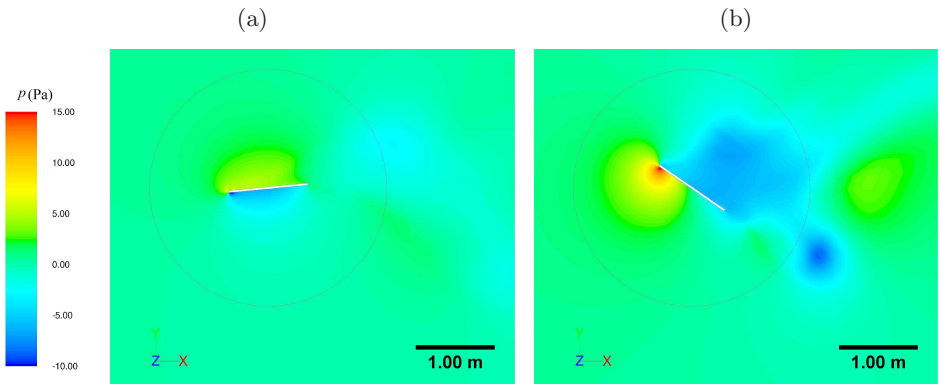

Figure 5.23: CFD predicted pressure field around a rotating plate with $\overline{\omega} = 0.28$ at (a) $\alpha_z \approx 0°$, and (b) $\alpha_z \approx 30°$.

speed between the plate's retreating edge and the mean flow. Conversely, the strength of the advancing edge vortex would be higher for larger plate rotational speeds due to a higher relative wind speed. All these factors would result in a lower magnitude of aerodynamic accelerating torque in post-autorotating plates. The second critical difference between the two modes of motion is that while in pre-autorotational cases, the tip vortices are only present in the wake face of the plate, concentrated near the advancing edge (Figure 5.22), in the post-autorotational cases, two additional tip vortices exist at the front of the plate, concentrated at the retreating edge as shown in Figure 5.24. These tip vortices have a complex interaction with the retreating edge vortex that is shed, forming a large hair-pin vortex attached to the plate. As a result, large negative pressures are observed at the front of the plate, concentrated near the retreating edge as shown in Figure 5.25. It is these negative pressures associated with the hair-pin vortex attached to the front of the plate that creates the large negative torque associated with aerodynamic damping at post-autorotational speeds.

The merging of the shed retreating edge vortex with the tip vortices at the front face in post-autorotational cases is partly facilitated by the slower advection of the shed retreating edge vortex away from the plate tip, as shown Figure 5.19(c), which is the result of a low relative wind speed between the plate tip and the mean free-stream flow. In the case of post-autorotational plates with $\overline{\omega} = 2.0$, at the $\alpha_z \approx 90^\circ$ position, a relative wind speed $(U_\mathrm{w} - \omega L/2)$ of approximately zero would be expected meaning that the shed vortices would be almost stationary relative to the plate-tip resulting into a strong interaction with the front face of the plate.

Based on these findings, it may be concluded that the aerodynamic behaviour of rotating plates is strongly dependant on the interaction of the plate with the flow-structures in its wake. This interaction creates regions of accelerating and decelerating aerodynamic torque as well as a stable point of autorotation at which plates would be expected to autorotate if there were no external torque. The findings are therefore similar to observations by Riabouchinsky (1935) for a Lancaster propeller's autorotation parallel to the flow (Section 2.3.1). The results are expected to be dependant on aspect ratio, with high aspect ratio plates which have less prominent tip vortices exhibiting different behaviour from the square plates considered in this study. Additional studies to assess the sensit-

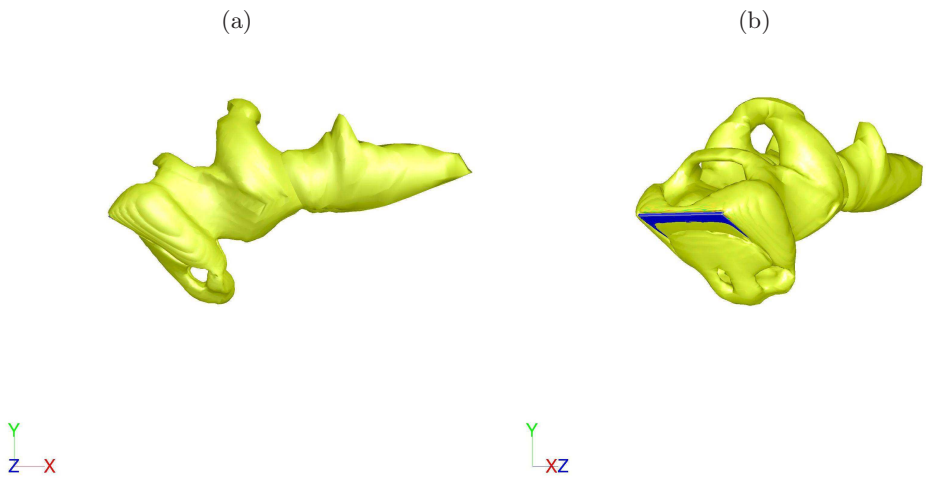

Figure 5.24: Iso-surfaces of $Q = 10$ showing showing flow structures in the wake and at the front face, near the retreating trailing edge, of a post-autorotational plate with $\overline{\omega} = 2.0$. (a) Side view and (b) Isometric view.

ivity of the coherent flow structures observed to turbulence modelling approach are also recommended.

5.4 Flat Plate Autorotation Model

A theoretical background of plate autorotation has already been presented in Section 2.3 along with a discussion of previous work on CFD modelling of plate autorotation in Section 2.3.3. This section describes the CFD-RBD model used for the simulation of 3D low aspect ratio plate autorotation as part of this research. The CFD-RBD coupling approach is described followed by a description of sub-models for additional phenomena such as bearing friction and mass eccentricity which played an important role in the experimental setup. The model is subsequently applied to simulate fixed-axis autorotation in Section 5.5, as well as the more general free-axis autorotation in Section 5.6.

5.4.1 CFD-RBD Coupling

In order to simulate plate autorotation, the 3D CFD model previously described has been sequentially coupled with the 6DOF rigid body dynamics model described in Section 4. Figure 5.26 illustrates the two-way sequential coupling approach used. ANSYS FLUENT (FLUENT Inc., 2009) is used as the 3D URANS solver while the RBD model is implemented as a user-defined-function code

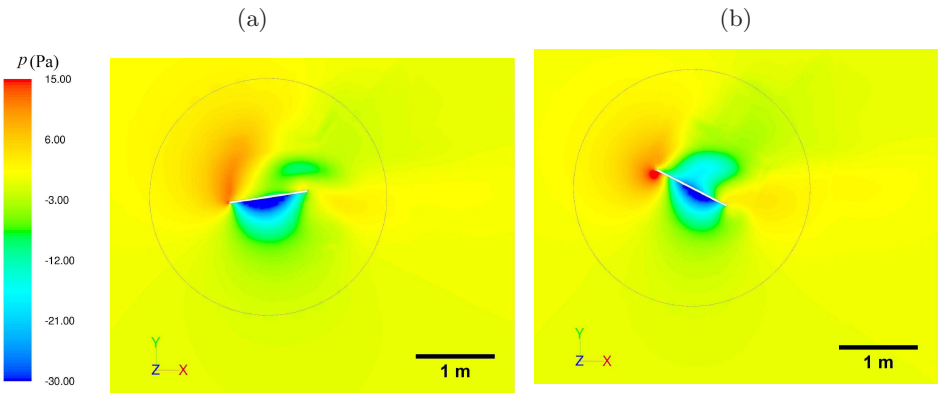

Figure 5.25: CFD predicted pressure field at the centre plane of a rotating plate with $\overline{\omega} = 2.0$ at instantaneous angles of attack of (a) $\alpha_z \approx 0°$, and (b) $\alpha_z \approx 30°$.

written in the C programming language.

For fixed axis autorotation cases, the 6DOF model is reduced to a 1DOF model by constraining motion of the plate in all three translational degrees of freedom and two rotational degrees of freedom. Similarly, for free-axis autorotation only the three translational degrees of freedom are constrained, resulting in a three rotational degrees of freedom system.

Aerodynamic forces acting on the plate are computed from the face pressure and skin friction from the CFD solution and used to compute the aerodynamic torque about the plate's geometric centre. The computed translational and rotational speeds of the mesh are then used to specify the instantaneous mesh velocity in the CFD model. This two-way coupling allows for an accurate representation of the non-linear FSI involved in plate autorotation and free-flight.

5.4.2 Additional Sub-models

5.4.2.1 Mass-Eccentricity

The term "mass eccentricity" is used to refer to the offset of the plate's centre of mass from the geometric centre of the plate. In most practical configurations, the axis of rotation corresponding to the plate's geometric centre-line does not run through the plate's centre of mass, generating an additional torque. A mass eccentricity model is incorporated in order to account for the effects of this additional eccentricity torque on the rotational motion of the plate.

Assuming a mass eccentricity error, e, during autorotation the plate would experience an additional torque, T_e, about its geometric centre line given by

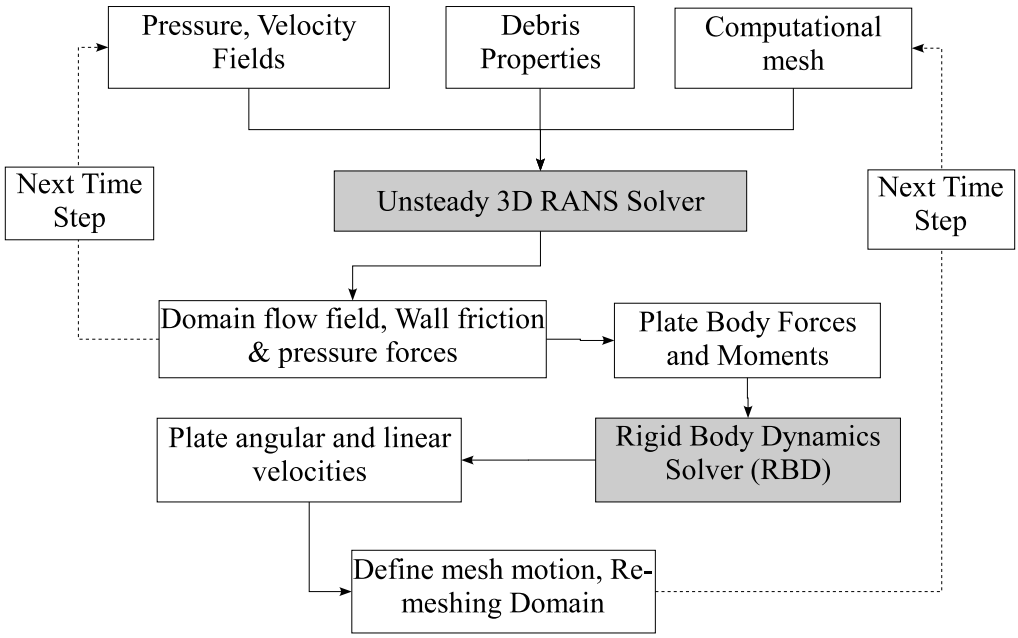

Figure 5.26: A schematic of the CFD-RBD sequential coupling algorithm.

$$T_e = mge \sin \phi, \tag{5.14}$$

where m is the mass of the plate, g is gravitational acceleration, and ϕ is the angular rotation of the plate about the Z-axis. In addition, using the parallel-axis theory, the mass moment of inertia of the ideal plate, I_{zz}, would be corrected according to

$$I^*_{zz} = I_{zz} + me^2, \tag{5.15}$$

where I^*_{zz} is the corrected mass moment of inertia of the plate about the rotation axis.

The model used in this thesis is constructed based on an assumption that in the experimental setup of the plate, small errors of up to 5% of the plate's length may occur while positioning the plate's centre of mass. Such errors would be expected due to the complexity of the data acquisition and plate mounting and support system used (Martinez-Vazquez et al., 2010). For a valid comparison of experimental and CFD-RBD results to be made, the effect of these errors would have to be allowed for. However, as the exact value of the eccentricity is

Figure 5.27: Roller bearing unit added to the experimental plate support frame to reduce bearing friction during autorotation (Martinez-Vazquez et al., 2010).

not known, a calibration approach has been adopted and is described in Section 5.5.3.3.

5.4.2.2 Bearing Friction

Previous experimental studies of plate autorotation (Iversen, 1979; Martinez-Vazquez et al., 2010) have indicated a significant contribution of bearing friction to the autorotational results. A bearing friction sub-model was therefore included in the RBD code to account for the contribution of bearing friction to the total torque.

A friction torque, T_{fric} is included in addition to the aerodynamic torque computed from the CFD model and the mass eccentricity torque. Roller bearings were considered, although the experimental bearing system as shown in Figure 5.27 is more accurately described as a lubricated steel on steel bearing connection.

The friction torque due to each bearing is then computed as

$$T_{\text{fric}} = \left(\frac{-\omega}{\mid \omega \mid}\right)(0.5\mu_r d)\sqrt{(mg - L)^2 + D^2}, \tag{5.16}$$

where mg is the weight of the plate, L is the aerodynamic lift force, D is the aerodynamic drag force, ω is the rotational speed about the axis of rotation, d is the bore diameter of the bearing block which is approximately 0.025 m, and μ_r is the rolling friction coefficient of the bearing block. The friction torque

Table 5.8: Bearing friction coefficients for various types of bearings (SKF, 2010).

Bearing Type	Coefficient of Friction
Deep groove ball bearings	1.5×10^{-3}
Cylindrical roller bearings	1.1×10^{-3} to 2.0×10^{-3}
Needle roller bearings	2.5×10^{-3}
Steel on Steel roller connection	5.0×10^{-3}

is pre-multiplied by $(\frac{-\omega}{|\omega|})$ so as to ensure that it always acts in the direction opposite to the plate's instantaneous direction of rotation. The bearing friction coefficients were estimated from a bearing manufacturer catalogue (SKF, 2010), which gives values for different roller bearing types as shown in Table 5.8.

5.5 Simulating Fixed-axis Autorotation

In the fixed-axis autorotation model, a square flat plate of mass (M) 2.7 kg, side length (L) 1 m and 0.025 m thickness (h) is used, with initial angles of attack ranging from 10° to 15°. Three main autorotation cases have been run with mean wind speeds, U_{w}, of 5 m/s, 7.5 m/s and 10.0 m/s.

Two different computational domain set-ups have been considered. The first is a control set-up referred to as the "cuboid" domain, which uses the symmetric computational grid and boundary conditions described in Figure 5.6 for the static 3D cases. In simulations using this domain, no mass eccentricity or bearing friction models are used.

The second computational set-up shown in Figure 5.28 is referred to as the "Auckland" domain and corresponds to the experimental set-up by Martinez-Vazquez et al. (2010) in the open section wind tunnel at the University of Auckland. Results from this computational domain were used in the CFD-RBD validation.

The Auckland domain inlet is modelled as a constant velocity boundary while the outlets were modelled as constant pressure boundaries. At the inlet, 1% turbulence intensity and 0.02 m turbulence length scale are specified, corresponding to typical low turbulence wind tunnel values from ESDU (1970). Altogether three outlet boundaries are defined, corresponding to both side walls and the far section of the top boundary. The inlet is a $3.5L$ square section while the test

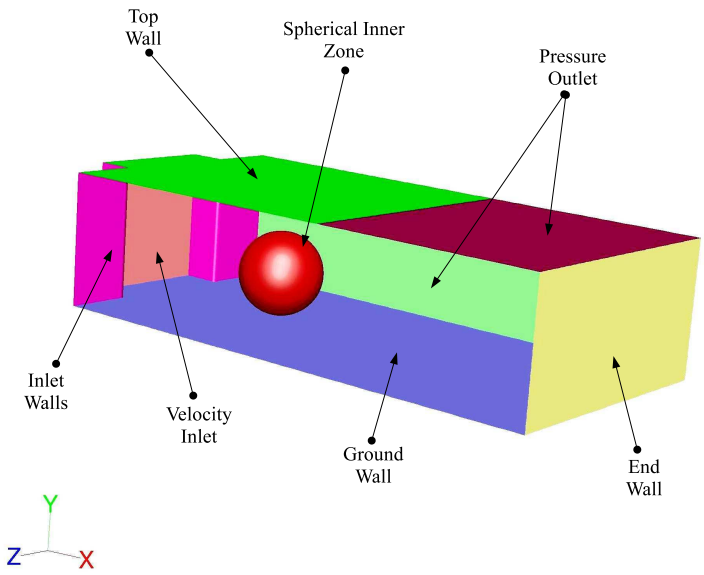

Figure 5.28: New CFD computational domain intended to reproduce experimental setup in experiments by Martinez-Vazquez et al. (2010).

section is $15L \times 7L \times 3.5L$. The plate's axis of rotation is $5L$ from the inlet and $1.2L$ from the bottom wall. The top wall stretched for $8L$ from the inlet before giving way to the top outflow boundary.

As in the Cuboid domain, the Auckland domain is split into two mesh regions, a spherical inner region that is free to rotate and contains the plate wall boundaries, and an outer region that is kept stationary. The two regions are connected through a non-conformal sliding mesh interface (FLUENT Inc., 2009). The Realizable $k-\epsilon$ turbulence model (Shih et al., 1995) is used for turbulence modelling with an enhanced wall function.

The domain is discretised using a structured hexahedral mesh of 291,000 cells, with mesh refinement close to the plate wall boundary, such that the first layer of cells close to the plate has a cell spacing of approximately 0.01 m with a cell size growth ratio of approximately 1.2 away from the wall boundary. Figure 5.29 shows a vertical cross sections through the computational grid.

In both the CFD and experimental cases, the plate, which is initially held static relative to the flow at a low initial angle of attack, is released and accelerates from rest up to a stable mean autorotational speed, with periodic fluctuations about this mean. The results are discussed in the following section.

It should be noted that unlike forced rotation and free-axis autorotation simu-

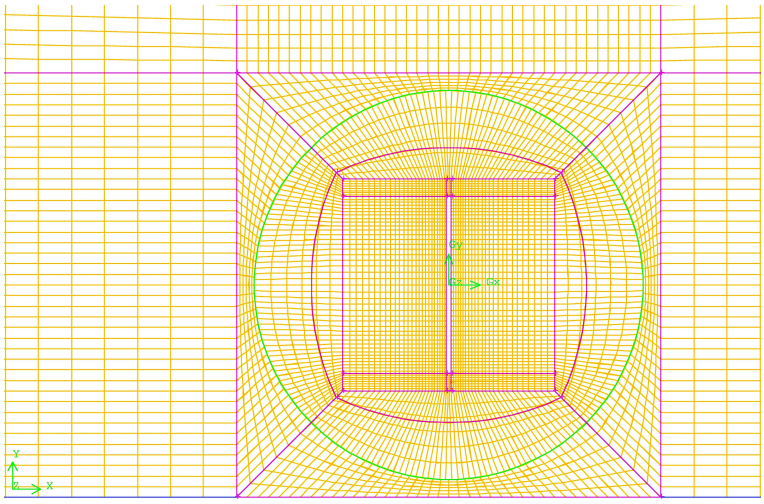

Figure 5.29: A vertical section through the Auckland computational grid showing mesh resolution close to the plate wall boundary.

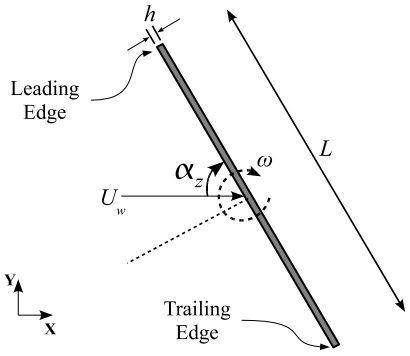

Figure 5.30: The clockwise-positive rotational convention used in the autorotational cases.

lations where a conventional right hand rule has been used to represent torque and rotational speed as positive in the anti-clockwise direction (Figure 2.1), for purposes of remaining consistent with existing literature and experimental results, the fixed-axis autorotation results presented in this section (section 5.5) use a clockwise positive convention for rotation and torque as illustrated in Figure 5.30.

5.5.1 Simulation Results

The six main fixed-axis autorotation cases discussed are listed in Table 5.9. Cases I-III use the Cuboid domain with no mass eccentricity applied, while cases IV to VI use the Auckland domain and simulations have been performed with a

mass eccentricity of 0.03 m applied. The eccentricity value used is not based on physical measurements which were difficult to obtain but has been chosen using a calibration approach discussed in Section 5.5.3, with the only constraint being that the error should reasonably be no more than 5% of the plate's length.

A segment of the CFD-RBD time-series for autorotation speeds in cases IV to VI, together with corresponding experimental measurements using a gyroscope (Martinez-Vazquez et al., 2010) are presented in Figure 5.31. Similarly Figure 5.32(a) shows rotational speed predictions for the cuboid domain cases I to III while Figure 5.32(b) - (d) show the associated aerodynamic forces and torque.

Table 5.10 summarises the CFD and experimental results for mean and RMS rotational speed (shown in parentheses). The cuboid domain CFD predictions for mean autorotational speed, $\mathrm{CFD}_{\mathrm{Cuboid}}$, are in agreement with the values from empirical fit expressions by Iversen (1979), $\mathrm{Expt}_{\mathrm{Iversen}}$. However, there is relatively poor agreement with recent measurements by Martinez-Vazquez et al. (2010), $\mathrm{Expt}_{\mathrm{Martinez-Vazquez}}$, although the $\mathrm{CFD}_{\mathrm{Auckland}}$ results which used a set-up that more closely matched the experiment, showed better agreement. The difference between $\mathrm{CFD}_{\mathrm{Cuboid}}$ and $\mathrm{CFD}_{\mathrm{Auckland}}$ are attributed to mass eccentricity error, bearing friction and local blockage effects which are absent from the $\mathrm{CFD}_{\mathrm{Cuboid}}$ cases. Sensitivity studies were performed for these factors and are discussed in more detail in Section 5.5.3.

Overall, the CFD-RBD model provided an accurate qualitative and quantitative representation of the behaviour of autorotating plates. The onset of autorotation was found to be sensitive to initial angle of attack and the plate's mass moment of inertia. For a given mass moment of inertia, plates starting from a lower initial angle of attack were more likely to autorotate, while for the same initial angle of attack, plates with a higher mass moment of inertia were more likely to autorotate. This sensitivity is due to the existence of both retarding and accelerating stages in a complete rotational cycle as illustrated in Figure 5.32(d) which shows typical aerodynamic torque predictions from the $\mathrm{CFD}_{\mathrm{Cuboid}}$ cases. In order for a plate to enter into autorotation, it must gain sufficient inertia during the positive torque half-period to overcome the negative torque in the retarding half-period as previously discussed in Section 2.3.2.

Table 5.9: List of different simulations run for fixed-axis autorotation.

No	Domain	U_{w} (m/s)	e/L (%)
I	Cuboid	5.0	0.0%
II	Cuboid	7.5	0.0%
III	Cuboid	10.0	0.0%
IV	Auckland	5.0	3.0%
V	Auckland	7.5	3.0%
VI	Auckland	10.0	3.0%

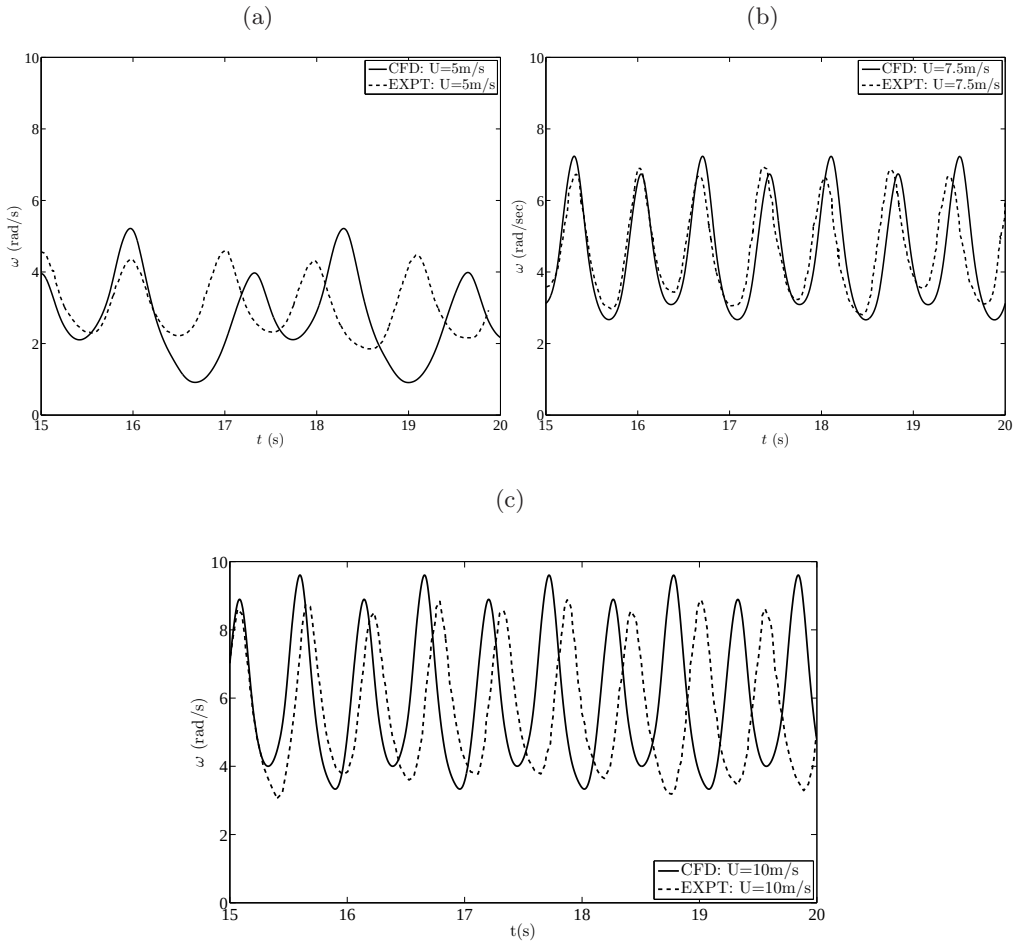

Figure 5.31: Auckland domain CFD-RBD predictions and experimental gyroscope measurements of rotational speed for a 1 m square flat plate in a uniform wind stream of (a) 5.0 m/s, (b) 7.5 m/s and (c) 10.0 m/s

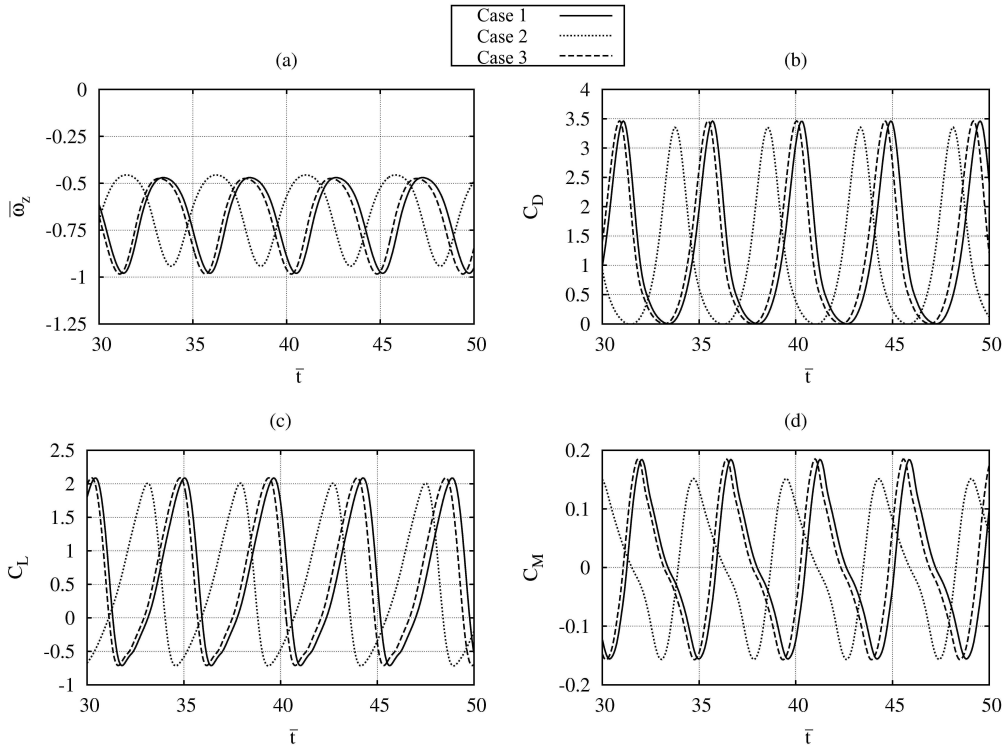

Figure 5.32: CFD-RBD Cuboid domain results for (a) rotational speed, (b) drag coefficient, (c) lift coefficient and (d) moment coefficient of an autorotating plate in uniform flow of different mean wind speed.

Table 5.10: Comparison of CFD predictions for average and RMS (in parentheses) of the dimensionless autorotation speeds, $\overline{\omega}$,together with corresponding experimental measurements from (Martinez-Vazquez et al., 2010), and values from empirical expressions by (Iversen, 1979).

U_w (m/s)	CFD_{Cuboid}	$CFD_{Auckland}$	$Expt_{Martinez-Vazquez}$	$Expt_{Iversen}$
5.0	0.69(0.71)	0.54(0.59)	0.62(0.64)	0.70(-)
7.5	0.66(0.68)	0.60(0.63)	0.63(0.66)	0.70(-)
10.0	0.69(0.71)	0.59(0.62)	0.57(0.60)	0.70(-)

5.5.2 Frequency Filtering of Experimental Signal

Prior to the validation of aerodynamic torque predictions, frequency filtering of the raw experimental measurements of aerodynamic torque (Martinez-Vazquez et al., 2010) has been performed in order to eliminate experimental noise.

A Discrete Fourier Transform (DFT) algorithm based on Frigo and Johnson (1998) is used to compute the frequency domain representation of the experimentally generated time-series. Frequency filtering is performed and the signal is then re-constructed as a complex-periodic signal using only the dominant harmonic frequencies. For a signal $x(t)$ containing a sequence $\{x_n\}$ of uniformly spaced time measurements of non-dimensionalised aerodynamic torque, C_M, the exact equivalent of a discrete Fourier Transform, X_k, is computed as

$$X_k = \sum_{n=0}^{N-1} x_n e^{-i2\pi kn \backslash N} \quad \dots k = 0, 1, 2, \dots (N-1), \tag{5.17}$$

where N is the number of elements in the raw signal sequence. The raw experimental signal is first de-trended in order to remove any linear static components such as those due to average autorotational lift. Figure 5.33 shows a 10 s segment of the raw experimental C_M time-signal.

Frequency (f), amplitude (A) and phase information (ϕ) are then obtained from the DFT, X_k, according to

$$f_i = \frac{i}{N\Delta t}, \quad \dots \quad i = 0, 1, 2, \dots, (N-1), \tag{5.18}$$

$$A_i = \frac{2(\text{abs}(X_k(i))}{N}, \quad \dots \quad i = 0, 1, 2, \dots, (N-1), \tag{5.19}$$

$$\phi_i = \arg(X_k(i)), \quad \dots \quad i = 0, 1, 2, \dots, (N-1). \tag{5.20}$$

The frequency-amplitude signal generated from the raw experimental data, shown in Figure 5.34, shows that the raw signal is predominantly complex-periodic, consisting of five major harmonics whose frequencies are all integral multiples of the first harmonic frequency, $f_1 = 0.42$. Table 5.11 shows the amplitude, frequency and phase information for the harmonics.

Using the harmonic frequencies and their corresponding amplitude and phase information, a sine-wave reconstruction of the original signal is computed. Given n number of harmonics, each with a frequency, f_i, that has a corresponding amp-

Table 5.11: Frequency, Amplitude and Phase information computed for the five major harmonic frequencies of the raw experimental data.

Harmonic Name	$F1$	$F2$	$F3$	$F4$	$F5$
Frequency (Hz)	0.42	0.84	1.26	1.68	2.10
Amplitude	0.031	0.09	0.032	0.018	0.018
Phase	-87	-154	-226	-298	-360

litude A_i, and phase ϕ_i, the filtered time-series y was computed as a combination of n sine waves according to:

$$y = \sum_{i=1}^{n} A_i \sin(2\pi f_i t + \phi_i) \quad \ldots i = 0, 1, 2, \ldots, n, \tag{5.21}$$

where t is the time and number of sine waves, $n = 5$. Figure 5.33 shows a segment of the raw experimental signal together with a complex periodic reconstruction of the signal using frequency and amplitude data from Table 5.11 to create the new filtered signal. Figure 5.34 shows the good agreement between the frequency representations of the raw experimental time signal and the reconstructed time signal. This reconstructed time signal of the experimental CM data is taken as a sufficiently accurate representative of the experimental results and is used in the subsequent validation of the CFD-RBD torque predictions.

5.5.3 CFD Aerodynamic Torque Validation

Using the filtered experimental time signal, the CFD-RBD computed aerodynamic torque is validated. Initial results for cases I to III, using the cuboid domain are illustrated in Figures 5.35 and 5.36, which show the CFD-RBD predictions and experimental measurements for aerodynamic torque.

As shown in Figure 5.36, the cuboid domain CFD predicts a complex periodic signal with only two harmonic frequencies. The first harmonic frequency corresponds to twice the rotational frequency of the plate (i.e. the time taken to complete a full 180° cycle) and may therefore be associated with periodic variations in aerodynamic torque due to changing angle of attack and vortex shedding. The second harmonic, with a frequency value of twice the first harmonic frequency, may be associated with non-linear effects due to asymmetry/hysterisis in the aerodynamic torque signal arising from delayed reattachment of flow when the angle of attack is decreasing as described in Smith (1971) and Richards et al.

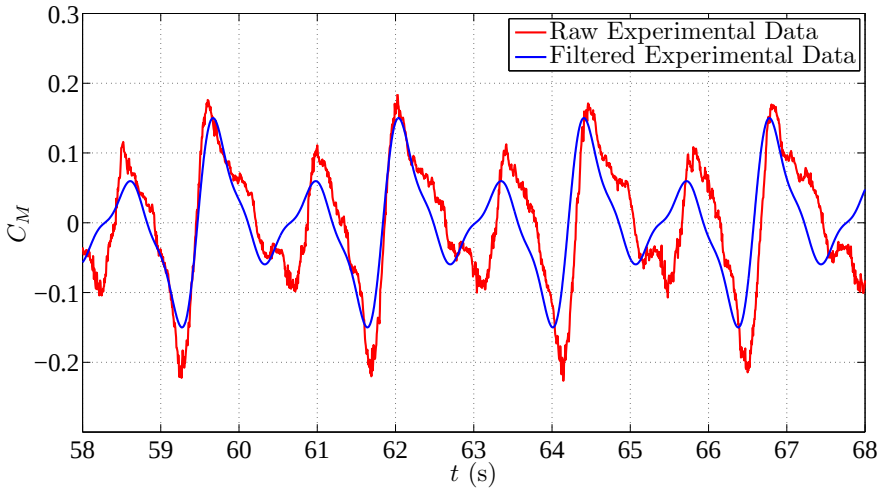

Figure 5.33: Raw and frequency filtered experimental time signals for moment coefficient (CM).

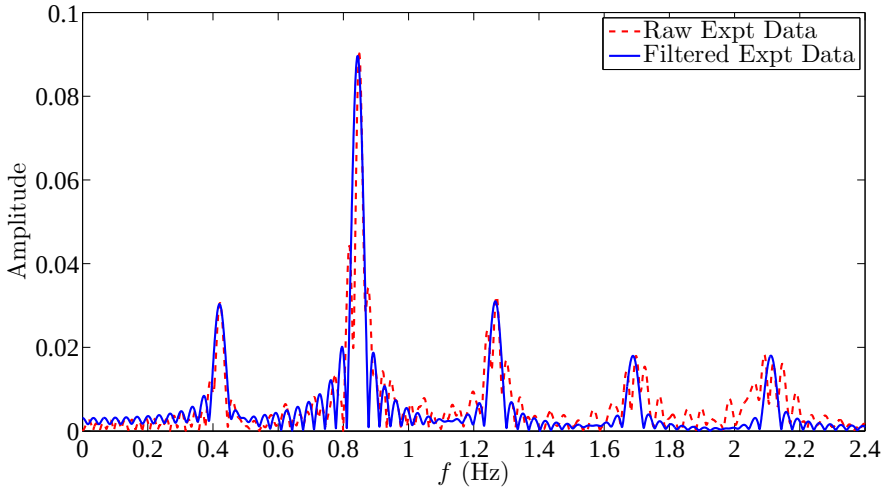

Figure 5.34: Frequency domain representations of raw and reconstructed time series of experimental moment coefficient (CM).

(2008). This alternation between increasing and decreasing angle of attack would be observed in every 90° cycle.

However significant differences do exist between the CFD signal and the filtered experimental signal when compared in both frequency and time domains. The filtered signal has three additional harmonics in the frequency domain that are likely associated with physical mechanisms present in the experimental setup which are not represented in the cuboid domain CFD-RBD setup. Sections 5.5.3.1 to 5.5.3.3 discuss the possible additional mechanisms in the experimental setup.

5.5.3.1 Domain Blockage Effects

In the Auckland experimental setup, the plate was supported so that it's axis of rotation was closer to the ground than the top wall of the wind tunnel (Martinez-Vazquez et al., 2010). A blockage effect is therefore likely due to the interaction of the plate with the flow between the plate-tip and the floor.

Simulations using the Auckland domain, which more closely matches the experimental setup were preformed with no eccentricity or bearing friction. The results in Figures 5.38 and 5.37 show a frequency shift on the plate's rotational speed relative to the symmetric cuboid in which no blockage effects were present. Although the domain asymmetry does not account for the additional harmonics, the results indicate that it does have a significant effect on the aerodynamic torque and rotational speed of the plate. This blockage effect therefore explains some of the differences in rotational speed between the cuboid domain CFD results and experimental measurements.

5.5.3.2 Bearing Friction

In addition, friction between the plate mounting cage and the support at the bearings could introduce a retarding torque on the plate, and this would influence the dynamics of the plate. A number of authors such as Iversen (1979) and Martinez-Vazquez et al. (2010) have suggested bearing friction as the likely explanation for the complex periodic nature of the experimental signal. To investigate this, an additional friction sub-model was added to the rigid body dynamics code as described in section 5.4.2. However for expected bearing friction coefficients within the range of values previously presented in Table 5.8, the effect of bearing friction torque was found to be negligible.

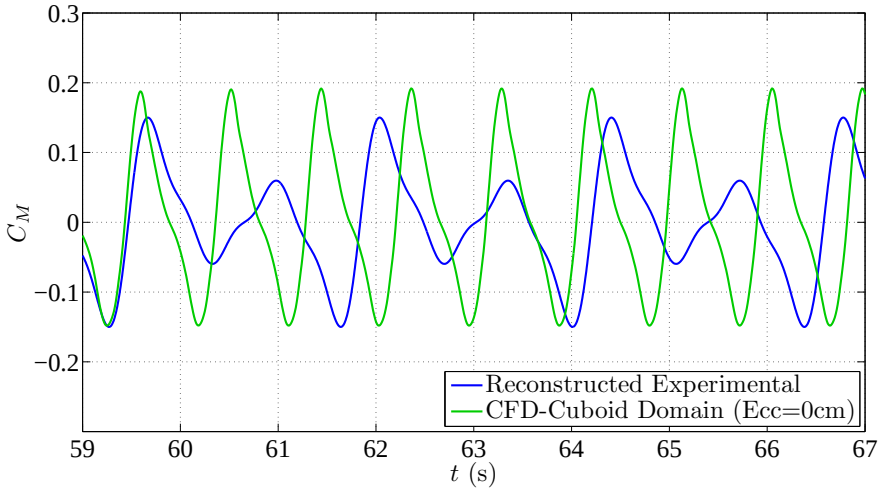

Figure 5.35: Time series of CFD computed moment coefficient for autorotation in a cuboid domain and filtered experimental moment coefficients.

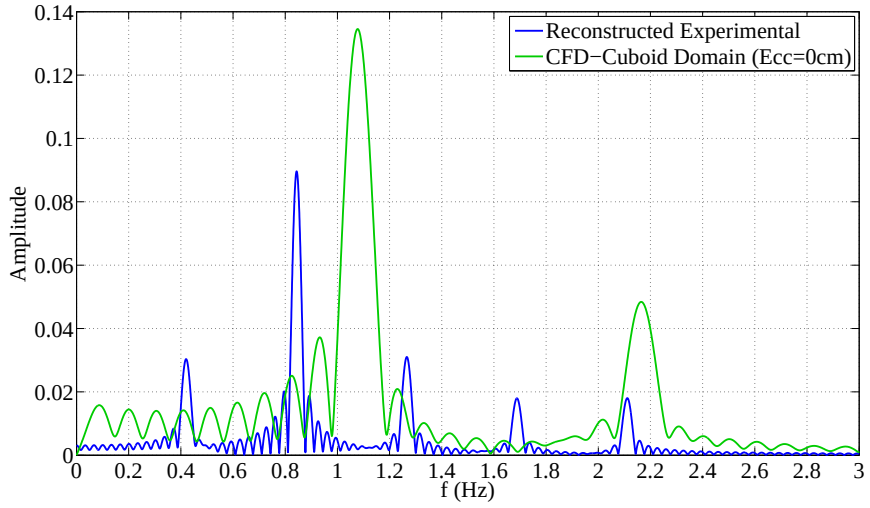

Figure 5.36: Frequency domain representations of CFD computed moment coefficient for autorotation in a cuboid domain and filtered experimental moment coefficients.

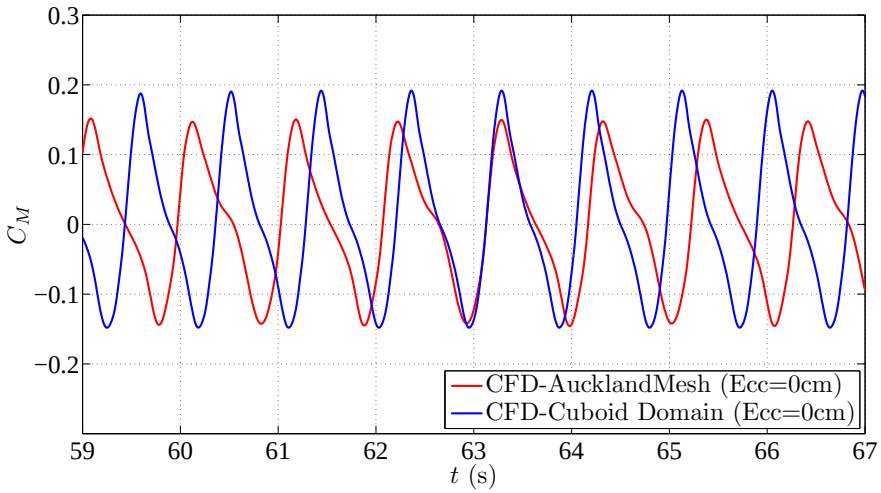

Figure 5.37: Time series of CFD computed moment coefficient for different domain configurations.

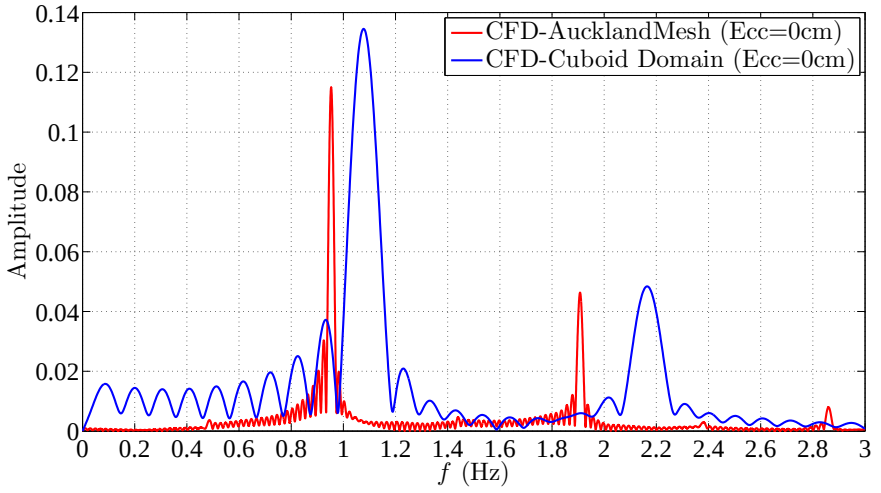

Figure 5.38: Frequency domain representation of CFD computed aerodynamic torque from a perfectly symmetrical low blockage domain (cuboid) and an asymmetric configuration similar to the experimental setup (Auckland).

Findings from existing literature also suggest that bearing friction is unlikely to cause a dual periodicity as other experimental studies of high aspect ratio free-falling plates (Hirata et al., 2009; Andersen et al., 2005) report a similar dual periodicity about both 180° and 360°. In these free-fall experiments however, there is no bearing friction and yet a dual periodicity is still observed in both low and high mass moment of inertia plates. Hirata et al. (2009) and Andersen et al. (2005) further found that although present in all plates, the 360° periodicity became more pronounced as the mass moment of inertia decreased. No detailed explanations for this phenomena have been given, however based on the results of this research, the mass eccentricity has been concluded to offer a possible explanation.

5.5.3.3 Mass Eccentricity

The effect of mass eccentricity on the aerodynamic behaviour of autorotating plate was investigated by performing simulations using the mass eccentricity torque sub-model described in Section 5.4.2. Figures 5.40 and 5.39 show the frequency and time-series representations of experimental data and CFD-RBD models for various eccentricity values.

The results revealed that the mass eccentricity has the effect of accelerating the motion of the plate in one half of the cycle ($90° \leq \alpha_z \leq 270°$), followed by a deceleration in the second half of the cycle. However, if the value of the mass eccentricity is too high, as in the 0.04 m case, the eccentricity torque has the overall effect of preventing plate autorotation. Lower mass eccentricities of 0.02 m and 0.03 m however resulted in stable autorotation cycles, with three additional harmonic frequencies observed in the Figure 5.40. The additional harmonics observed in the mass eccentricity cases are be associated with the acceleration and deceleration effects of the eccentricity torque.

Both frequency and time domain results for aerodynamic torque in the 0.02 m and 0.03 m cases were found to compare well with the experimental results, with the 3 cm case offering the closest match both in terms of harmonic frequency values and number of harmonics. Results are sensitive to mass eccentricity changes of as little as 1% of plate length.

Mass eccentricity appears to offer the best explanation to the experimental observations presented in Martinez-Vazquez et al. (2010) and together with the

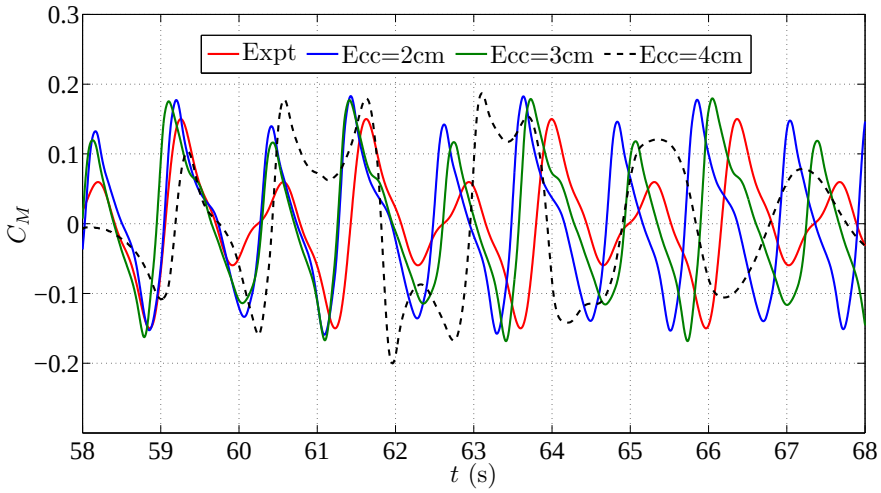

Figure 5.39: Time series of CFD computed moment coefficient for different values of mass eccentricity.

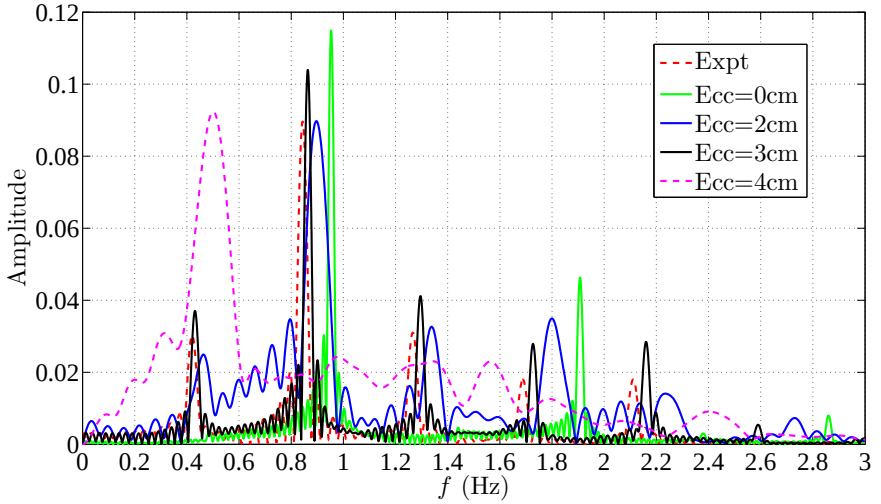

Figure 5.40: Frequency domain representation of CFD computed aerodynamic torque for various mass eccentricity values.

domain blockage effect, accounts for most of the difference between the computational and experimental results. The CFD-RBD modelling approach together with the additional sub-models has been shown to adequately represent the non-linear FSI that governs the motion of autorotating and free-falling plates.
In order to improve accuracy of the results, further investigations are required in order to more accurately determine the exact value of aerodynamic torque, which results indicate should lie between 0.03 m and 0.04 m.

5.5.4 Surface Pressure Distribution

During the autorotation experiments by Martinez-Vazquez et al. (2010), in addition to the gyroscope and data loggers, 24 surface pressure taps were embedded within the plate. Each pressure tap measured the instantaneous differential (net) pressure between a point at the front of the plate and another point at the same geometric location on the rear of the plate. Using these differential pressure measurements, the distribution of net pressure on the plate could be determined and has been used to provide further validation of the CFD-RBD model. Figure 5.41 illustrates the pressure tap locations on the plate, with the rotational axis along the line $x = 0$.
For purposes of comparison, CFD-RBD pressure predictions at the 24 experimental pressure tap locations are interpolated from the CFD face pressure solution obtained at the 1600 grid cells on each of the plate's front and back faces. CFD differential pressure values are then calculated and compared with the equivalent experimental measurements. A segment of the time-series showing the normal pressure coefficient, $C_{NP} = ({}^{i}P_{\text{face1}} - {}^{i}P_{\text{face2}})/(0.5\rho U_{\text{w}}^2)$, where $({}^{i}P_{\text{face1}} - {}^{i}P_{\text{face2}})$ is the differential pressure at sensor i, is shown in Figure 5.42(a) for experimental measurements (Martinez-Vazquez et al., 2010) and Figure 5.42(b) for the CFD results.
The experimental and CFD results shown in Figure 5.42 have been averaged over a series of successive rotational cycles to obtain a representative pressure-phase relationship. Figures 5.43 - 5.45 show the resulting phase-pressured differential pressure curves for sensor locations: S1, S2, S3, S6, S7, S8, S11, S12 and S13. As defined in Figure 5.41, sensors S1, S2 and S3 located close to the leading or trailing edge and would capture pressure effects by the leading and trailing edge vortices, sensors S1, S6, S11 are at the plate side edges and would show pressure

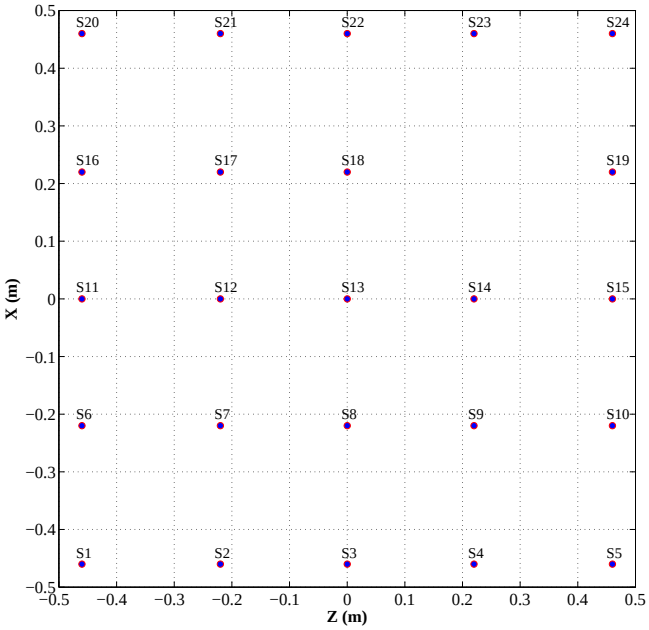

Figure 5.41: Physical location of pressure taps in experimental set-up by Martinez-Vazquez et al. (2010), represented on a flat plate at $\alpha_z = 0°$.

fluctuations due to the tip vortices, while sensors S7, S8, S12 and S13 near the centre of the plate would represent pressure fluctuations away from the edges. The CFD results are found to be in fairly good qualitative and quantitative agreement with experimental measurements and the CFD-RBD model can be concluded to give an accurate representation of the pressure distribution on the surface of the plate. However, significantly larger peak pressures are sometimes observed in the CFD data for sensor locations near the plate side-edges where tip vortices are expected. The discrepancies in results at these sensors may be attributed to inaccurate representation of vortex core pressure by the URANS models which do not resolve the flow structures but rather represent their gross statistical properties. These discrepancies may also be due to experimental error arising from the presence of a plate support frame in very close proximity to the side edges in the experimental set-up, which would disrupt the flow near the edges and interact with the large tip vortices. Further investigations are required to explain this discrepancy. The CFD results are however still within acceptable limits, with an average (across all tap locations) normalised root-mean-square

(a)

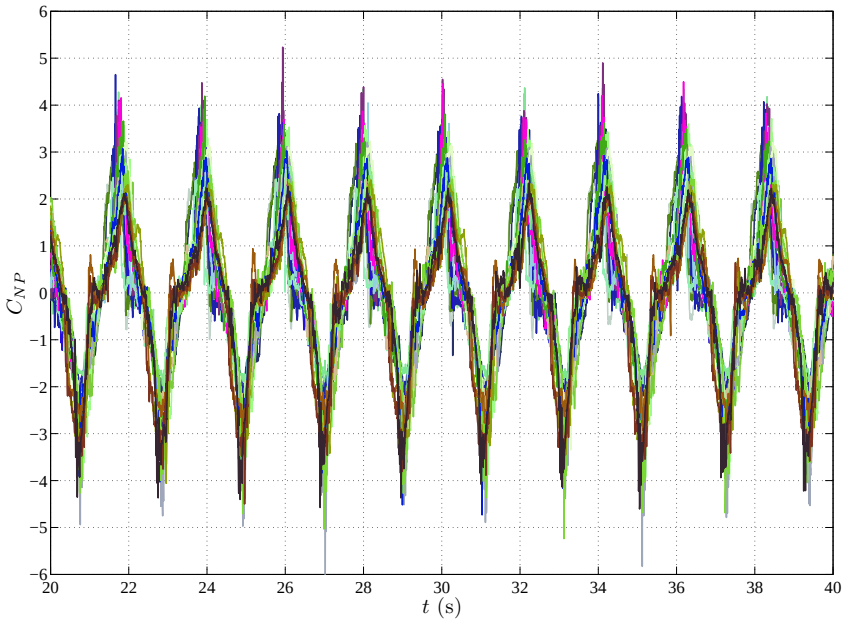

(b)

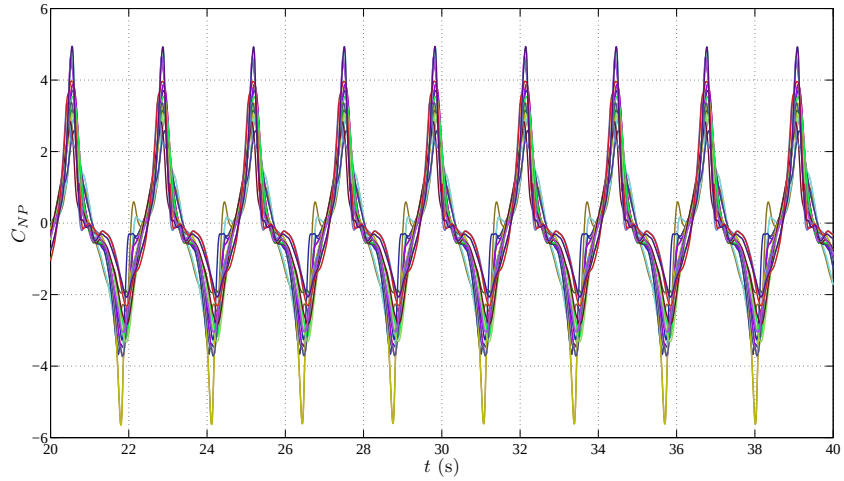

Figure 5.42: Time-series of differential pressure coefficients (normal force coefficients), C_{NP}, from (a) experimental measurements (Martinez-Vazquez et al., 2010) and (b) CFD predictions, for an autorotating flat plate in a $U_{\mathrm{w}} = 5$ m/s uniform wind stream.

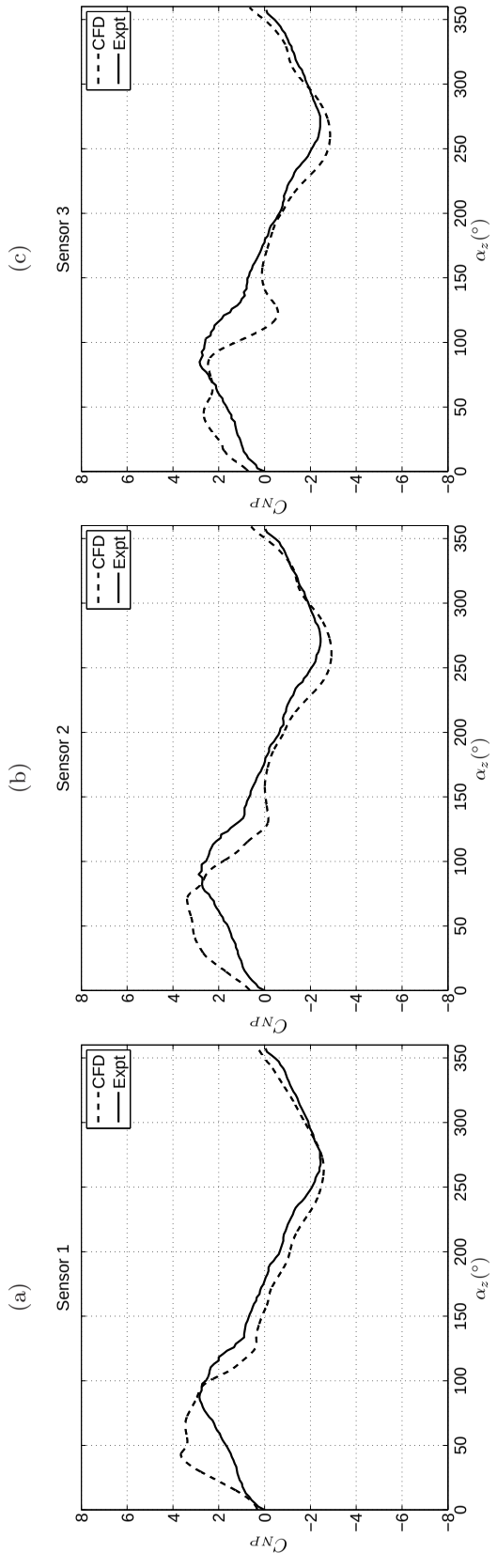

Figure 5.43: CFD and experimental (Martinez-Vazquez et al., 2010) phase-averaged net pressure coefficients, C_{NP} at various sensor locations (a) S1, (b) S2 and (c) S3.

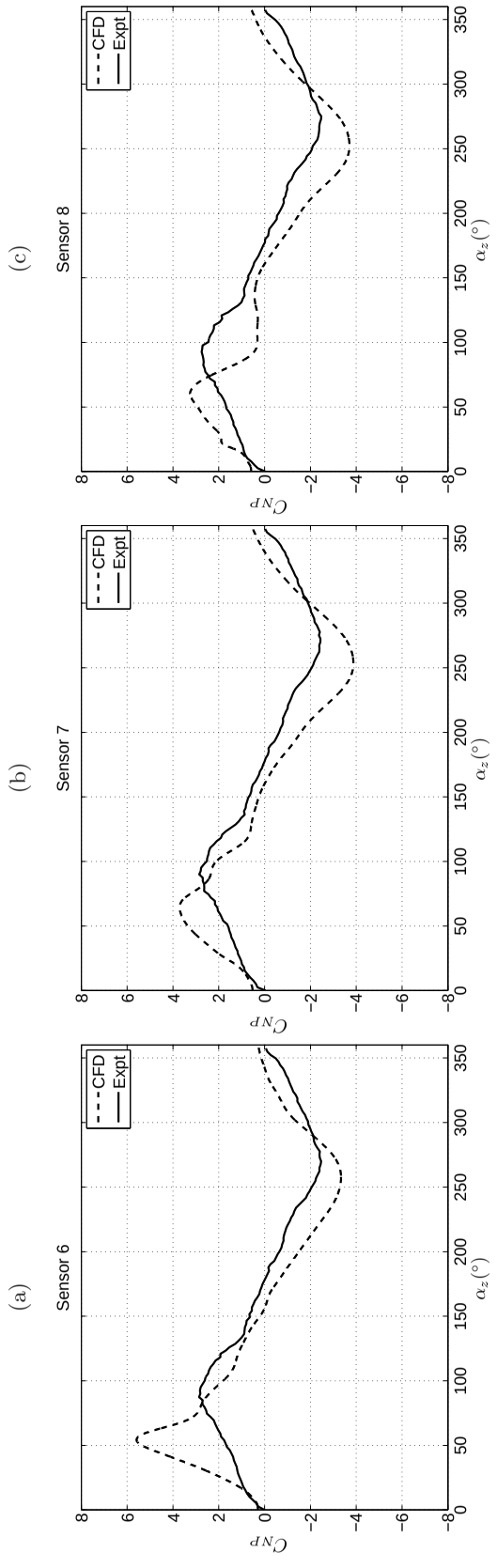

Figure 5.44: CFD and experimental (Martinez-Vazquez et al., 2010) phase-averaged net pressure coefficients, C_{NP} at various sensor locations (a) S6, (b) S7 and (c) S8.

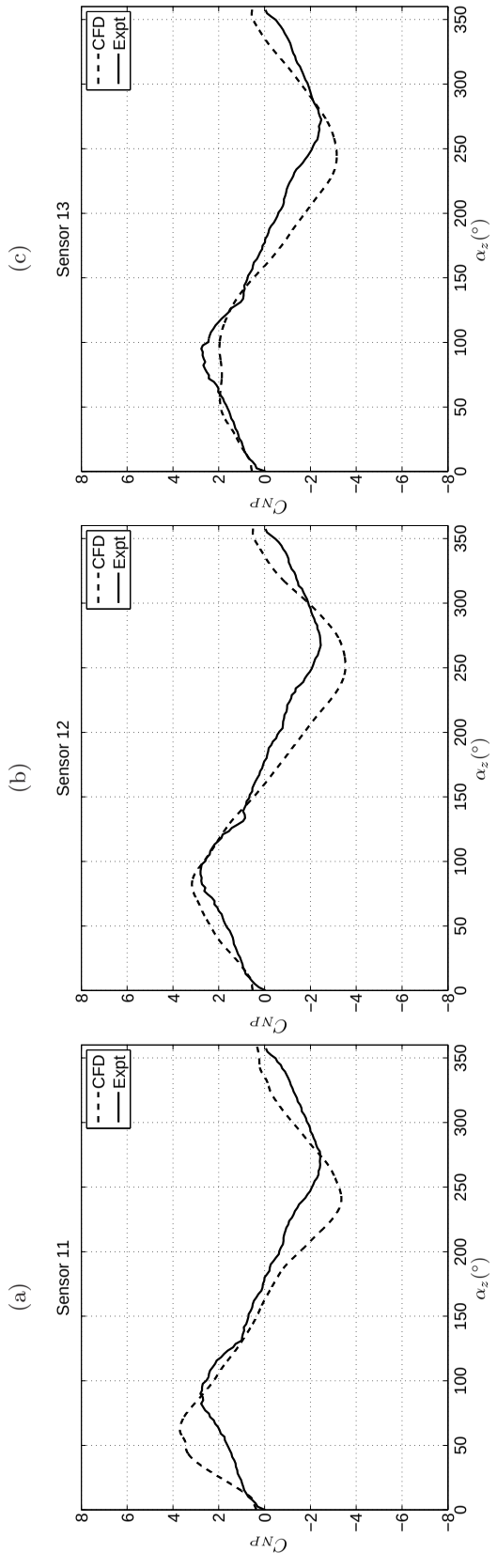

Figure 5.45: CFD and experimental (Martinez-Vazquez et al., 2010) phase-averaged net pressure coefficients, C_{NP} at various sensor locations (a) S11, (b) S12 and (c) S13.

error (NRMSE) of approximately 18%.

The accurate prediction of the surface pressure distribution is necessary in order to correctly determine the centre of pressure location and estimate the aerodynamic torque acting on the plate. Based on the CFD solution, the front face (windward), back face (wake) and the differential pressure distribution across the plate surface at different instantaneous angles of attack are shown in Figures 5.46 - 5.48. Q-criterion iso-surfaces showing the 3D vortex cores at these angles of attack are shown in Figures 5.49 - 5.51 in order to more directly highlight the role of the coherent flow structures in determining the instantaneous pressure distribution on the plate.

In Figure 5.47 the influence of tip vortices can be seen as distinct negative pressure peaks along the side edges (left and right edges) of the back face, while the retreating edge vortex creates negative pressure peaks at the retreating edge (top edge). The large stagnation pressure on the front face, close to the advancing edge (bottom edge) is also visible as a positive pressure peak in Figure 5.46.

With the plate autorotating in the clockwise direction, at lower angles of attack, $\alpha_z < 30°$, the positive stagnation pressure at the front face is concentrated near the retreating edge (top edge) which is also the leading edge. At higher angles of attack, this positive stagnation pressure peaks is centred closer to the advancing edge, even in Figure 5.46(c) and 5.46(d) when the advancing edge is not the leading edge. This may be attributed to effective local wind speed which is higher at the advancing edge than at the trailing edge, resulting in larger advancing edge stagnation pressures.

At the rear face of the plate the negative pressure peak at the top edge, associated with the retreating edge vortex is observed in Figures 5.47(a) and 5.47(b). The magnitude of these negative peak pressures increases until the $\alpha_z \approx 90°$ position, Figure 5.47(d), when the retreating edge vortex is shed into the wake. Tip vortices attached to the plate side edges are also observed to create increasingly negative pressure peaks close to the plate edges as angle of attack increases.

Two trailing edge vortices are present in the flow, however, these appear to be dominated by the large tip vortices and are eventually shed at $\alpha_z \approx 90°$ and $\alpha_z \approx 160°$. The second trailing edge vortex is quickly transported into the wake and does not have a large impact on plate pressures.

The negative pressure from the wake flow structures, together with the positive

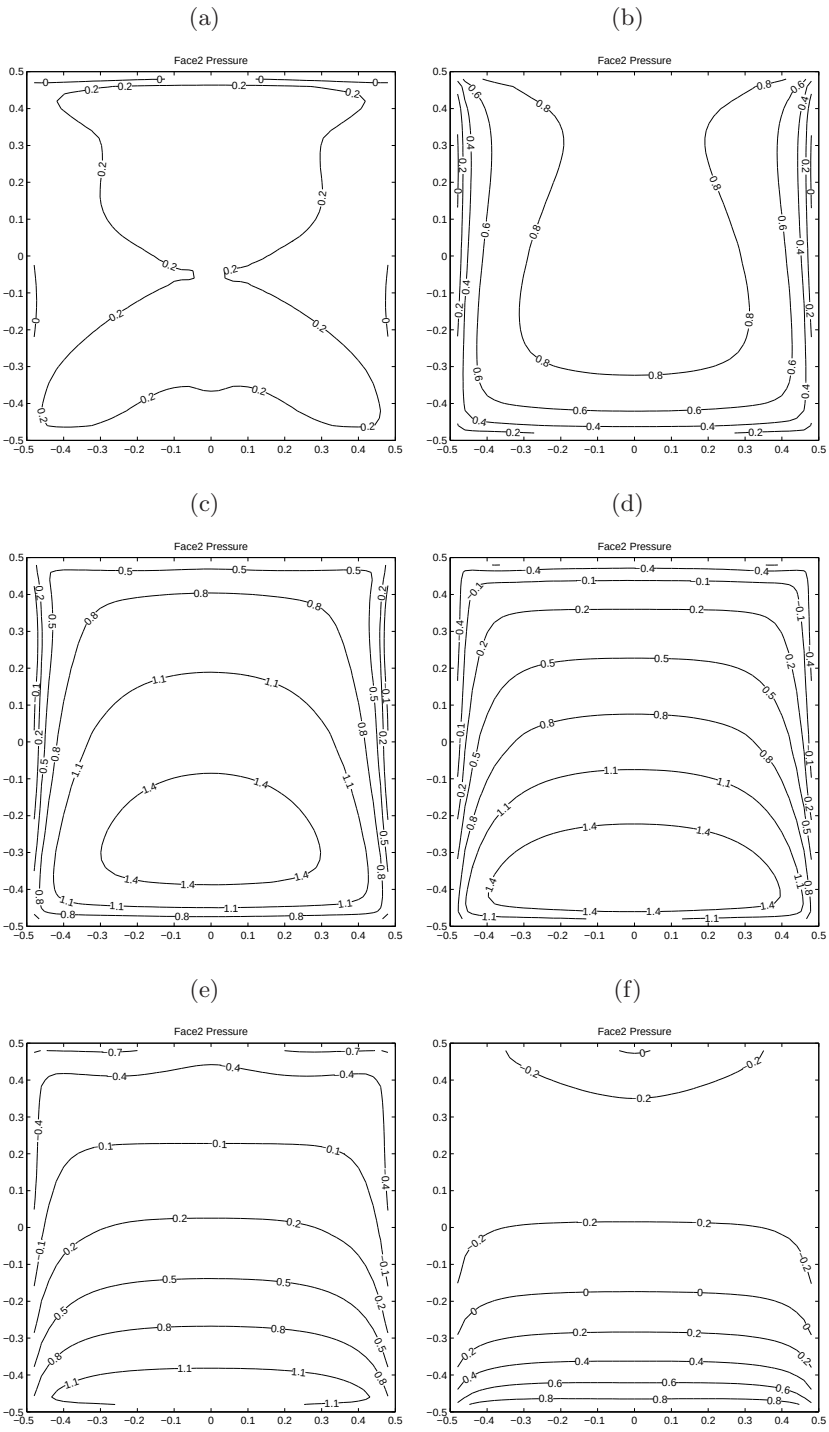

Figure 5.46: Contours of CFD predicted instantaneous pressure coefficients showing the surface pressure distribution on the front face at various angles of attack; (a) $\alpha_z = 0°$, (b) $\alpha_z = 30°$, (c) $\alpha_z = 60°$, (d) $\alpha_z = 90°$, (e) $\alpha_z = 120°$ and (f) $\alpha_z = 150°$. The top and bottom edges of each figure correspond to the top and bottom edges of the plate.

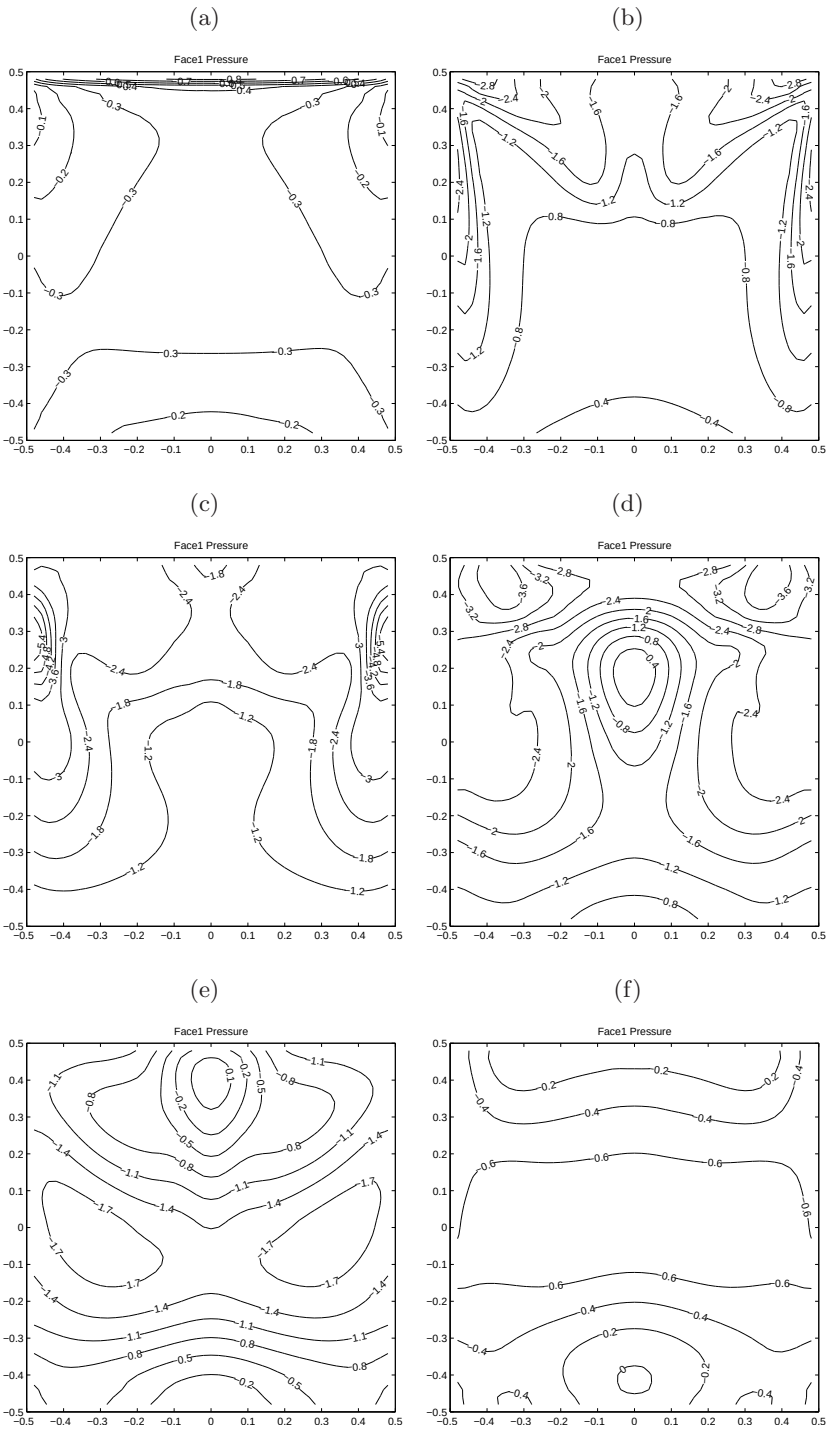

Figure 5.47: Contours of CFD predicted instantaneous pressure coefficients showing the surface pressure distribution on the rear face at various angles of attack;(a) $\alpha_z = 0°$, (b) $\alpha_z = 30°$, (c) $\alpha_z = 60°$, (d) $\alpha_z = 90°$, (e) $\alpha_z = 120°$ and (f) $\alpha_z = 150°$. The top and bottom edges of each figure correspond to the top and bottom edges of the plate.

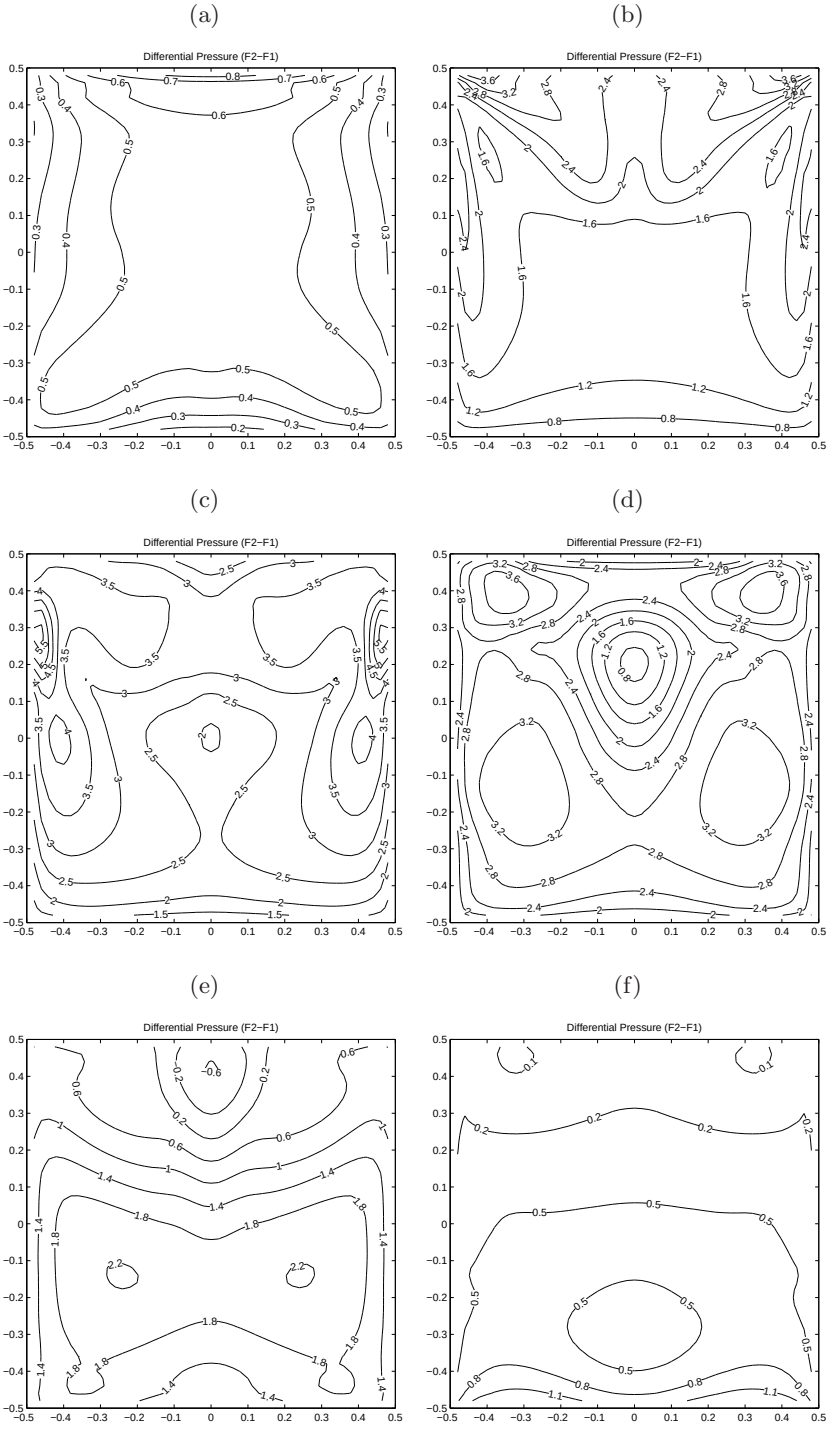

Figure 5.48: Contours of CFD predicted instantaneous net pressure coefficients for various angles of attack; (a) $\alpha_z = 0°$, (b) $\alpha_z = 30°$, (c) $\alpha_z = 60°$, (d) $\alpha_z = 90°$, (e) $\alpha_z = 120°$ and (f) $\alpha_z = 150°$. The top and bottom edges of each figure correspond to the top and bottom edges of the plate.

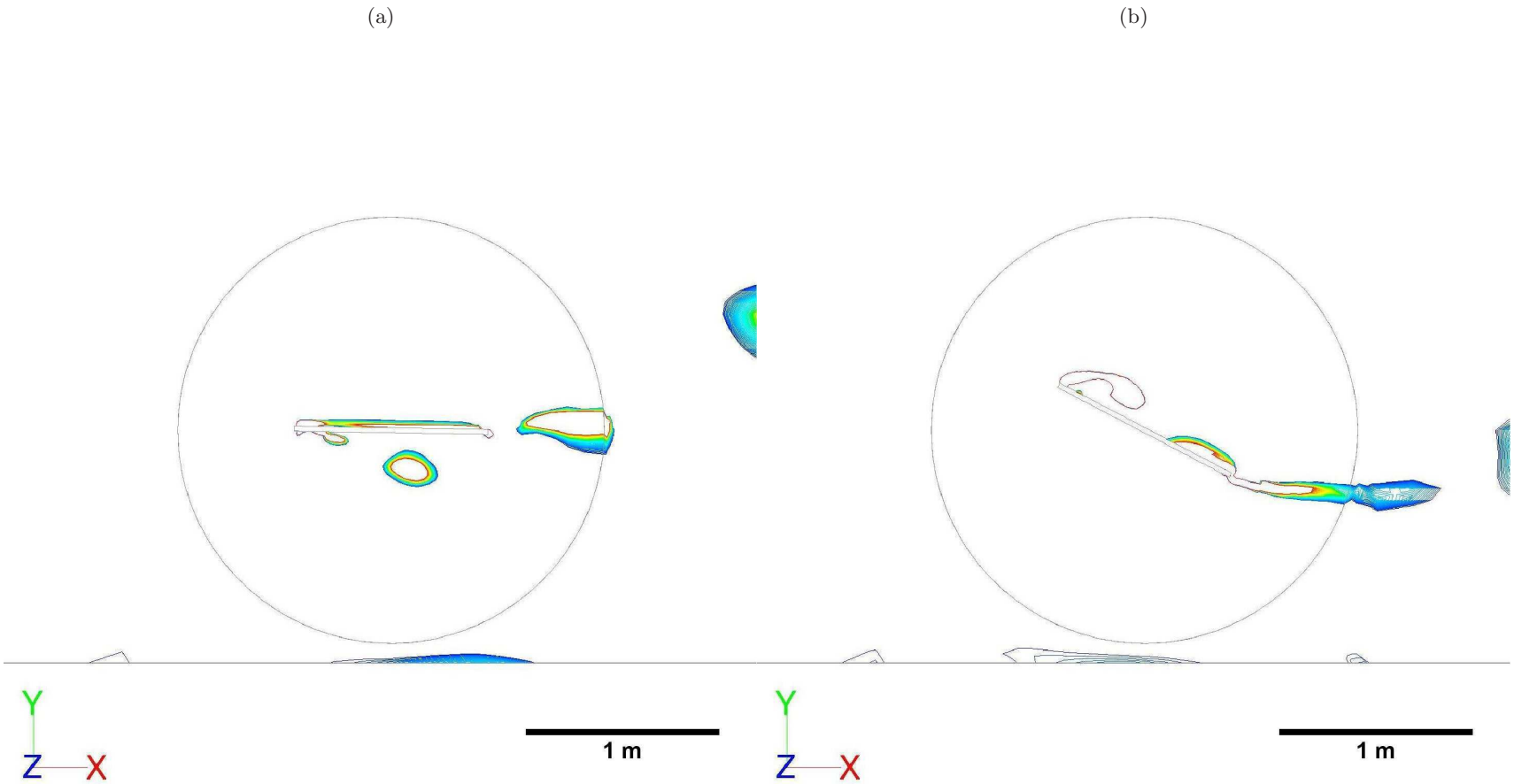

Figure 5.49: Contours of Q-value showing leading and trailing edge vortices in the wake of an autorotating plate at (a) $\alpha_z = 0°$, (b) $\alpha_z = 30°$.

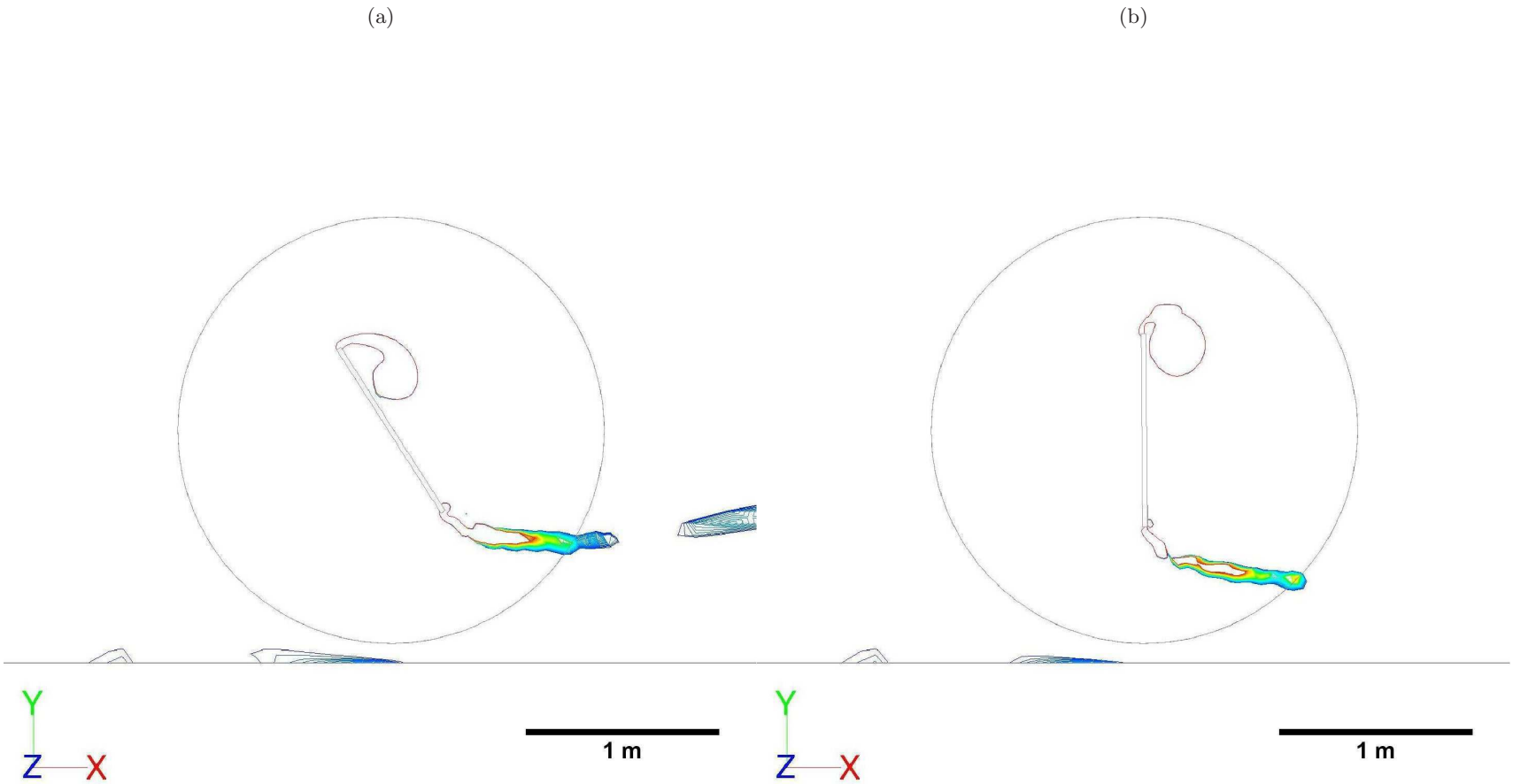

Figure 5.50: Contours of Q-value showing leading and trailing edge vortices in the wake of an autorotating plate at (a) $\alpha_z = 60°$, (b) $\alpha_z = 90°$.

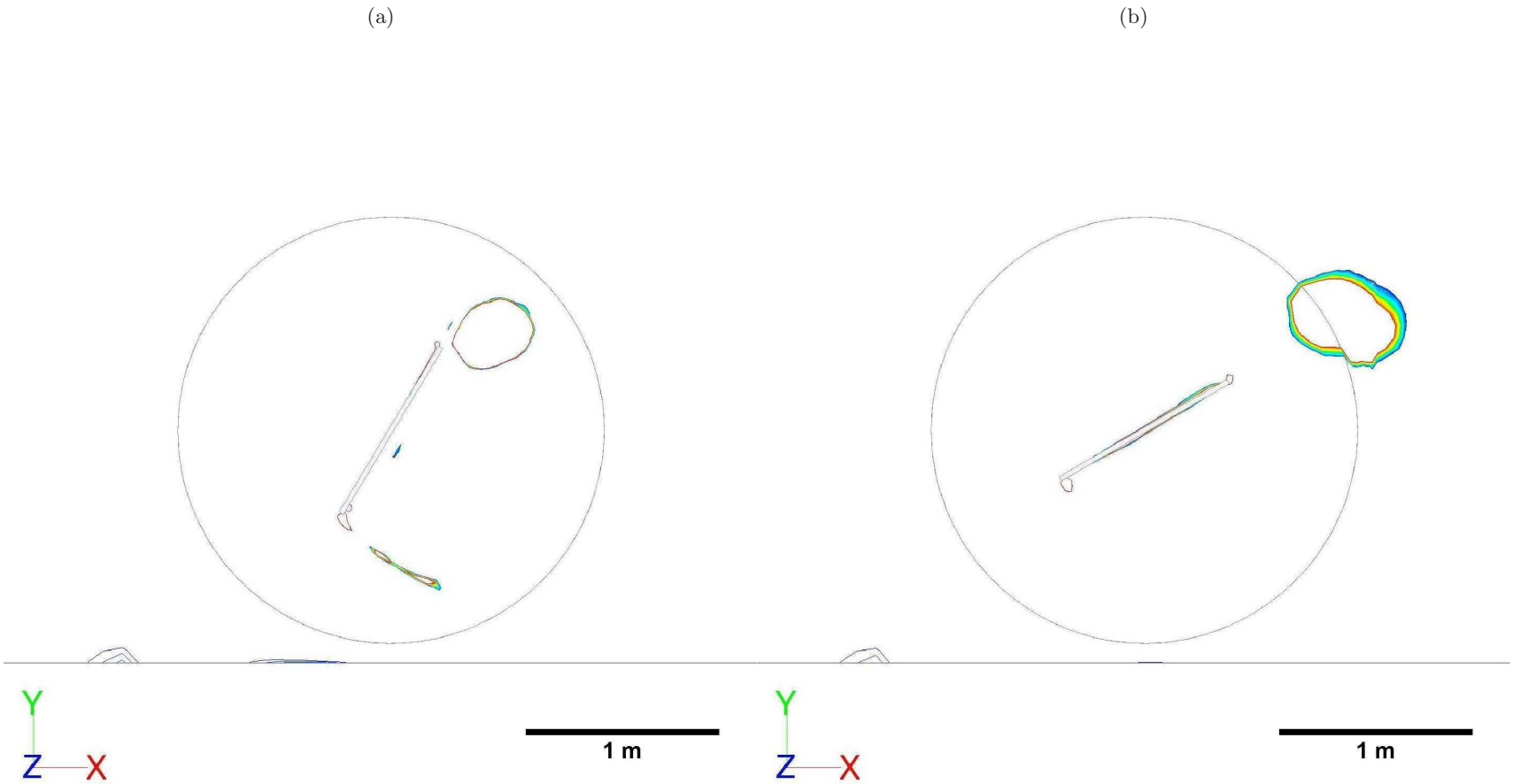

Figure 5.51: Contours of Q-value showing leading and trailing edge vortices in the wake of an autorotating plate at (a) $\alpha_z = 120°$, (b) $\alpha_z = 150°$.

stagnation pressure at the front of the plate create the positive net pressure distribution shown in Figure 5.48. As illustrated in Figure 5.48(a - d), for $0° \leq \alpha_z \leq 90°$ the net pressure in the top half of the plate is much greater than the net pressure in the bottom half, resulting in a positive accelerating torque. Beyond $\alpha_z \approx 90°$ however, Figure 5.48(e - f), the net pressure in the bottom half of the plate is greater than the net pressure in the top half of the plate, creating a decelerating torque.

5.6 Simulating Free-axis Autorotation

For many practical and unconstrained problems, such as windborne debris flight, fixed axis autorotation which is a special case of plate autorotation is not a sufficient representation the plates behaviour. The plate will more likely undergo three-dimensional autorotation about an arbitrary axis determined by Fluid-Structure Interaction. This complex 3D spinning behaviour is very difficult to model experimentally as most plate mounting systems will only allow autorotation about a single fixed axis. It is therefore necessary to extend the validated model of fixed-axis autorotation to include low aspect ratio (3D) plates with three rotational degrees of freedom.

The CFD-RBD model has been used to demonstrate complex free-axis autorotation cases, where plate motion is not constrained to any fixed axis and only the plate's centre of mass is constrained from motion, creating a three rotational degree of freedom system. The cuboid domain described in Figure 5.6 has been used.

The plates initial orientation was setup so that $\phi = -14.5°$, $\theta = -3.8°$ and $\psi = 75.5°$. As a result of the initial orientation, aerodynamic torque was developed about the X, Y and Z axes leading to complex 3D spinning. For plates whose initial orientation is normal to the flow in the horizontal plane, only the fixed-axis autorotation mode is observed. The results are therefore found to be strongly dependant on the initial orientation of the plate.

The simulations were carried out at mean wind speeds of 5 m/s and the stable aerodynamic coefficients for drag force, C_D, in the X-direction, lift force, C_L, in the Y-direction, and side force C_S in the Z-direction are shown in Figure 5.52 together with the aerodynamic torque about the X, Y and Z axes (C_{MX}, C_{MY} and C_{MZ} respectively).

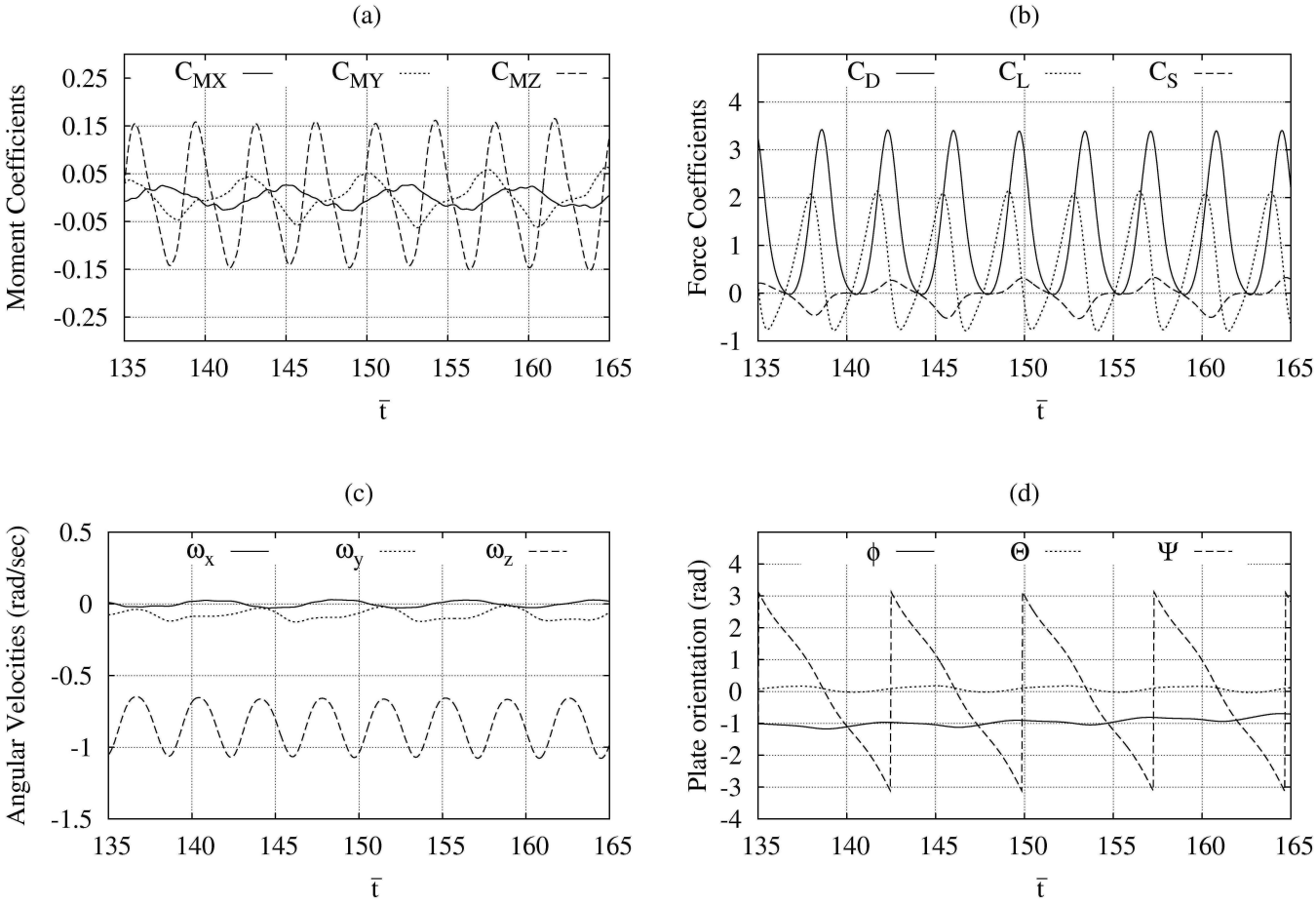

Figure 5.52: Three-degree of freedom CFD-RBD predictions for (a) aerodynamic torque, (b) aerodynamic force, (c) rotational speed and (d) orientation of a flat plate in free-axis autorotation about its centre of mass.

Similar to fixed-axis autorotation, plates were observed to enter into stable autorotation with the main distinction being that with free-axis autorotation, a stable rotational speed is reached about all three axes. This can alternatively be viewed as autorotation about an arbitrary axis, which has components in the X- Y- and Z-directions. This arbitrary axis of rotation is determined by a complex non-linear interaction between the plate and the flow, and is a function of the plate's initial orientation and mass moment of inertia tensor. Further investigations are recommended in order to better understand this behaviour.

5.7 Conclusions

Two-dimensional CFD models have been found to be inadequate even for high-aspect ratio plates and 3D simulations are recommended. Static plate sensitivity studies for grid size and time resolution have shown results to be mesh and time-step independent.

3D static plate CFD models have been found to be sensitive to near-wall grid resolution and turbulence modelling approach. URANS models which predict the statistics of a grossly unsteady flow have difficulty in reproducing the unsteadiness in the coherent flow structures in the wake of a static plate. However comparisons with more computationally expensive DES simulations confirm that although wake unsteadiness exists and produces fluctuations in the body forces of low aspect-ratio plates, these fluctuations have a weak effect on plate motion. The additional computational effort in reproducing these weak fluctuations has therefore been found to be unjustified and a URANS turbulence modelling approach with the Realisable $k - \varepsilon$ model is preferred. In the case of rotating plates, this URANS approach has been shown to be capable of reproducing the strong unsteadiness in the flow.

A CFD-RBD sequential coupling approach has been presented and used to simulate the unsteady aerodynamics of forced rotating and autorotating plates. The results of the forced rotation studies reveal a strong dependency of mean and fluctuating aerodynamic loading on rotational speed. Quasi-steady theory as proposed by Tachikawa (1983) is shown to be incorrect in as far as predicting the fluctuating component is concerned and new empirical expressions based on CFD results are presented.

Three modes of motion are identified in rotating plates depending on the ro-

tational speed; pre-autorotation, autorotational and post-autorotational. The point of stable autorotation is identified below which the FSI results in aerodynamic acceleration and beyond which the FSI results in aerodynamic damping. The main flow structure responsible for determining the plate's aerodynamic acceleration and damping is identified as the leading-edge vortex at the retreating edge. Tip vortices also play a significant role, while the advancing edge vortex was found to have a relatively weak influence.

The CFD-RBD model has been validated against experimental measurements and shown to accurately reproduce the rotational dynamics as well as the surface pressure distribution on fixed-axis autorotating plates. The surface pressure distribution is found to be strongly influenced by the unsteady flow structures in the wake of the plate. Autorotational dynamics of the plate are also shown to be strongly dependant on the centre of mass and local blockage effects present in the experimental setup.

Finally, the validated model has been used to demonstrate free-axis autorotation about the plate's centre of mass and its sensitivity to initial orientation. The following chapter extends the three rotational degree of freedom model presented here to include plate translation and simulate windborne debris flight.

Chapter 6

Simulating 3D Windborne Debris Flight

In this chapter, the validated CFD-RBD model, previously applied to simulate plate autorotation in section 5.4 is here extended to include 3D plate translation in order to simulate the 6DOF flight of plate-type windborne debris. While previous coupled CFD-RBD models of plates have been limited to 2D free-fall motion with 3DOF (Jin and Xu, 2008), and the prescribed motion of 3D flapping plates (Dong et al., 2006), this research extends this work to include the numerical investigation of the non-linear FSI involved in windborne debris flight. The resulting 6DOF debris flight model is used to perform parametric studies for initial orientation, flow properties, plate properties, and complex launch conditions. Comparisons are also made between the CFD-RBD model predictions and quasi-steady solutions to the debris flight equations.

6.1 Model Description

A 3.0 kg square plate of side, $L = 1.0$ m and thickness, $h = 0.0254$ m is positioned in a domain of size $80L \times 30L \times 30L$. Figure 6.1 illustrates the computational domain and associated boundaries. The plate is initially positioned with its centre of mass $10L$ from the inlet and top boundary, $20L$ from the bottom boundary and $15L$ from each of the side boundaries.

The domain is split into a spherical inner region which is discretised using a 3D structured hexahedral mesh of approximately 280,000 cells, and an outer region discretised using an unstructured tetrahedral mesh of approximately 570,000 cells. The spherical inner region of radius $2L$ is rotated and translated monolithically with the plate in order to preserve mesh quality in the near-wall region, while the stationary outer zone is re-meshed at each time step in order to accommodate the motion of the inner zone. Cell volume, skewness and length scale constraints are used to determine whether to re-mesh the domain as well as which cells are to be re-meshed in order to preserve mesh quality in the outer re-

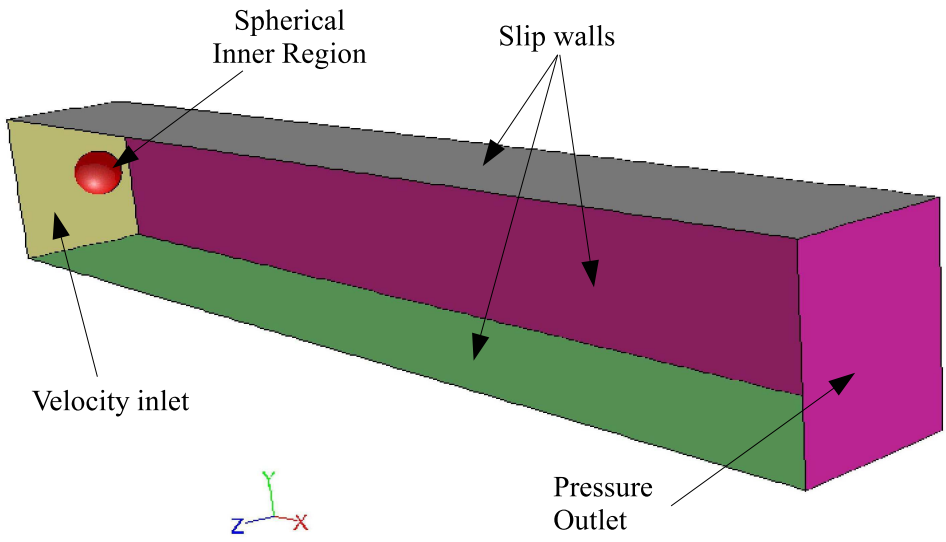

Figure 6.1: Computational domain and boundaries of the free-flight simulations.

gion. No non-conformal interface is applied in the free-flight simulations, rather the inner and outer regions are connected through a single shared surface.

The plate walls are modelled as a rigid wall boundaries with a no-slip condition. The inlet is modelled as a constant inflow velocity boundary while the outlet is modelled as a constant pressure boundary, and the side, top and bottom boundaries are modelled as walls with a free-slip condition. A uniform wind speed, U_{w} of 20 m/s (Re $=1.3 \times 10^6$, based on L) is imposed at the inlet with a turbulence intensity and length scale of 1% and 0.02 m respectively which correspond to typical low turbulence wind tunnel values (ESDU, 1970).

The Realisable $k-\varepsilon$ model is used with a two-layer enhanced wall function for near-wall turbulence modelling. Second order upwind spatial discretisation is used for the momentum, turbulent kinetic energy and turbulent dissipation rate, with standard interpolation for the pressure variable. The SIMPLE algorithm is used for Pressure-Velocity coupling and only first order implicit time-stepping scheme is available for temporal discretisation since previous mesh information is discarded after the data is interpolated onto the new mesh. A time-step size of 5×10^{-3} s is used and results have been found to be time-step independent. For each case, a precursor steady-state simulation is performed on the static plate in order to obtain an accurate initial solution for the flow around the plate.

The CFD model is used to obtain the aerodynamic forces acting on the plate,

which together with the self-weight of the plate are used to compute the velocities for the inner spherical region using the 6DOF RBD model presented in Section 4. The sequential coupling between the CFD model and this RBD model is described in Section 5.4.1.

6.2 Sensitivity to Initial Orientation

Using the model, a parametric study is performed to assess the sensitivity of plate-type windborne debris to initial orientation. Results are compared against findings from existing free-flight experiments by Lin et al. (2007). The CFD-RBD model is demonstrated as a reliable tool for the investigation of windborne debris flight behaviour.

Free flight simulations have been performed at a Tachikawa number, K, of approximately 8.3, which corresponds to typical values for large roofing sheets in a wind storm. Initially, 77 cases were set-up to cover the broad range of possible initial orientations in 3D space, and these are sub-divided into two batches.

Batch 1 - Single Plane Motion: In the first batch of 36 simulations (batch 1) the plates have been setup at initial angles of attack in the vertical X-Y plane, α_z, as shown in Figure 2.1, ranging from $-85°$ through to $90°$ at intervals of $5°$. In batch 1 simulations, the plates are initially held normal to the flow in the horizontal X-Z plane.

Batch 2 - 3D Flight: A second batch of 41 simulations (batch 2) are performed with the plate rotated at $15°$ intervals about the $Z-axis$ and the $Y-axis$ such that it's initial orientation is no longer normal to the flow laterally. In these cases, an initial orientation, ψ, about the Z-axis is applied, resulting in an angle of attack $\alpha_z = (90° - \psi)$, followed by a second rotation θ about the Y-axis. These two rotations would correspond to a pitch followed by a yaw of the plate as previously illustrated in Figure 4.1.

6.2.1 Results

Batch 1 simulations resulted in no significant lateral crosswind motion even though plates were unconstrained to translate and rotate in the lateral horizontal plane. Plate motion was therefore essentially two-dimensional.

Figure 6.2(a) from the batch 1 simulation results shows the non-dimensionalised

horizontal distance, $Kx^* = Kxg/U^2$, against non-dimensionalised time, $Kt^* = Ktg/U$, while Figure 6.2(b) shows results for non-dimensionalised horizontal speed, $\overline{u} = u/U_{\mathrm{w}}$, against non-dimensionalised horizontal distance.

The CFD-RBD model results compare well with experimentally derived fit expressions from Lin et al. (2006). The results demonstrate the significant role of initial angle of attack in determining the final flight behaviour of the plate. A non-linear least squares data fit expression of the CFD-RBD data for non-dimensionalised horizontal distance versus time is computed as the rational polynomial function;

$$Kx^* = \frac{C_1(Kt^*) + C_2(Kt^*)^2 + C_3(Kt^*)^3 + C_4(Kt^*)^4 + C_5(Kt^*)^5}{D_0 + D_1(Kt^*) + D_2(Kt^*)^2 + D_3(Kt^*)^3 + D_4(Kt^*)^4}, \qquad (6.1)$$

where the polynomial coefficients C_i and D_i are fit coefficients, computed as: $C_1 = 0.01737, C_2 = 0.06659, C_3 = 0.6404, C_4 = -0.08606, C_5 = 0.003026, D_0 = 1.0, D_1 = 0.9675, D_2 = 0.5874, D_3 = -0.09255, D_4 = 0.003449$. Unlike previous polynomial fit expressions of experimental data by (Lin et al., 2006), expressed in (2.23), Figure 6.2(a) also shows that this new fifth order rational polynomial has better extrapolation properties and does not diverge outside the range of data used to derive the expression. The new fit expression in (6.1) is therefore valid for longer flight durations than the original fit expression by Lin et al. (2006) shown in (2.23).

Expression (2.22) for non-dimensionalised horizontal wind speed, by Lin et al. (2006) is found to give an accurate mean representation of the final flight speed of the debris plates. However, a larger spread of terminal horizontal wind-speeds is observed in the CFD-RBD model results, which give a $\sigma_{\overline{u}} \approx 0.162$, in contrast to experimental observations by Lin et al. (2006), where a $\sigma_{\overline{u}} \approx 0.0814$ was observed. This discrepancy between the two results can be attributed to the fact that the Lin's expressions are derived from a narrow range of data, with typical flight times of $t^* \leq 0.8$ (approximately 0.6 s), while the CFD data is derived for plates with longer flight durations of $1.6 \leq t^* \leq 2.2$.

In the Batch 2 simulations, as a result of the plate's non-zero yaw, considerable side-force and torque is generated about the vertical and horizontal axes as previously illustrated in the free-axis autorotation cases (Section 5.6). Significant horizontal cross-wind motion and complex 3D free-axis autorotation are observed

(a)

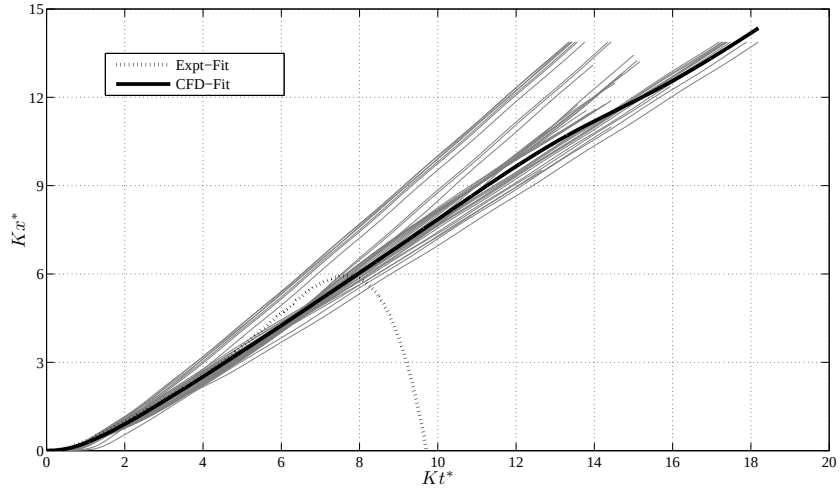

(b)

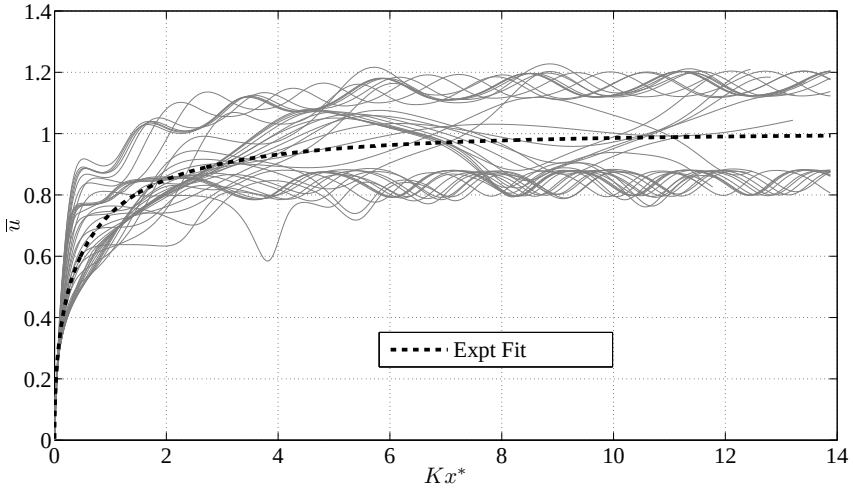

Figure 6.2: CFD-RBD predicted trajectories for batch 1 cases with $-85° \leq \alpha_z \leq 90°$, showing (a) experimental (Lin et al., 2006) and CFD-RBD based fit expressions for non-dimensionalised horizontal distance, and (b) CFD-RBD predictions for non-dimensionalised horizontal speed, together with a an experimentally derived fit expression (Lin et al., 2006).

and Figure 6.3 illustrates the broad range of debris trajectories observed.

6.2.2 Debris Flight Modes

The debris trajectories for batch 1 cases can be categorized into three distinct modes of flight; *Flutter (Mode 1), Transitional (Mode 2) and Autorotational (Mode 3)*, based on the plate's rotational behaviour. Figure 6.4 illustrates the corresponding modes observed for various initial angles of attack. The asymmetry of mode behaviour about $\alpha_z = 90^\circ$ initial orientation is attributed in part to the contribution of the plates vertical velocity, which affects the effective angle of attack.

Figures 6.5, 6.6 and 6.7 show respectively, the non-dimensionalised rotational speed, translational speed and trajectory observed for plates in each flight mode.

Mode 1, flutter, is mainly translational and is observed for plates with an initial angle of attack in the range $70^\circ < \alpha_z < 95^\circ$. As shown in Figure 6.5(a), the rotational motion of fluttering plates is characterized by oscillations between positive and negative values of $\overline{\omega}$. Values of $\overline{\omega}$ generally remain within the range $|\overline{\omega}| < |\overline{\omega}_o|$, where $\overline{\omega}_o$ is the stable autorotational speed, which for a plate with the mass and inertia under consideration in these simulations is approximately 1.0 as shown by the dotted line in Figure 6.5(c).

This value of $\overline{\omega}_o$ is higher than the CFD-RBD and experimental fit predictions of $\overline{\omega}_o \approx 0.70$ for a fixed-axis autorotating plate of similar dimensions (Table 5.10). This is a result of additional non-linear effects due to the periodic fluctuations in the magnitude and direction of the wind speed relative the the plate in the free-flight cases, while in the fixed-axis autorotational simulations presented in Section 5.4, the mean wind speed is kept constant.

The RMS of $\overline{\omega}_o$ increases from one cycle to the next for fluttering plates, and given a long enough flight duration, plates in the flutter mode would eventually reach $\overline{\omega} \approx \overline{\omega}_o$ and transition into stable autorotation. It is therefore worth noting that although traditionally a distinction has been made between these different flight modes for descriptive purposes, in reality they constitute different stages of autorotational flight as well as an indication of the dimensionless time required to reach stable flight.

(a)

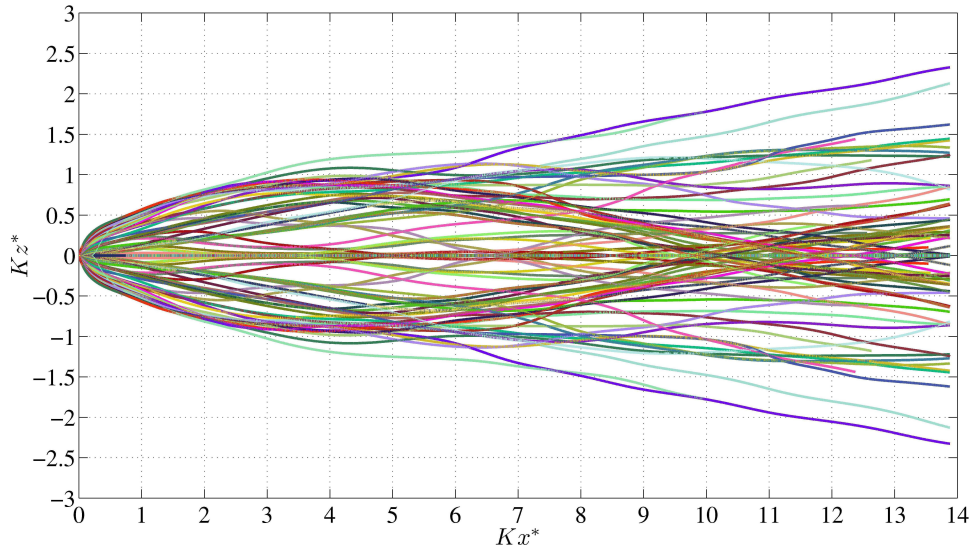

(b)

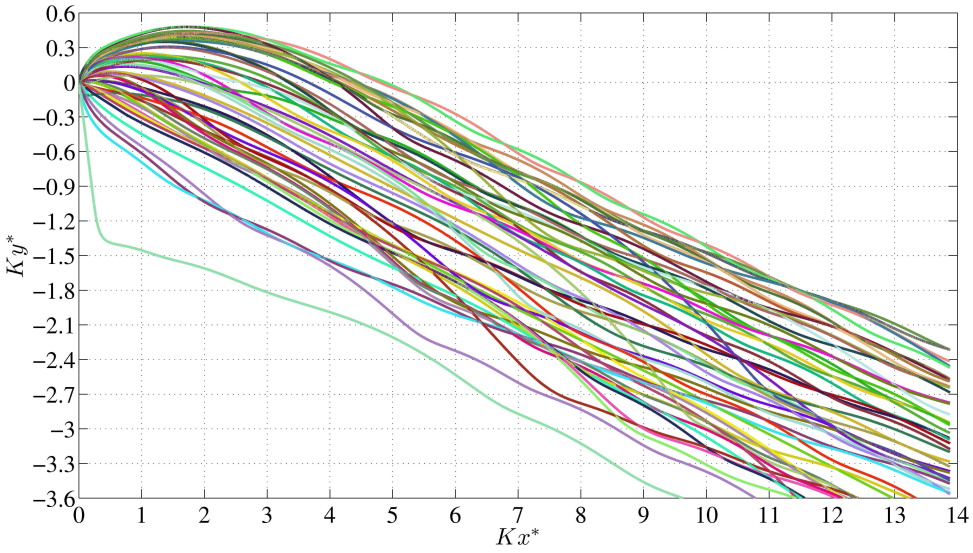

Figure 6.3: (a) Plan and (b) Side elevations showing broad range of trajectories from batch 2 cases.

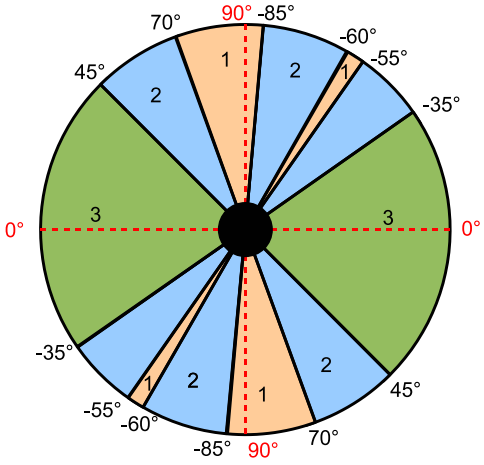

Figure 6.4: Schematic illustrating debris flight modes observed for different initial angles of attack in the batch 1 cases.

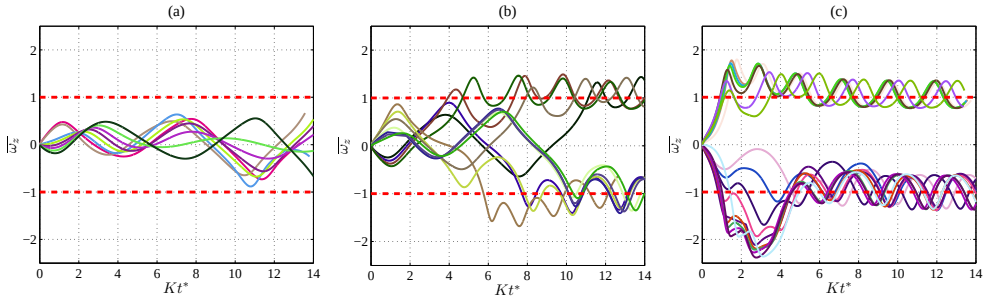

Figure 6.5: Non-dimensionalised rotational velocity against non-dimensionalised time for (a) mode 1, flutter, (b) mode 2, transitional, and (c) mode 3, autorotational, trajectories.

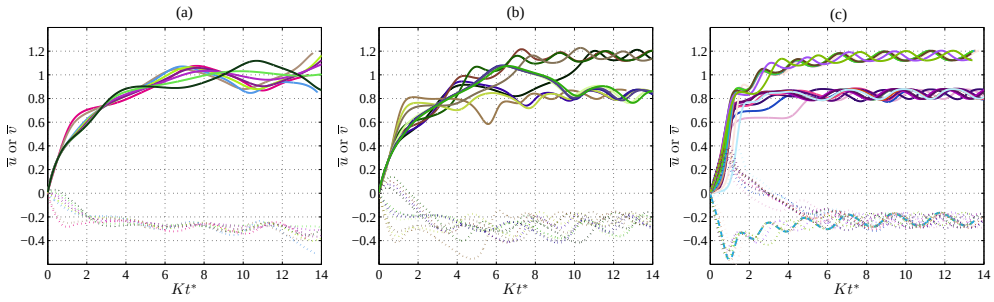

Figure 6.6: CFD-RBD predicted non-dimensionalised time-series of vertical (dashed lines) and horizontal (solid lines) plate speed for (a) mode 1, flutter, (b) mode 2, transitional, and (c) mode 3, autorotational, trajectories.

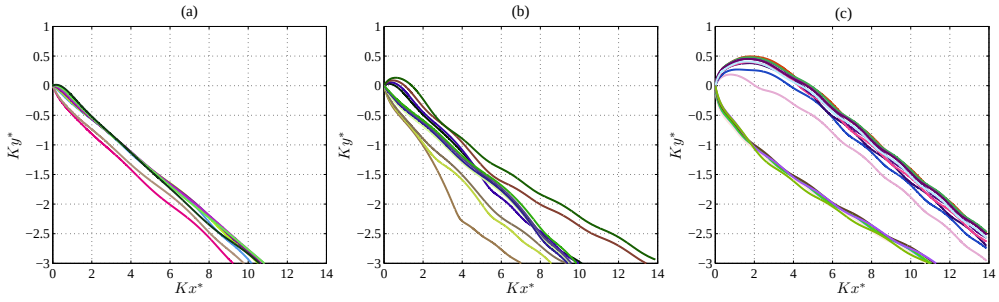

Figure 6.7: CFD-RBD predicted non-dimensionalised centre of gravity position for (a) mode 1, flutter, (b) mode 2, transitional, and (c) mode 3, autorotational, trajectories.

Mode 2, transitional, behaviour is observed for plates with an initial angle of attack in the range $50° \leq \alpha_z \leq 65°$ or $100° \leq \alpha_z \leq 140°$. These transitional mode plates initially exhibit oscillations between positive and negative values of $\overline{\omega}$ but eventually enter into stable autorotation when $\overline{\omega} \approx \overline{\omega}_o$ as shown in Figure 6.5(b).

Based on the results from mode 1 and mode 2 plates, it can be concluded that provided the flight duration is long enough and the mass moment of inertia of the plate is sufficiently large to allow plate autorotation (see Section 2.3.2), a free-flying plate will enter into autorotation at a stable value of $\overline{\omega}_o$, regardless of the initial orientation. Plate geometry and mass moment of inertia are therefore crucial parameters in determining whether plate autorotation occurs. However, the rotational direction and time required to reach stable autorotation are found to be strongly dependant on the initial orientation of the plate.

Mode 3, Autorotational flight, occurs for $-35° < \alpha_z < 45°$. Plates rotate with either positive or negative velocities from the start, with no change in rotational direction during the simulation, and quickly reach the stable autorotational speed, $\overline{\omega}_o$, as shown in Figure 6.5(c). The plate's rotational direction is strongly influenced by initial orientation, with plates having an initial orientation in the range $-35° \leq \alpha_z < 0°$ exhibiting $\overline{\omega} > 0$ while plates with initial orientation $0° \leq \alpha_z \leq 45°$ have $\overline{\omega} < 0$.

It should be noted, however, that due to the positive (upward) high initial lift experienced by plates of initial angle of attack, $\alpha_z > 0°$, in contrast to the negative (downward) lift experienced by plates of initial angle, $\alpha_z < 0°$, the plates with a

positive initial angle of attack are observed to fly further for the flight durations considered despite having a lower maximum horizontal velocity. A convergence in trajectories is apparent as illustrated in Figure 6.7(c), implying that given longer flight durations, plates with negative initial angle of attack would in fact catch up with the positive initial angle of attack plates and subsequently fly further.

In all modes, the terminal vertical velocity of the plate is found to be relatively independent of initial orientation. The horizontal velocity is however strongly influenced by the rotational direction of the plate. Plates with a terminal $\overline{\omega} > 0$ fly with $\overline{u} > 1$, while plates with terminal $\overline{\omega} < 0$ exhibit $\overline{u} < 1$. Plates in the transitional flight mode with an unstable $\overline{\omega}$ of zero mean (Figure 6.5(a)), exhibit an oscillating $\overline{u}$ with values close to 1.0, as shown in Figure 6.6(a). These CFD-RBD results reveal that existing assumptions that $\overline{u}$ has an asymptotic limit of 1.0 are in fact incorrect and need to be re-evaluated.

This coupling between the rotational direction and the terminal plate horizontal speed can be explained by the presence of autorotational drag, lift and torque. As previously demonstrated using forced rotation simulations in Section 5.3, these autorotational coefficients vary with the plate's instantaneous rotational speed and they act in a direction determined by the the plate's direction of rotation. Depending on the direction of rotation, the autorotational drag will either act to accelerate or decelerate the plate. This is further discussed in more detail in Section 6.3.

Mode 4, *complex 3D spinning* is the final mode and this was observed for plates in batch 2. Figure 6.8 shows the computed trajectory results for these complex 3D spinning mode plates. Terminal horizontal and vertical speeds, $\overline{u}$, and $\overline{v}$, are in the same range as modes 1-3 plates. In addition, complex 3D spinning mode plates exhibit significant horizontal cross-wind speeds (Figure 6.8(e)), as well as rotations about the X-axis and vertical Y-axis. This flight mode has been identified by Kordi and Kopp (2009b) as the the most common flight mode.

The CFD-RBD model is shown to both qualitatively and quantitatively reproduce all the 4 major flight modes observed experimentally by Kordi and Kopp (2009b, 2011) in their destructive wind tunnel studies. Figure 6.9 shows instant-

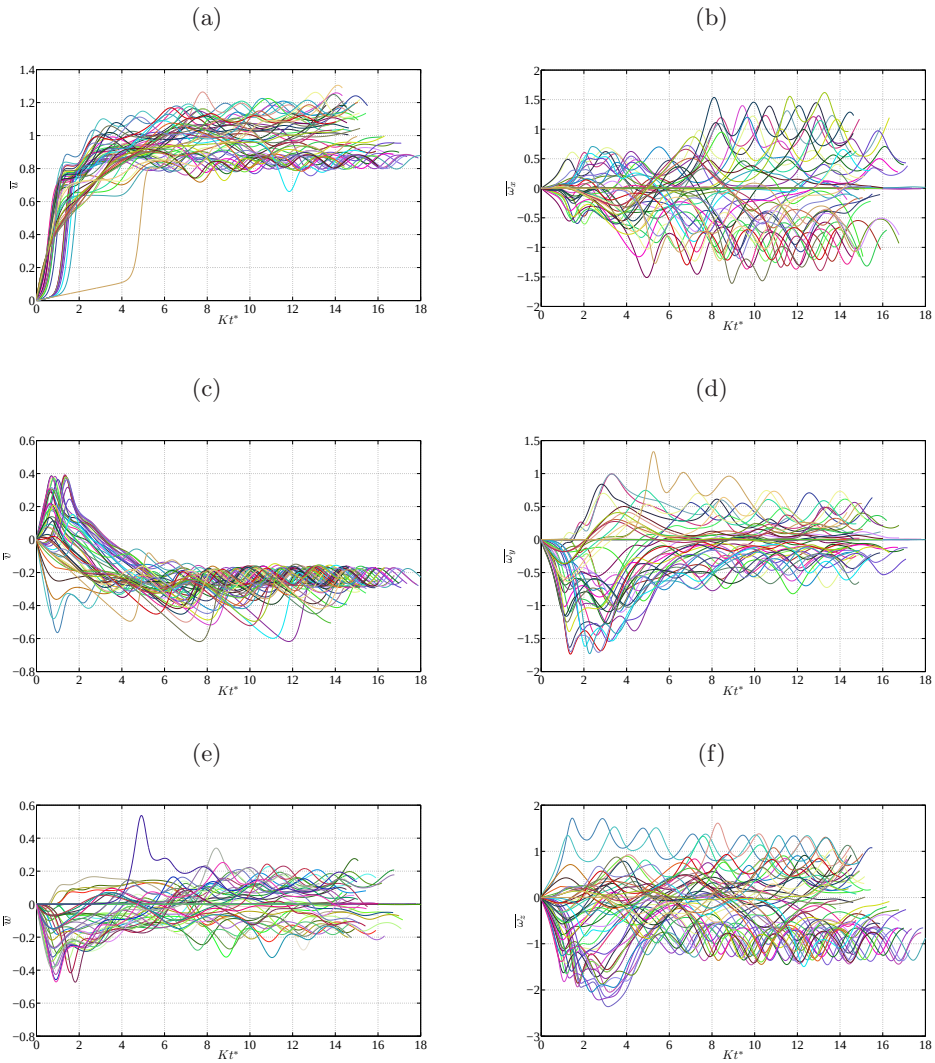

Figure 6.8: Non-dimensionalised translational speed (left) and rotational speed (right) for batch 2 cases.

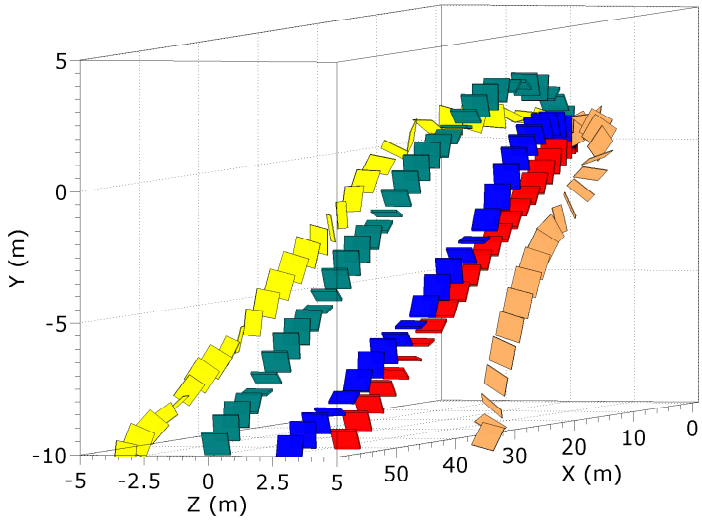

Figure 6.9: Instantaneous orientations of plates in flutter (red), transitional (blue), autorotational (green) and complex 3D spinning (yellow and brown) modes of flight.

aneous snapshots of a plate in each of the four flight modes observed for both batch 1 and 2 cases.

6.2.3 Debris Impact Location

The main application of debris trajectory information derived from the CFD-RBD simulation would be in the prediction of debris impact and damage probabilities for a given target area and debris sources. The key trajectory outputs required in order to perform this risk analysis include, the likelihood of impact from debris as well as the expected impact momentum and orientation (Lin and Vanmarcke, 2010).

The impact point distribution on a vertical plane is illustrated by Figure 6.10 which shows vertical sections through the CFD-RBD predicted trajectories for mode 1-4 plates. The results reveal that although distribution of trajectories on a vertical plane is initially circular as experimentally observed in a wind tunnel by Tachikawa (1988), the distribution progressively becomes more elliptical with increasing distance from the launch position. Predictions for impact location and kinetic energy onto a horizontal plane may also be obtained as shown in Figure 6.11 for launch heights of 3.0 m and 10.0 m. This landing location information is used to compute the number of impacts over a given area for a given set of

simulations, as shown in Figure 6.12, which is valuable for debris risk assessment. The impact kinetic energy is indicated by the point size in Figure 6.11 and would be useful in computing the likelihood of damage upon impact (Wills et al., 2002). More extensive simulations are required in order to derive more realistic debris distribution pattern and impact probabilities. In addition to initial orientation, it is necessary to incorporate different debris types and properties, various wind flow conditions as well as the debris launch conditions. The effect on debris flight trajectories of some of these factors are discussed in the Section 6.4.
The CFD-RBD models has nonetheless been demonstrated as a reliable tool for the numerical prediction of the complex behaviour of plate type windborne projectiles as well as a source for debris impact distribution and momentum information for use in debris risk models. Using CFD-RBD models would help remove some of the practical restrictions of experimental investigations which have been limited to relatively short non-dimensionalised flight times.

6.3 Fluid-Rigid Body Interaction

To better understand the different debris flight modes involved in plate type debris flight, the FSI behaviour associated with each flight mode has been investigated. Results from CFD predictions for the flow field around autorotational, transitional and flutter mode plates have been used to identify the main vortex structures in the plate's wake. In addition, the role of rotational direction in determining the terminal horizontal plate speed is discussed.

6.3.1 Flow Around a Free-Flying Plate

The coherent flow structures in the wake of the plate are similar to those identified in plate autorotation (Section 5.4) namely, a retreating edge vortex that strongly interacts with the plate, an advancing edge vortex that shows a relatively weak interaction with the plate and two tip vortices at the side-edges of the plate. Debris trajectories have been split into two distinct stages - the *launch stage* at $0 < Kt^* < 6.5$, and the *stable flight stage* at $Kt^* > 6.5$, with each stage exhibiting different plate-wake interaction.

Plate-wake interaction during the launch stage: The main distinction between the launch and stable flight stages is that during the launch stage, the plate has a strong interaction with the flow structures in its wake. Figures 6.13

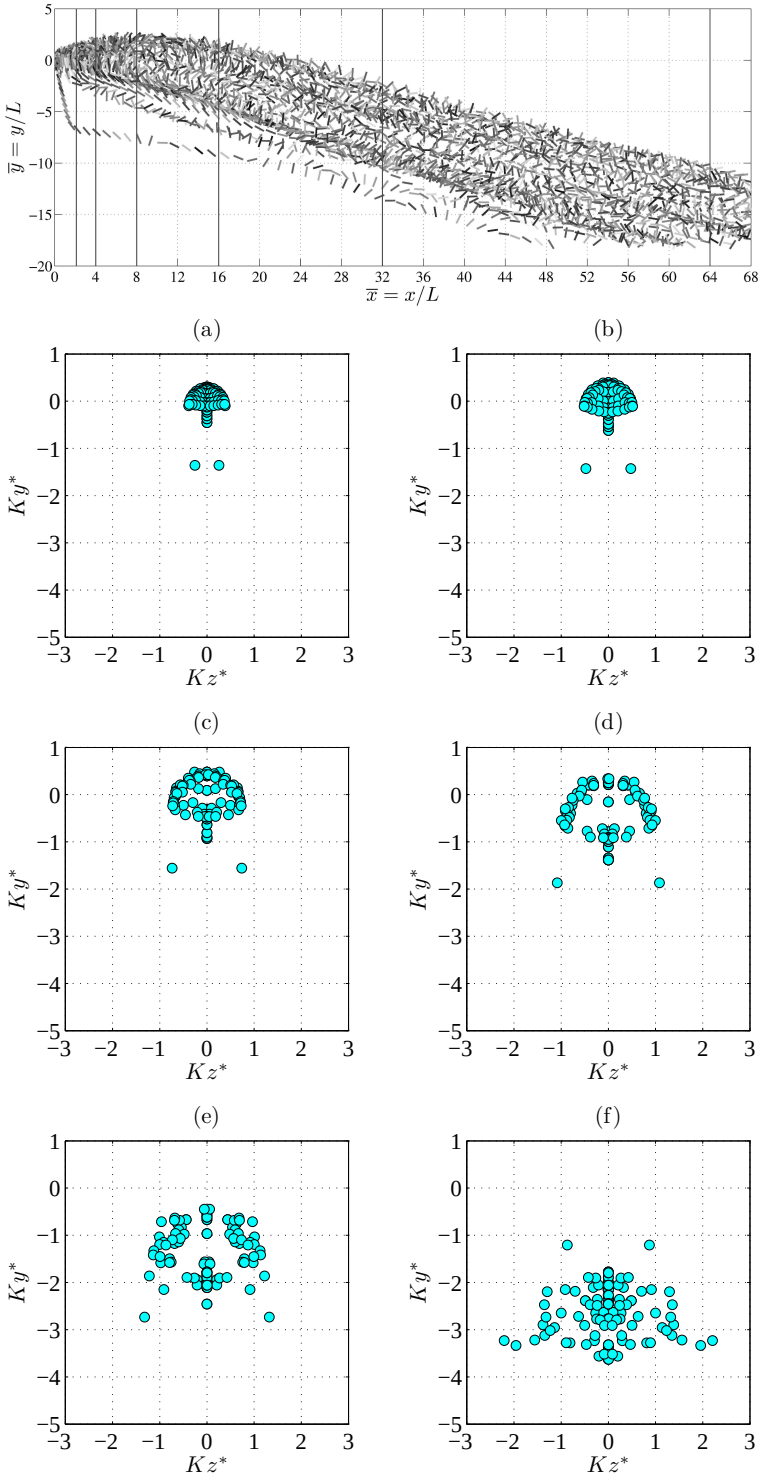

Figure 6.10: Vertical section showing plate locations in the Z-Y plane at a distance in the along-wind direction of; (a) $2L$ (b) $4L$ (c) $8L$ (d) $16L$ (e) $32L$ and (f) $64L$ from the plate's launch position.

(a)

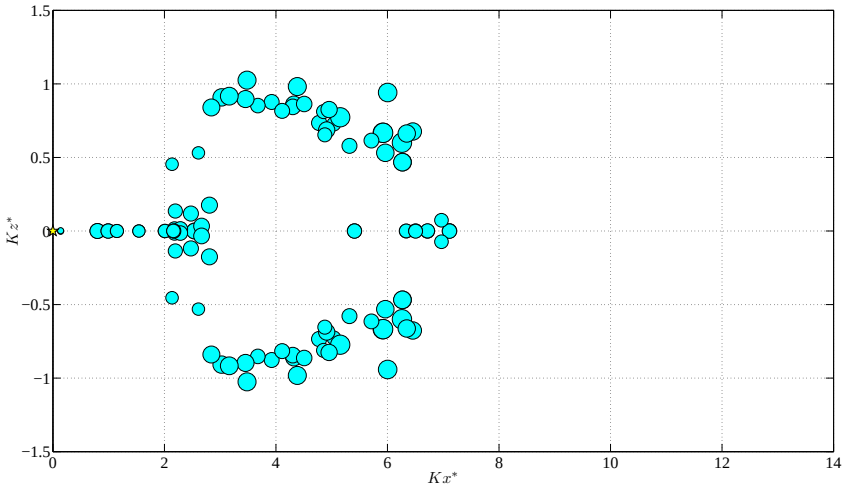

(b)

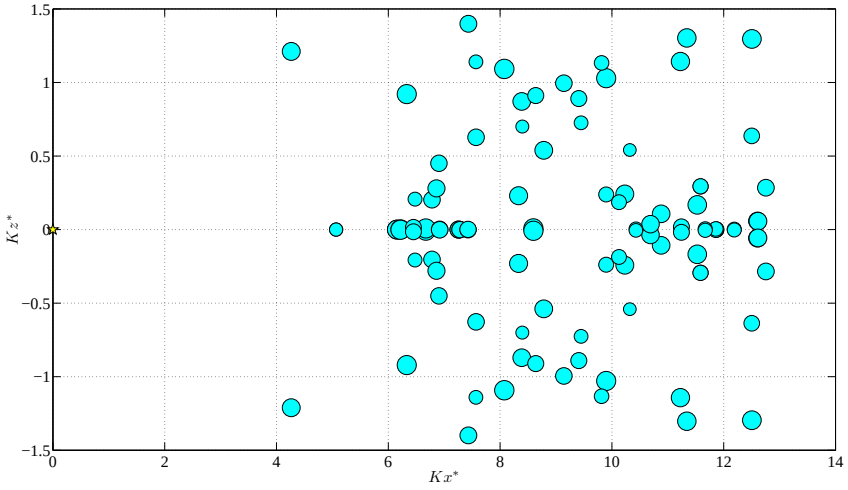

Figure 6.11: Scatter plot of debris impact location relative to the launch position (★) for (a) 3 m launch height and (b) 10 m launch height, with points scaled according to impact kinetic energy.

(a)

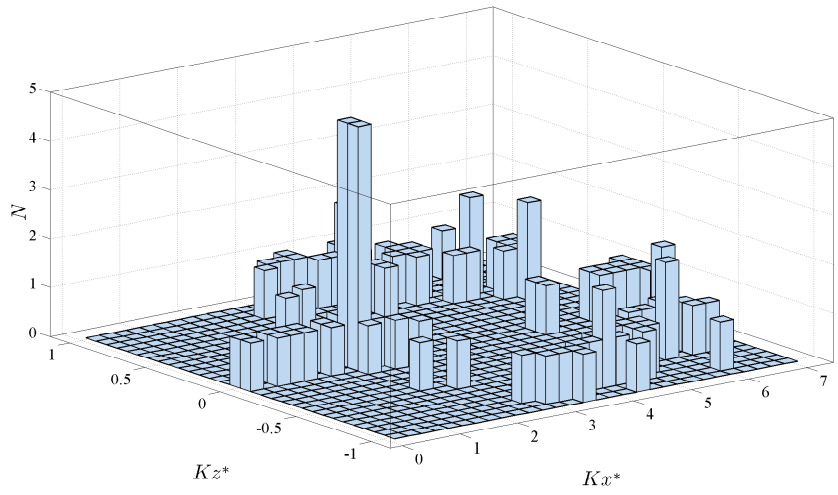

(b)

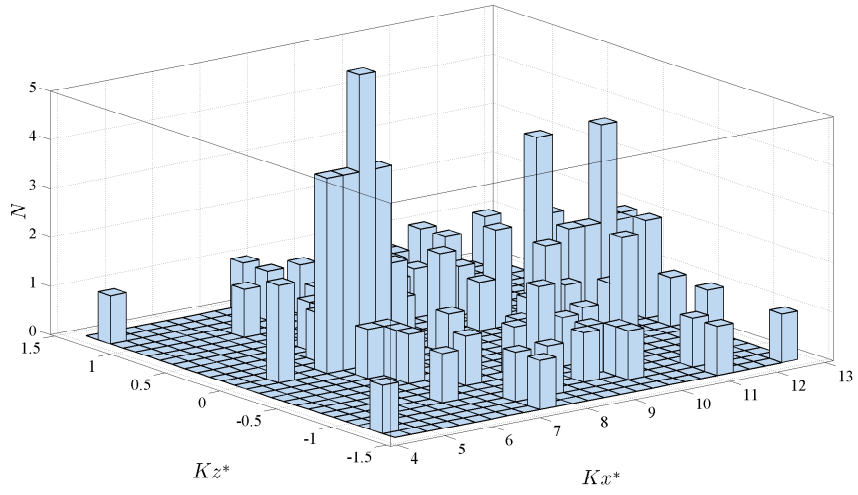

Figure 6.12: Estimated number of impacts at a given ground location for (a) 3 m launch height and (b) 10 m launch height.

- 6.16 illustrate the plate's interaction with the vortex structures in it's wake during the launch stage.

In addition, during the plate launch stage, unlike the fixed-axis autorotational behaviour where the retreating edge vortex is shed at approximately 90°, here the retreating edge vortex remains stably attached until $\alpha_z \approx 180°$. The strong non-linear interaction between the plate and this stably attached vortex is responsible for the large translational and rotational accelerations experienced by the plate in the launch stage. While Taylor's frozen turbulence hypothesis (Taylor, 1938) implies that the vortices shed from the plate should normally be translated away from the plate at the instantaneous relative wind speed, due to the plate's rapid acceleration the vortices shed into its wake are not translated away quickly enough. This would explain the strong plate-wake interaction and delayed vortex shedding observed. Similar behaviour is observed between the plate and its stably attached retreating edge vortex in the flutter mode cases where the mean relative wind speed is approximately zero since the plate translates with $\overline{u} = 1.0$. Fixed-axis autorotation, previously described in Section 5.4, does not accurately represent the strongly unsteady behaviour involved in plate launch and flutter modes. As a result, the use of quasi-steady force models based on fixed-axis autorotation theory is questionable in these scenarios. A detailed comparison of quasi-steady analytical models and URANS CFD predictions is presented in Section 6.5.

Plate-wake interaction during the stable flight stage: As the plate continues to accelerate, it eventually reaches a terminal vertical and horizontal translational speed and settles into a stable flight stage. In this stable flight stage, the plate exhibits FSI effects equivalent to fixed-axis plate autorotation as shown in Figures 6.17 - 6.18. Vortex shedding is observed from the retreating and advancing edges as well as the side edges in each rotational cycle. The findings reveal that fixed-axis autorotation is a sufficient qualitative representation of plate behaviour in the stable flight stage and as a result, quasi-steady force models are expected to perform well in these cases.

Autorotational lift and drag components resulting from the plate's interaction with the flow structures in its wake are observed to play an important role in determining the terminal horizontal speed of the plate. Figures 6.17 - 6.18 show

(a)

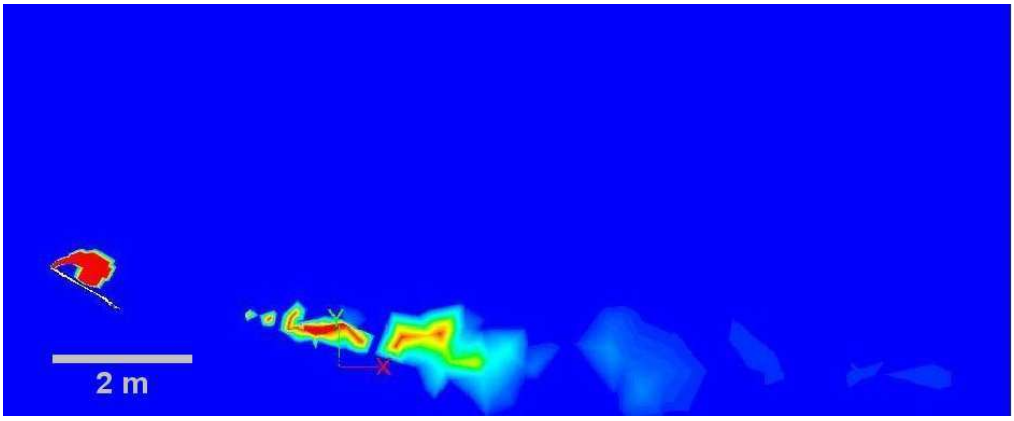

(b)

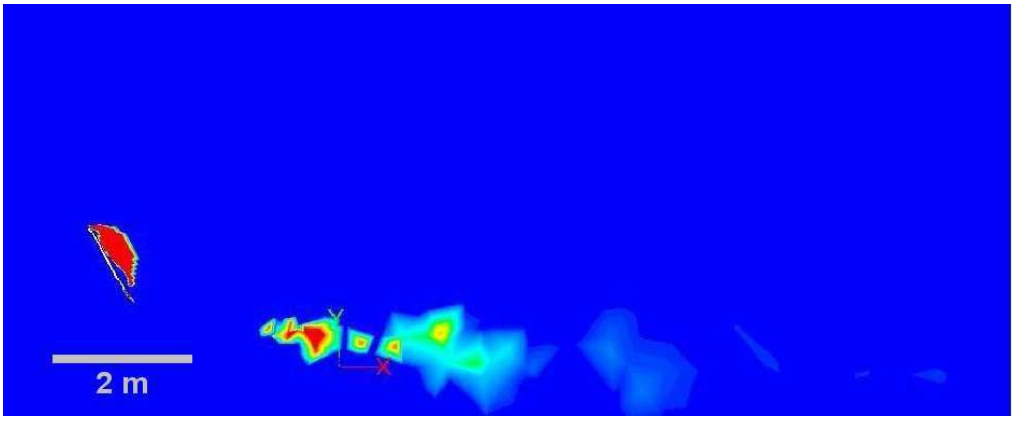

(c)

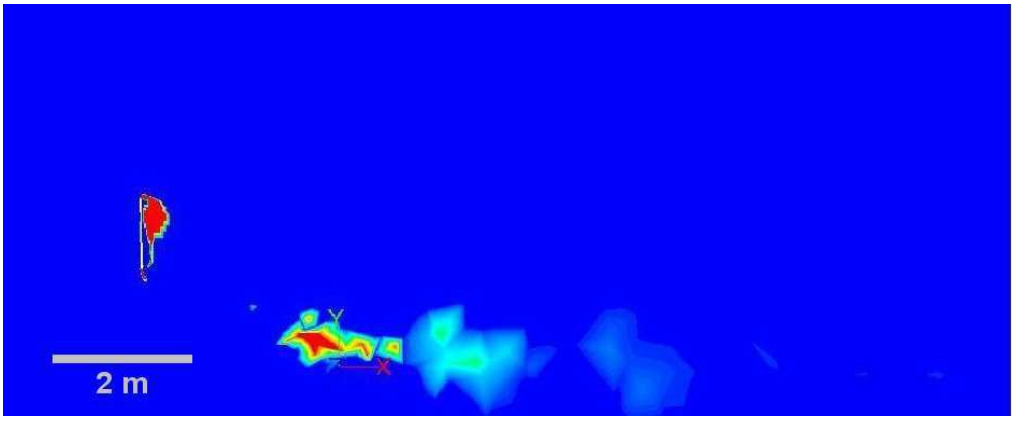

Figure 6.13: Q-value contours at instantaneous angles of attack of (a) 30°, (b) 60° and (c) 90°, during the launch stage for a plate of initial $\alpha_z = 30°$.

(a)

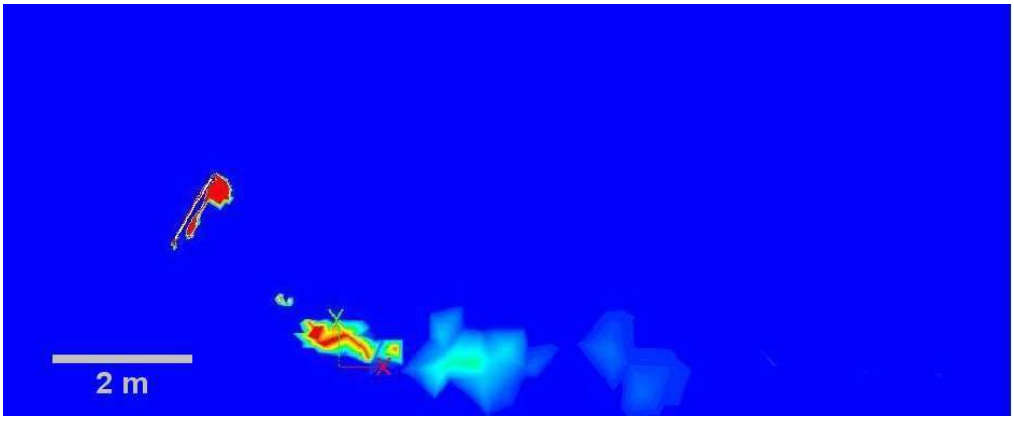

(b)

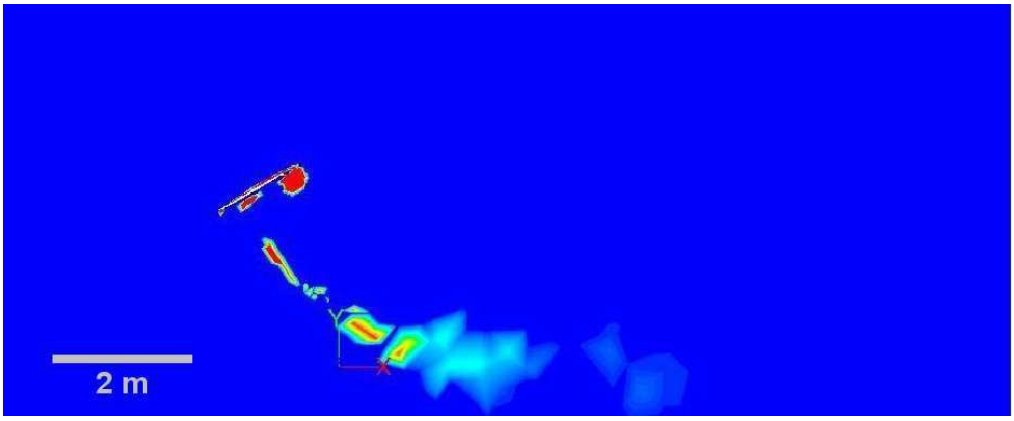

(c)

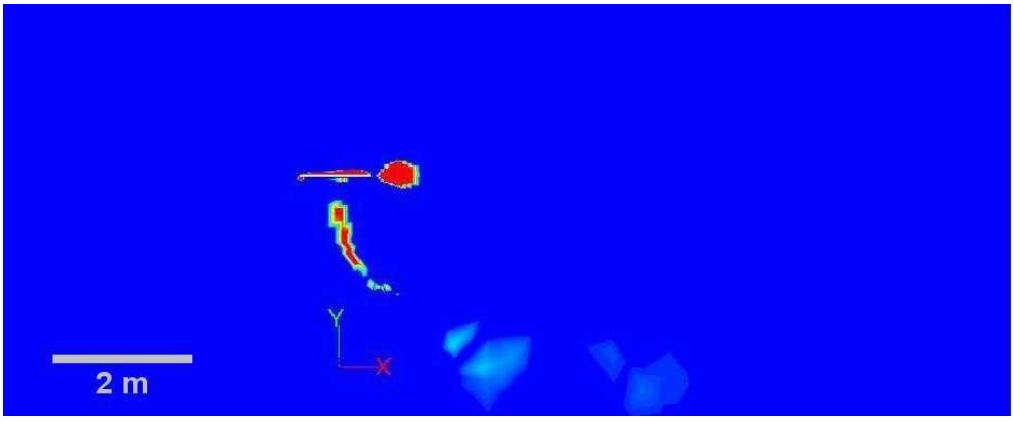

Figure 6.14: Q-value contours at instantaneous angles of attack of (a) 120°, (b) 150° and (c) 180°, during the launch stage for a plate of initial $\alpha_z = 30°$.

(a)

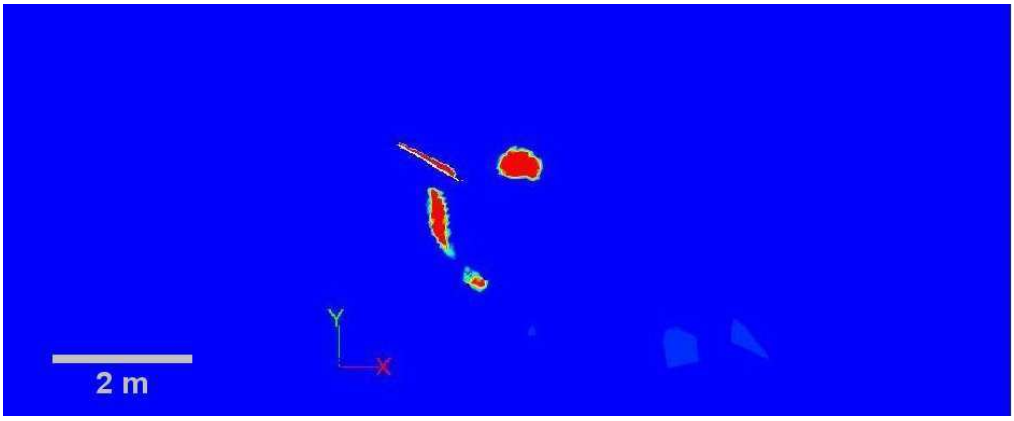

(b)

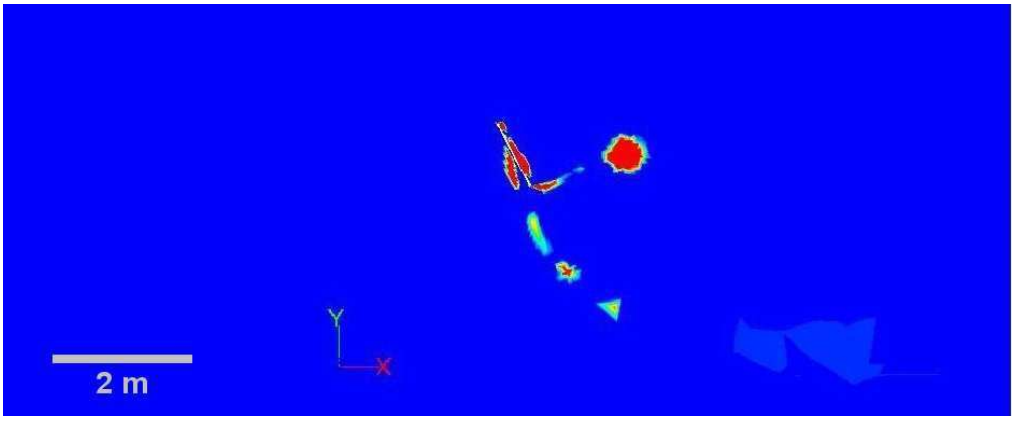

(c)

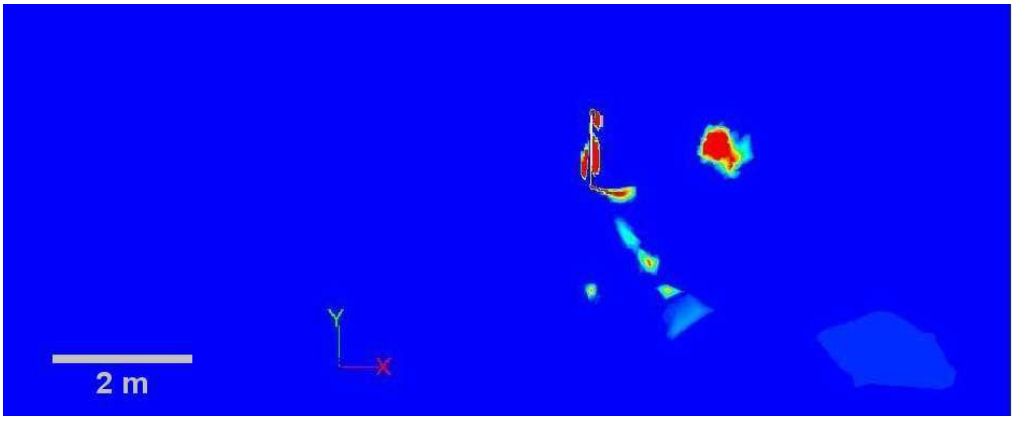

Figure 6.15: Q-value contours at instantaneous angles of attack of (a) 210°, (b) 240° and (c) 270°, during the launch stage for a plate of initial $\alpha_z = 30°$.

(a)

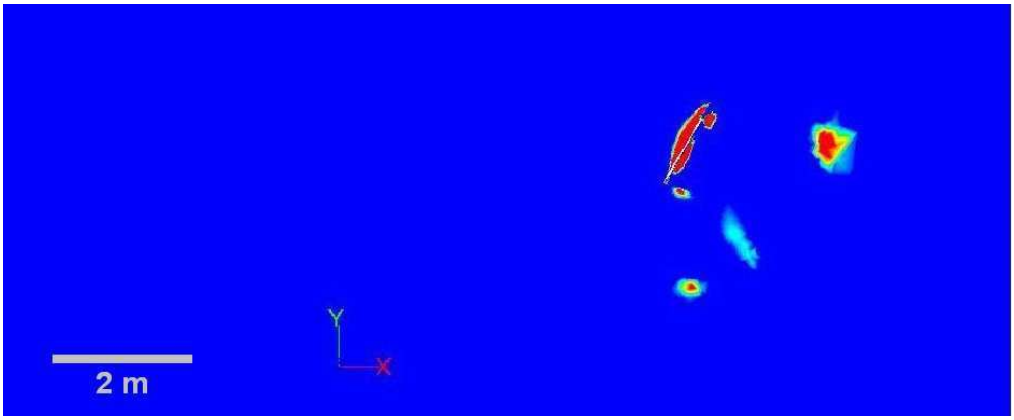

(b)

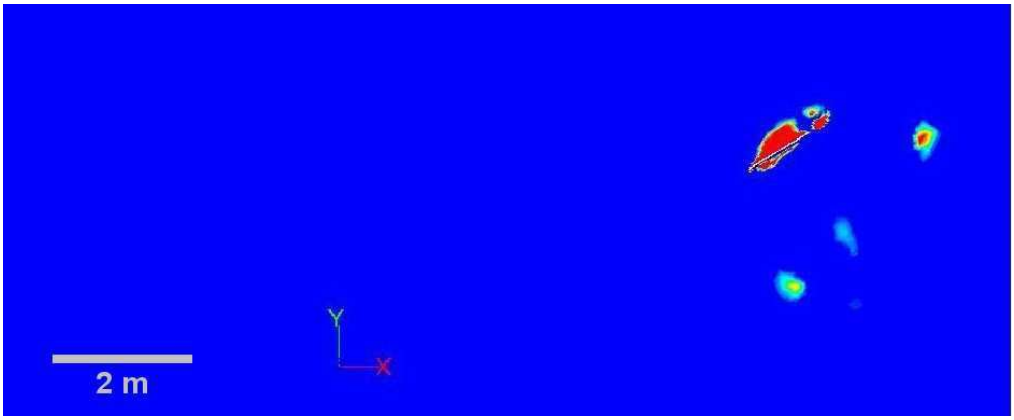

(c)

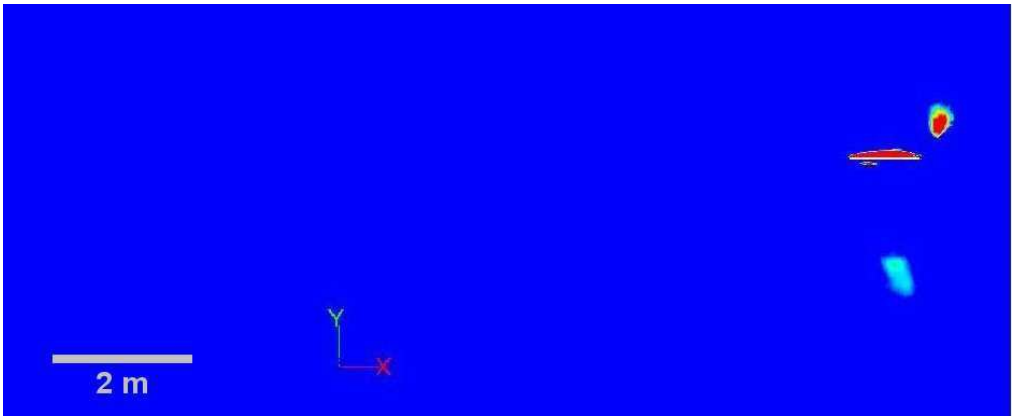

Figure 6.16: Q-value contours at instantaneous angles of attack of (a) 300°, (b) 330° and (c) 360°, during the launch stage for a plate of initial $\alpha_z = 30°$.

(a)

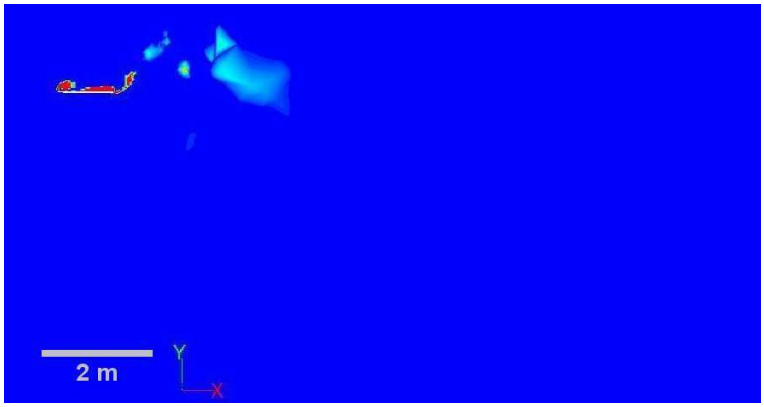

(b)

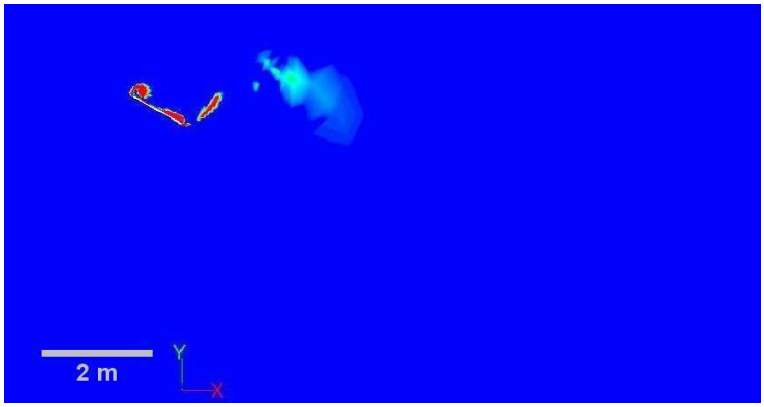

(c)

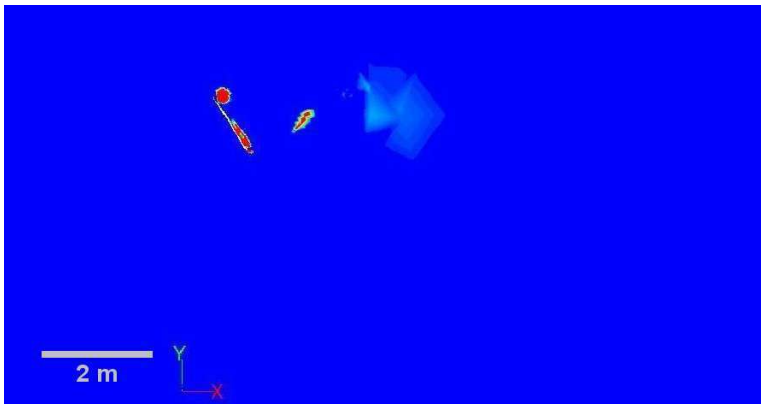

Figure 6.17: Contours of Q-criterion value showing the strong interaction between an autorotational flight mode plate with a negative or clockwise rotational speed and the flow structures in its wake. Contours are taken at instantaneous angles of attack of (a) 0°, (b) 30° and (c) 60°, relative to the mean horizontal wind flow.

(a)

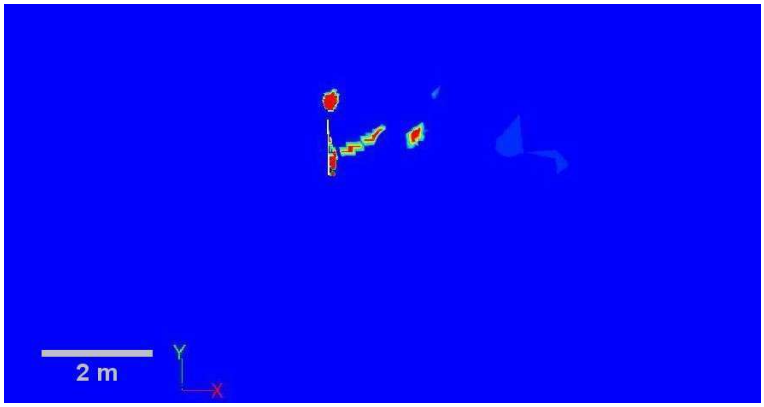

(b)

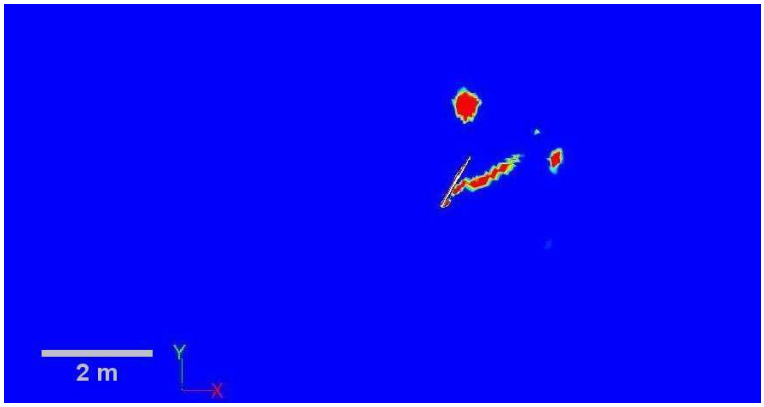

(c)

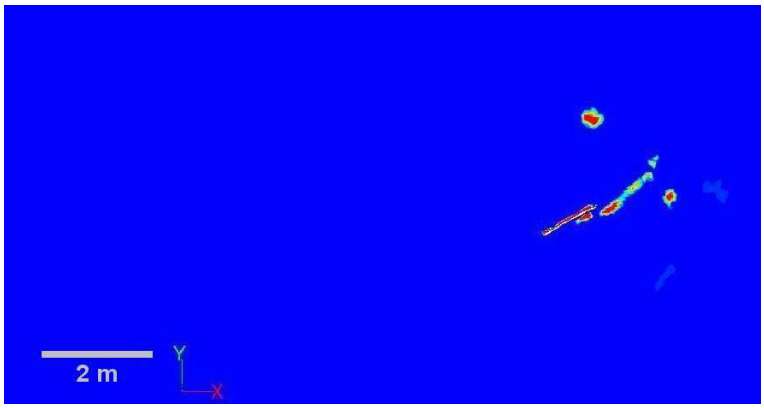

Figure 6.18: Contours of Q-criterion value showing the strong interaction between an autorotational flight mode plate with a negative or clockwise rotational speed and the flow structures in its wake. Contours are taken at instantaneous angles of attack of (a) 90°, (b) 120° and (c) 150°, relative to the mean horizontal wind flow.

the flow structures around a plate with negative (clockwise) rotational speed, while Figures 6.19 - 6.19 show the flow structures around a plate with positive (anti-clockwise) rotational speed.

Depending on the direction of rotation, the plate's interaction with the retreating edge vortex during stable flight will result in a negative autorotational drag and positive autorotational lift or positive autorotational drag and negative autorotational lift.

6.3.2 Effects of Rotational Direction

Results in section 6.2.2 show that the direction of rotation is strongly dependant on the initial orientation for autorotational plates. We may decompose the flow field into a vertical wind component flow associated with the relative downward motion between the plate and the surrounding air, and a horizontal wind flow component due to the mean horizontal relative wind speed. The mean force in the X-direction, F_{X}, and the mean force in the Y-direction, F_{Y}, over a rotational cycle may then also be decomposed into components due to the horizontal and vertical wind speeds, as illustrated in Figure 6.21.

As previously discussed in Section 5.3, the magnitude of these autorotational forces is related to the magnitude of rotational speed and the direction of the forces is dependant on the direction of rotation. For clockwise (negative) rotational speeds, as shown in Figure 6.21(a,c), the horizontal and vertical forces acting on the plate may be computed according to

$$F_{\mathrm{X}} = D_{\mathrm{H}} - L_{\mathrm{V}}, \tag{6.2}$$

$$F_{\mathrm{Y}} = D_{\mathrm{V}} + L_{\mathrm{H}} - mg, \tag{6.3}$$

Similarly, for a plate with anti-clockwise (positive) rotational speed, shown in Figure 6.21(b,d), the horizontal and vertical forces acting on the plate over a rotational cycle are

$$F_{\mathrm{X}} = D_{\mathrm{H}} + L_{\mathrm{V}}, \tag{6.4}$$

$$F_{\mathrm{Y}} = D_{\mathrm{V}} - L_{\mathrm{H}} - mg, \tag{6.5}$$

Let us start at $Kt^* \approx 1.0$, when both positive and negative rotational speed plates have reached their peak vertical speeds, and have similar horizontal speeds $\overline{u} \approx 0.4$ as shown in Figure 6.6. In the clockwise rotating plates, the vertical

(a)

(b)

(c)

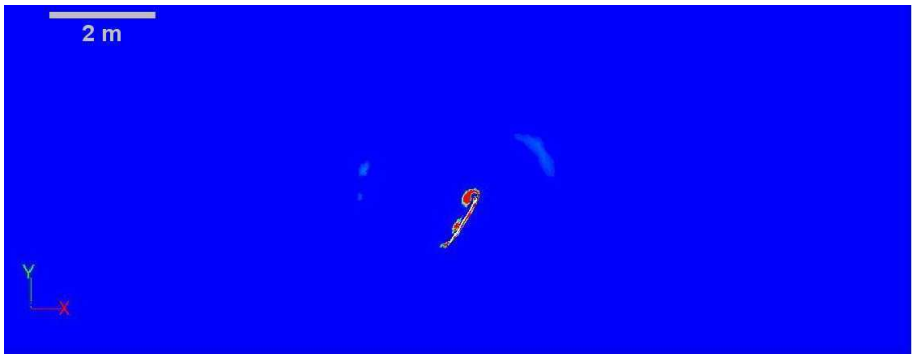

Figure 6.19: Contours of Q-criterion value showing the strong interaction between an autorotational flight mode plate with a positive or anti-clockwise rotational speed and the flow structures in its wake. Contours are taken at instantaneous angles of attack of (a) 0°, (b) -30° and (c) -60°, relative to the mean horizontal wind flow.

(a)

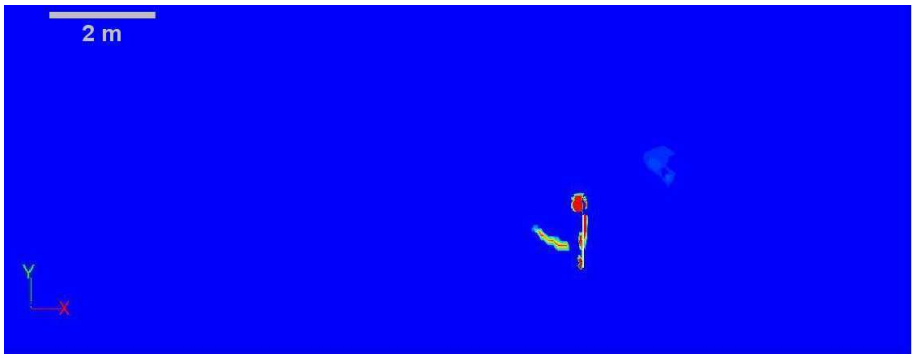

(b)

(c)

Figure 6.20: Contours of Q-criterion value showing the strong interaction between an autorotational flight mode plate with a positive or anti-clockwise rotational speed and the flow structures in its wake. Contours are taken at instantaneous angles of attack of (a) -90°, (b) -120° and (c) -150° relative to the mean horizontal wind flow.

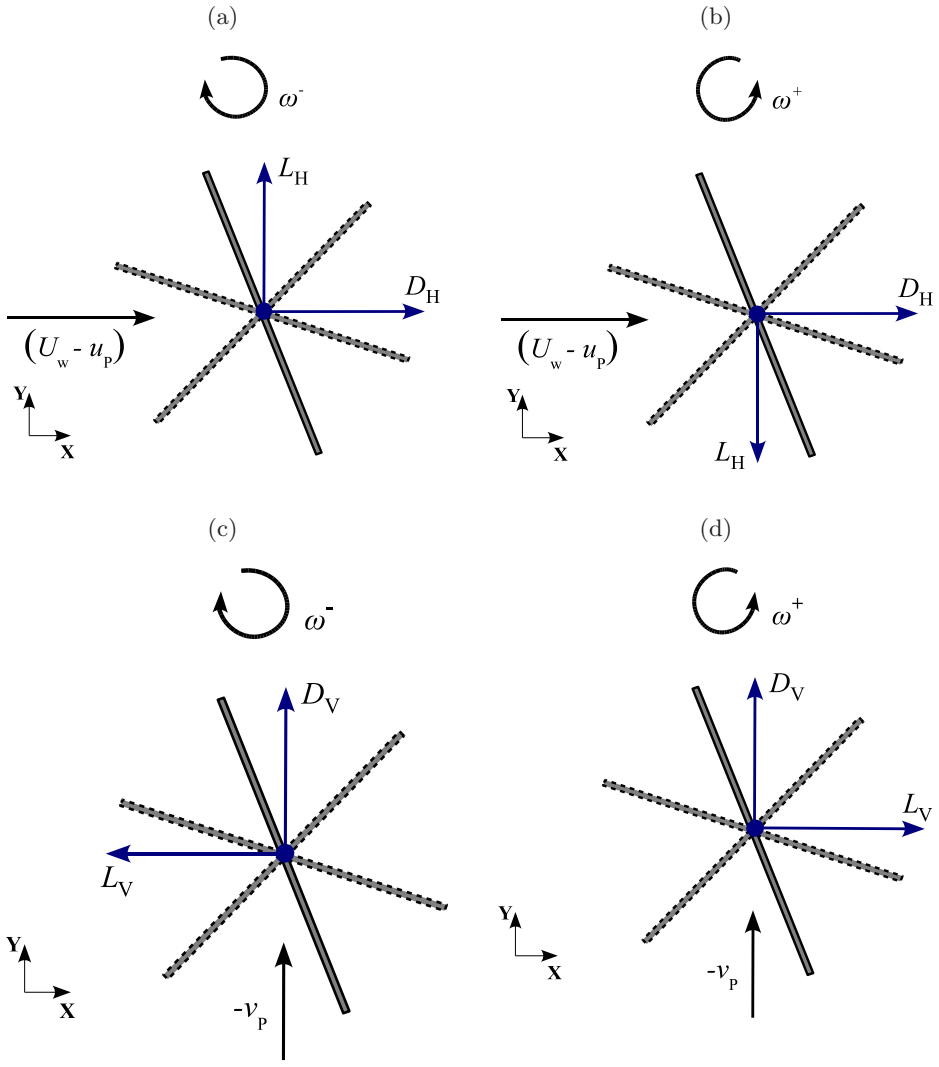

Figure 6.21: Decomposition of mean drag and lift acting on a free-flying plate over a single rotational cycle into; (a, b) the autorotational forces associated with the horizontal velocity component and (c, d) autorotational forces associated with the vertical velocity component, for clockwise or negative rotations (left) and anti-clockwise or positive rotations (right).

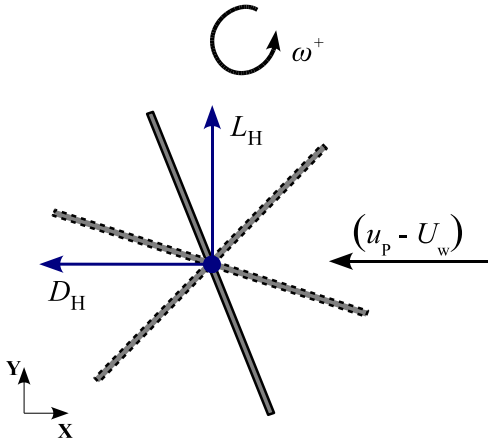

Figure 6.22: Decomposition of the mean autorotational drag and lift on a free-flying plate with instantaneous $\overline{u} > 1.0$ and a positive (anti-clockwise) rotational speed.

velocity, $\overline{v}$, will initially decrease from its peak positive value to zero and become negative as the plate reaches its maximum elevation and starts to fall downwards at $Kt^* \approx 3.0$. As the magnitude of v_p increases, L_V will also increase until $D_\mathrm{H} = L_\mathrm{V}$ and $D_\mathrm{V} + L_\mathrm{H} = mg$, hence $F_\mathrm{X} = F_\mathrm{Y} = 0.0$ and the plate continues in flight with a terminal vertical and horizontal velocity. This occurs when $\overline{v} \approx -0.2$ and $\overline{u} \approx 0.8U_\mathrm{w}$.

However in anti-clockwise rotating plates, since D_H and L_V both act to accelerate the plate, it will continue to accelerate beyond $u_p \approx 0.8U_\mathrm{w}$, until $u_p \approx U_\mathrm{w}$, implying a zero horizontal component of wind speed, and as a result, $D_\mathrm{H} = L_\mathrm{H} = 0$. However, a significant horizontal accelerating force, $F_\mathrm{X} = L_\mathrm{V}$ is still present and this continues to drive the horizontal velocity of the plate such that $u_\mathrm{p} > U_\mathrm{w}$ (i.e. $\overline{u} > 1.0$). As u_p continues to increase beyond U_w, the horizontal component of relative wind speed becomes reversed and consequently, the drag and lift forces associated with this negative relative wind speed are also reversed as illustrated in Figure 6.22.

As a result, the new horizontal and vertical force may be computed as

$$F_\mathrm{X} = L_\mathrm{V} - D_\mathrm{H}, \tag{6.6}$$

$$F_\mathrm{Y} = D_\mathrm{V} + L_\mathrm{H} - mg. \tag{6.7}$$

Subsequently, as u_p increases further, eventually at $\overline{u} \approx 1.2$, $L_\mathrm{V} = D_\mathrm{H}$ and

$D_V + L_H = mg$, hence $F_X = F_Y = 0.0$, and the plate continues to fly at a terminal horizontal and vertical velocity.

The terminal vertical and horizontal speeds of the plate are therefore thought to be controlled by the autorotational drag and lift associated with the non-linear interaction between the plate and the flow. Figure 6.23 shows the time-series of horizontal and vertical aerodynamic forces acting on the plate for both clockwise and anti-clockwise rotational directions. The plate with initial angle of attack, $\alpha_o = 30°$ flies with a clockwise rotational speed, while the plate with $\alpha_o = -30°$ flies with an anti-clockwise rotational speed.

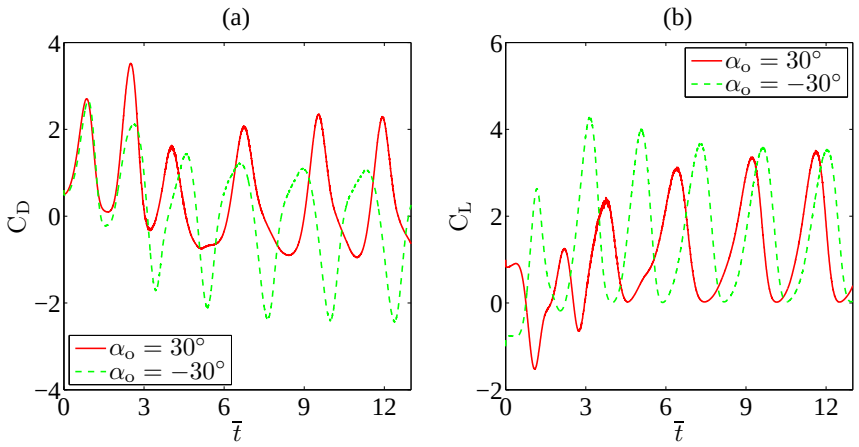

Figure 6.23: CFD computed time-series of the non-dimensionalised aerodynamic forces acting on free-flying plates, decomposed into; (a) horizontal force coefficient, C_{FX}, and (b) vertical force coefficient, C_{FY}. Plates with initial angle of attack, $\alpha_o = 30°$ fly with a clockwise rotational speed, while plates with $\alpha_o = -30°$ fly with an anti-clockwise rotational speed.

As a result of the non-linear interaction described in this section, a rotating plate is able to convert some of its gravitational potential energy into lateral kinetic energy. Depending on the direction of rotation this will result in plates exhibiting terminal horizontal wind speeds higher than the mean wind speed or consistently lower than the mean wind speed. Only flutter mode plates with $\overline{\omega} \approx 0.0$ will fly with a terminal horizontal speed of approximately 1.0.

6.4 Parametric Studies

The results discussed in the previous section were obtained from simulations performed using the same flow conditions and plate properties. As discussed in section 2.4, aside from initial orientation, debris trajectories have been shown to be sensitive to variations in flow properties - parameterised using the Tachikawa number, $K(= \rho U_w^2 A/2mg)$, which is a function of the Froude number and buoyancy parameter, - and plate properties - parameterised using the non-dimensional inertial parameter, $\Delta_{zz}(= ML^2/I_{zz})$, the thickness ratio, $\tau = h/L$, and aspect ratio B/L. In this section, the CFD-RBD model is applied to the numerical investigation of the effects of these parameters on debris flight behaviour.

In order to achieve this, an additional 35 simulations have been carried out, including each of the four flight modes identified in Section 6.2.2 at a Tachikawa number of 8.3. The cases are sub-divided into 7 subgroups, A to G depending on the initial orientation and expected flight as shown in Table 6.1. Cases A and D represent autorotational mode plates, case B represents transitional mode plates, case C represents flutter mode plates, while cases labelled E, F and G are expected to enter into a complex 3D spinning mode. A description of the cases run for the whole range of initial orientations is presented in Table 6.2.

For each of the 7 case groups, each corresponding to a different initial orientation, a total of 5 simulations were run. Cases numbered 1,2 and 3 in each case group refer to simulations performed to assess the sensitivity of the simulation to K by varying the inflow wind speed, while keeping the plate's mass and geometry properties constant. The results of these simulations are reported in section 6.4.1.

Cases numbered 4 and 5 were performed to illustrate the effect of variations in the plate's geometric and mass properties for a constant K. Cases 4 and 1 are together used to investigate the effects of τ and Δ_{zz} on trajectory dispersion, while cases numbers 4 and 5 together are used to illustrate the effects of variations in B/L. The results of these sensitivity studies for plate parameters are reported in section 6.4.2

For all the cases run as part of the parametric studies, the same boundary conditions, turbulence model, discretisation scheme and pressure-velocity coupling

Table 6.1: A list of the initial orientations used for parametric study simulations.

Batch	Orientation			Mode
	θ_o (°)	ϕ_o (°)	ψ_o (°)	
A	0.00	0.00	75.00	Autorotational
B	0.00	0.00	45.00	Transitional
C	0.00	0.00	15.00	Flutter
D	0.00	0.00	-75.00	Autorotational
E	10.73	10.54	45.99	3D Spinning
F	35.26	30.00	54.74	3D Spinning
G	69.25	43.08	75.49	3D Spinning

scheme described in Section 6.1 have been used.

6.4.1 Tachikawa Number

21 simulations are performed at three different wind speeds of 20.0 m/s, 17.5 m/s and 15.0 m/s to illustrate the effect of varying flow parameters on plate behaviour. The results are shown in Figures 6.24 - 6.26.

As shown in Figure 6.24 (a,c,e), with increasing K, plates are observed to fly higher and further due to the greater influence of aerodynamic forces relative to gravitational forces. Even when non-dimensionalised using K, the variation in mean trajectory is still evident. The dispersion of trajectories away from the mean is also observed to increase with increasing Tachikawa number. The direct implication of this is that although K is shown to be an adequate parameterisation of debris flight range, the validity of fit expressions for Kx^* and Ky^*, such as (2.23) by Lin et al. (2006) and (6.1) is questionable. Although such expressions have become incorporated into debris risk models (Lin and Vanmarcke, 2010), they are clearly not valid away from the Tachikawa numbers for which they are derived.

The non-dimensionalised terminal horizontal, vertical and rotational speeds, are found to be independent of K, as shown in Figure 6.25 and Figure 6.26(b,d,f). As a result, fit expressions for $\overline{u}$, such as (2.22) may be expected to remain valid over a range of K. The lateral cross-wind velocity component in the 3D spinning mode cases is found to be sensitive to K as shown in Figure 6.26(a,c,e). As a result, a significant difference in the overall lateral dispersion of trajectories is

Table 6.2: CFD-RBD cases run as part of the parametric study for windborne debris flight. All plates are of thickness, $h = 0.025$ m.

Case	L (m)	B (m)	$\rho_{\mathrm{m}}/\rho_{\mathrm{a}}$	U_{w}	K	Fr	$1/\tau$	Δ_{zz}	B/L
A1	1.00	1.00	97.959	20.0	8.325	6.386	40.00	11.993	1.00
A2	1.00	1.00	97.959	17.5	6.374	5.587	40.00	11.993	1.00
A3	1.00	1.00	97.959	15.0	4.683	4.789	40.00	11.993	1.00
A4	0.56	0.56	55.102	15.0	8.325	6.385	22.50	11.976	1.00
A5	0.56	1.00	55.102	15.0	8.325	6.385	22.50	11.976	1.78
B1	1.00	1.00	97.959	20.0	8.325	6.386	40.00	11.993	1.00
B2	1.00	1.00	97.959	17.5	6.374	5.587	40.00	11.993	1.00
B3	1.00	1.00	97.959	15.0	4.683	4.789	40.00	11.993	1.00
B4	0.56	0.56	55.102	15.0	8.325	6.385	22.50	11.976	1.00
B5	0.56	1.00	55.102	15.0	8.325	6.385	22.50	11.976	1.78
C1	1.00	1.00	97.959	20.0	8.325	6.386	40.00	11.993	1.00
C2	1.00	1.00	97.959	17.5	6.374	5.587	40.00	11.993	1.00
C3	1.00	1.00	97.959	15.0	4.683	4.789	40.00	11.993	1.00
C4	0.56	0.56	55.102	15.0	8.325	6.385	22.50	11.976	1.00
C5	0.56	1.00	55.102	15.0	8.325	6.385	22.50	11.976	1.78
D1	1.00	1.00	97.959	20.0	8.325	6.386	40.00	11.993	1.00
D2	1.00	1.00	97.959	17.5	6.374	5.587	40.00	11.993	1.00
D3	1.00	1.00	97.959	15.0	4.683	4.789	40.00	11.993	1.00
D4	0.56	0.56	55.102	15.0	8.325	6.385	22.50	11.976	1.00
D5	0.56	1.00	55.102	15.0	8.325	6.385	22.50	11.976	1.78
E1	1.00	1.00	97.959	20.0	8.325	6.386	40.00	11.993	1.00
E2	1.00	1.00	97.959	17.5	6.374	5.587	40.00	11.993	1.00
E3	1.00	1.00	97.959	15.0	4.683	4.789	40.00	11.993	1.00
E4	0.56	0.56	55.102	15.0	8.325	6.385	22.50	11.976	1.00
E5	0.56	1.00	55.102	15.0	8.325	6.385	22.50	11.976	1.78
F1	1.00	1.00	97.959	20.0	8.325	6.386	40.00	11.993	1.00
F2	1.00	1.00	97.959	17.5	6.374	5.587	40.00	11.993	1.00
F3	1.00	1.00	97.959	15.0	4.683	4.789	40.00	11.993	1.00
F4	0.56	0.56	55.102	15.0	8.325	6.385	22.50	11.976	1.00
F5	0.56	1.00	55.102	15.0	8.325	6.385	22.50	11.976	1.78
G1	1.00	1.00	97.959	20.0	8.325	6.386	40.00	11.993	1.00
G2	1.00	1.00	97.959	17.5	6.374	5.587	40.00	11.993	1.00
G3	1.00	1.00	97.959	15.0	4.683	4.789	40.00	11.993	1.00
G4	0.56	0.56	55.102	15.0	8.325	6.385	22.50	11.976	1.00
G5	0.56	1.00	55.102	15.0	8.325	6.385	22.50	11.976	1.78

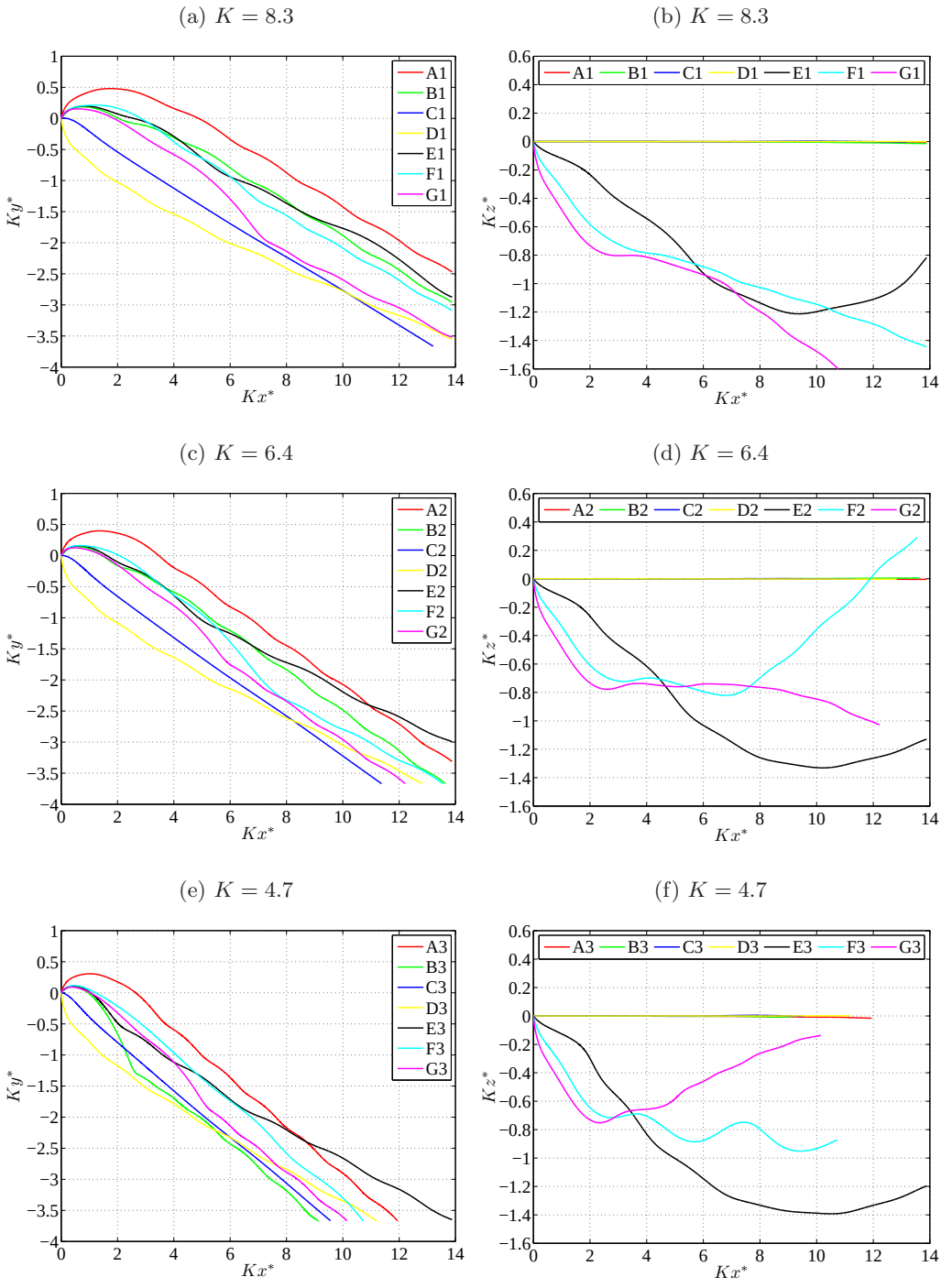

Figure 6.24: CFD-RBD predictions of trajectory in the X-Y plane (left) plate trajectory in the X-Z plane (right) for plates of various initial angles of attack and in flow conditions of Tachikawa number; (a,b) $K = 8.3$, (c,d) $K = 6.4$ and (e,f) and $K = 4.7$.

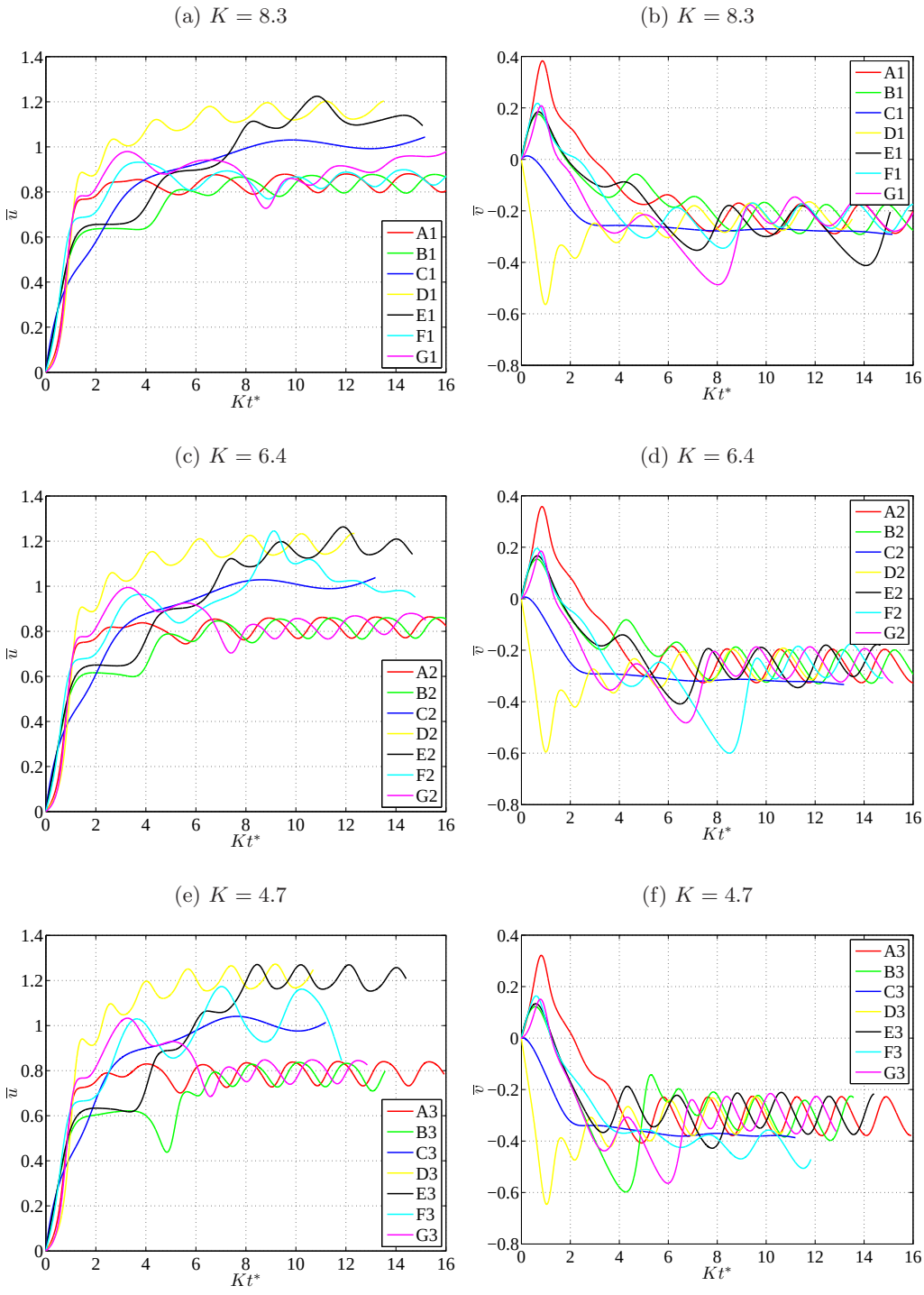

Figure 6.25: CFD-RBD predictions of horizontal along-wind velocity (left) and vertical velocity (right) of plates with varying initial angle of attack and in flow conditions of Tachikawa number; (a,b) $K = 8.3$, (c,d) $K = 6.4$ and (e,f) and $K = 4.7$.

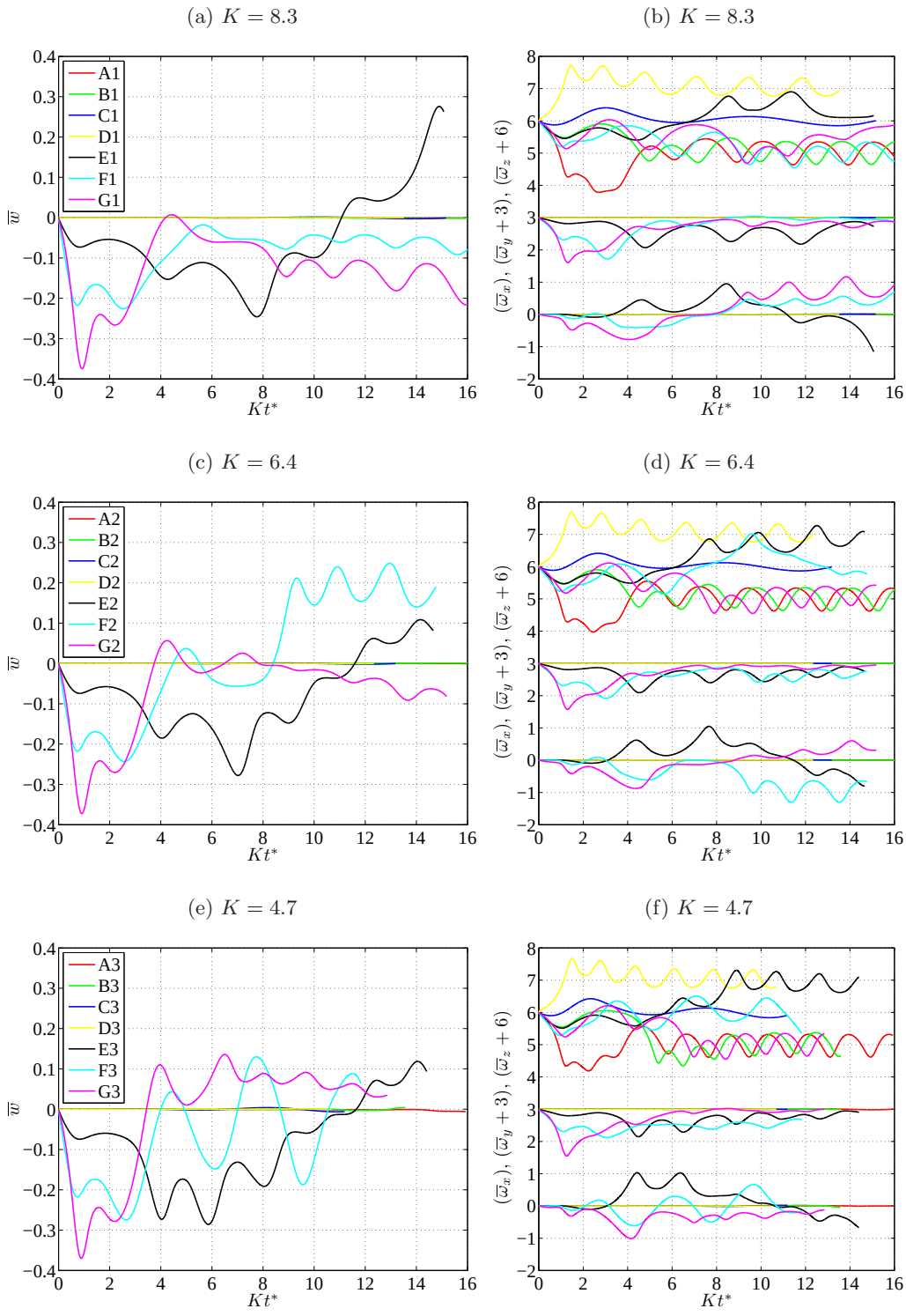

Figure 6.26: CFD-RBD predictions of dimensionless horizontal cross-wind velocity (left) and dimensionless rotational speeds (right) of plates with varying initial angle of attack and in flow conditions of Tachikawa number; (a,b) $K = 8.3$, (c,d) $K = 6.4$ and (e,f) and $K = 4.7$.

therefore observed, with increasing dispersion with increasing K. For instance; cases groups F (F1, F2, F3) and G (G1, G2, G3) in Figure 6.24(b,d,f) exhibit greater lateral dispersion with increasing K while cases group E (E1, E2, E3), showed a decrease in lateral dispersion.

The results of the K sensitivity study agree with previous experimental findings on the relationship between along-wind dispersion and K (Lin et al., 2006). A similar relationship is shown to exist for the overall debris dispersion in the along-wind direction. The mean dimensionless trajectory (Kx^* versus Ky^*) is shown to vary with K and as a result, existing expressions for Kx^* as a function of Kt^* are only valid for the K value used to derive them.

6.4.2 Plate Properties: τ, Δ_{zz}, B/L.

To investigate the sensitivity of the CFD-RBD predicted debris dispersion to the plate's geometric and mass properties, an additional 14 simulations have been performed.

For each of the 7 initial orientations A-G described in Table 6.1 a fourth case, numbered 4 in Table 6.2, is run using a 0.563 m square plate of thickness 0.025m. The plate's density is adjusted appropriately in order to ensure that at a mean horizontal wind flow, $U_{\mathrm{w}} = 15.0$ m/s, the Tachikawa number, K and Froude number Fr_L are the same as in the number 1 cases (i.e $K = 8.325$ and $\mathrm{Fr}_L = 6.386$). The result is two set of cases, A1 - G1 and A4 - G4, with the same set of initial orientations, aspect ratio and flow parameter but considerably lower thickness ratio, τ, and non-dimensionalised mass moment of inertia about the Z-axis, Δ_{zz}, in the A4-G4 cases. Similarly a fifth case, numbered 5 in Table 6.2 is run for each initial orientation, and the plate's K, Fr_L, τ and Δ_{zz} are kept constant relative to cases numbered 4, but the plate's breadth is increased to give a higher aspect ratio, B/L.

The results for cases A1-G1 and A4-G4 are presented in Figures 6.27 - 6.28 illustrating the sensitivity of debris dispersion to τ and Δ_{zz} while Figures 6.29 - 6.30 contrasts results for cases A4-G4 and A5-G5 and highlights the influence of plate aspect ratio.

For plates of same B/L, K, and initial angle of attack, different qualitative flight modes may be observed due to changes in Δ_{zz} and τ. For instance, consider case E1 which has a plate of $M = 3.0$ kg and $I_{zz} = 0.25$ kgm^2, and case E4 which

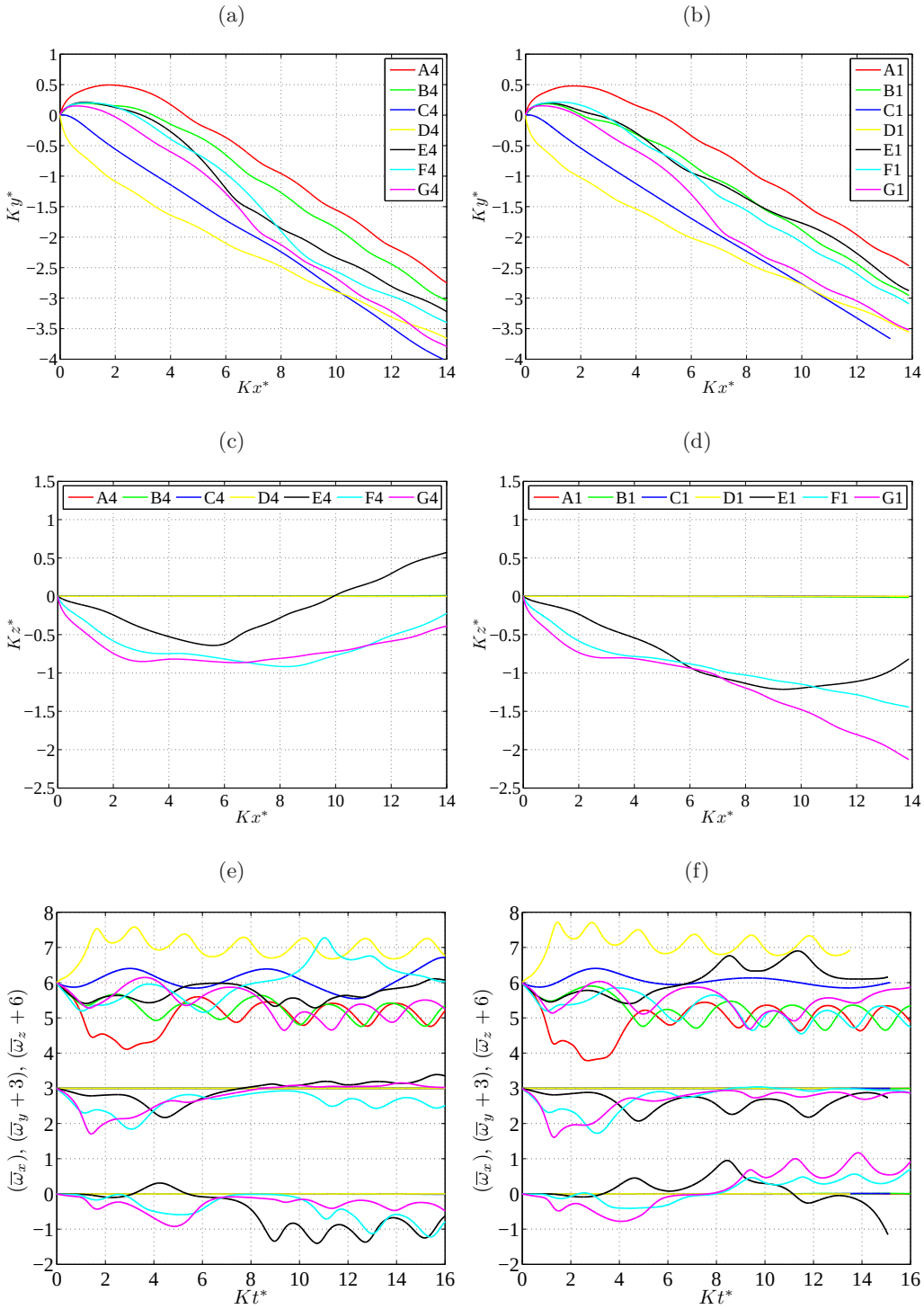

Figure 6.27: CFD-RBD predictions of; (a,b) plate trajectory in the X-Y plane, (c,d) plate trajectory in the X-Z plane, and (e,f) non-dimensionalised rotational speed, for plates with varying initial angle of attack and $\Delta_{zz} = 11.976$, $1/\tau = 22.50$ (left) and $\Delta_{zz} = 11.993$, $1/\tau = 40.00$ (right).

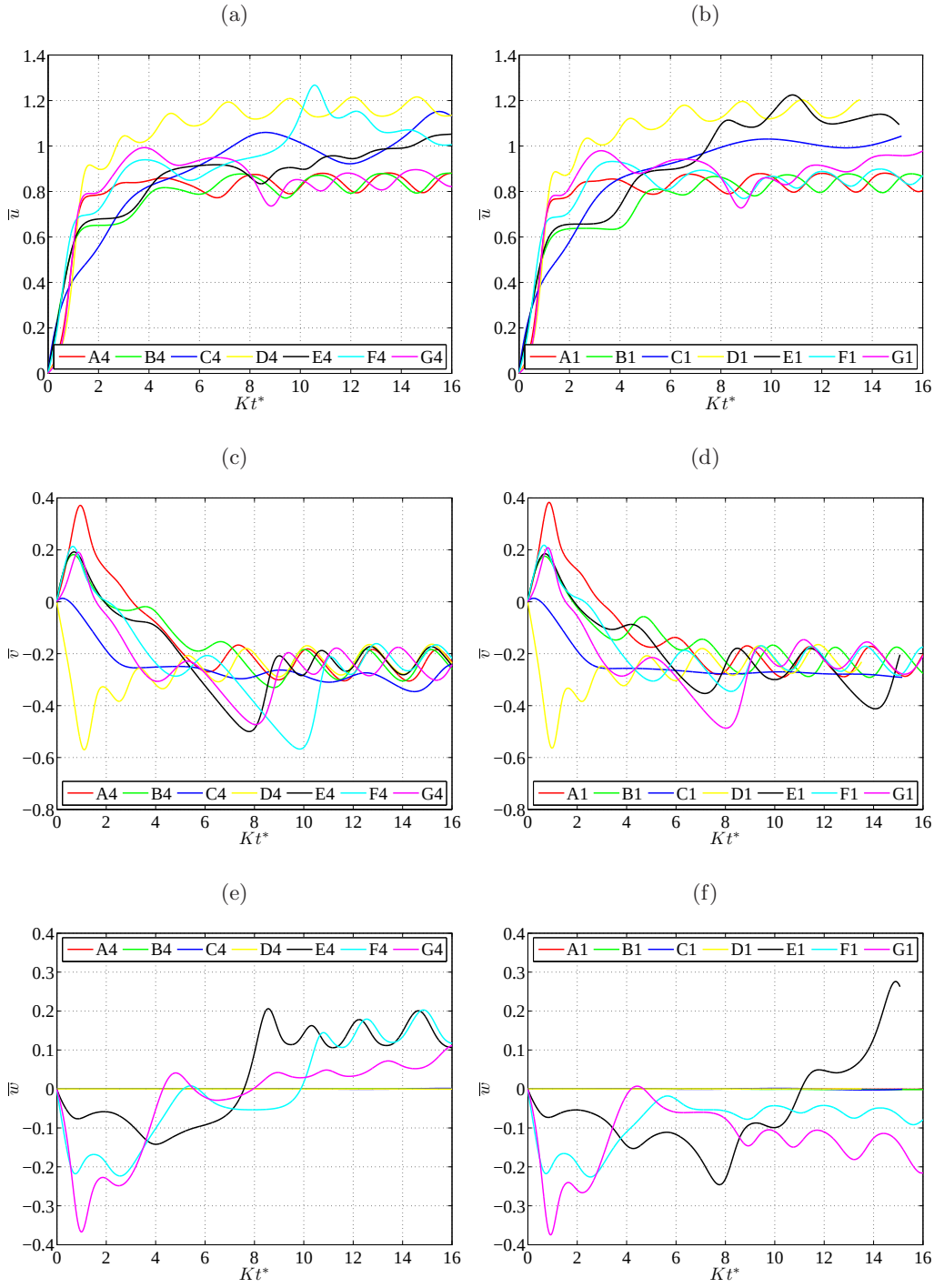

Figure 6.28: CFD-RBD predictions of; (a,b) horizontal along-wind velocity, (c,d) vertical velocity, and (e,f) horizontal cross-wind velocity, for plates with varying initial angle of attack and $\Delta_{zz} = 11.976$, $1/\tau = 22.50$ (left) and $\Delta_{zz} = 11.993$, $1/\tau = 40.00$ (right).

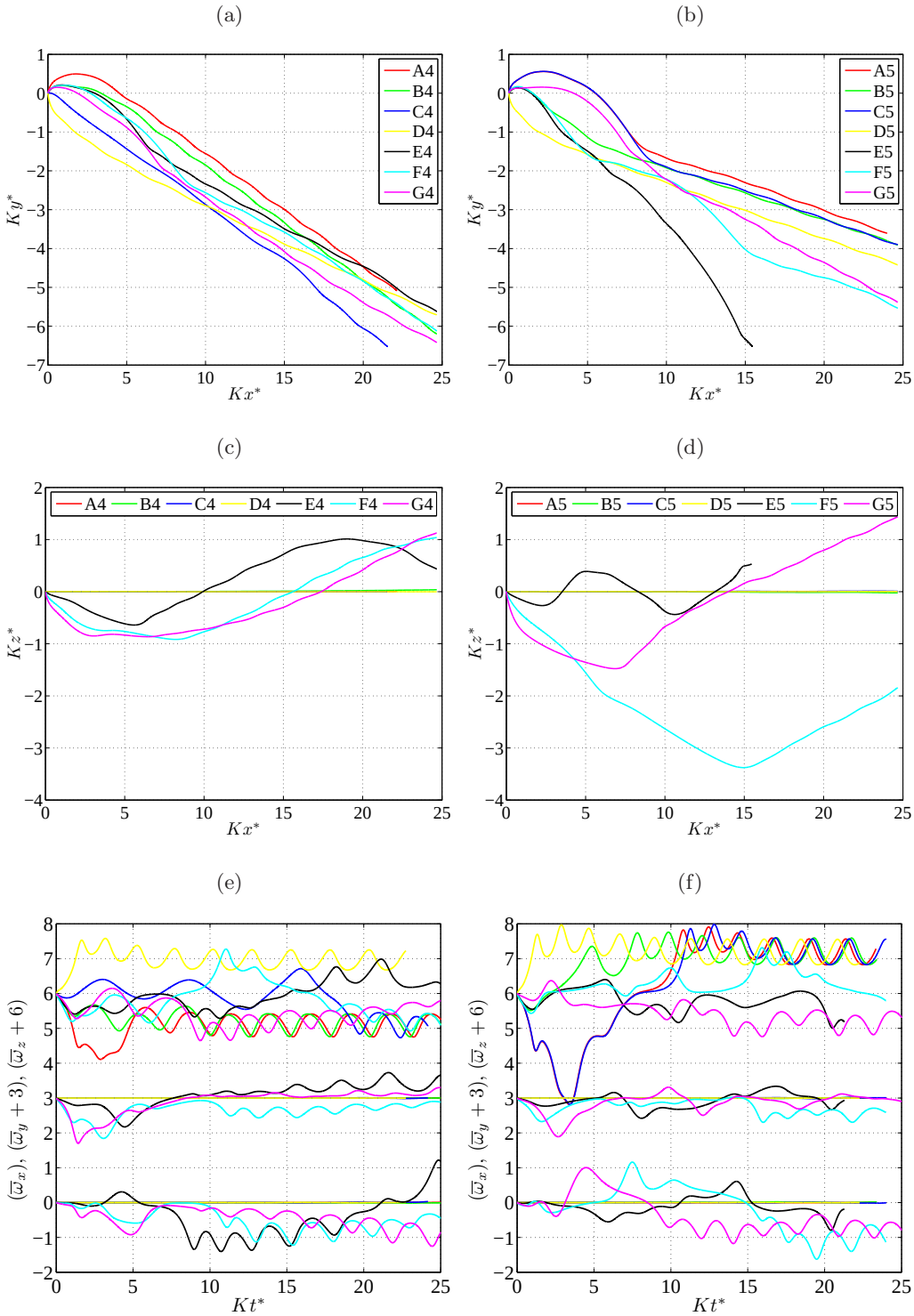

Figure 6.29: CFD-RBD predictions of; (a,b) plate trajectory in the X-Y plane, (c,d) plate trajectory in the X-Z plane, and (e,f) non-dimensionalised rotational speed, for plates with varying initial angle of attack and aspect ratio, $B/L = 1.0$ (left) and $B/L = 1.78$ (right).

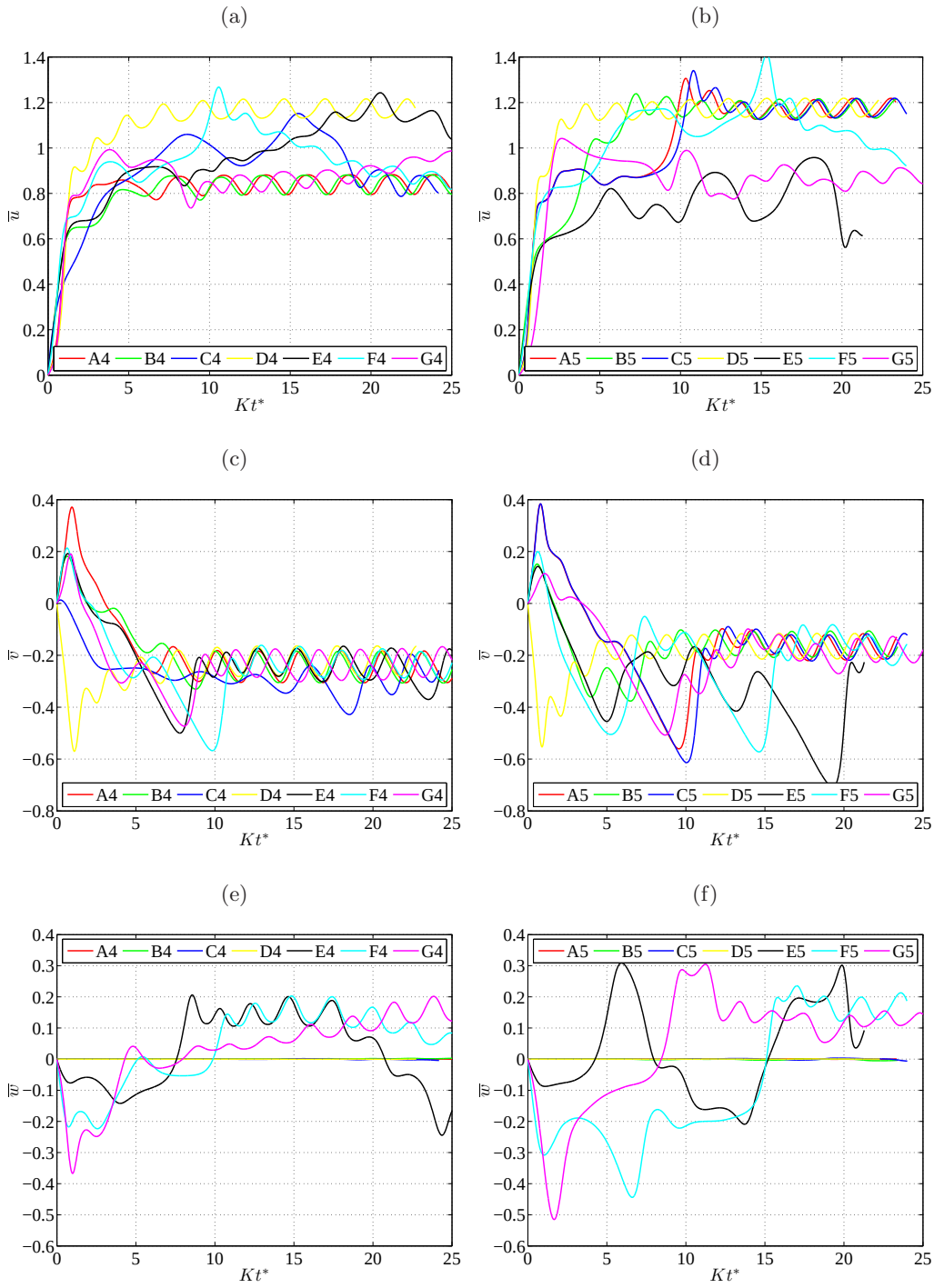

Figure 6.30: CFD-RBD predictions of; (a,b) horizontal along-wind velocity, (c,d) vertical velocity, and (e,f) horizontal cross-wind velocity, for plates with varying initial angle of attack and aspect ratio, $B/L = 1.0$ (left) and $B/L = 1.78$ (right).

has a plate of $M = 0.534$ kg and $I_{zz} = 0.014$ kgm^2. The results for these two cases shown in Figures 6.27 and 6.28, reveal that with increasing Δ_{zz}, the plate changes from a flutter mode of flight at $\Delta_{zz} = 11.976$ (E4) to an autorotational mode of flight at $\Delta_{zz} = 11.993$ (E1).

Δ_{zz} and τ are shown to affect both the qualitative flight modes observed as well as the overall dispersion of debris, with a marked sensitivity observed for the horizontal cross-wind dispersion in the complex 3D spinning cases. Much greater lateral dispersion is observed with increasing Δ_{zz} and $1/\tau$ as shown in Figure 6.27(c,d).

Plate dispersion and impact velocity were found to be highly sensitive to aspect ratio, B/L. As shown in Figure 6.29 and 6.30, a much greater dispersion is observed in both the along-wind and the cross-wind directions with increasing aspect ratio. Aspect ratio also had an effect on the observed flight modes, with no flutter mode cases observed at higher aspect ratios.

Further CFD-RBD studies are recommended, over a wider range of K, Δ and B/L in order to derive appropriate relationships for the influence of these parameters on the the dispersion of plate-type debris. The limited results presented nonetheless demonstrate the ability of CFD-RBD simulations to reproduce the chaotic behaviour of plate-type windborne debris. CFD-RBD models therefore constitute a viable analytical model for the Monte-Carlo simulation of plate-type windborne debris, as well as the parametric study of debris dispersion.

6.5 Comparisons with Analytical Solutions

The predictions from CFD-RBD models have been compared against those from quasi-steady numerical solutions to the debris flight equations, (2.10) - (2.12) (Tachikawa, 1983). Two different quasi-steady models have been considered, a recent 2D model proposed by Kordi and Kopp (2009b), hereafter referred to as QS1, and an improved quasi-steady force model based on the findings on forced rotating plates, hereafter referred to as QS2.

As previously discussed in Section 2.4, one of the fundamental assumptions of existing quasi-steady models, such as QS1, is a decomposition of aerodynamic coefficients into a static and an autorotational component according to (2.18) and (2.19). Using forced rotation simulations, this assumed decomposition has been shown to be false in Section 5.3.

In order to provide a more accurate representation of the aerodynamic forces on a rotating plate, an improved quasi-steady force model has been used in QS2. The aerodynamic drag, C_D, lift, C_L, and torque, C_M are expressed as functions of both the instantaneous non-dimensionalised rotational speed, $\overline{\omega}$, and the effective angle of attack, α according to

$$C_D = (C_D)_{\text{avg}} + \sqrt{2\big((C_D)^2_{\text{rms}} - (C_D)^2_{\text{avg}}\big)}\ \sin(2\alpha - \pi/2) \tag{6.8}$$

$$C_L = k_1(C_L)_{\text{avg}} + \sqrt{2\big((C_L)^2_{\text{rms}} - (C_L)^2_{\text{avg}}\big)}\ \sin(2\alpha) \tag{6.9}$$

$$C_M = k_1(C_M)_{\text{avg}} - \sqrt{2\big((C_M)^2_{\text{rms}} - (C_M)^2_{\text{avg}}\big)}\ \sin(2\alpha), \tag{6.10}$$

where

$$k_1 = \begin{cases} \frac{\overline{\omega}}{|\overline{\omega}|} & \text{if } \overline{\omega} \neq 0 \\ 0 & \text{if } \overline{\omega} = 0 \end{cases} \tag{6.11}$$

The "avg" and "rms" subscripts denote the mean and RMS of the force coeffecients over a complete rotational cycle, which are functions of rotational speed and are computed using expressions (5.8) to (5.13).

The results of the two analytical models, QS1 and QS2, are compared with CFD predictions for a case in each of the three single-plane flight modes identified in Section 6.2. No comparisons are made against the complex 3D spinning mode as the QS models are limited to 3DOF. The trajectory results from four cases are presented in Figure 6.31. These include two autorotational mode cases with $\alpha_o = \pm 30°$, shown in Figure 6.31(c, f, i), one transitional mode case of $\alpha_o = 50°$, shown in Figure 6.31(b, e, h), and one flutter mode case of $\alpha_o = 90°$, shown in Figure 6.31(a, d, g).

Both quasi-steady models, QS1 and QS2 are unable to sufficiently predict the behaviour of flutter mode plates, as shown in Figure 6.31(a, d, g), and transitional mode plates, as shown in Figure 6.31(b, e, h), which modes are reproduced by the CFD-RBD simulations. In the autorotational cases, shown in Figure 6.31(c, f, i), the CFD-RBD and quasi-steady models predict the same qualitative mode of flight, together with comparable predictions of the overall debris dispersion.

Although the quasi-steady models based on fixed-axis autorotation theory are able to adequately represent the autorotational mode of flight, they are unable to capture the strongly unsteady FSI involved in the flutter and transitional mode cases. Similar limitations of quasi-steady models have been observed in

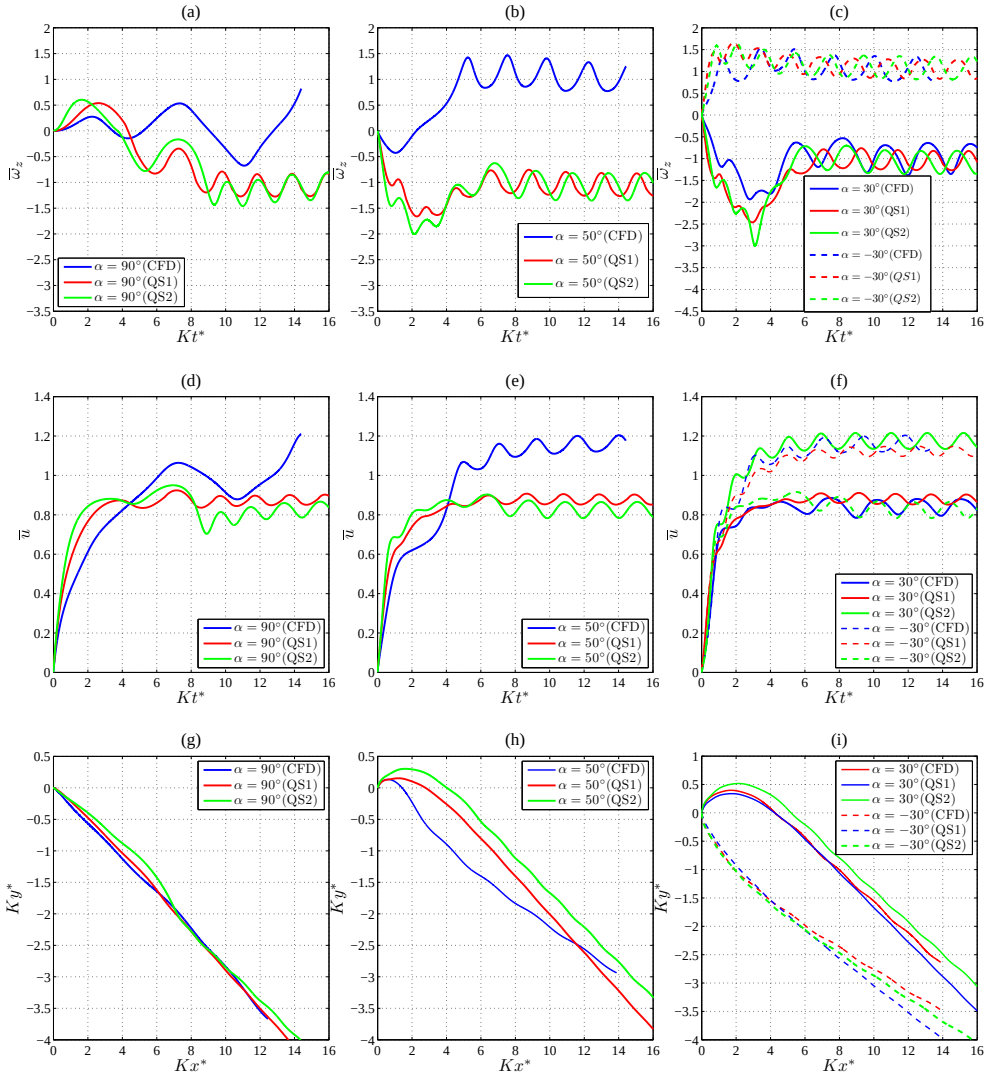

Figure 6.31: CFD-RBD results (CFD) and quasi-steady analytical model (QS) predictions of (a,b,c) rotational speed, (d,e,f) translational speed and (g,h,i) trajectory, for flutter (left), transitional (centre) and autorotational (right) flight modes.

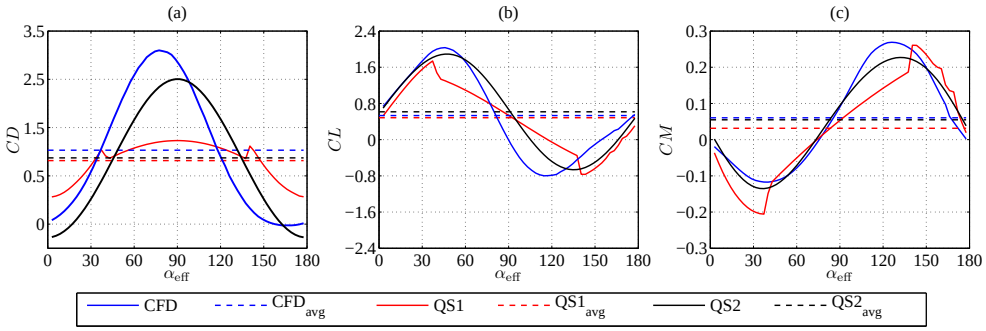

Figure 6.32: A comparison between phase-averaged CFD-RBD aerodynamic forces (CFD) and quasi-steady forces (QS1 and QS2) averaged over consecutive rotational cycles during the stable autorotational stage of flight. Data presented is for a plate with initial $\alpha_z = 30°$.

studies involving free-falling plates (Andersen et al., 2005) and hovering insect flight (Wang, 2005) where a similar strong interaction between the plate and its own wake is observed. In these scenarios, CFD-RBD models which directly simulate the complex non-linear interaction involved offer the best approach for evaluating aerodynamic forces and dynamic response.

Figure 6.32 shows phase averaged aerodynamic coefficients of the final three cycles of flight in a plate with initial angle of attack 30° which would be undergoing stable autorotation. The results are plotted against the effective angle of attack which takes into account the relative horizontal and vertical wind speed. Although comparable values of the average aerodynamic force and torque are obtained for all three models (QS1, QS2 and CFD-RBD), QS1 predictions for the unsteady force coefficients are different from those obtained from QS2 which gives better agreement with CFD-RBD predictions. This is mainly attributed to the inaccurate force decomposition used in QS1. QS2 which uses expressions (6.11) is shown to offers a more accurate representation of the quasi-steady forces involved in plate autorotation and debris flight.

Although the QS2 model based on forced rotation results shows improved quasi-steady force predictions, there is room for further improvements aimed in particular at incorporating corrections to account for the effects of strong accelerations in the mean flow.

6.6 Incorporating Complex Launch Conditions

In the preceding discussions, the CFD-RBD model has been successfully applied to the numerical investigation of flat plates in uniform flow fields. Apart from the initial orientation, flow parameters and plate properties discussed in the preceding sections, debris flight is also affected by complex initial launch conditions which are not easily parameterised. According to Kordi et al. (2010), the common quasi-steady approach to windborne debris flight neglects two important facts:

(i) windborne debris initiating from a real roof is affected by the building aerodynamics and the local velocities on the roof and in the wake, and

(ii) the debris flies in the turbulent wind defined by both the terrain and the gust structure causing failure.

To investigate these effects, destructive wind tunnel studies have previously been carried out by Kordi and Kopp (2011), Kordi et al. (2010) and Visscher and Kopp (2007). The results of these experimental studies, reveal that debris flight behaviour is strongly influenced by the complex flow fields above the roof of a building as well as the scaled restraint force.

CFD-RBD models offer an additional tool for the investigation of these effects because of their ability to simulate these complex flow fields around buildings as well as the non-linear interaction between debris and this flow.

In this section, the CFD-RBD model is extended to include the complex velocity fields on the roof and in the wake of the building and how they influence the subsequent flight behaviour of a typical roofing sheet. An unsteady and non-uniform flow field around a low rise residential building is simulated using the CFD model. A square flat plate of length $L = 0.5$ m and thickness, h =0.0125 m is considered. The plate is initially held static at the eaves of the building, as shown in Figure 6.33(a) and then subsequently released into the flow and is transported downstream. The results of two different cases are presented here, Case1 with a 1.0 kg plate and Case2 with a 6.35 kg plate, which is typical of a clay roofing tile.

The building has a square planform, with length $12L$, an eaves height of $6L$ and a double-pitched roof with a 20° slope. Figure 6.33 illustrates the model

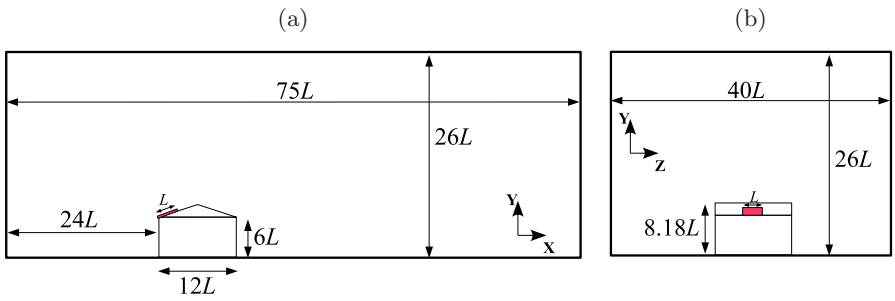

Figure 6.33: Sections through the computational domain used in the complex launch simulations, showing the launch position of the plate as well as the domain size.

building, together with the initial plate position on the wind-ward side of the roof. The computational domain has dimensions $75L \times 26L \times 40L$ and the same boundary conditions described in Section 6.1 for uniform flow cases are applied. For the precursor simulations performed to assess the performance of different building representation models, a similar domain is used, but with a size of $100L \times 13L \times 60L$.

The ABL profile, which represents 10-minute averages of wind speed has not been simulated, instead a uniform inflow condition is used, with the wind speed approximately equal to the peak 3 s gusts expected. An inflow wind speed of 35 m/s (126 km/hr) is used, which is within the range of full-scale failure wind speeds typically observed in experimental studies by Visscher and Kopp (2007). Further studies incorporating recent methods for simulating ABL profiles, such as Parente et al. (2011) and restraint force models by Kordi and Kopp (2011) are recommended.

As with the free-flight cases, the plate is held in an inner mesh region that translates and rotates monolithically with the plate in order to preserve mesh quality close to the plate walls, while the outer region of the domain is re-meshed to accommodate plate motion. Since the plate is initially expected to coincide with wall boundaries of the roof, the use of body fitting meshes and building walls is unfeasible. In order to address this limitation, the buildings have been represented as porous regions of high viscous resistance, as opposed to the traditional approach of using wall bounded volumes. As a result of this porous building approach, the region occupied by the building can be re-meshed

as the plate approaches the building and in addition, the plate can initially lie in contact with the geometric plane corresponding to the roof.

A set of geometric expressions prescribing the volume bounded by the building's walls are used to define the mesh region occupied by the building. In this region a source term, S_i, is added to the momentum equations in order to represent the momentum loss in each cell due to viscous resistance of the porous media as

$$S_i = -\frac{\mu}{\alpha} v_i, \tag{6.12}$$

where μ is the dynamic viscosity of the fluid, v_i is the velocity component in the i direction, and α is the permeability of the media, which is assumed to be homogenous. After calibration studies aimed at selecting an appropriate value of α that results in a near-zero velocity at the surface of the porous region, a very low permeability value of $\alpha \approx 10^{-9}$ has been used. Using this porous building approach, multiple buildings could be defined with relative ease with boundaries in very close proximity or even co-incident with the plate's walls.

Precursor simulations have been run, without any debris present in order to compare the flow field from the porous building model to that from the wall bounded building model. Figures 6.34 and 6.35 show the vertical profile of the horizontal wind speed and turbulent kinetic energy for each of the two building representations. The flow solution using the porous building model is shown to give a qualitatively and quantitatively similar prediction for the velocity flow field around the building, although the turbulent kinetic energy is over-predicted close to the building. Further improvements for the turbulent quantities may be obtained by incorporating appropriate source terms into the k and ε equations in the building region.

Figure 6.36(a,b) shows instantaneous snapshots of the plate during flight for both Case1 and Case2, while Figure 6.37 shows the velocity time-series for Case1. In a uniform flow, plates of similar negative initial angle of attack attack would be expected to experience negative lift and positive torque during launch. However, in the more realistic flow scenario presented, the roof launch plates are shown to experience positive initial lift and negative torque due to the large suction pressures at the windward eaves of the building. Similar findings have been reported from recent destructive wind tunnel studies of launch and flight of a plate from a low rise building roof by Kordi and Kopp (2011).

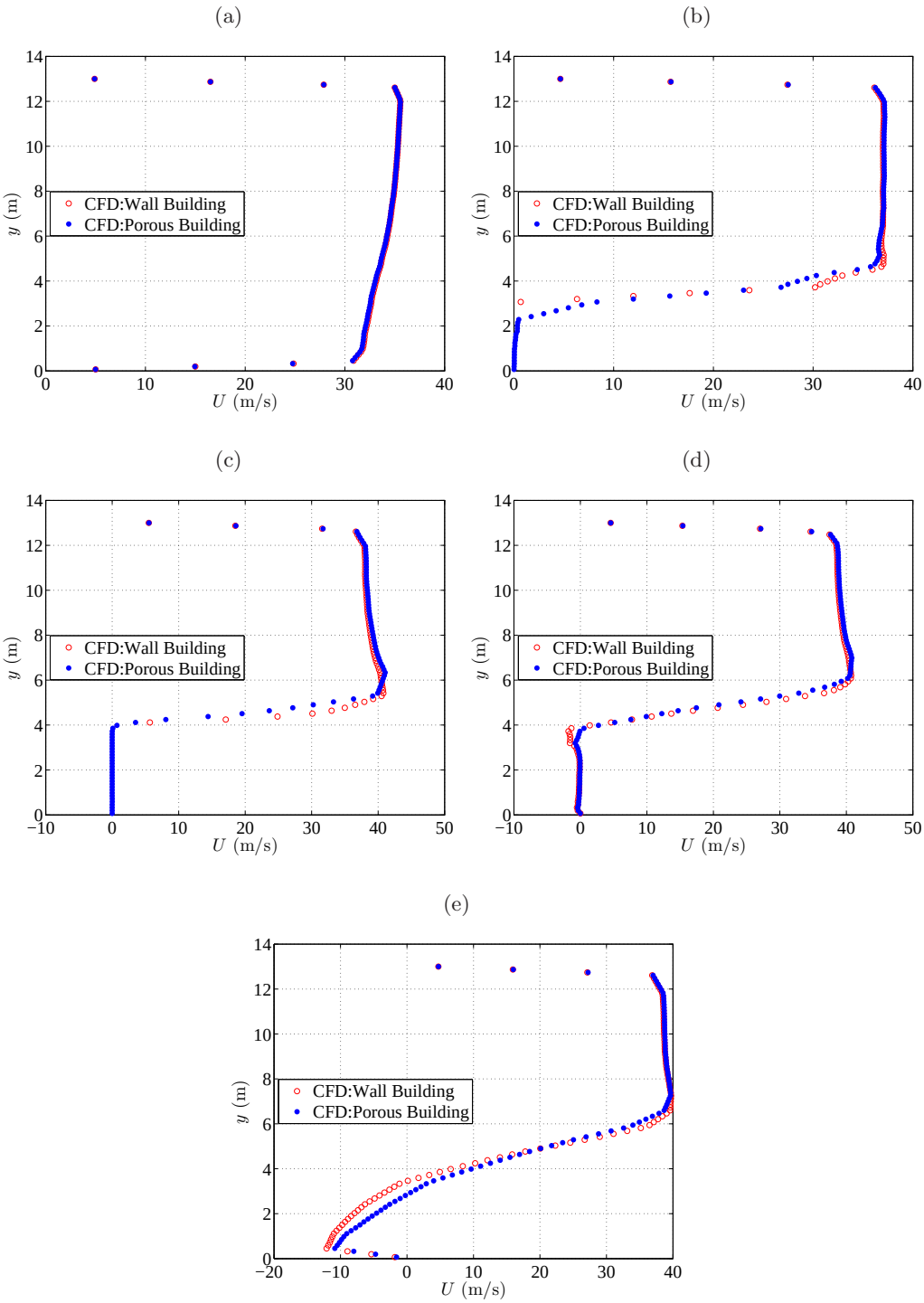

Figure 6.34: Vertical profiles of the horizontal component of wind speed, U, for both porous region and wall bounded buildings, taken at (a) $12L$ upstream of the building, (b) the building's upstream face position, (c) the building ridge, (d) the building's downstream face position and (e) $24L$ downstream of the building.

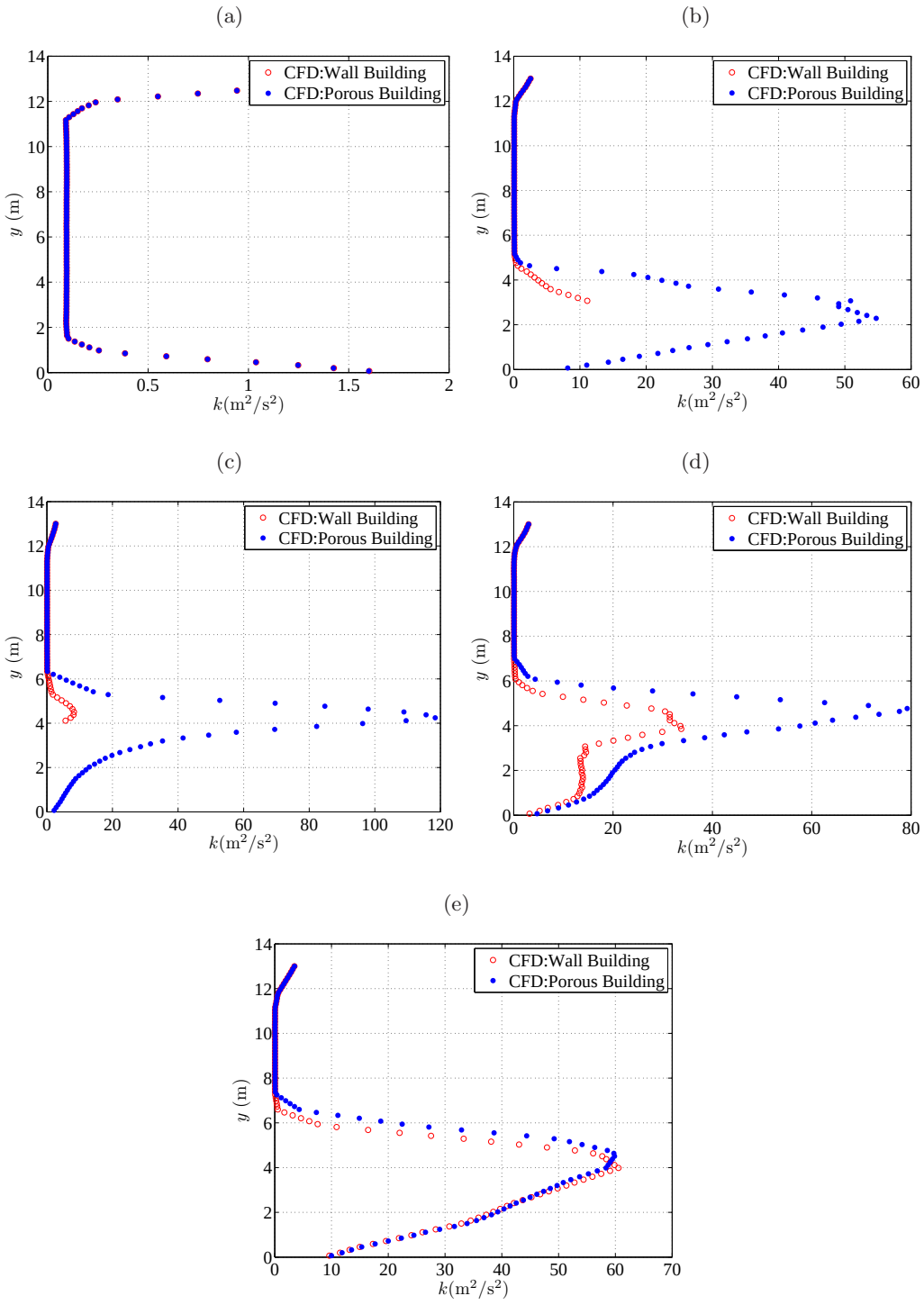

Figure 6.35: Vertical profiles of turbulent kinetic energy, k, for both porous region and wall bounded buildings, taken at (a) $12L$ upstream of the building, (b) the building's upstream face position, (c) the building ridge, (d) the building's downstream face position and (e) $24L$ downstream of the building.

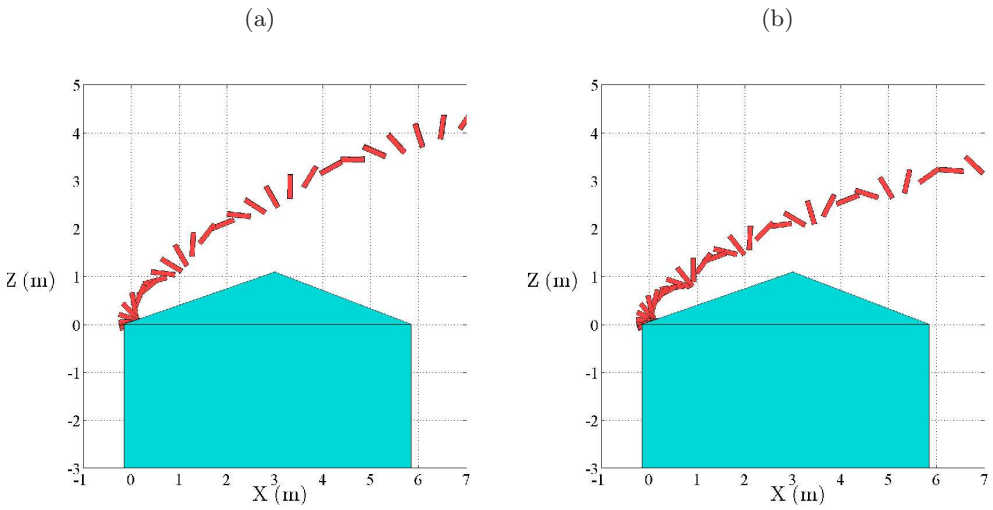

Figure 6.36: Instantaneous snapshots of plate position and orientation during flight for (a) Case1 - 1 kg plate and (b) Case2 - 6.35 kg plate.

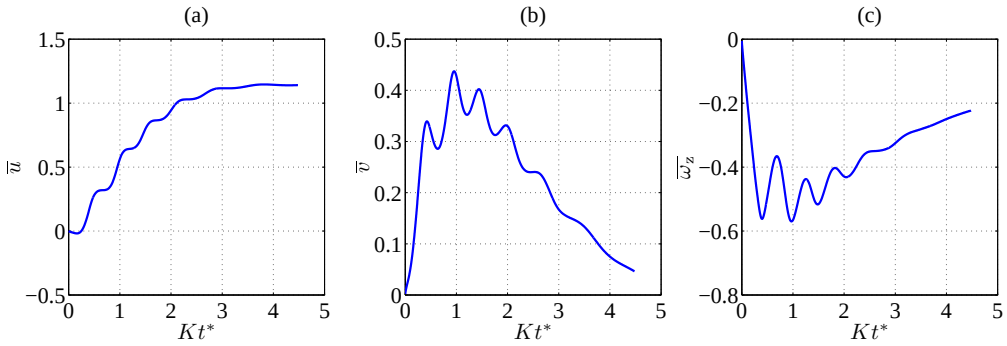

Figure 6.37: Predictions for (a) horizontal plate speed, (b) vertical plate speed and (c) Rotational speed about the Z-axis, for Case1.

The plate trajectory is shown to be significantly affected by the flow field at the launch position, most notably, the suction pressures at the eaves which create the large positive vertical velocity, and a slight negative initial horizontal velocity. As both cases represent high lift trajectories, no significant interaction with the recirculation region in the wake of the building was observed.

The results of this simulation show that although the modelling of failure and flight of plate type roof components has traditionally been restricted to experimental investigations, such as Kordi and Kopp (2011), the CFD-RBD models presented in the present research are capable of numerically reproducing this behaviour and allowing more detailed investigations of the FSI involved. Fur-

ther simulations incorporating hold down restraint forces, different plate sizes and varying inflow wind direction relative to the building, as experimentally modelled by Kordi and Kopp (2011) are recommended.

6.7 Concluding Remarks

CFD-RBD models have been shown to adequately predict the flight behaviour of plate type windborne debris. The results for translational speed and mean trajectory are in good agreement with fit expressions of experimental data by Lin et al. (2006). Using the results of the CFD-RBD models, the likely impact location and energy may be obtained for use in debris risk and damage modelling. With no *a-priori* information about the quasi-steady aerodynamic properties of the debris, the CFD-RBD models are shown to sufficiently predict debris flight trajectories in uniform, smooth flows with an ability to reproduce all the key flight modes previously observed in experimental studies. Although fixed-axis autorotation has been shown to be an accurate description for the stable flight stage, this is not the case in the initial launch stage when the plate experiences large accelerations resulting in a strongly non-linear interaction with its wake. The role of autorotation in determining the terminal velocities of the plates has been explained based on an analysis of the FSI involved in debris flight, and the phenomena of plate over-speeding explained.

The CFD-RBD model is extended from the uniform flow field scenarios to the more complex flow conditions involved in typical debris launch and is demonstrated as valuable tool for understanding the launch and the parametric study of debris flight. Wider parametric studies are recommended as well as an investigation into the influence of ABL turbulence effects and the sensitivity of CFD-RBD predictions to the turbulence modelling approach. The difficulties in modelling complex launch conditions using body-fitted meshes are illustrated and immersed boundary and overset grid methods are recommended for future CFD studies.

An improved quasi-steady model based on forced rotation CFD predictions has been presented and is shown to provide a more accurate estimate of the fluctuating component of aerodynamic forces. However, although both the improved quasi-steady analytical model and previous analytical models provide sufficiently accurate representations of debris flight behaviour in the autorotational mode

of flight, they are unable to adequately represent flutter and transitional modes as well as the plate's launch behaviour. This limitation arises from an inherent inability of quasi-steady models based on stable autorotation to represent the the strong non-linear interaction between the plate and its wake in unstable conditions. Similar failures may be expected from quasi-steady models when extended to complex and non-uniform launch flow fields. In these scenarios, the CFD-RBD model is shown to be the most suitable modelling approach.

Because the CFD-RBD modelling approach requires no *a-priori* knowledge of debris aerodynamics, as this is directly simulated, and easily incorporates complex flow and initial conditions, the CFD-RBD model is the most complete numerical model for the simulation of plate-type windborne debris flight.

Chapter 7

Conclusions and Recommendations

This chapter summarises the conclusions reached by the present study together with proposed recommendations for future work.

7.1 Conclusions

Rigid Body Dynamics modelling: The Euler angle parametrisations of orientation commonly used in 3D analytical debris flight models have singular orientations that make them unsuitable for 3D flight simulation. An alternative quaternion based RBD model has been presented in Chapter 4. This model is singularity free and more computationally efficient in terms of reducing the numerical error in the solution which results in numerical drift and non-orthogonality of the rotational matrix. Orthogonality in the quaternion formulation is easily guaranteed by enforcement of a single unit norm constraint equation using a post-correct at the end of each time step, leading to a more accurate solution.

Static plate CFD simulations: Static plate CFD simulations have been performed in Chapter 5. Based on the results of these simulations, 3D URANS CFD models are shown to be more suitable than 2D URANS models for the numerical prediction of the aerodynamic forces acting on plates. This is due to the more accurate representation of the 3D nature of turbulence in the 3D simulations.

The behaviour of the plate's wake in URANS simulations is shown to be sensitive to near-wall grid resolution with coarse grids predicting steady separated flow at high angles of attack where unsteady separated flows have been experimentally observed. For these large separated flows occurring at high angles of attack, a fine near-wall mesh resolution, together with a two-layer enhanced wall function are recommended.

Even with the enhanced wall function and fine grid, the URANS models predict

a stably attached LEV, where fine and coarse grid DES simulations predict smaller scales and a greater degree of wake unsteadiness in the LEV. However, for low aspect ratio plates, the force fluctuations associated with small scale wake unsteadiness are shown to be weak, a finding that us consistent with experimental observations of low aspect ratio bodies by Bearman (1984). The additional computational cost and finer near-wall and wake region meshes required to perform an accurate DES simulation for low aspect ratio plates is therefore unjustified and a Realisable $k-\varepsilon$ model has been found to be sufficient.

Insights into the aerodynamics of rotating plates: As shown in Chapter 5, coupling the CFD model sequentially with a 6DOF RBD model allows for an accurate simulation of the non-linear FSI involved in plate autorotation. Rotating plates show a stronger interaction with flow structures in the wake of the plate resulting in greater mean and RMS of aerodynamic drag, lift and torque compared to static cases.

Unlike previous work that has focused on fixed axis autorotation of high aspect ratio 2D plates, the model presented in this research extends this work to 3D low aspect ratio plates and free-axis autorotation. In fixed-axis autorotation, the tip vortices present at the side edges of the plate have been found to play an important role in delaying separation and also interact with the leading and trailing edge vortices to form hair-pin vortices that are periodically shed from the plate. The vortex shedding frequency is controlled by the plate's rotational speed, with a vortex shed from each of the leading and trailing edges during a typical 180° cycle. The plate's rotation is however in turn limited by the vortex shedding leading to stable autorotation.

The leading edge vortex at the retreating edge plays a dominant role in creating the aerodynamic acceleration and damping that make autorotation possible. At rotational speeds lower than the speed of autorotation, the low pressure associated with the core of the retreating edge vortex is responsible for the large accelerating torque that leads to an increase in rotational speed up to the point of autorotation. At rotational speeds beyond the plate's autorotational speed, the vortex shed from the plate's retreating edge is not translated away quickly enough and interacts with the front of the plate creating a damping torque. Using the results of forced rotation simulations, an empirical relationship between

the aerodynamic forces and rotational speed has been derived. Surface pressure predictions have been validated against existing experimental measurements and CFD-RBD simulations using URANS models are shown to provide an adequate representation of the pressure distribution and rotational dynamics of rotating plates.

Coupled CFD-RBD flight simulations and parametric studies: The CFD-RBD model is extended to 6DOF debris flight in Chapter 6. CFD-RBD predictions for debris flight have been found to be in good agreement with available experimental observations for horizontal displacement and terminal translational speed. Altogether four primary flight modes have been identified depending on the initial orientation of the plate; autorotational, transitional, flutter and complex 3D spinning. Based on CFD-RBD model predictions of the expected trajectory, estimates of the impact probability and energy may be computed for a given launch height and these results would be useful for the probabilistic modelling of debris damage risk.

The plate's terminal horizontal velocity is shown to be dependant on the direction of rotation, with the autorotational effects resulting in plates overspeeding with a non-dimensionalised horizontal speed greater than one, or flying with a non-dimensionalised speed consistently below one. Previous assumptions, suggesting a non-dimensionalised terminal horizontal speed of one are shown to be invalid, except for flutter mode plates which have relatively low rotational speeds. This coupling between the terminal horizontal speed and rotational direction is due to the direction of the autorotational component associated with the vertical components of relative wind speed.

CFD-RBD predictions have been contrasted against predictions from a 2D quasi-steady analytical model. Although the 2D quasi-steady analytical model is found to perform reasonably well for autorotational mode plates, they do not account for the strongly unsteady FSI involved in the launch stages and flutter mode of flight and hence perform poorly in these cases. In addition, the Tachikawa assumption about the fluctuating component of aerodynamic forces, which is at the core of quasi-steady force models, is found to be incorrect and an improved quasi-steady force model has been proposed based on the results of CFD forced rotation simulations. However, even with an improved force model, the quasi-

steady analytical models of plate type windborne debris flight are shown to still be limited when applied to strongly non-linear and unsteady flow conditions. Finally, while traditionally numerical models have been limited to uniform steady wind-flow and simple launch conditions involving only initial orientation, CFD-RBD model can be extended to more realistic flow conditions. Using CFD-RBD simulations, the complex launch flow field above the roof-top is directly simulated and its impact on debris flight accounted for. The porous region building model presented in this thesis is a simple method of obtaining qualitatively similar flow fields to those observed with conventional wall bounded building models. The results of the the porous building model simulations demonstrate the applicability of CFD-RBD simulations to these complex launch conditions whose investigation has previously been restricted to experimental studies.

7.2 Recommendations

A number of avenues exist for further improvement and application of the CFD-RBD modelling approach presented.

In the autorotation experimental setup, measurements of the flow in the wake of the plates were not taken and as a result, data is currently unavailable for validation of the CFD-RBD predicted flow structures. Further studies are recommended in order to obtain the velocity and pressure measurements required to validate the predicted flow structures. CFD-RBD simulations of autorotation and free-flight using DES and LES turbulence modelling approaches are also recommended in future studies.

Limited parametric studies have been performed using the CFD-RBD model for K, I^*, τ and B/L which are the key parameters determining debris flight mode and overall distribution of trajectories. Additional simulations are however recommended in order to fully understand and quantify the effects of these various parameters on debris distribution and impact energy.

A wider set of the complex launch simulations should be carried out and comparisons made against existing destructive wind tunnel data from (Kordi and Kopp, 2011) in order to validate the CFD-RBD predictions. In addition, a restraint force model for building components should also be incorporated into the simulations. Accuracy and performance in these complex launch cases can be improved by using an immersed boundary method or grid overset methods as

opposed to the porous building model and body fitting grids used in the present study. For the body-fitting grid cases, further optimisation of the domain decomposition, mesh motion strategy and mesh size is recommended in order to reduce the overall computational cost of a typical CFD-RBD flight simulation.
For all the results presented in this thesis, an ABL profile has not been simulated, but rather a uniform gust front has been assumed. Further studies investigating the implications for debris flight of ABL profile simulations using URANS models (Parente et al., 2011) as well non-uniform gust fronts using LES (Xie and Castro, 2008; Revuz et al., 2010), are therefore recommended.
Finally, due to the sensitivity of debris trajectories to a variety of parameters and launch conditions, a Monte-Carlo type simulation with randomly generated flow and debris parameters is recommended as the most suitable approach for debris risk modelling. The CFD-RBD models presented in this research provide the most complete numerical model for the deterministic step of these Monte-Carlo type simulations. Further automation of the grid generation, boundary condition definition and post-processing is recommended in order to make the CFD-RBD approach more amenable to Monte-Carlo type simulation.

Bibliography

AAWE. American Association for Wind Engineering - Photo Gallery, 2011. URL http://www.aawe.org/gallery/.

F. H. Abernathy. Flow over an inclined plate. *Transactions of the ASME : Journal of Basic Engineering.*, Paper No. 61 - WA-124:380–388, 1962.

ABI. The vulnerability of UK property to wind storm damage. Technical report, Association of British Insurers, July 2003.

ABI. The financial risks of climate change. Technical report, Association of British Insurers, June 2005.

Kelly Aerospace. Wind Turbine Ice Protection Systems, 2011. URL http://www.kellyaerospace.com/wind_turbine_deice.html.

AIAA. Guide for the verification and validation of computational fluid dynamics simulations. Technical Report AIAA-G-077-1998, American Institute of Aeronautics and Astronautics, Reston, VA, 1998.

A. Andersen, U. Persavento, and Z. J. Wang. Unsteady aerodynamics of fluttering and tumbling plates. *Journal of Fluid Mechanics*, 541:65–90, 2005.

P. R. Andronov, D. A. Grigorenko, S. V. Guvernyuk, and G. Ya. Dynnikova. Numerical simulation of plate autorotation in a viscous fluid flow. *Journal of Fluid Dynamics*, 42 - 5:719–731, 2007.

C. J. Baker. The debris flight equations. *Journal of Wind Engineering and Industrial Aerodynamics*, 95:329353, 2007.

B. S. Baldwin and H. Lomax. Thin layer approximation and algebraic model for separated turbulent flows. In *16th AIAA Aerospace Sciences Meeting, Jan. 16-18, Huntsville, Ala.*, volume 257, 1978.

J. W. Baumgarte. Stabilization of constraints and integrals of motion in dynamical systems. *Computer Methods in Applied Mechanics and Engineering*, 1:1–16, 1972.

BBC. BBC Birmingham Tornado Picture Gallery, 2005. URL http://news.bbc.co.uk/1/hi/in_pictures/4725711.stm.

P. W. Bearman. Vortex shedding from oscillating bluff bodies. *Annual Review of Fluid Mechanics*, 16:195–222, 1984.

A. Bechmann and N. N. Sorensen. Hybrid RANS/LES method for wind flow over complex terrain. *Wind Energy*, 13-1:36–50, 2010.

S. E. Belcher and J. C. R. Hunt. Turbulent flow over hills and waves. *Annual Review of Fluid Mechanics*, 30:507–538, 1998.

A. L. Braun and A. M. Awruch. Aerodynamic and aeroelastic analyses on the CAARC standard tall building model using numerical simulation. *Computers and Structures*, 87:564–581, 2009.

M. Breuer, N. Jovicic, and K. Mazaev. Comparison of DES, RANS and LES for the separated flow around a flat plate at high incidence. *International Journal for Numerical Methods in Fluids*, 41:357–388, 2003.

J. D. Brown, D. W. Bogdanoff, L. A. Yates, M. C. Wilder, and S. M. Murman. Complex-trajectory aerodynamics data for code validation from a new free-flight facility. AIAA Paper 2006-0662, AIAA Paper, January 2006.

T. Burton, D. Sharpe, N. Jenkins, and E. Bossanyi. *Handbook of Wind Energy*. John Wiley & Sons, Ltd, 2001.

A. G. Bustamante and G. W. Stone. The autorotation characteristics of various shapes for subsonic and hypersonic flows. AIAA paper 69 (1969), p. 132. Technical report, Sandia National Laboratories, USA, 1969.

R. Cattin, S. Kunz, A. Heimo, G. Russi, M. Russi, and M. Tiefgraber. Wind turbine ice throw studies in the swiss alps. In *European Wind Energy Conference, Milan, Italy, 7-10 May*, 2007.

I. Celik and W. M. Zhang. Calculation of numerical uncertainty using Richardson extrapolation: Application to some simple turbulent flow calculations. *Journal of Fluids Engineering*, 117:439–445, 1995.

J. M. Chen and Y.-C. Fang. Strouhal numbers of inclined flat plates. *Journal of Wind Engineering and Industrial Aerodynamics*, 61(2-3):99–112, 1996.

A. J. Chorin. *Numerical Study of Thermal Convection in a Fluid Heated from Below*. PhD thesis, Department of Mathematics, New York University, 1966.

A. J. Chorin. On convergence of discrete approximations to the NavierStokes equations. *Mathematics of Computation*, 23:341353, 1969.

J. C. K. Chou. Quaternion kinematic and dynamic differential equations. *IEEE Transactions on Robotics and Automation*, 8-1:53–64, 1992.

M. B. Cline. Rigid body simulation with contact and constraints. Master's thesis, The University of British Columbia, 2002.

M. B. Cline and D. K. Pai. Post-stabilization for rigid body simulation with contact and constraints. In *Proceedings of the IEEE International Conference on Robotics and Automation*, 2003.

M. Costello, S. Gatto, and J. Sahu. Using computational fluid dynamics-rigid body dynamic (CFD-RBD) results to generate aerodynamic models for projectile flight simulation. ARL Paper ARL-TR-4270, Army Research Laboratory, September 2007.

R. Courant, K. Friedrichs, and H. Lewy. On the partial difference equations of mathematical physics. *IBM Journal*, 11:215–234, 1967.

L. Davidson. An introduction to turbulence models, November 2003.

J. W. Deardorff. A numerical study of three-dimensional turbulent channel flow at large reynolds numbers. *Journal of Fluid Mechanics*, 41:453, 1970.

J. Diebel. Representing attitude: Euler angles, unit quaternions, and rotation vectors. Technical report, Stanford University, California, 2006.

J. Donea, A. Huerta, J.-Ph. Ponthot, and A. Rodriguez-Ferran. Arbitrary lagrangianeulerian methods. In *Encyclopedia of Computational Mechanics: Fundamentals. Volume 1: Fundamentals*, pages 1–25. John Wiley & Sons, Ltd, 2004.

H. Dong, R. Mittal, and A. M. Najjar. Wake topology and hydrodynamic performance of low-aspect-ratio flapping foil. *Journal of Fluid Dynamics*, 566: 309–343, 2006.

ESDU. Fluid Forces and Moments on Flat Plates. Data Item 70015. Engineering Science Data Unit, London, UK, September 1970.

ESDU. Characteristics of Atmospheric Turbulence Near the Ground. Data Item 85020. Engineering Science Data Unit, London, UK, October 1985.

ESDU. Characteristics of Atmospheric Turbulence Near the Ground. Part III: Variations in Space and Time for Strong Winds (Neutral Atmosphere). Data Item 86010. Engineering Science Data Unit, London, UK, October 1986.

FARSITE. FARSITE Technical Reference, 2011. URL http://www-laep.ced.berkeley.edu/~itr/literature/farsite/.

FLUENT Inc. *FLUENT 12.1 Documentation*, 2009.

J. Franke, C. Hirsch, A.G. Jensen, H.W. Krus, M. Schatzmann, P.S. Westbury, S.D. Miles, J.A. Wisse, and N.G. Wright. Recommendations on the use of cfd in wind engineering. In *Proceedings of the International Conference on Urban Wind Engineering and Building Aerodynamics. COST Action C14, Impact of Wind and Storm on City Life Built Environment*, 2004.

M. Frigo and S. G. Johnson. FFTW: An adaptive software architecture for the FFT. In *Proceedings of the International Conference on Acoustics, Speech, and Signal Processing*, volume 3, pages 1381–1384, 1998.

J. C. Glaser and L. L. Northup. Aerodynamic study of autorotating flat plates. Technical Report ISU-ERL-Ames 71037, Engineering Research Institute, Iowa State University, 1971.

R. Gomez. Space shuttle RTF ascent aerodynamics and debris transport analyses. High-End Computing at NASA 1, National

Aeronautics and Space Administration, November 2006. URL http://www.hec.nasa.gov/news/reports/HEC_NASA_2006.pdf.

R. Gomez, D. Vicker, S. E. Rogers, M. J. Atosmis, W. M. Chan, R. Meakin, and S. M. Murman. STS-107 investigation ascent CFD support. In *In 34th AIAA Fluid Dynamics Conference, 28 June - 1 July, Portland, Oregon*, 2004.

D. T. Greenwood. *Advanced Dynamics*. Cambridge University Press, 2003.

S. Gupta and J. G. Leishman. Dynamic stall modelling of the S809 aerofoil and comparison with experiments. *Wind Energy*, 9:521–547, 2006.

W. R. Hamilton. On quaternions. *Proceedings of the Royal Irish Academy*, 3: 1–16, 1847.

D. M. Hargreaves and N. G. Wright. On the use of the k-epsilon model in commercial CFD software to model the neutral atmospheric boundary-layer. *Journal of Wind Engineering and Industrial Aerodynamics*, 95-5:355–369, 2007.

F. H. Harlow and J. E. Welch. Numerical calculation of time-dependent viscous incompressible flow of fluid with free surface. *Physics of Fluids*, 8:21822189, 1965.

K. Hirata, K. Shimizu, K. Fukuhara, K. Yamauchi, D. Kawaguchi, and J. Funaki. Aerodynamic characteristics of a tumbling plate under free flight. *Journal of Fluid Science and Technology*, 4-1:168–187, 2009.

C. Hirsch. *Numerical Computation of Internal and External Flows. Volume 1: Fundamentals of Computational Fluid Dynamics*. Elsevier, 2007.

C. W. Hirt, B. D. Nichols, and N. C. Romero. SOLA: A numerical solution algorithm for transient fluid flows. Technical report, Los Alamos Scientific Lab., NM., January 1975.

Sighard F. Hoerner. *Fluid-Dynamic Drag*. Published by the Author, 1958.

J. D. Holmes. Trajectories of spheres in strong winds with application to wind-borne debris. *Journal of Wind Engineering and Industrial Aerodynamics*, 92: 9–22, 2004.

J. D. Holmes. Windborne debris and damage risk models: A review. *Journal of Wind and Structures*, 13-2:95–108, 2010.

J. D. Holmes, C. J. Baker, and Y. Tamura. Tachikawa number: A proposal. *Journal of Wind Engineering and Industrial Aerodynamics*, 94:41–47, 2006a.

J. D. Holmes, C. W. Letchford, and N. Lin. Investigations of plate-type windborne debris - part II: Computed trajectories. *Journal of Wind Engineering and Industrial Aerodynamics*, 94:21–39, 2006b.

J. Hunt, S. Leibovich, and K. Richards. Turbulent shear flow over low hills. *Quarterly Journal of the Royal Meteorological Society*, 114:1435–1470, 1988a.

J. C. R. Hunt, A. A. Wray, and P. Moin. Eddies, stream, and convergence zones in turbulent flows. Technical report, Center for Turbulence Research Report CTR-S88, 193-208, 1988b.

G. Iaccarino, A. Ooi, P. A. Durbin, and M. Behnia. Reynolds averaged simulation of unsteady separated flow. *International Journal of Heat and Fluid Flow*, 24: 147–156, 2003.

R. I. Issa. Solution of the implicitly discretised fluid flow equations by operator-splitting. *Journal of Computational Physics*, 62-1:40–65, 1986.

J. D. Iversen. Autorotating flat-plate wings: the effect of the moment of inertia, geometry and Reynolds number. *Journal of Fluid Mechanics*, 92-2:327–348, 1979.

P. S. Jackson and J. C. R. Hunt. Turbulent wind flow over a low hill. *Quarterly Journal of the Royal Meteorological Society*, 101:929–955, 1975.

C. Jin and K. Xu. Numerical study of the unsteady aerodynamics of freely falling plates. *Communications in Computational Physics*, 3-4:834–851, 2008.

B. Kader. Temperature and concentration profiles in fully turbulent boundary layers. *International Journal of Heat and Mass Transfer*, 24-9:1541–1544, 1993.

J. C Kaimal and J. J. Finnigan. *Atmospheric Boundary Layer Flows : Their Structure and Measurement*. Oxford University Press, 1994.

B. Kakimpa, D. M. Hargreaves, and J. S. Owen. Coupled CFD-RBD modeling of wind-borne debris flight. In *The Fifth International Symposium on Computational Wind Engineering, Chapel Hill, North Carolina, USA, May 23-27*, 2010a.

B. Kakimpa, D. M. Hargreaves, and J. S. Owen. Aerodynamic characterisation of static and auto-rotating plates using coupled CFD-RBD simulations. In *The Fifth International Symposium on Computational Wind Engineering, Chapel Hill, North Carolina, USA, May 23-27*, 2010b.

J. Katsura, Y. Taniike, and T. Maruyama. Damage due to Typhoon 9119 (human damage), Study on strong-wind disasters due to Typhoon No.19 in 1991, 1992.

S. E. Kim and D. Choudhury. A near-wall treatment using wall functions sensitized to pressure gradient. In *ASME FED Vol. 217, Separated and Complex Flows,*. ASME, 1995.

V. Kolar. Vortex identification: New requirements and limitations. *International Journal of Heat and Fluid Flow*, 28-4:638–652, 2007.

B. Kordi and G. A. Kopp. The debris flight equations by C.J. Baker. *Journal of Wind Engineering and Industrial Aerodynamics*, 97(3-4):151–154, 2009a.

B. Kordi and G. A. Kopp. Evaluation of quasi-steady theory applied to windborne flat plates in uniform flow. *Journal of Engineering Mechanics*, 135-7: 657–668, 2009b.

B. Kordi and G. A. Kopp. Effects of initial conditions on the flight of windborne plate debris. *Journal of Wind Engineering & Industrial Aerodynamics*, 99-5: 601–614, 2011.

B. Kordi, G. Traczuk, and G. A. Kopp. Effects of wind direction on the flight trajectories of roof sheathing panels under high winds. *Journal of Wind and Structures*, 13-2:145–167, 2010.

S. Kortas, P.Mindykowski, J. L. Consalvi, H. Mhiri, and B. Porterie. Experimental validation of a numerical model for the transport of firebrands. *Fire Safety Journal*, 44:1095–1102, 2009.

D. Kwak, J. L. C. Chang, S. P. Shanks, and S. R. Chakravarthy. A three-dimensional incompressible NavierStokes flow solver using primitive variables. *AIAA Journal*, 24:390396, 1986.

J. W. Larsen, S. R. K. Nielsen, and S. Krenk. Dynamic stall model for wind turbine airfoils. *Journal of Fluids and Structures*, 23:959–982, 2007.

B. E. Launder and B. I. Sharma. Application of the energy dissipation model of turbulence to the calculation of flow near a spinning disc. *Letters in Heat and Mass Transfer*, 1-2:131–138, 1974.

B. E. Launder and D. B. Spalding. The numerical computation of turbulent flows. *Computer Methods in Applied Mechanics and Engineering*, 3:269–289, 1974.

B. E. Launder, G. J. Reece, and W. Rodi. Progress in the development of a Reynolds stress turbulence closure. *Journal of Fluid Mechanics*, 68:537–566, 1975.

A. J. H. Lee. A general study of tornado-generated missiles. *Nuclear Engineering and Design*, 30:418–433, 1974.

D. Lentink, W. B. Dickson, J. L. van Leeuwen, and M. H. Dickinson. Leading-edge vortices elevate lift of autorotating plant seeds. *Science*, 324:1438–1440, 2009.

M. Y. Y. Lin, E. W. F. Larson, and J. D. Collins. Determination of debris risk to the public due to the Columbia breakup during reentry. Technical report, Columbia Accident Investigation Board, September 2003.

N. Lin and E. Vanmarcke. Windborne debris risk assessment. *Probabilistic Engineering Mechanics*, 23:523–530, 2008.

N. Lin and E. Vanmarcke. Windborne debris risk analysis - Part I: introduction and methodology. *Journal of Wind and Structures*, 13-2:191–206, 2010.

N. Lin, C. W. Letchford, and J. D. Holmes. Investigation of plate-type windborne debris. part i. experiments in wind tunnel and full scale. *Journal of Wind Engineering and Industrial Aerodynamics*, 94:51–76, 2006.

N. Lin, J. D. Holmes, and C. W. Letchford. Trajectories of wind-borne debris in horizontal winds and applications to impact testing. *Journal of Structural Engineering*, 133-2:274–282, 2007.

H. J. Lugt. Autorotation of an elliptic cylinder about an axis perpendicular to the flow. *Journal of Fluid Mechanics*, 99-4:817–840, 1980.

H. J. Lugt. Autorotation. *Annual Review of Fluid Mechanics*, 15:123–147, 1983.

J. L. Lumley, G. Berkooz, J. Elezgaray, P. Holmes, A. Poje, and C. Volte. *Simulation and Modelling of Turbulent Flows*, chapter 1: Fundamental Aspects of Incompressible and Compressible Turbulent Flows, pages 5–13. Oxford University Press, Incorporated, 1996.

Y. F. Luna, A. Mochidaa, H. Yoshinoa, and S. Murakamib. Applicability of linear type revised kepsilon models to flow over topographic features. *Journal of Wind Engineering and Industrial Aerodynamics*, 95-5:371–384, 2007.

R. W. Macdonald. Modelling the mean velocity profile in the urban canopy layer. *Boundary-Layer Meteorology*, 97-1:25–45, 2000.

J. Mann, Y. Liu, Y. Kim, and D. K. P. Yue. Deterministic and stochastic predictions of motion dynamics of cylindrical mines falling through water. *IEEE Journal of Oceanic Engineering*, 32-1:21–33, 2007.

T. P. Marshall and S. Robinson. The Birmingham, U.K. tornado: 28 July 2005. In *23rd Conference on Severe Local Storms, November*, November 2006.

P. Martinez-Vazquez, C. J. Baker, M. Sterling, A. Quinn, and P. J. Richards. Aerodynamic forces on fixed and rotating plates. *Journal of Wind and Structures*, 13-2:127–144, 2010.

F. J. Masters, K. R. Gurley, N. Shah, and G. Fernandez. The vulnerability of residential window glass to lightweight windborne debris. *Engineering Structures*, 32:911–921, 2010.

J. C. Maxwell. Rotation of a falling card. *Cambridge and Dublin Mathematical Journal*, 9:145, 1854.

J. M. McDonough. Lectures in computational fluid dynamics of incompressible flow: Mathematics, algorithms and implementations. Departments of Mechanical Engineering and Mathematics University of Kentucky, 2007.

J. E. Minor. Windborne debris and the building envelope. *Journal of Wind Engineering and Industrial Aerodynamics*, 53:207–227, 1994.

J. E. Minor and W. L. Beason. Window glass failures in windstorms. *ASCE Journal of the Structural Division*, 102-1:147–160, 1976.

R. Mittal, V. Seshadri, and H. S. Udaykumar. Flutter, tumble and vortex induced autorotation. *Journal of Theoretical and Computational Fluid Dynamics*, 17:165–170, 2004.

S. Murakami. Foreword: Current status of computational wind engineering. *Journal of Wind Engineering and Industrial Aerodynamics*, 35:viii, 1990.

S. Murakami, A. Mochida, and H. Kazuki. Three-dimensional numerical simulation of air flow around a cubic model by means of large eddy simulation. *Journal of Wind Engineering and Industrial Aerodynamics*, 25-3:291–305, 1987.

S. M. Murman, M. J. Aftosmis, and M. J. Berger. Implicit approaches for moving boundaries in a 3D cartesian method. In *41st AIAA Aerospace Sciences Meeting, January 6-9, Reno, NV*, January 2003a.

S. M. Murman, M. Field, M. J. Aftosmis, and M. J. Berger. Simulations of 6DOF motion with a cartesian method. In *41st AIAA Aerospace Sciences Meeting, January 6-9, Reno, NV*, January 2003b.

S. M. Murman, M. J. Aftosmis, and S. E. Rogers. Characterization of space shuttle ascent debris aerodynamics using CFD methods. In *43rd AIAA Aerospace Sciences Meeting*, 2005.

NAHB Research Center. Windborne debris: Impact resistance of residential glazing. Technical report, U.S. Department of Housing and Urban Development, National Association of Home Builders (NAHB) Research Center, 2002.

NASA. NASA Software Applications: Cart3D and Debris, 2011. URL http://www.nas.nasa.gov/Resources/Applications/applications.html.

W. L. Oberkampf and T. G. Trucano. Verification and validation in computational fluid dynamics. Technical report, Sandia National Laboratories, Albuquerque, New Mexico, 2002.

S. Orszag and G. Patterson. Numerical simulation of turbulence. In M. Rosenblatt and C. Van Atta, editors, *Statistical Models and Turbulence*, volume 12 of *Lecture Notes in Physics*, pages 127–147. Springer Berlin / Heidelberg, 1972.

J. S. Owen, D. M. Hargreaves, and X. P. Gu. Modelling the mechanisms of vortex induced reponse in bridge decks. In *7th UK Conference on Wind Engineering, Glasgow*, 2006.

A. Parente, C. Gorle, J. v. Beeck, and C. Benocci. A comprehensive modelling approach for the neutral atmospheric boundary layer: Consistent inflow conditions,wall function and turbulence model. *Boundary-Layer Meteorology*, 140:411–428, 2011.

S. V. Patankar. *Numerical Heat Transfer and Fluid Flow.* McGraw-Hill, New York, 1980.

E. L. Petersen, N. G. Mortensen, L. Landberg, J. Hujstrup, and H. P. Frank. Wind Power Meteorology. Part I: Climate and Turbulence. *Wind Energy*, 1: 2–22, 1998.

J. Revuz, D.M. Hargreaves, and J.S. Owen. Application of a method for generating turbulent inflow based on inverse fourier transforms for large eddy simulations. In *Proceedings of the 5^{th} International Symposium on Computational Wind Engineering, Chapel Hill, North Carolina, USA, May 23-27*, 2010.

C. M. Rhie and L. W. Chow. Numerical study of the turbulent flow past an airfoil with trailing edge separation. *AIAA Journal*, 21-11:1525–1532, 1983.

D. P. Riabouchinsky. Thirty years of theoretical and experimental research in fluid mechanics. *Journal of the Royal Aeronautical Society*, 39:282–348, 1935.

P. J. Richards and R. P. Hoxey. Appropriate boundary conditions for computational wind engineering models using the k-epsilon turbulence model. *Journal of Wind Engineering and Industrial Aerodynamics*, 46 & 47:145–153, 1993.

P. J. Richards and S. E. Norris. Appropriate boundary conditions for computational wind engineering models revisited. *Journal of Wind Engineering and Industrial Aerodynamics*, 99-4:257–266, 2011.

P. J. Richards, N. Williams, B. Laing, M. McCarty, and M. Pond. Numerical calculation of the three-dimensional motion of wind-borne debris. *Journal of Wind Engineering and Industrial Aerodynamics*, 96:2188–2202, 2008.

P. J. Roache. Quantification of uncertainty in computational fluid dynamics. *Annual Review of Fluid Mechanics*, 29:123–60, 1997.

A. C. Robinson. On the use of quaternions in simulation of rigid-body motion. Technical report, Aeronautical Reserach Laboratory, Wright Air Development Centre, Ohio, USA, December 1958.

W. Rodi. Comparison of LES and RANS calculations of the flow around bluff bodies. *Journal of Wind Engineering and Industrial Aerodynamics*, 69-71: 55–75, 1997.

J. Sarrate, A. Huerta, and J. Donea. Arbitrary lagrangian-eulerian formulation for fluid-rigid body interaction. *Computer Methods in Applied Mechanics and Engineering*, 190(24-25):3171–3188, 2001.

A. Scarabino and P. Giacopinelli. Analysis of the two dimensional sheet debris flight equations: initial and final state. *Journal of Wind and Structures*, 13-2: 109–125, 2010.

G. Schewe. Reynolds number effects in flow around more-or-less bluff bodies. *Journal of Wind Engineering and Industrial Aerodynamics*, 89:1267–1289, 2001.

H. Schlichting. *Boundary Layer Theory.* McGraw Hill, New York, 7th edition, 1979.

F. G. Schmitt. About boussinesq's turbulent viscosity hypothesis: historical remarks and a direct evaluation of its validity. *Comptes Rendus Mcanique*, 335:617–627, 2007.

P. J. Schneider and B. A. Schauer. HAZUS - Its Development and its Future. *Natural Hazards Review*, 7 - 2:40–44, 2006.

H. Seifert, A. Westerhellweg, and J. Krning. Risk analysis of ice throw from wind turbines. In *BOREAS VI: Wind Energy Production in Cold Climates, 6-9 April, Pyha, Finland*, 2003.

V. Seshadri, R. Mittal, and H. S. Udaykumar. Vortex induced auto-rotation of a hinged plate: A computational study. In *4th ASME-JSME Joint Fluids Engineering Conference*, 2003.

C. T. Shaw. *Using Computational Fluid Dynamics*. Prentice Hall, 1992.

T. H. Shih, W. W. Liou, A. Shabbir, Z. Yang, and J. Zhu. A new k-epsilon eddy-viscosity model for high Reynolds number turbulent flows - model development and validation. *Computers & Fluids*, 24-3:227–238, 1995.

B. W. Skews. Autorotation of rectangular plates. *Journal of Fluid Mechanics*, 217:33–40, 1990.

SKF. SKF ball bearing product manual, 2010. URL http://www.skf.com/portal/skf/home6.

J. Smagorinsky. General circulation experiments with the primitive equations. I: the basic experiment. *Monthly Weather Review*, 91:99165, 1963.

E. H. Smith. Autorotating wings: an experimental investigation. *Journal of Fluid Mechanics*, 50-3:513–534, 1971.

P. Spalart and S. Allmaras. A one-equation turbulence model for aerodynamic flows. Technical Report AIAA-92-0439, American Institute of Aeronautics and Astronautics, 1992.

P. Spalart, W. Jou, M. Strelets, and S. Allmaras. Comments of feasibility of LES for wings, and on a hybrid RANS/LES approach. In *International Conference on DNS/LES, Aug. 4-8, Ruston, Louisiana*, 1997.

D. B. Spalding. *GENMIXA General Computer Program for Two-Dimensional Parabolic Phenomena*. Pergamon Press, New York, 1977.

J. Stuelpnagel. On the parametrization of the three-dimensional rotation group. *Society for Industrial and Applied Mathematics*, 6-4:422–430, October 1964.

R. B. Stull. *An Introduction to Boundary Layer Meteorology*. Kluwer Academic Publishers, 1988.

O. G. Sutton. *Micrometeorology*. McGraw Hill, New York, 1953.

M. Tachikawa. Trajectories of flat plates in uniform flow with application to wind-generated missiles. *Journal of Wind Engineering and Industrial Aerodynamics*, 14:443–453, 1983.

M. Tachikawa. A method for estimating the distribution of trajectories of wind-borne missiles. *Journal of Wind Engineering and Industrial Aerodynamics*, 29:175–184, 1988.

K. Taira and T. Colonius. Three-dimensional flows around low-aspect-ratio flat-plate wings at low Reynolds numbers. *Journal of Fluid Mechanics*, 623:187–207, 2009.

K. Taira, W. B. Dickson, T. Colonius, and M. H. Dickinson. Unsteadiness in flow over a flat plate at angle-of-attack at low Reynolds numbers. In *45th AIAA Aerospace Sciences Meeting and Exhibition*, 2007.

Y. Tamura. Wind-induced damage to buildings and disaster risk reduction. In *7th Asia-Pacific Conference on Wind Engineering, Taipei, Taiwan, November 8-12*, 2009.

G. I. Taylor. The spectrum of turbulence. In *Proceedings of the Royal Society of London*, volume 164 of *Series A, Mathematical and Physical Sciences*, pages 476 –490, February 1938.

H. Tennekes and J. L. Lumley. *A First Course in Turbulence*. The MIT Press, 1997.

L. A. Twisdale, W. L. Dunn, and T. L. Davis. Tornado missile transport analysis. *Nuclear Engineering and Design*, 51:295–308, 1979.

Y. Uematsu, J. Suzuya, and T. Nozawa. Building damage in Aomori and Akita prefectures due to Typhoon No.19 of 1991. *Journal of Wind Engineering, Japan Association for Wind Engineering,*, 51:35–47, 1992.

C. O. Unanwa, J. R. McDonald, K. C. Mehta, and D. A. Smith. The development of wind damage bands for buildings. *Journal of Wind Engineering and Industrial Aerodynamics*, 84:119–149, 2000.

H. K. Versteeg and W. Malalasekera. *An Introduction to Computational Fluid Dynamic: The Finite Volume Method*. Pearson Education Limited, 2007.

P. J. Vickery, J. X. Lin, and L. A. Twisdale Jr. Analysis of hurricane pressure cycling following missile impact for residential structures. *Journal of Wind Engineering and Industrial Aerodynamics*, 91:1703–1730, 2003.

B. T. Visscher and G. A. Kopp. Trajectories of roof sheathing panels under high winds. *Journal of Wind Engineering and Industrial Aerodynamics*, 95: 697–713, 2007.

Z. J. Wang. Dissecting insect flight. *Annual Review of Fluid Mechanics*, 37: 183–210, 2005.

G. S. West and C. J. Apelt. The effects of tunnel blockage and aspect ratio on the mean flow past a circular cylinder with Reynolds numbers between 10,000 and 100,000. *Journal of Fluid Mechanics*, 114:361–377, 1982.

J. Wieringa. Gust factors over open water and built-up country. *Boundary-Layer Meteorology*, 3:424–441, 1973. ISSN 0006-8314.

D. C. Wilcox. Re-assessment of the scale-determining equation for advanced turbulence models. *AIAA Journal*, 26-11:1299–1310, 1988.

D. C. Wilcox. *Turbulence Modeling for CFD*. DCW Industries Inc., 1994.

J. A. B. Wills, B. E. Lee, and T. A. Wyatt. A model of wind-borne debris damage. *Journal of Wind Engineering and Industrial Aerodynamics*, 90:555–565, 2002.

N. Wood. Wind flow over complex terrain: A historical perspective and the prospect for large eddy modelling. *Boundary-layer Meteorology*, 96:11–32, 2000.

N.G. Wright and G.J. Easom. Non-linear k-e turbulence model results for flow over a building at full-scale. *Applied Mathematical Modelling*, 27:1013–1033, 2003.

Z.-T. Xie and I. P. Castro. Efficient generation of inflow conditions for large eddy simulation of street-scale flows. *Flow, Turbulence Combustion*, 81:449–470, 2008.

V. Yakhot, S. A. Orszag, S. Thangam, T. B. Gatski, and C. G. Speziale. Development of turbulence models for shear flows by a double expansion technique. *Physics of Fluids A*, 4-7:1510–1520, 1992.

K. Yelmgren. The autorotation of magnus rotors. Technical report, Dept. Aerosp. Eng. Rep. Univ. Notre Dame, South Bend, Ind. 115, 1966.

Y. Yi, G. Ming, S. Chen, and X. Jin. New inflow boundary conditions for modeling the neutral equilibrium atmospheric boundary layer in computational wind engineering. *Journal of Wind Engineering and Industrial Aerodynamics*, 97:88–95, 2009.

Appendices

Appendix A

The CFD Modelling Process

Numerical solutions of the Navier-Stokes equations are usually computed for a given geometrical or physical context. The spatial domain of interest is therefore discretised using computational grids (meshes) based on the particular numerical solution technique used. This could be a finite difference method, a finite element method or a spectral method. The most common of which is a finite difference formulation known as the Finite Volume Method (FVM). In the FVM, the computational domain is subdivided into discrete volumes of fluid known as *Control Volumes*. The governing equations of fluid flow are then discretised and solved for each control volume in the domain.

A complete CFD process involves the use of numerical algorithms to solve for $\mathbf{U}$, p and any other variables such as temperature that describe the flow problem. To do achieve this, the CFD process may be sub-divided into three main stages: *Pre-processing, Solving* and *Post-processing*.

A.1 Pre-processing

During the pre-processing stage, a conceptual model of the fluid flow problem is developed. Existing information about the physical and chemical nature of the problem (i.e. whether it is laminar or turbulent, steady or unsteady, viscous or inviscid, compressible of incompressible, single or multi-phase, reactive or unreactive, etc.) is used to define a system of equations that sufficiently describes the problem. This system of equations usually involves some formulation of the Navier-Stokes equations together with additional equations for any associated phenomena or constraints. Subsequently the region of interest, commonly re-

ferred to as the computational domain, is defined along with a mathematical definition of the domain boundaries and fluid properties.

The physical computational domain is then discretised into a number of control volumes using a computational grid (see section A.5.1). According to Versteeg and Malalasekera (2007), over 50% of the time spent on a CFD project in industry is devoted to the definition of domain geometry and grid generation. Similarly, for unsteady problems, the duration of simulation is defined and the time-domain is subdivided into discrete time-steps (see section A.6 for a discussion on temporal discretisation). Finally, the model of the problem is initialised by defining initial values for all the model variables at the solution points.

A.2 Solving

With the problem adequately defined, the governing partial differential equations of fluid flow are integrated over all the control volumes in the domain to give a system of algebraic equations. The resulting system of linear algebraic equations is then solved by an iterative method such as the Gauss-Siedel Method, the Successive Over-relaxation (SOR) method, the Conjugate Gradient Method (CGM) or Multigrid methods (Hirsch, 2007).

A.3 Post-processing

After the iterative matrix solver has converged upon a solution with a sufficient degree of accuracy, the resulting $\mathbf{U}$ and p fields obtained are then analysed in order to extract key information about the fluid flow and any associated phenomena. This is known as post-processing. Typical outputs include vector plots, line plots, streamlines, contour plots and iso-surfaces.

A.4 Verification and Validation

Finally, it is important to determine the level of accuracy and reliability of the CFD model before utilising its results. To do this, verification and validation studies are performed.

Verification is defined as the process of determining whether a model implementation accurately represents the developer's conceptual description of a model and the solution to the model. According to Oberkampf and Trucano (2002), given a numerical procedure (or CFD code) that is stable, consistent,

and robust, the five major sources of errors in CFD solutions are: (i) insufficient spatial discretisation convergence, (ii) insufficient temporal discretisation convergence, (iii) insufficient convergence of an iterative procedure, (iv) computer round-off, and (v) computer programming errors. The fundamental strategy of verification is the identification, quantification, and reduction of these errors in the computational model and its solution. While the computer programming error is dealt with during *code verification*, the first four error sources are collectively dealt with as part of *solution verification* or solution error assessment. The main focus of verification studies performed during this research has been on solution verification in the form of checks for spatial and temporal grid convergence studies as well as convergence of iterative procedures. Computer code verification has not been performed as a pre-compiled commercial CFD code, ANSYS FLUENT (FLUENT Inc., 2009), has been used for all of the CFD modelling in this research.

Validation is the process of determining the degree to which the model is accurate in its representation of the real world from the perspective of the intended use of the model (AIAA, 1998). This would usually involve comparisons between verified model results and experimental measurements which are taken as the best measure of reality.

Oberkampf and Trucano (2002) note that it is important to remember that this strategy does not assume that the experimental measurements are more accurate than the computational results. The strategy only asserts that experimental measurements are the most faithful reflections of reality for the purposes of validation. Estimation of error must therefore be performed both on the model and the experimental data.

For some engineering simulations, the important physical modelling parameters are not known *a priori*. It is common engineering practice in these cases to adjust the modelling parameters within a reasonable range of values, so that improved agreement with the experimental data is obtained. These types of practical engineering activities that occur during model validation may more appropriately be described as *calibration* (Oberkampf and Trucano, 2002). During this research, model calibration has been performed for some parameters such as bearing friction and mass eccentricity, whose values were not easily obtainable although a general range of possible values were known.

For complex systems, it might also be infeasible or impractical to conduct true validation experiments on the complete system (Oberkampf and Trucano, 2002). The recommended strategy in these cases is to use a building-block approach where the performance of the system is assessed at different levels of physical coupling and complexity (AIAA, 1998). This building-block approach has been adopted in this research with validation of free-flight broken down into the simpler blocks of purely translational and purely autorotation motion.

A.5 Spatial Discretisation

A.5.1 Computational Mesh

In the Finite Volume method, the domain is split into discrete volume units known as control volumes /cells using a computational mesh. One of the crucial steps in the CFD pre-processing stage, after the domain of interest has been defined, is building a computational mesh sub-dividing the continuous domain into these discrete control volumes. This is frequently referred to as mesh generation and the governing equations are later solved over each control volume in the mesh.

Depending on the nature of the problem, the mesh may be two- or three-dimensional (2D or 3D) and may be further classified according to the type of elements used. The most common 2D mesh elements are *triangular* and *quadrilateral* elements, while the most common 3D elements are *hexahedral*, *wedge (prism)*, *pyramid*, *tetrahedral*, and more recently, *polyhedral* elements.

Computational grids may further be classified based on the arrangement and topology of the elements as *structured* or *unstructured* as illustrated in Figure A.1. Structured meshes have elements arranged in a regular topology that can be expressed as a two or three dimensional array. These meshes are sometimes referred to as mapped meshes as they can be seen as a cuboid mesh that has been stretched and mapped onto some other geometry (Shaw, 1992). Unstructured meshes on the other hand have elements arranged in an irregular topology that cannot be easily expressed as a two- or three-dimensional array. The cell connectivity information must therefore be explicitly stated and this increases the storage requirements. However unlike the structured mesh that is limited to quadrilateral (2D) or hexahedral (3D) elements, an unstructured mesh allows

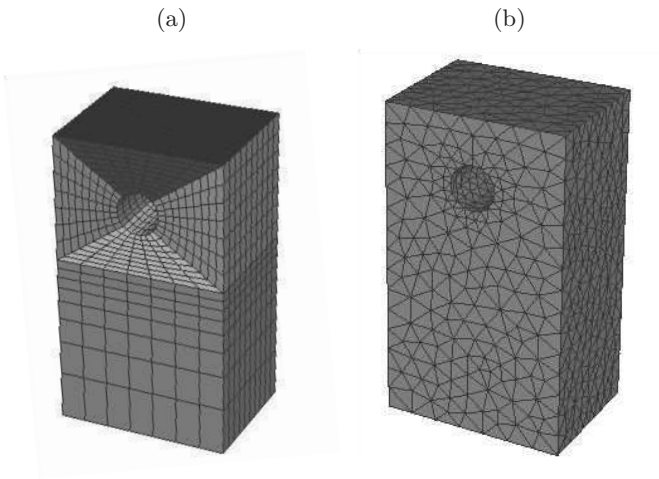

Figure A.1: (a) A structured mesh of hexahedral cells and (b) an unstructured mesh of tetrahedral cells.

the use of multiple element types in a single mesh.

The accuracy of a CFD simulation is strongly dependant on the quality of the computational grid. Grid quality expresses the smoothness, regularity and distortion of the mesh as well as whether it adequately resolves flow in the critical regions. A number of mesh quality parameters are used to quantify these aspects and include: cell area/volume, cell skewness, cell aspect ratio and cell size growth factors.

In CFD simulations involving wall boundaries, the mesh must be designed to adequately resolve the wall boundary layer. For turbulent flows, this is achieved by designing the mesh to ensure that the dimensionless wall distance, y^+, of the first interior cell centre is consistent with that of the wall function applied. y^+ is defined as

$$y^+ = \frac{u_\tau y}{\nu}, \tag{A.1}$$

where $\nu(= \mu/\rho)$ is the fluid kinematic viscosity. u_τ is the friction velocity defined by wall shear stress, τ_w, and fluid density, ρ, as

$$u_\tau = \sqrt{\frac{\tau_w}{\rho}}. \tag{A.2}$$

As part of model verification, it will often be required to adapt the grid until a sufficient quality and resolution mesh is obtained. Grid convergence studies are also performed, based on the Richardson extrapolation (Celik and Zhang, 1995)

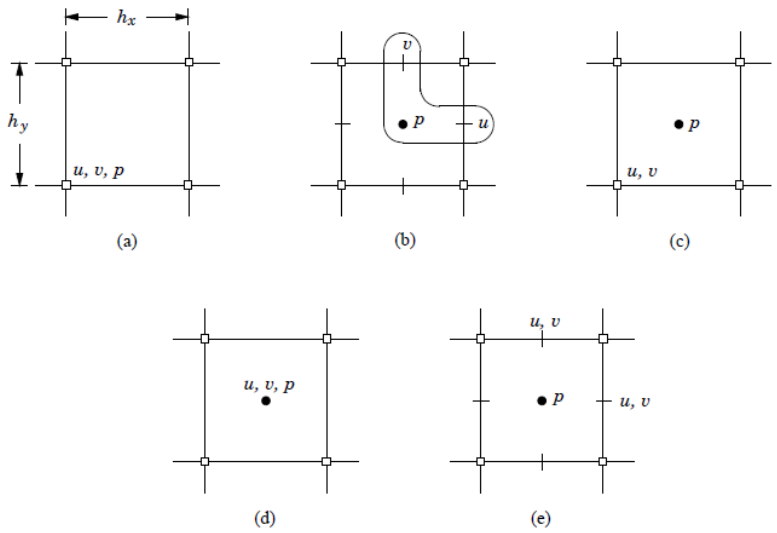

Figure A.2: Grid structures for solving the 2-D incompressible Navier-Stokes equations: (a) natural unstaggered, (b) staggered, (c) partially staggered, (d) cell-centered unstaggered and (e) staggered with multiple momentum equations (McDonough, 2007).

in order to assess the sensitivity of results to mesh quality and quantify the error due to spatial discretisation.

A.5.2 Grid Structure

A correct treatment of pressure-velocity coupling requires the correct combination of discretisation of the equations and the grid structure used, in terms of where in the control volume the solution variables are computed and stored. A number of grid structuring approaches are available as illustrated for a 2D mesh in Figure A.2.

Each grid structure has its merits and drawbacks. The natural unstaggered grid has the advantage of allowing a straightforward implementation of boundary conditions as grid points coincide with boundary points. However, it is possible with this structure to satisfy the divergence-free condition (A.16) with physically unrealistic velocity fields and for unrealistic pressure fields to go undetected (McDonough, 2007). This leads to a problem known as checker-boarding where an un-physical solution can become stable due to the effective decoupling of pressure and velocity. One of the ways to address this problem is to use a staggered grid structure proposed by Harlow and Welch (1965). In the staggered

grid, the problem of pressure-velocity decoupling observed on the natural grid is avoided, however some of the drawbacks of this approach are include the relatively counter-intuitive implementation and the fact that boundary conditions are often not exactly enforced. Similar grid structures such as the partially staggered structure and the staggered with multiple momentum equations structure have subsequently been proposed, but these required a substantial amount of additional calculations as well as complex algorithms yet some of the drawbacks of the simple staggered grid still occur (McDonough, 2007).

Eventually, the cell-centered unstaggered grid structure (also known as the co-located scheme) introduced by Rhie and Chow (1983) has become the most successful and most widely implemented in incompressible flow cases. This co-located structure is applied in FLUENT (FLUENT Inc., 2009), and will be the main focus of this section. One of the main drawbacks of this approach is that since all variables are stored at the cell centres, it is not possible to exactly satisfy all boundary conditions hence results are expected to be generally less accurate than those computed on a staggered grid (McDonough, 2007).

A.5.3 Discretisation Schemes

In order to compute convection and diffusion fluxes of scalars through the cell faces, the face values, ϕ_f are usually required. In the co-located scheme, these are obtained by interpolation from the computed cell centre values using a suitable discretisation scheme.

For convective terms, upwinding schemes are often used, in which the face values are computed from cell centre values of cells that are located upstream relative to the direction of the normal velocity v_n through the face. Other possible schemes include power law, QUICK and MUSCL schemes. For diffusion terms on the other hand, central differencing schemes are usually used with second-order or higher accuracy. A brief descriptions of these schemes is presented here.

The First Order Upwind Scheme assumes the cell centre value, ϕ, to be the average cell values and valid throughout the entire cell including at the cell faces. Therefore when using this scheme the face values, ϕ_f, are set equal to the cell centre value in the upstream cell.

The Second Order Upwind Scheme on the other hand offers second order accuracy and computes cell face values, ϕ_f, using a Taylor series expansion of the cell-centred values according to

$$\phi_f = \phi + \nabla\phi \cdot \vec{r}, \tag{A.3}$$

where ϕ and $\nabla\phi$ are the cell-centred value and its gradient in the upstream cell, and $\vec{r}$ is the displacement vector from the upstream cell centroid to the face centroid. The gradients, $\nabla\phi$, must be determined for each cell using a suitable gradient method, allowing for higher order upwinding schemes to be derived.

The Power Law Scheme interpolates the face values of a variable, ϕ, using an exact solution to the one-dimensional convection-diffusion equation

$$\frac{\partial}{\partial x}(\rho u\phi) = \frac{\partial}{\partial x}\Gamma\frac{\partial\phi}{\partial x}, \tag{A.4}$$

where diffusivity, Γ and ρu are constant across the interval ∂x. Integrating (A.4) yields (A.5) which describes how ϕ varies with x.

$$\frac{\phi(x) - \phi_0}{\phi_L - \phi_0} = \frac{e^{(\mathrm{Pe}\frac{x}{L})} - 1}{e^{(\mathrm{Pe})} - 1} \tag{A.5}$$

where, $\phi_0 = \phi|_{x=0}$, $\phi_L = \phi|_{x=L}$, and Pe is the Peclet number: $\mathrm{Pe} = \frac{\rho u L}{\Gamma}$. For large Pe, the value of ϕ at $x = L/2$ is approximately equal to the upstream value, which is the equivalent of a first-order upwind scheme.

The Central Differencing Scheme computes face values for a variable, ϕ_f by averaging the multidimensional linear reconstructions of ϕ obtained from the two cells that share the face. The resulting expression for ϕ_f is

$$\phi_f = \frac{1}{2}(\phi_0 + \phi_1) + \frac{1}{2}(\bigtriangledown\phi_0 \cdot \vec{r_0} + \bigtriangledown\phi_1 \cdot \vec{r_1}) \tag{A.6}$$

where the indices 0 and 1 refer to the cells that share face f, $\bigtriangledown\phi_0$ and $\bigtriangledown\phi_1$ are the reconstructed gradients in cells 0 and 1, respectively, and $\vec{r}$ is the vector directed from the cell centroid to the face. The central differencing scheme can produce unbounded oscillating solutions which can lead to numerical instability.

The QUICK scheme is suitable for quadrilateral and hexahedral meshes where unique upstream and downstream faces and cells can be identified. The scheme gives higher-order values of the convected variable ϕ at a face by using a *weighted*

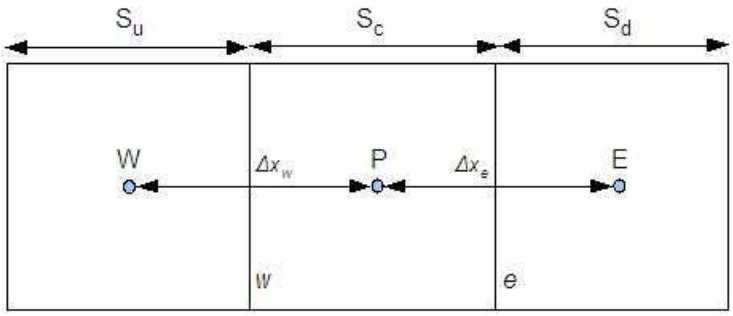

Figure A.3: One-dimensional control volume between two neighbouring control volumes.

average of second order upwind and central interpolation of variables. Consider the one-dimensional control volume set-up shown in Figure A.3.

Assuming flow from left to right in Figure A.3, the face value of e is given by

$$\phi_e = \theta\left[\frac{S_d}{S_c+S_d}\phi_P + \frac{S_c}{S_c+S_d}\phi_E\right] + (1-\theta)\left[\frac{S_u+2S_c}{S_u+S_c}\phi_P - \frac{S_c}{S_u+S_c}\phi_W\right], \quad \text{(A.7)}$$

where, $\theta = 1$ results in a second-order central interpolation, while $\theta = 0$ results in a second order upwind value. The traditional QUICK scheme is obtained by setting $\theta = 1/8$ while some implementations have a solution dependant value of θ.

This scheme is more accurate on structured grids that are aligned with the flow direction although it may be extended to unstructured grids.

A Third Order MUSCL Scheme calculates face values by *blending* a central differencing scheme with a second-order upwind scheme. This scheme is based on the *Monotone Upstream-Centered Schemes for Conservation Laws* (MUSCL) with face values, ϕ_f calculated according to

$$\phi_f = \theta\phi_{f,CD} + (1-\theta)\phi_{f,SOU}, \quad \text{(A.8)}$$

where $\phi_{f,CD}$ is computed using the central differencing scheme and defined by (A.6), and $\phi_{f,SOU}$ is computed using the second-order upwind scheme as defined in (A.3).

Compared to the second order upwind scheme, the third order MUSCL has the potential to improve spatial accuracy for all mesh types even in cases exhibiting sudden flux (shock), discontinuities or large gradients by reducing numerical

diffusion especially with 3D flows. It also has the advantage over the QUICK scheme of being applicable to arbitrary and unstructured meshes. However, the third order MUSCL scheme can still produce incorrect estimates when the field under consideration has discontinuities or sudden flux changes.

A.6 Temporal Discretisation

For unsteady simulations, in addition to the spatial discretisation described in section A.5, the time domain is split into a number of discrete time-steps, Δt, and every term in the Navier-Stokes equations is integrated over this time-step. The evolution of a variable, ϕ in time is then given by

$$\frac{\partial \phi}{\partial t} = F(\phi), \tag{A.9}$$

where F incorporates any spatial discretisation. The time derivative may then be computed using a number of differencing schemes such as first-order backward differencing:

$$\frac{\phi^{n+1} - \phi^n}{\Delta t} = F(\phi), \tag{A.10}$$

and second-order backward differencing:

$$\frac{3\phi^{n+1} - 4\phi^n + \phi^{n-1}}{\Delta t} = F(\phi), \tag{A.11}$$

where, ϕ is a scalar quantity, ϕ^{n+1} is its value at the next time level, $t + \Delta t$, ϕ^n is the value at the current time level, t, and ϕ^{n-1} is the value at the previous time level, $t - \Delta t$. After the discretisation of the time derivative, $F(\phi)$ may be calculated by applying either an implicit or an explicit time integration scheme.

Implicit Time Stepping. With the implicit time integration schemes, the spatial discretisation F is estimated at the next time level $n + 1$ at which the value of ϕ is sought. For the first order implicit time stepping scheme, this is expressed as

$$\phi^{n+1} = \phi^n + \Delta t F(\phi^{n+1}). \tag{A.12}$$

The equation is "implicit" since ϕ^{n+1} is not explicitly expressed in terms of the known values ϕ^n at the previous time level. The spatial discretisation of ϕ^{n+1} is incorporated into $F(\phi^{n+1})$. This scheme holds the advantage of being unconditionally stable irrespective of the time-step size. However the time-step size still has to be sufficiently small to resolve the smallest timescales occurring within the flow.

Explicit Time Stepping. For explicit time integration schemes, $F(\phi)$ is evaluated at the current level using known values, ϕ^n,

$$\phi^{n+1} = \phi^n + \Delta t F(\phi^n). \tag{A.13}$$

It is referred to as explicit integration since ϕ^{n+1} is explicitly expressed in terms of the existing solution values, ϕ^n. This scheme is only conditionally stable. In order to maintain the stability of the explicit method, time step size Δt must obey the the Courant-Friedrich-Lewy (CFL) condition (Courant et al., 1967), which for a one-dimensional problem is

$$Cr = \frac{u\Delta t}{\Delta x} \leq k \tag{A.14}$$

where Cr is the Courant number and k is a constant whose value depends on the type of problem being solved. For advection dominated problems, $k = 1$. In order to maintain numerical stability of the explicit scheme, the time-step size throughout the domain must be the minimum required to satisfy the CFL condition for all the cells in the domain.

Due to the conditional instability of the explicit time-stepping scheme, only first and second order implicit time-stepping was used in this research.

A.7 Pressure-Velocity Coupling

After discretisation of the fluid flow equations, a set of linear algebraic equations results. For compressible flow solvers, the velocity field values are given by the discretised momentum equations with the continuity equation used to obtain the density field, while the pressure field is determined from the equation of state. This however is not the case for incompressible flows.

In solving the incompressible Navier-Stokes equations, a numerical difficulty known as the pressure-velocity coupling problem arises. Usually, a velocity field $\mathbf{U}$ is obtained from solving the discretised momentum equation (3.20), leaving only the continuity equation (3.21) (also referred to as the divergence-free condition) for computing the pressure p. However, as p is not explicitly included in (3.21), an additional expression for pressure known as the Pressure Poisson Equation (PPE) is derived from computing the divergence of (3.20), while assuming the divergence-free condition given by (3.21) to hold.

$$\frac{\partial(\nabla \cdot \mathbf{U})}{\partial t} + \nabla \cdot (\mathbf{U} \cdot \nabla \mathbf{U}) = -\frac{1}{\rho}\nabla \cdot (\nabla p + \nabla \cdot \boldsymbol{\tau} + \mathbf{F_B}), \tag{A.15}$$

$$\nabla^2 p = \nabla \cdot \mathbf{F_B} - \rho \nabla \cdot (\mathbf{U} \cdot \nabla \mathbf{U}), \tag{A.16}$$

where $\nabla^2 = \nabla \cdot \nabla$ is the Laplace operator. The set of discretised momentum equations and the discretised PPE for pressure form a system of algebraic equations with linear inter-dependencies, and in which the continuity principle is not explicitly enforced. While (A.16) requires that the velocity field used to compute the pressure be divergence free, it does not explicitly enforce this condition and the velocity field obtained from solving the discretised momentum (3.20) will seldom be divergence-free.

A number of solver algorithms have been developed to address these Pressure-Velocity coupling difficulties. These solver algorithms may be considered as either coupled or segregated depending on whether the system of equations is solved sequentially (i.e. segregated from one another) or solved together as a coupled system of equations. Some of the most commonly used segregated solution algorithms to-date include: the Marker-and-Cell Method (MAC) by Harlow and Welch (1965); the SOLA algorithm by Hirt et al. (1975); the Artificial Compressibility method by Chorin (1966); Kwak et al. (1986); projection methods by Chorin (1966, 1969); the Semi-Implicit Method for Pressure Linked Equations (SIMPLE) algorithm by Spalding (1977) and Patankar (1980) and the Pressure Implicit with Splitting of Operators (PISO) algorithm by Issa (1986).

The SIMPLE algorithm and its variants have become the most widely used and are at the core of many commercial CFD codes such as FLUENT Inc. (2009). They are used for most of the simulations performed during this research.

Appendix B

Arbitrary Lagrangian-Eulerian (ALE) Methods

The numerical simulation of wind engineering problems often involves the non-linear interaction between the fluid and moving wall boundaries. This could be due to the oscillation of the wall boundaries making up a tall building or the complex 3D spinning of plate type windborne debris. It is often necessary in these cases to cope with fairly large deformations of the domain as the fluid moves while allowing a clear delineation of the fluid-structure interface and an accurate solution of the resulting fluid flow field.

There are two traditional approaches to this problem, the Lagrangian approach and the Eulerian approach. In the Lagrangian approach, commonly used in structural mechanics, each individual node of the computational domain follows an associated material particle during motion. While this allows for the easy tracking of free surfaces and fluid-structure interfaces, it is unable to account for large distortions of the computational domain without frequent re-meshing. However, the Eulerian approach, which is widely used in fluid dynamics, involves fixing the computational mesh and allowing the fluid to move relative to the mesh. Although this allows for the easy handling of large distortions in the fluid, the Eulerian approach is unable to precisely define the fluid-structure interface (Donea et al., 2004).

The Arbitrary Lagrangian-Eulerian (ALE) method is an attempt to combine the advantages of Lagrangian and Eulerian descriptions while minimizing their drawbacks. In the ALE description, the nodes of the computational mesh may be moved with the continuum in normal Lagrangian fashion, or be held fixed in Eulerian manner, or, be moved in some arbitrarily specified way to give a

continuous rezoning capability (Donea et al., 2004). To achieve this, the ALE introduces translational and rotational velocities for the fluid mesh nodes as $\mathbf{u_g}$ and $\omega_\mathbf{p}$, respectively. At the fluid-structure interface, these fluid mesh velocities must coincide with the structural node velocities.

Subsequently, starting from the Eulerian description of the mass, momentum and energy conservation equations as stated in (3.21), (3.20) and (3.22), a new ALE formulation of the fluid flow equations is obtained by replacing the fluid velocity, $\mathbf{U}$, with the relative velocity between the fluid and the moving mesh, $\mathbf{U_r}$, to give

$$\nabla \cdot \mathbf{U_r} = 0, \tag{B.1}$$

$$\frac{\partial \mathbf{U_r}}{\partial t} + \mathbf{U_r} \cdot \nabla \mathbf{U} = \frac{1}{\rho}(-\nabla p + \nabla \cdot \boldsymbol{\tau} + \mathbf{F_B}), \tag{B.2}$$

$$\mathbf{U_r} = \mathbf{U} - (\omega_\mathbf{p} \times \mathbf{r}) - \mathbf{u_g}. \tag{B.3}$$

It is important to note that in the resulting formulation, the arbitrary motion of the computational mesh is only reflected in the left-hand side, which has led to some authors refereing to this as the *quasi-Eulerian* description.

The ALE formulation of the Navier-Stokes equations has been successfully used for the numerical simulation of fluid-rigid body interaction by Sarrate et al. (2001), and the present research uses a similar approach.

Appendix C

Rigid Body Dynamics Model

```
#include "udf.h"
#include "math.h"


#define R2D      180.0/M_PI /* Convert radians to degrees
*/
#define D2R      M_PI/180.0 /* Convert degrees to radians
*/
static real      MASS; /* MASS of object (kg) */
static real      IXX,IYY,IZZ; /* moment of intertia (Nms^2) */
static int BodyId; /* ID of zone refering to plate */
static real theta[3];
static real      velBody[3];      /* Translational velocity */
static real      grav_acc[3]; /* Gravitational Acceleration*/
static real      centreOfGravity[3]; /* Plate Centre of gravity */
static real omegaBody_old_p[3] = {0.0, 0.0, 0.0};

void collect_data_from_panel()
{
/* Collect data from the associated 6DOF-RBD panel */
#if !RP_NODE
MASS = RP_Get_Real("quatrbd/mass");
IXX = RP_Get_Real("quatrbd/ixx");
IYY = RP_Get_Real("quatrbd/iyy");
IZZ = RP_Get_Real("quatrbd/izz");
theta[0] = D2R*RP_Get_Real("quatrbd/theta-x");
theta[1] = D2R*RP_Get_Real("quatrbd/theta-y");
theta[2] = D2R*RP_Get_Real("quatrbd/theta-z");
velBody[0] = RP_Get_Real("quatrbd/velbody-x");
velBody[1] = RP_Get_Real("quatrbd/velbody-y");
velBody[2] = RP_Get_Real("quatrbd/velbody-z");
omegaBody_old_p[0] = RP_Get_Real("quatrbd/omega-x");
omegaBody_old_p[1] = RP_Get_Real("quatrbd/omega-y");
```

```
omegaBody_old_p[2] = RP_Get_Real("quatrbd/omega-z");
grav_acc[0] = RP_Get_Real("quatrbd/gravity-x");
grav_acc[1] = RP_Get_Real("quatrbd/gravity-y");
grav_acc[2] = RP_Get_Real("quatrbd/gravity-z");
centreOfGravity[0] = RP_Get_Real("quatrbd/cog-x");
centreOfGravity[1] = RP_Get_Real("quatrbd/cog-y");
centreOfGravity[2] = RP_Get_Real("quatrbd/cog-z");
BodyId = RP_Get_Integer("quatrbd/body-id");
#endif

/* Pass arrays and variables to nodes */
host_to_node_real_4(MASS,IXX,IYY,IZZ);
host_to_node_int_1(BodyId);
host_to_node_real(theta,3);              /* Pass array */
host_to_node_real(velBody,3);            /* Pass array */
host_to_node_real(grav_acc,3);           /* Pass array */
host_to_node_real(centreOfGravity,3);    /* Pass array */
host_to_node_real(omegaBody_old_p,3);    /* Pass array */

}
```

```
DEFINE_CG_MOTION(Flight6DOF, dt, vel, omega, time, deltaT)
{
static real forceBody_i[3] = {0.0, 0.0, 0.0};
static real momentBody_i[3] = {0.0, 0.0, 0.0};
static real momentBody_p[3] = {0.0, 0.0, 0.0};
static real omegaBody_i[3] = {0.0, 0.0, 0.0};
static real omegaBody_p[3] = {0.0, 0.0, 0.0};
static real q[4]; /* Rotational Quaternion */
```

```
static real qdot[4]; /* Quaternion rate of change */
static real rotKE;
static real transKE;
static int udf_step_count=0;
real R[3][3]; /* Rotational matrix */
real Wq[3][4]; /* Rotational rates matrix */
real Qerr; /* Unit normality constraint error */
int i,j; /* General iteration loop counters */
Domain *domain = Get_Domain(1);
Thread *ft;

#if RP_HOST
FILE *file; /* Pointer to log file */
#endif

/* If this is the first step of the UDF */
if(udf_step_count==0)
{
collect_data_from_panel();

/* Set Quaternion to initial orientation */
q[0] = cos(theta[0]*0.5)*cos(theta[1]*0.5)*
cos(theta[2]*0.5) + sin(theta[0]*0.5)*
sin(theta[1]*0.5)*sin(theta[2]*0.5);

q[1] = -cos(theta[0]*0.5)*sin(theta[1]*0.5)*
sin(theta[2]*0.5) + sin(theta[0]*0.5)*
cos(theta[1]*0.5)*cos(theta[2]*0.5);

q[2] = cos(theta[0]*0.5)*sin(theta[1]*0.5)*
cos(theta[2]*0.5) + sin(theta[0]*0.5)*
cos(theta[1]*0.5)*sin(theta[2]*0.5);
```

```
q[3] = cos(theta[0]*0.5)*cos(theta[1]*0.5)*
sin(theta[2]*0.5) - sin(theta[0]*0.5)*
sin(theta[1]*0.5)*cos(theta[2]*0.5);

/* Enforcing normality constraint error */
Qerr = q[0]*q[0] + q[1]*q[1] + q[2]*q[2] +
q[3]*q[3] - 1.0;

do /* apply post-correction step repeatedly */
{
for(i=0;i<4;i++)
{
q[i] += -0.5*Qerr*q[i];
}
Qerr = q[0]*q[0] + q[1]*q[1] + q[2]*q[2] +
q[3]*q[3] - 1.0;
} while((Qerr > 1.0e-10) || (Qerr < -1.0e-10));
/************************************************/

udf_step_count=1;
}

/* Get the thread for the debris plate walls */
ft = Lookup_Thread(domain, BodyId);

/* Get CFD computed aerodynamic forces and moments */
Compute_Force_And_Moment(domain, ft, centreOfGravity,
forceBody_i, momentBody_i, TRUE);

/********Pass data from nodes to host**************/
node_to_host_real(forceBody_i,3);
node_to_host_real(momentBody_i,3);
/************************************************/
```

```
/* Add gravity force and any other body forces */
for(i=0;i<3;i++)
forceBody_i[i] += grav_acc[i]*MASS;

/* Compute Translational Velocity */
for(i=0;i<3;i++)
velBody[i] += forceBody_i[i]*deltaT/MASS;

/* Compute new centre of gravity position */
for(i=0;i<3;i++)
centreOfGravity[i] += velBody[i]*deltaT;

/* Compute 3D rotational transformation matrix R */
R[0][0] = q[0]*q[0] + q[1]*q[1] - q[2]*q[2] -
q[3]*q[3];

R[0][1] = 2.0*q[1]*q[2] + 2.0*q[0]*q[3];

R[0][2] = 2.0*q[1]*q[3] - 2.0*q[0]*q[2];

R[1][0] = 2.0*q[1]*q[2] - 2.0*q[0]*q[3];

R[1][1] = q[0]*q[0] - q[1]*q[1] + q[2]*q[2] -
q[3]*q[3];

R[1][2] = 2.0*q[2]*q[3] + 2.0*q[0]*q[1];

R[2][0] = 2.0*q[1]*q[3] + 2.0*q[0]*q[2];

R[2][1] = 2.0*q[2]*q[3] - 2.0*q[0]*q[1];

R[2][2] = q[0]*q[0] - q[1]*q[1] - q[2]*q[2] +
```

```
q[3]*q[3];

/* Transform torque into plate-fixed coordinates */
for (i=0; i<3; i++)
{
momentBody_p[i]=0.0;
for (j=0; j<3; j++)
momentBody_p[i] += R[i][j]*momentBody_i[j];
}

/*Compute plate-fixed angular velocity */
omegaBody_p[0] = omegaBody_old_p[0] + (momentBody_p[0] -
(IZZ - IYY)*omegaBody_old_p[1]*omegaBody_old_p[2])*
deltaT/IXX;

omegaBody_p[1] = omegaBody_old_p[1] + (momentBody_p[1] -
(IXX - IZZ)*omegaBody_old_p[0]*omegaBody_old_p[2])*
deltaT/IYY;

omegaBody_p[2] = omegaBody_old_p[2] + (momentBody_p[2] -
(IYY - IXX)*omegaBody_old_p[0]*omegaBody_old_p[1])*
deltaT/IZZ;

/* Store the new angular frequency for next time step */
for (i=0;i<3;i++)
omegaBody_old_p[i] = omegaBody_p[i];

/* Transform rotational speed into global coordinates */
for (i=0; i<3; i++)
{
omegaBody_i[i]=0.0;
for (j=0; j<3; j++)
omegaBody_i[i] += R[j][i]*omegaBody_p[j];
```

```
}

/*******************************************************
* Update linear and angular velocity of the MOVING ZONE. *
*******************************************************/
NV_V(omega,=,omegaBody_i);
NV_V(vel,=,velBody);

/********Pass data from host to nodes**************/
host_to_node_real(omega,3);
host_to_node_real(vel,3);
host_to_node_real(centreOfGravity,3);
/*************************************************/



/* Compute new rotational quaternion */
Wq[0][0] = -q[1];
Wq[0][1] = q[0];
Wq[0][2] = q[3];
Wq[0][3] = -q[2];

Wq[1][0] = -q[2];
Wq[1][1] = -q[3];
Wq[1][2] = q[0];
Wq[1][3] = q[1];

Wq[2][0] = -q[3];
Wq[2][1] = q[2];
Wq[2][2] = -q[1];
Wq[2][3] = q[0];
```

```
for(i=0;i<4;i++)
{
qdot[i] = 0.0;
for(j=0;j<3;j++)
{
qdot[i] += 0.5*Wq[j][i]*omegaBody_p[j];
}
q[i] += qdot[i]*deltaT;
}

/* Enforcing normality constraint error */
Qerr = q[0]*q[0] + q[1]*q[1] + q[2]*q[2] +
q[3]*q[3] - 1.0;

do /* apply post-correction step repeatedly */
{
for(i=0;i<4;i++)
{
q[i] += -0.5*Qerr*q[i];
}
Qerr = q[0]*q[0] + q[1]*q[1] + q[2]*q[2] +
q[3]*q[3] - 1.0;
} while((Qerr > 1.0e-10) || (Qerr < -1.0e-10));
/************************************************/

/* Compute Euler angles */

theta[0] = atan2((2.0*q[2]*q[3] + 2.0*q[0]*q[1]) ,
(q[0]*q[0] - q[1]*q[1] - q[2]*q[2] + q[3]*q[3]));

theta[1] = -asin(2.0*q[1]*q[3] - 2.0*q[0]*q[2]);

theta[2] = atan2((2.0*q[1]*q[2] + 2.0*q[0]*q[3]) ,
```

```
(q[0]*q[0] + q[1]*q[1] - q[2]*q[2] - q[3]*q[3]));

/* Compute translational and rotational kinetic energy */

rotKE = 0.5*IXX*omegaBody_p[0]*omegaBody_p[0] +
0.5*IYY*omegaBody_p[1]*omegaBody_p[1] +
0.5*IZZ*omegaBody_p[2]*omegaBody_p[2];

transKE = 0.5*MASS*(velBody[0]*velBody[0] +
velBody[1]*velBody[1] + velBody[2]*velBody[2]);

#if RP_HOST
Message("\n \t\t RBD Results !!! \t\t \n omega_x = %12.3e(N)
omega_y = %12.3e(N)  omega_z = %12.3e(N)", omega[0],
omega[1],omega[2]);

Message("\n vel_x = %12.3e(Nm)  vel_y = %12.3e(Nm)
vel_z = %12.3e(Nm)", vel[0],vel[1],vel[2]);

Message("\n \t\t RBD Results !!! \t\t \n F_x = %12.3e(N)
F_y = %12.3e(N)  F_z = %12.3e(N)",forceBody_i[0],
forceBody_i[1],forceBody_i[2]);

Message("\n M_x = %12.3e(Nm)  M_y = %12.3e(Nm)
M_z = %12.3e(Nm)",momentBody_i[0],momentBody_i[1],
momentBody_i[2]);

Message("\n CoG_x = %12.3e(deg)  CoG_y = %12.3e (deg)
CoG_z = %12.3e(deg)\n", centreOfGravity[0],
centreOfGravity[1],centreOfGravity[2]);

Message("\n theta_x = %12.3e(deg)  theta_y = %12.3e (deg)
theta_z = %12.3e(deg)\n Qerr = %12.3e \n", theta[0]*R2D,
```

```
theta[1]*R2D, theta[2]*R2D, Qerr);

/* Open the file for appending data */
file = fopen("QuaternionFreeFlight3dLog.dat", "a");

/*Write data to file */
fprintf(file,"%15.6e", CURRENT_TIME);

fprintf(file, "%15.6e%15.6e%15.6e",
centreOfGravity[0], centreOfGravity[1], centreOfGravity[2]);

fprintf(file,"%15.6e%15.6e%15.6e",
theta[0]*R2D, theta[1]*R2D, theta[2]*R2D);

fprintf(file,"%15.6e%15.6e%15.6e",omega[0],omega[1],omega[2]);

fprintf(file,"%15.6e%15.6e%15.6e",vel[0],vel[1],vel[2]);

fprintf(file, "%15.6e%15.6e%15.6e",
forceBody_i[0], forceBody_i[1], forceBody_i[2]);

fprintf(file, "%15.6e%15.6e%15.6e",
momentBody_i[0], momentBody_i[1], momentBody_i[2]);

fprintf(file,"%15.6e%15.6e%15.6e\n", Qerr, rotKE, transKE);
/* Close the file */
fclose(file);

#endif

}
```

Appendix D

Porous Building Model

```
#include "udf.h"
#include "math.h"

#define UDM_CR 0 /* UDM to store resistance */
#define CR0 1.0E+09 /*Resistance of the porous medium */


/* Compute factor to correct roughness
1 = Cell Within Planes,
0 = Cell Entirely outside Planes. */

real RoughnessCorrection(cell_t cell, Thread *cellThread)
{
real factor;
int n,j;
Node *node;
real dNSum1 = 0.0;
real dNSum2 = 0.0;

/*
Define planes enclosing house region and for each plane,
set the 3D plane equation: (aX+bY+cZ+d=0). */

for (j=0; j<6; j++)
{
real coeffA =0.0, coeffB=0.0, coeffC=0.0, coeffD=0.0;
switch (j)
{
case 0:          /* Windward roof plane */
coeffA = -0.364;
coeffB = 1.0;
coeffC = 0.0;
coeffD = 0.05;
```

```
break;
case 1:          /* Left Wall, plane X=-0.14 */
coeffA = -1;
coeffB = 0;
coeffC = 0;
coeffD = -0.14;
break;
case 2:          /* , plane Z=3.0 */
coeffA = 0;
coeffB = 0;
coeffC = 1;
coeffD = -3.0;
break;
case 3:          /* , plane Z=-3.0 */
coeffA = 0;
coeffB = 0;
coeffC = -1;
coeffD = -3.0;
break;
case 4:          /* Right Wall, plane X=5.85 */
coeffA = 1;
coeffB = 0;
coeffC = 0;
coeffD = -5.85;
break;
case 5:          /* Leeward roof plane */
coeffA = 0.364;
coeffB = 1.0;
coeffC = 0.0;
coeffD = -2.179;
break;
}
```

```
c_node_loop(cell,cellThread,n)
{
real xN, yN, zN, dN;
node = C_NODE(cell,cellThread,n);

/* Store the nodal coordinates */
xN = NODE_X(node);
yN = NODE_Y(node);
zN = NODE_Z(node);

/* Calculate the distance from node to plane */
dN = (coeffA*xN + coeffB*yN + coeffC*zN + coeffD)
/sqrt(coeffA*coeffA + coeffB*coeffB + coeffC*coeffC);

dNSum1 += dN;
dNSum2 += fabs(dN);
}
}

factor = pow((0.5*(1.0 - (dNSum1/dNSum2))),1000);
return (factor);
}




/* UDF to define viscous resistance profile */
DEFINE_PROFILE(Viscous_Resistance, ct, i)
{
cell_t c;

begin_c_loop(c,ct)
{
```

```
real factor = 1.0;

factor *= RoughnessCorrection(c, ct);

/* Store resistance coefficient of each cell. */
C_UDMI(c,ct,0) = factor*CR0;

/* Update profile */
C_PROFILE(c,ct,i) = C_UDMI(c,ct,UDM_CR);
}
end_c_loop(c,ct);
}
```